Preparation and Manipulation of an ^{87}Rb Bose-Einstein Condensate

Aidan Arnold

A thesis submitted for the degree of

Doctor of Philosophy in Physics

at the University of Sussex

November 9, 1999

Declaration

I hereby declare that this thesis has not been submitted, either in the same or different form, to this or any other university for a degree.

Signature:

Acknowledgements

Right! Now the fun part... thanking all the wonderful people who've helped me these last three busy years!

First of all, I must give a huge vote of thanks to my supervisor Malcolm. You've always had time when I was stuck, and I've learnt a great deal about experimental atomic physics under your expert tutelage. Your bottomless bag of tricks for things computer-related have always proved extremely handy – somehow you always managed to get *Mathematica* and *Labview* doing exactly what I wanted, in about the same time it took to explain the problem!

Ben, you were a complete fountain of knowledge regarding electronics, and many thanks for all your help with Quickroute PCBs! If it wasn't 'out back' then it probably wasn't worth having anyway. I think you've truly earnt the lifetime title of 'Super Find-It Man.' Thanks for putting me up at your place for the last stressed-out month too!

A tonne of thanks are due to Ifan, for his quick wit, and even better impression of a New Zealand accent. Your extensive library of references and proof-reading skills were extremely useful, and you always had a sympathetic ear when things seemed about ready to go down the gurgler.

Giles you're a LATEX/PERL guru, thanks a mill' for your cool BIDS to BibTEX converter, and help with other TEXrelated ordeals!

Thanks to Simon, for never physically attacking me even when I wanted the lab lights out for the twenty thousandth time :-) It was always good working with you and Calum in what was, at times, a very crowded house.

Huge thanks must in fact go to *everyone* at SCOAP – you're a truly great bunch of people to work with and you've all helped me in so many ways. Thanks must especially go to Ed, for bringing such a cool group together in the first place! I've really enjoyed my stay here.

Mum and Dad, you've supported me my whole life, and I'll never ever be able to thank you enough. I couldn't have wished for better parents!

My dear Sonja, thanks heaps for all of your help with proof-reading and figures in the eleventh hour. Most importantly of all however, I'm indebted to you for making me realise what life is all about... here's to a long and happy future together!

Preparation and Manipulation of an ^{87}Rb Bose-Einstein Condensate

Aidan Arnold

A thesis submitted for the degree of

Doctor of Philosophy in Physics

at the University of Sussex

November 9, 1999

Summary

This thesis details the experimental realisation and magnetic manipulation of an ^{87}Rb Bose-Einstein Condensate (BEC).

An introduction to the concepts and mechanisms leading to the formation of a Bose-Einstein condensate is given, as well as a brief overview of BEC manipulation techniques and recent BEC experiments. This is followed by a theoretical discussion of the evolution of BECs, detailing in particular their statistical and quantum mechanical properties. The results of this chapter will be used later in the thesis to analyse experimental data regarding the temperature-dependent ground state population, ballistic expansion and magnetic manipulation of BECs.

Elaboration of the various theoretical mechanisms involved in BEC production and detection will ensue. This chapter will be followed by an account of our experimental implementation of these BEC formation techniques, concluding with the creation of the Sussex rubidium BEC. Simplicity and durability are novel aspects of the BEC apparatus design, which incorporates easy-to-build stable diode lasers, a low power double magneto-optical trap (MOT) employing a loading technique based solely on light-pressure, the omission of dark or compressed MOT stages in the BEC sequence, a stable magnetic trap regulated by straightforward power MOSFET banks and an extra high vacuum essentially maintained by a single low-throughput ion pump.

Magnetic mirrors for laser-cooled atoms have now been produced with excellent optical quality. A natural extension of this work is the use of these 'hard' magnetic mirrors as atom optical elements to focus and image coherent atomic sources such as BECs. In this thesis first steps in this direction are reported with the demonstration of reflection and focusing of an ^{87}Rb BEC by a soft magnetic mirror. Studies of the BEC's dynamics as the mirror's radius of curvature is varied relative to the drop height are also presented.

Contents

List of Figures

List of Tables

List of abbreviations

ADC	Analogue to digital converter
AOM	Acousto-optic modulator
BEC	Bose-Einstein condensation/condensate
BS	Beamsplitter
(C/D)MOT	(Compressed/dark) magneto-optical trap
CCD	Charged coupled device (camera)
DAC	Digital to analogue converter
GPE	Gross-Pitaevskii equation
HP	High pressure (MOT)
IP	Ioffe-Pritchard (magnetic trap)
LP	Low pressure (MOT)
(MOS)FET	(Metal-oxide semiconductor) field effect transistor
ND	Neutral density
NEG	Non-evaporable getter (vacuum pump)
OD	Optical density
PCB	Printed circuit board
PSD	Phase-space density
PZT	Piezo-electric transducer
RGA	Residual gas analyser
RF	Radio frequency
SRS	Stanford research systems
TFA	Thomas-Fermi approximation
TOP	Time-orbiting potential (magnetic trap)
TTL	Transistor transistor logic
VCA	Voltage-controlled attenuator
VCO	Voltage-controlled oscillator
XHV	Extra high vacuum

Physical constants

(Refs. [1, 2, 3, 4])

Planck's constant	$h = 6.626 \times 10^{-34}$ J s
Reduced Planck's constant	$\hbar = \frac{h}{2\pi} = 1.055 \times 10^{-34}$ J s
Boltzmann's constant	$k_B = 1.381 \times 10^{-23}$ J/K
Speed of light	$c = 2.998 \times 10^{8}$ m/s
Permeability of free space	$\mu_0 = 4\pi \times 10^{-7}$ H/m
Permittivity of free space	$\varepsilon_0 = 8.854 \times 10^{-12}$ F/m
Earth's surface gravitational acceleration (UK)	$g = 9.81$ m/s^2
Electron charge	$e = 1.602 \times 10^{-19}$ C
Electron mass	$m_e = 9.109 \times 10^{-31}$ kg
Proton mass	$m_p = 1.673 \times 10^{-27}$ kg
Atomic mass unit	$m_{amu} = 1.661 \times 10^{-27}$ kg
Bohr radius	$a_0 = 5.292 \times 10^{-11}$ m
Bohr magneton	$\mu_B = \frac{e\hbar}{2m_e} = 9.274 \times 10^{-24}$ J/T
Nuclear magneton	$\mu_N = -\frac{e\hbar}{2m_p} = -5.051 \times 10^{-27}$ J/T
Proton magnetic moment	$\mu_p = 2.793\,\mu_N$

Rubidium atomic constants

Mass of ^{87}Rb, ^{85}Rb	$m_{87} = 86.91\,m_{amu}$, $m_{85} = 84.91\,m_{amu}$
^{87}Rb, ^{85}Rb magnetic moment	$\mu_{87} = 2.751\,\mu_N$, $\mu_{85} = 1.353\,\mu_N$
^{87}Rb, ^{85}Rb nuclear spin	$I_{87} = 3/2$, $I_{85} = 5/2$
Rb D2 linewidth	$\Gamma = 2\pi\Gamma_\nu = 2\pi \times (6.065(10)\,\text{MHz})$
Rb D1 linewidth	$\Gamma = 2\pi\Gamma_\nu = 2\pi \times (5.745(10)\,\text{MHz})$
Rb D2 frequency	$\nu_{D2} = 384.23$ THz
Rb D1 frequency	$\nu_{D1} = 377.11$ THz

Chapter 1

An introduction to BEC

1.1 Breakthrough

The concept of atoms as particles is familiar to many, however at the microscopic level the classical laws of physics break down and the wave nature of matter becomes apparent – this is the realm of quantum mechanics. In a quantum mechanical description atoms divide into two species: fermions (with half-integer spin) and bosons (with integer spin). Two fermions can never exist in the same quantum state, whereas bosons can and in fact prefer to occupy states which are already inhabited by other bosons.

In the mid-1920s Bose and Einstein predicted a striking quantum mechanical phenomenon [5, 6, 7] later to be known as Bose-Einstein condensation (BEC) [8, 9]. BEC is a phase transition which occurs if an atomic distribution comprised of bosons is cold and dense enough that the atomic separation nears the atomic thermal de Broglie wavelength, Λ_{dB}. Then a macroscopic fraction of atoms in the distribution condense into the same, lowest energy (Heisenberg uncertainty limited) quantum state. BEC is a collective effect in that the individual atoms act in phase with each other. The relationship between BEC and atoms is thus analagous in many ways to that between laser and thermal light, for example in terms of the coherence and the amplification of the respective atomic and photonic quantum mechanical wavefunctions. One may in fact argue that Bose-Einstein condensation is akin with the realisation of an atomic laser.

The quantity used to describe the Bose-Einstein phase transition is the phase space density (PSD). This is defined as

$$\text{PSD} = n\Lambda_{dB}{}^3, \tag{1.1}$$

where n denotes the atomic number density, and the thermal de Broglie wavelength at the atomic temperature T is $\Lambda_{dB} = h/\sqrt{2\pi m k_B T}$. In a three dimensional harmonic potential the Bose-Einstein phase transition occurs when an atomic ensemble is cold and dense enough to reach the critical phase-space density $\text{PSD} = \zeta(3) = 1.202$ (this will be derived in Ch. 2).

Although manifestations of quantum degeneracy had been seen previously in other atomic systems – namely in the sometimes counter-intuitive properties of superconductivity, exciton condensation, and ^{3}He/^{4}He superfluidity [8] – the strong inter-atomic forces in these systems limited the relative number of atoms in the Bose condensed fraction and made interpretation of the nature of these macroscopic quantum systems extremely difficult. The density and temperature at the superfluid transition in liquid ^{4}He are $n = 2.4 \times 10^{22}$ cm^{-3}, $T = 2$ K respectively [8], with a phase-space density of PSD ≈ 6. Ideally, one would like a material whose atoms are far enough apart to have minimal interaction, yet be cold enough to have a sufficiently long de Broglie wavelength for condensation.

All atoms have a vapour phase at low density and relatively high temperature. At higher densities condensed matter phases exist, however the intermediate densities are thermodynamically forbidden except at high temperatures [10]. This would at first appear to rule out the possibility of a gaseous BEC, yet precisely this was achieved in 1995, when three groups observed BEC in the atomic vapours of different alkali metal species: ^{87}Rb, ^{23}Na and ^{7}Li (the first entries of Table 1.1). The key to their achievement lay in the high rates of two-body elastic collisions within their respective atomic samples (ensuring thermal equilibrium), but low rates of three-body recombination (preventing chemical equilibrium). This metastable atomic vapour can therefore exist, for a limited time, in the thermodynamically forbidden regime.

Even with this consideration, given the very low PSD $\left(\approx 10^{-18} \right)$ of room temperature atomic gases, it had long appeared that the observation of gaseous BEC would remain an elusive goal. These remarkable new BECs therefore had to occur at extremely low temperatures – a few tens of nano-Kelvin. The counter-intuitive world of quantum mechanics had in the past often been limited to text books, yet here was a macroscopic quantum object that could be observed on a video camera!

1.2   The path to gaseous BEC

The experimental goal of BEC in an atomic vapour has typically been reached by a three-stage sequential process:

- laser cooling and trapping
- magnetic trapping
- evaporative cooling

The exception to this rule was hydrogen, as the paucity of laser sources with sufficient power at the required frequency meant that alternatives to laser cooling had to be sought (Table 1.1). This three stage path was also taken at the University of Sussex, and these stages will be briefly outlined below. For each step of the path through phase space taken at Sussex there is a corresponding point in Fig. 1.1, and an associated experimental image of the atomic cloud in Fig. 1.2.
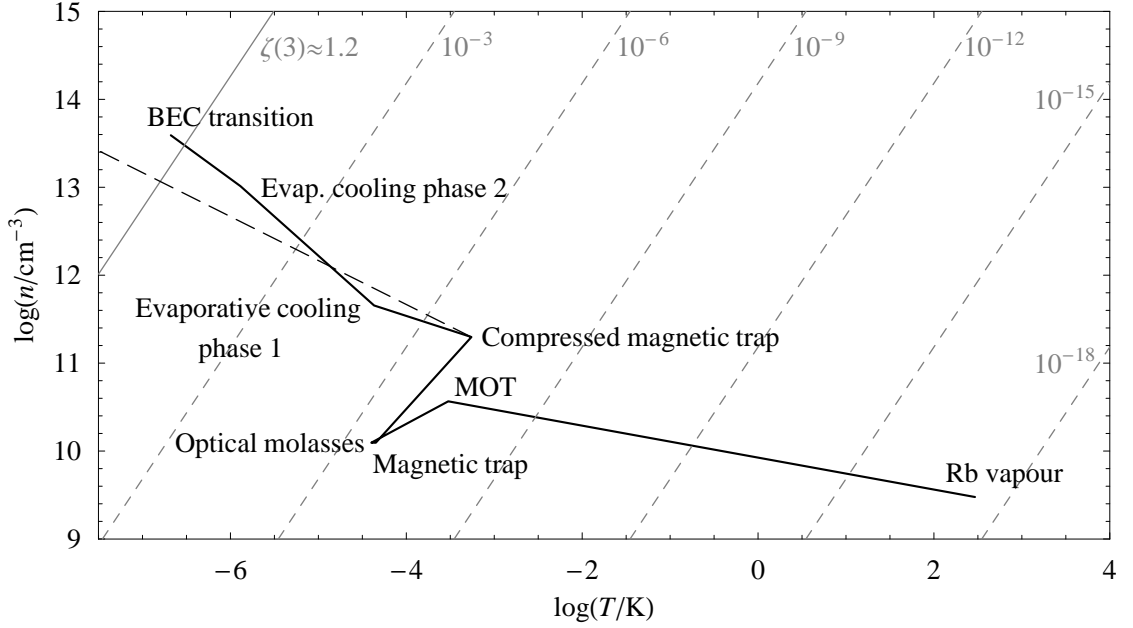
Figure 1.1: The path through phase space which led to the Sussex BEC (black line). Dashed grey lines indicate contours of constant phase space density $\left(\frac{\Delta \log(n)}{\Delta \log(T)} = \frac{3}{2} \right)$ numbered by their associated PSD, and the solid grey line marks the PSD above which condensation occurs. The black dashed line (with slope $\frac{\Delta \log(n)}{\Delta \log(T)} = -\frac{1}{2}$) is a contour of constant elastic collision rate within a harmonic magnetic trap.

Probably the biggest step toward gaseous BEC occurred with the realisation of three-dimensional laser-cooling at AT&T Bell Labs in 1985 [11]. The concept of 'Doppler' laser-cooling can be qualitatively explained by considering an atom irradiated by two counter-propagating laser beams with identical frequency ν. Suppose that the laser light has a slightly lower frequency than (i.e. is red-detuned from) an energy level transition within the atom, with frequency ν_0. If the atom has a velocity component along the propagation axis of the laser beam pair, then due to the Doppler effect the atom will observe a higher laser frequency (closer to resonance with the atomic transition) in the laser it moves *towards*. The laser beam the atom is moving *away* from is observed to have a lower frequency and so appears to be detuned further from resonance. Therefore as soon as an atom moves toward either of the two laser beams it will absorb more photons from this beam than from the laser it is moving away from.

This creates an imbalance in the light pressure force on the atom of the form $\mathbf{F} \propto -\mathbf{v}_{\parallel}$, where $\mathbf{v}_{\parallel}$ is the atom's velocity along the propagation axis of the laser beams. Thus red-detuned counter-propagating laser beam pairs create a viscous force, which acts to decrease the atom's speed and therefore temperature. The same argument shows that blue-detuned laser beams cause heating. The viscous nature of the force in the red-detuned laser configuration led to the term 'optical molasses.' It will be shown in section 3.1 that atoms in optical molasses can feel decelerations 10^4 times stronger than gravity. The

first experiment on three-dimensional optical molasses (created by three orthogonal counter-propagating laser beam pairs) reached temperatures around $200\,\mu$K [11].

In 1987 it was realised that atoms could be exposed to a modified form of optical molasses which created both damping and restoring forces – cooling the atoms and simultaneously providing strong spatial confinement. This 'magneto-optical trap' (MOT) [12] depends on the Zeeman effect and will be discussed in more detail in section 3.1. The MOT (Fig. 1.2 (image 1)) relies on appropriately circularly polarised red-detuned laser beams and a quadrupole magnetic field (Fig. 1.3) to produce a restoring force $\mathbf{F} \propto -(x, y, 2z) \approx -\mathbf{r}$, where $\mathbf{r}$ is the displacement of an atom from the centre of the trap. Atoms undergo a very large increase in phase space density when they are magneto-optically trapped from a room temperature vapour, as can be seen in Fig. 1.1.

The final temperature of atomic clouds laser cooled using 'Doppler' (and later 'sub-Doppler') cooling mechanisms is determined by the balance between the viscous cooling forces and heating due to the statistical nature of photon absorption and emission. In the case of Doppler cooling this leads to the 'Doppler temperature' (Eq. 3.4) which was predicted to limit temperatures attainable with the simple two-level Doppler cooling mechanism [13] described earlier. Shortly after the development of the first MOT, experiments in optical molasses surprisingly reached temperatures below the Doppler temperature. The new, more complex, cooling mechanisms responsible for these sub-Doppler temperatures relied on the light shifts and optical pumping which are evident in the multi-level energy system of 'real' atoms [14]. Sub-Doppler cooling mechanisms were observed in low intensity (and/or far red-detuned) optical molasses if stray magnetic fields were decreased below the level of $100\,$mG. High density and relatively low temperature atomic clouds can therefore be initially captured in a MOT, then subjected to further cooling in optical molasses. The maximal PSD increase after applying molasses can be obtained by striking a balance between the final temperature reached and the density loss due to atomic Brownian motion within the optical molasses (Fig. 1.2 (image 2)).

The statistical nature of photon absorption also creates a lower limit on the temperature of sub-Doppler cooling mechanisms. When atoms absorb light they acquire a momentum of at least one photon recoil momentum, $\Delta p = h/\lambda$. This leads to the recoil temperature T_R (Eq. 3.15), a lower limit on most sub-Doppler cooling mechanisms. Experimental temperatures as low as $T \approx 10 T_R$ ($2\,\mu$K in caesium) were achieved. With a lower bound on T, it is necessary to increase the PSD of atomic clouds by increasing their density. Unfortunately the density in MOTs and molasses is also limited, in this case by the Coulomb-like repulsion of closely packed radiating atoms [15], although the upper limit on density was increased to some extent through the use of 'dark' [16, 17, 18] and 'compressed' [19] MOTs.

The inherent temperature and density limitations in MOTs and molasses are co-dependent: low temperatures correlate with low densities and vice versa. These limitations curtail phase-space density increases higher than around PSD $= 10^{-6}$ by ordinary optical means. Further increases in PSD therefore
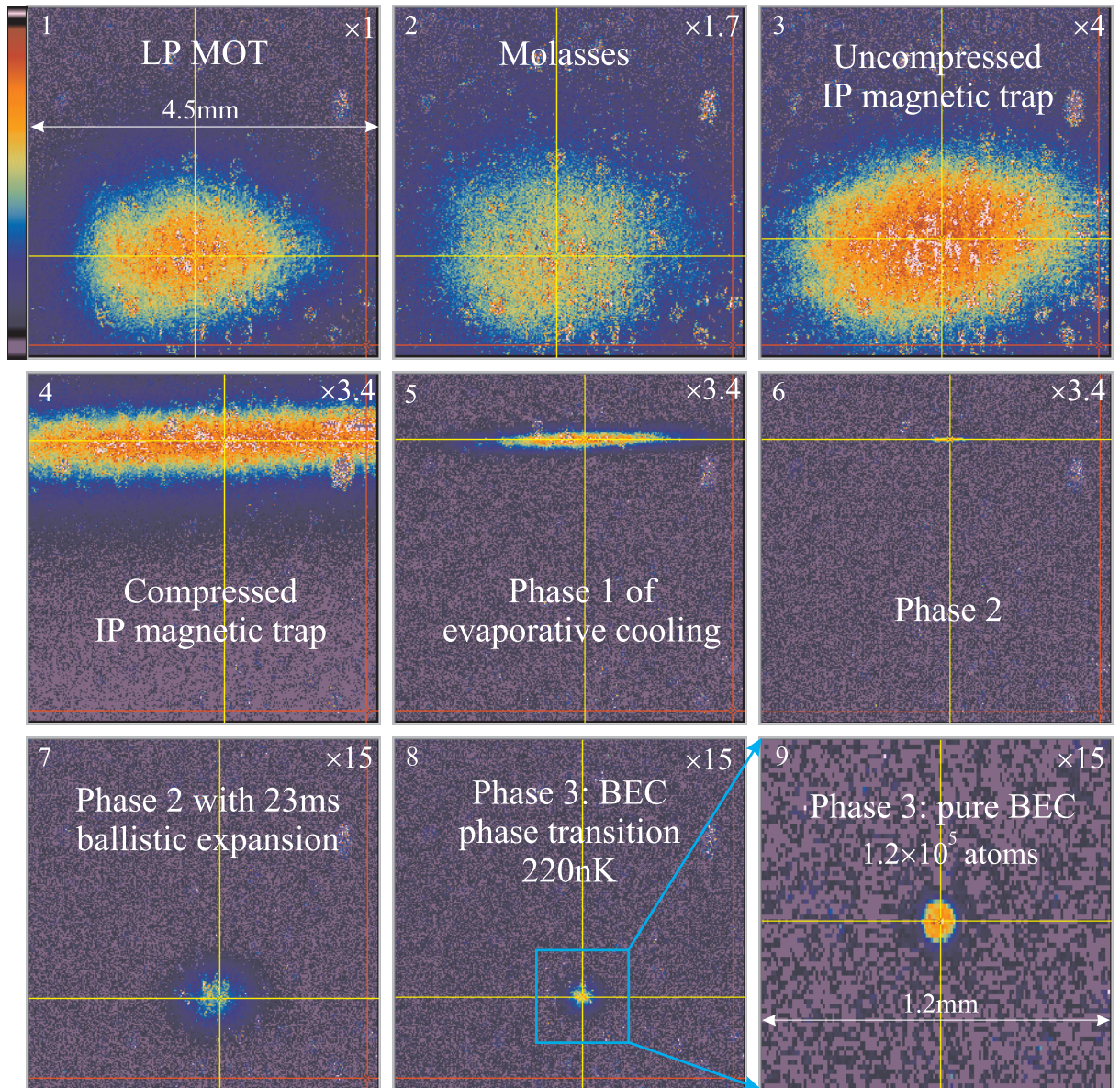
Figure 1.2: Absorption images (section 3.1.7) of the experimental steps leading to the Sussex BEC. The number in the top left-hand corner of each image indicates the stage in the sequence, and the scale factor indicates the relative height of the images, weighted by the optical density and log scale magnification factor.
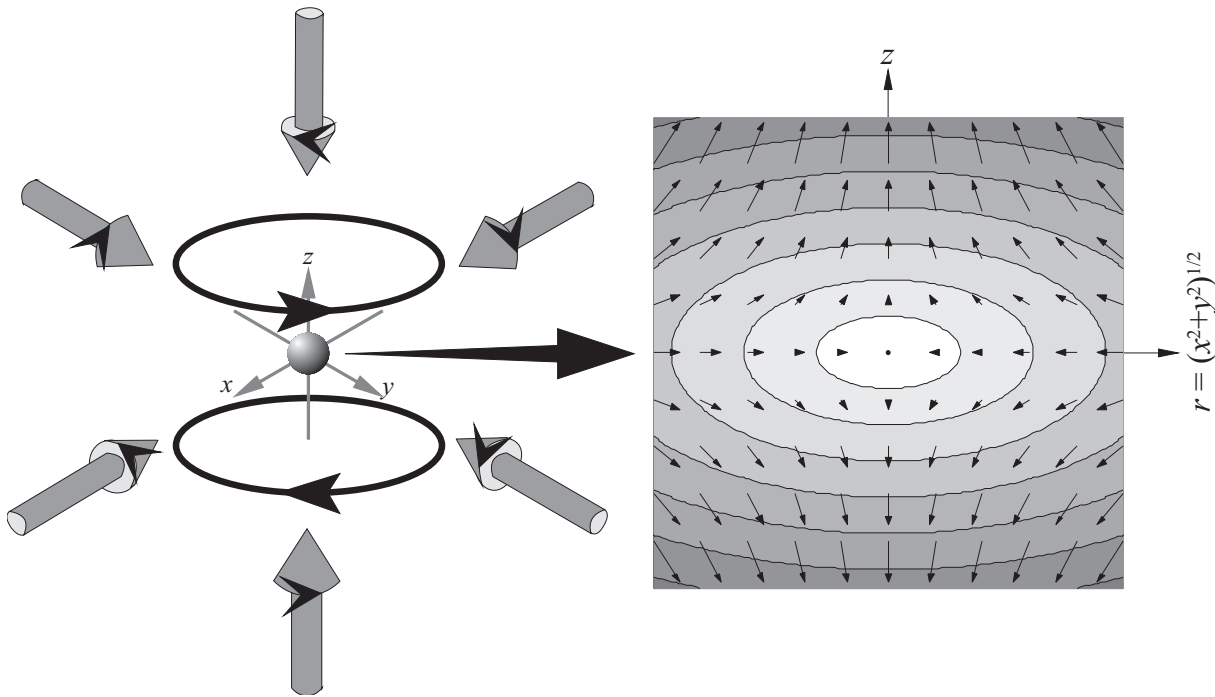
Figure 1.3: The magnetic field coils and laser beams of a magneto-optical trap (left image). The respective circular polarisations of the laser beams are as indicated. The image to the right depicts the cylindrically symmetric first-order magnetic vector field generated by the coils. The contours indicate the magnitude of the magnetic field.

require the implementation of another method for cooling and compression.

The next experimental step toward BEC exploits the fact that atoms have a magnetic moment, $\boldsymbol{\mu}$. An atom's potential energy in a magnetic field is $U(\mathbf{r}) = -\boldsymbol{\mu} \cdot \mathbf{B}(\mathbf{r})$. After being trapped and cooled in the MOT and optical molasses the atoms are next optically pumped into quantum states with the atomic magnetic moment anti-aligned with the magnetic field. The atoms will then be magnetically trapped at spatial minima in the magnitude of an applied magnetic field. For MOTs it is important to perform experiments in ultra high vacuum systems ($P \approx 10^{-9}$ torr) to reduce losses of the low temperature MOT atoms due to collisions with thermal background gases. Low background pressure is even more important for magnetic traps because of their shallower trapping potential. In a MOT the damping forces can prevent atomic loss due to glancing collisions from background atoms, but this cannot occur in the conservative magnetic trap potential.

Initial magnetic traps used the simple quadrupole field generated by an anti-Helmholtz coil pair (Fig. 1.3). Problems occur when the atoms pass in close proximity to the magnetic field zero at the centre of the trap however, as non-adiabatic motion can occur when the spatially varying magnetic field vector rotates in the reference frame of the atom faster than the atom's magnetic moment precesses around the local magnetic field vector with the Larmor frequency ($\nu_L \approx \frac{\mu_B}{h}|\mathbf{B}|$). Thus, near the zero field point,

atoms can spin flip into anti-trapped states and are expelled from the magnetic trap. Problems with these 'holes' in quadrupole magnetic traps were solved by the construction of traps with non-zero magnetic field minima: in particular the time-orbiting potential [20] and Ioffe-Pritchard [21, 22] magnetic traps.

Atoms are initially loaded into a magnetic trap with relatively weak spring constants in order to provide a potential that has an equilibrium atomic distribution which matches the density and temperature of the atoms after optical pumping (Fig. 1.2 (image 3)). This 'mode-matching' prevents increases in the phase space density. The trapping potential is then steepened by adiabatically increasing the current in the magnetic field coils (Fig. 1.2 (image 4)). This compression stage should not alter the phase space density, however the elastic collision rate between trapped atoms is increased (Fig. 1.1), which will be of interest to us in the last stage of BEC creation.

In a magnetic trap the atoms are freed from the temperature-limiting statistical fluctuations of laser cooling forces and the density-limiting effects of reradiated light, however cooling cannot occur directly in a conservative magnetic trapping potential. Therefore the final experimental process, radio frequency (RF) evaporative cooling, is used to both lower the temperature and raise the density of the atoms in the magnetic trap.

RF evaporative cooling is essentially the same principle whereby one cools a cup of coffee by blowing the steam off the top. The high energy atoms are selectively removed, allowing the remaining atoms to rethermalise at a lower temperature. If the rate γ_{el} of rethermalising atomic elastic (i.e. 'good') collisions is a sufficiently high multiple of the loss rate $\gamma_{loss} = 1/\tau_{loss}$ from the magnetic trap due to background gas and inelastic (i.e. 'bad') collisions then 'runaway' evaporation can occur. Runaway evaporation happens when the ratio $R = \gamma_{el}\tau_{loss}$ is above the critical value $R_{crit} \approx 150$ (Sec. 3.3). When $R > R_{crit}$ it is possible to make the elastic collision rate (and evaporation efficiency) within the atomic cloud rapidly increase with time. Conversely when $R < R_{crit}$ the collision rate and efficiency will rapidly drop. Atoms at the runaway threshold $R \cong R_{crit}$ maintain a relatively constant elastic collision rate (cf. Fig. 1.1) – the atomic temperature decreases at the same rate as the number of trapped atoms and so the phase space density increases by two orders of magnitude for every factor of 10 loss in atom number.

Because evaporation is a lossy process (the number of trapped atoms typically drops by a factor of 1000), it pays to start with large numbers of atoms in the initial MOT phase in order to create large BECs. So far this has primarily been achieved through the use of double MOT systems [23], or MOTs loaded from atomic beams slowed by σ^- Zeeman [24, 25] or chirped [26, 27, 28] slowers.

A summary of the world's experimental BEC groups and their techniques is shown in Table 1.1. Simplicity and durability are the novel aspects of the Sussex BEC apparatus design, which incorporates easy-to-build stable diode lasers, a low power double magneto-optical trap (MOT) employing a simple loading scheme, the omission of dark or compressed MOT sequences, a highly stable magnetic trap regulated by straightforward power MOSFET banks and an extra high vacuum essentially maintained by

a single low-throughput ion pump.

Group	Atom$_{|F,m_F\rangle}$	Loading/MOT type	B trap	ν_r, ν_z (Hz)	N_{MOT}, η_B	N_{BEC}
JILA$_1$* [29]-[32]	^{87}Rb$_{|2,2\rangle}$	MOT/(D+C)MOT	TOP	$(42, 120) \times 3^{\frac{1}{2}}$	$1\ 10^7, 40\%$	$5\ 10^3$
JILA$_2$ [33, 34]	^{87}Rb$_{|2,2\rangle+|1,-1\rangle}$	$2\times$MOT/CMOT	IPBB	$400, 11$	$1\ 10^9, 50\%$	$2\ 10^6$
JILA$_3$ [35]-[38]	^{87}Rb$_{|2,1\rangle+|1,-1\rangle}$	$2\times$MOT/MOT?	TOP	$35, 99$	$1\ 10^9, 50\%$	$5\ 10^5$
MIT(Na)$_1$* [39]	^{23}Na$_{|1,-1\rangle}$	ZS/DMOT	Q+OP	$235, 410, 745$	$>10^{10}, 10\%$	$5\ 10^5$
MIT(Na)$_2$ [40]-[56]	^{23}Na$_{|1,m_F\rangle}$	ZS/DMOT	IPC+DT	$250, 19$	$>10^{10}, 20\%$	10^7
Rice [57]-[63]	^{7}Li$_{|2,2\rangle}$	ZS/molasses	IPPM	$150, 130$	NA, $2\ 10^8$	$<2\ 10^3$
Texas [64]	^{87}Rb$_{|2,2\rangle}$	ZS/DMOT	TOP	$64, 181$	$5\ 10^9, 30\%$	$2\ 10^5$
Rowland [65, 66]	^{23}Na$_{|1,-1\rangle}$	ZS/DMOT	IP4D	$326, 27$	$6\ 10^9$	$2\ 10^6$
Yale [67, 68]	^{87}Rb$_{|2,2\rangle}$	MOT/(D+C)MOT	TOP	$(41, 117) \uparrow$	$1\ 10^8, 10\%$	$3\ 10^4$
Konstanz [69, 70]	^{87}Rb$_{|2,2\rangle}$	$2\times$MOT/CMOT	IPCC	$280, 24$	$>1\ 10^9$	$1\ 10^5$
München [71, 72]	^{87}Rb$_{|2,2\rangle}$	$2\times$MOT/CMOT	IP3C	$200, 20$	$1\ 10^9$	$6\ 10^5$
NIST [73]-[76]	^{23}Na$_{|1,-1\rangle}$	ZS/DMOT	TOP	$180, 250, 360$	$>10^{10}$	10^{6-7}
ENS [77]	^{87}Rb$_{|2,2\rangle}$	$2\times$MOT/MOT?	IP3C+B	$157, 12$	$1\ 10^9$	$3\ 10^5$
MIT(H) [78, 79]	^{1}H$_{|1,1\rangle}$	^{4}He fridge/NA	IPSC	$3900, 10$	NA, see ref.	$1\ 10^9$
Orsay [80, 81]	^{87}Rb$_{|1,-1\rangle}$	ZS/DMOT	IPFe	$75, 25$	$1\ 10^9, 60\%$	$>2\ 10^5$
Hannover	^{87}Rb$_{|2,2\rangle}$	CS/(D+C)MOT	IPC	$333, 17$	$5\ 10^8, 40\%$	$>10^5$
Otago [82]	^{87}Rb$_{|2,2\rangle}$	$2\times$MOT/CMOT	TOP	$(29, 81) \times 10^{\frac{1}{2}}$	$5\ 10^9, 20\%$	$2\ 10^5$
Sussex	^{87}Rb$_{|2,2\rangle}$	$2\times$MOT/MOT	IPBB	$223, 11$	$6\ 10^8, 50\%$	$1\ 10^5$
Tokyo [83]	^{87}Rb$_{|1,-1\rangle}$	$2\times$MOT/MOT	IPC	$158, 12$	$2\ 10^9, 40\%$	$3\ 10^5$
Kyoto	^{87}Rb$_{|2,2\rangle}$	$2\times$MOT/CMOT	IPC	$210, 17$	$1\ 10^9, 50\%$	$3\ 10^5$
Oxford	^{87}Rb$_{|2,2\rangle}$	$2\times$MOT/CMOT	TOP	$(29, 81) \times 20^{\frac{1}{2}}$	$6\ 10^8, 30\%$	$1\ 10^4$
Firenze	^{87}Rb$_{|2,2\rangle}$	$2\times$MOT/CMOT	IP3C+B	$190, 13$	$2\ 10^9$	$2\ 10^5$

Table 1.1: The present list of laboratories (by institution, then chronologically) who have produced BECs, with a summary of publications and experimental parameters: ν_r, ν_z denote the radial and axial trapping frequencies of cylindrically symmetric magnetic traps, N_{MOT}, N_{BEC} refer to the number of atoms in the MOT and BEC respectively, and η_B is the transfer efficiency from MOT to magnetic trap. Asterisks indicate early BEC rigs that are no longer in use. For two-component BECs, trap frequencies are given for the species with the highest magnetic moment. Abbreviations used: DMOT=dark MOT, CMOT=compressed MOT, $2\times$MOT=double MOT, (Z/C)S=(σ^- Zeeman/chirped) atomic beam slower, TOP=time-orbiting potential, IP(BB/C/PM/4D/CC/3C(+B)/SC/Fe)=Ioffe-Pritchard (baseball/cloverleaf/permanent magnet/four-dee/clip coil/three coil(+bias)/superconducting/iron-core), Q+OP=quadrupole+optical plug [39], DT=dipole trap [47, 84].

1.3 Recent developments

The dilute nature of the atomic vapour BEC allowed comparison of the ground state population's temperature dependence with the early theoretical predictions of Bose and Einstein, yielding strikingly close agreement [31, 40, 64, 67]. A particularly notable experiment involved two spatially separated BECs which were allowed to expand and overlap, creating a high visibility atomic matter wave interference pattern – in analogy with the spatial intensity modulation generated by the interference of two laser beams [44].

So far, experiments have looked at BEC collective and hydrodynamic excitations [30, 32, 42, 50], their statistical correlations [34], ballistic expansion [69, 70, 85], Feshbach resonances [48, 54] and the collapse of BECs with attractive interactions [63]. Electromagnetically induced transparency (EIT) enables the observation of drastically reduced light speed group velocities within a cold atomic vapour (particularly in the case of BEC [66]).

BECs have been observed non-destructively [41], enabling studies of their formation [49] and the propagation of 'sound' within the BEC [45, 46]. They have been coupled out of magnetic traps either with radio frequency (RF) waves [43, 72, 82], or stimulated Raman transitions [74], to create pulsed or quasi-continuous beams of coherent atoms – atom lasers.

Multiple spin-component condensates have been observed [33]. The dynamical interaction [35, 36] of the components and their relative phase [37] have also been studied. Spin component dynamics have been seen for BECs in 'optical dipole' traps [47, 53]. The adiabatic application of a dipole laser beam can be used to greatly enhance an atomic cloud's PSD, allowing early and reversible condensation [51].

Fundamental phenomena, commonly studied with light, have now been observed in BECs: Bragg diffraction [73], Bragg spectroscopy [55] and even four-wave mixing [75]. There have been reports of quantum tunnelling across spin domains [56], and quantum interference of a BEC tunnelling through a standing light wave.

Some very interesting recent developments in the field were the generation of vortices in BECs [86], the realisation of superradiant Rayleigh scattering from a BEC [87] and the first observation of a degenerate Fermi gas (the equivalent quantum degenerate regime as BEC for fermionic species) [88].

Several review articles [9, 89, 90, 91, 92, 93, 94, 95, 10, 96] and a recent book [8] are devoted to both BEC experiment and theory. After the first experimental observations of BEC in 1995 the various theory papers on the topic rapidly became too numerous to mention in detail. The Georgia Southern University BEC web page [97] is a good source of information on both experimental and theoretical BEC, with a comprehensive bibliography. Many preprints of BEC related papers appear on the Los Alamos National Laboratory preprint archive [98].

1.4   Magnetic manipulation of a BEC

With so many rapidly evolving experiments being performed on this new state of quantum matter, it is now interesting to develop elements with which BECs can be coherently transported and manipulated. Just as laser light can be reflected by mirrors, diffracted by gratings or coupled into fibres, atom-optical analogues exist for atoms. It has even become possible to generate atomic holograms [99].

The majority of atom-optical elements (with exceptions [99, 100, 101]) can be grouped into the two classes, optical and magnetic [102]. The optical elements make use of the energy level perturbations arising in atoms due to the AC Stark shift. The (spatially varying) atomic ground state energy level Stark shift due to laser light with intensity profile $I(\mathbf{r})$ and large detuning Δ_ν takes the approximate form

$$U(\mathbf{r}) \propto I(\mathbf{r})/\Delta_\nu, \tag{1.2}$$

where the detuning $\Delta_\nu = \nu - \nu_0$ is the difference between the laser frequency ν and the atomic transition frequency ν_0 between ground and excited state. A more exact form of Eq. 1.2 can be found in Ref. [103] and this energy shift is often referred to as the electric dipole potential. The rate at which photons are absorbed and emitted from dipole laser beams (again in the limit of large Δ_ν) obeys the approximate law $R \propto I(\mathbf{r})/\Delta_\nu{}^2$. In order to obtain deep dipole potentials, with a low light scattering rate, it is therefore necessary to use very high light intensities and large laser detunings. Atoms are attracted to spatial intensity maxima of red-detuned dipole laser beams, and the intensity minima of blue-detuned beams.

Dipole atomic traps have been generated from one or more focused laser beams [104, 105], light sheets [106, 107] or standing waves [108]. Evanescent light waves have been used to create an atom-optical mirror [109] for cold atoms [110] as originally suggested by Cook and Hill [111]. High laser powers are normally necessary for dipole manipulation of cold atoms, due to the low depth of the energy potential, however BECs have such low internal energies that they can be non-destructively restrained and manipulated with only a few mW of laser light [47]. The BEC group at Hannover has recently observed reflection of a BEC from the time-averaged potential of a rapidly rastered dipole laser beam [112].

On the magnetic side of atom optics, the first magnetic mirror for cold atoms was developed by members of the Sussex Centre for Optical and Atomic Physics, whilst at Yale University [113]. These atomic mirrors were based on an idea of Opat *et al.* [114] and have now been produced with excellent optical quality [115]. A natural extension of this work would be the use of these relatively 'hard' (interaction distance $\ll$ drop height) magnetic mirrors to focus and image coherent atomic sources such as BECs. At present, limitations with the vacuum pressure caused by outgassing from these magnetic mirrors have precluded their inclusion inside a BEC apparatus. First steps toward magnetic mirrors are

reported in this thesis however, with the development of a 'soft' magnetic mirror demonstrating novel magnetic reflection and adjustable focusing of an^{87}Rb BEC [116].
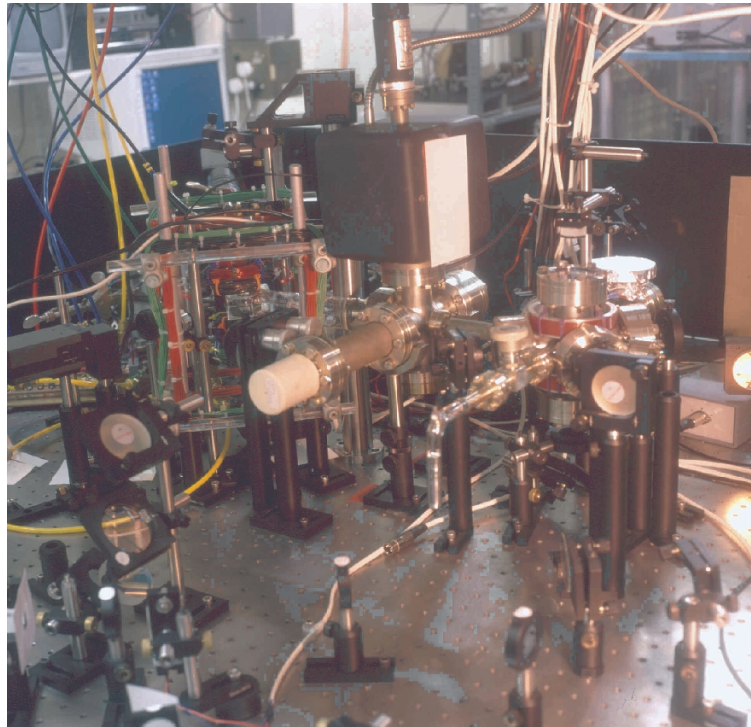
Figure 1.4: The Sussex BEC experimental set-up.

1.5 Thesis outline

Chapter 2 gives a brief description of the theoretical statistical and quantum mechanical properties of BECs, both within and outside magnetic traps.

In chapter 3 the theory behind the techniques used to obtain and observe Bose-Einstein condensation will be discussed, and the history of these topics will be briefly reviewed. The three primary areas that will be covered are laser cooling trapping and imaging, magnetic trapping, and evaporative cooling.

Chapter 4 details the experimental realisation of BEC through implementation of the processes presented in chapter 3. The novel features of the Sussex BEC will be discussed, and chapter 4 concludes with the first observation of BEC in the UK.

Comparisons of the properties of the Sussex condensate with theory and prior experiments are presented in chapter 5. Topics include: the condensed atom fraction as a function of temperature, anisotropic ballistic expansion of the BEC, and quasi-continuous RF output coupling. Finally the experimental results of our investigation into adjustable magnetic reflection and focusing of BECs will be considered.

The thesis culminates in chapter 6 with a summary of the thesis, and a discussion of directions for future experimentation.

Chapter 2

The theory of BEC

This chapter briefly covers two theoretical aspects of BEC: the statistical mechanics of BEC and simple quantum mechanical models for BEC.

In the statistical mechanics section the distribution of atomic population across energy levels, and in particular the relative ground state occupation N_0/N, is derived as a function of temperature T. The onset of BEC is characterised by a phase transition at the critical temperature, T_C. Deviations from the approximate ground state occupation $\frac{N_0}{N} = 1 - (T/T_C)^3$ due to the finite number of atoms and anisotropic magnetic potential are considered. The theory follows Ref. [117] and the results will be used in chapter 5 for comparison with experimental results.

In the quantum mechanics section, modifications to the single-atom Schrödinger equation are briefly summarised which allow for inter-atomic repulsion/attraction in a many-atom system. Various approximations result in the Gross-Pitaevskii equation. When the atom number is sufficiently large to make the inter-atomic and external potential energies considerably greater than the kinetic energy, one enters the Thomas-Fermi regime [118] and the Gross-Pitaevskii equation (sans kinetic energy term) yields a simple analytic approximation for the atomic wavefunction.

A good approximation for the time-dependent three-dimensional ballistic expansion of a BEC in the Thomas-Fermi regime has been produced by Castin and Dum [85]. The main results of their derivation are briefly recapped, in a form that will allow us to further generalise their results. The original model will be used to fit experimental BEC ballistic expansion data in chapter 5, and extensions of the Thomas-Fermi expansion model will also be made – enabling theoretical comparison with the time-dependent three-dimensional experimental bouncing data of chapter 5.

2.1 Statistical mechanics

Quantitative information about the Bose-Einstein phase transition can be obtained by considering the statistical mechanics of atoms at temperature T obeying a Bose-Einstein energy distribution:

$$N_i(E_i) = \frac{1}{e^{\beta(E_i-\mu)}-1} = \frac{ze^{-\beta(E_i-E_0)}}{1-ze^{-\beta(E_i-E_0)}}, \quad i \in \mathbf{Z} \geq 1, \tag{2.1}$$

where $N_i(E_i)$ is the population of atoms in the (possibly degenerate) atomic state with energy E_i, μ is the chemical potential, E_0 is the ground state energy, $z(\mu,T) = e^{\beta(\mu-E_0)}$ the fugacity and $\beta = (k_B T)^{-1}$. This result can be derived from first principles with the grand canonical ensemble [119]. The notation and approach used here is be similar to that of Refs. [117, 120].

The total atom number and energy in the system are given by

$$N = \sum_{i=0}^{\infty} N_i, \quad E = \sum_{i=0}^{\infty} E_i N_i. \tag{2.2}$$

Atomic ensembles in BEC experiments are typically held in a three-dimensional harmonic potential with spring constants $k_{x_d} = m\omega_{x_d}{}^2 \ (d \in \{1,2,3\})$ and corresponding quantised energy levels

$$E_i' = E_i - E_0 = E_{n_x,n_y,n_z} - E_0 = \hbar\left(n_x\omega_x + n_y\omega_y + n_z\omega_z\right), \quad (n_x,n_y,n_z) \in \mathbf{Z} \geq 0, \tag{2.3}$$

where $E_0 = \hbar/2\left(\omega_x + \omega_y + \omega_z\right)$. The Bose-Einstein condensation behaviour of atoms confined in other forms of trapping potential are detailed in Ref. [121].

Using a substitution which initially appears to complicate matters,

$$\frac{ze^{-\beta E_i'}}{1-ze^{-\beta E_i'}} = \sum_{j=1}^{\infty} z^j\, e^{-j\beta E_i'}, \tag{2.4}$$

one can (assuming absolute convergence) exchange the order of the double summation which results from combining Eq. 2.2 and 2.4 to obtain

$$
\begin{aligned}
N(\mu,T) = \sum_{j=1}^{\infty} z^j \left(\sum_{i=0}^{\infty} e^{-j\beta E_i'} \right) &= \sum_{j=1}^{\infty} z^j \left(\prod_{d=1}^{3} \left(\sum_{n_{x_d}=0}^{\infty} e^{-jn_{x_d}\epsilon_d} \right) \right) \\
&= \sum_{j=1}^{\infty} z^j \left(\prod_{d=1}^{3} \frac{1}{1-e^{-j\epsilon_d}} \right),
\end{aligned}
\tag{2.5}
$$

where $\epsilon_d = \beta\hbar\omega_{x_d}$.

A good approximation for $\frac{1}{1-e^{-x}}$ is made by solving for $\alpha(x)$ in the relation:

$$\frac{1}{1-e^{-x}} = 1 + \frac{e^{-x\alpha(x)}}{x}, \tag{2.6}$$

i.e.

$$\alpha(x) = \frac{\ln\left(\frac{1-e^{-x}}{xe^{-x}}\right)}{x}.$$

The function $\alpha(x)$ has a very mild x dependence, with Taylor expansion:

$$\alpha(x) = \frac{1}{2} + \frac{x}{24} - \frac{x^3}{2880} + \dots \quad \Rightarrow \quad \alpha(x) \approx 1/2, \quad 0 < x < 5 \tag{2.7}$$

and so the simple approximation

$$\frac{1}{1 - e^{-x}} = 1 + \frac{e^{-x/2}}{x} \tag{2.8}$$

has a relatively large range of validity.

Applying this approximation to Eq. 2.5, one obtains

$$N(\mu, T) = \sum_{j=1}^{\infty} z^j \left(1 + \frac{1}{j} \left[\sum_{d=1}^{3} \frac{1}{\epsilon_d} \left(e^{-\frac{\epsilon_d}{2}} \right)^j \right] + \frac{1}{j^2} \left[\frac{1}{\epsilon_1 \epsilon_2} \left(e^{-\frac{\epsilon_1 + \epsilon_2}{2}} \right)^j + \text{c.p.} \right] \right.$$
$$\left. + \frac{1}{j^3} \frac{1}{\epsilon_1 \epsilon_2 \epsilon_3} \left(e^{-\frac{\epsilon_1 + \epsilon_2 + \epsilon_3}{2}} \right)^j \right), \tag{2.9}$$

where c.p. denotes terms generated from the cyclic permutation $\epsilon_1, \epsilon_2 \to \epsilon_2, \epsilon_3 \to \epsilon_3, \epsilon_1$.

The total atom number can be re-expressed as

$$N(\mu, T) = g_0(z) + \left[\sum_{d=1}^{3} \frac{1}{\epsilon_d} g_1 \left(z e^{-\frac{\epsilon_d}{2}} \right) \right] + \left[\frac{1}{\epsilon_1 \epsilon_2} g_2 \left(z e^{-(\epsilon_1 + \epsilon_2)/2} \right) + \text{c.p.} \right] +$$
$$\frac{1}{\epsilon_1 \epsilon_2 \epsilon_3} g_3 \left(z e^{-(\epsilon_1 + \epsilon_2 + \epsilon_3)/2} \right), \tag{2.10}$$

where the polylogarithm function is defined $g_n(x) = \sum_{j=1}^{\infty} \frac{x^j}{j^n}$ and the ground state occupation is $N_0(\mu, T) = g_0(z)$. After substituting the fugacity $z(\mu, T) = e^{\beta(\mu - E_0)}$ into Eq. 2.10, it can be seen more clearly that N depends only on μ and T. Eq. 2.10 is then inverted numerically, yielding the chemical potential $\mu_N(T)$ for a fixed value of N. The relative ground state occupation is thus given by $\frac{N_0(\mu_N(T), T)}{N(\mu_N(T), T)}$.

Other thermodynamic quantities (in particular the energy E and specific heat C) can be derived in a similar manner to the atom number [117], however these variables will not be needed in this thesis.

In the limit of very large atom number, where the transition temperature is high enough to satisfy the criterion $1 \gg \epsilon_d \Rightarrow k_B T \gg \hbar\omega_{x_d}$, Eq. 2.10 is dominated by the g_3 term which simplifies to $g_3(1) = \zeta(3) = 1.202$, where $\zeta(x)$ is the Riemann Zeta function. The simple analytic expression

$$\frac{N_0}{N} = 1 - \zeta(3) \left(\frac{k_B}{\hbar\overline{\omega}} \right)^3 \frac{T^3}{N} = 1 - \frac{T^3}{T_C^3} \tag{2.11}$$

is therefore obtained, where the critical temperature is

$$T_C = \left(\frac{N}{\zeta(3)} \right)^{\frac{1}{3}} \frac{\hbar\overline{\omega}}{k_B} \tag{2.12}$$

using the geometric mean of the angular trapping frequencies $\overline{\omega} = (\omega_x \omega_y \omega_z)^{1/3}$. This can be linked to Eq. 1.1 by considering the density distribution of N atoms in a harmonic potential, namely

$$n(\mathbf{r}) = n_0 \exp\left(-\frac{m}{2 k_B T} (\omega_x^2 x^2 + \omega_y^2 y^2 + \omega_z^2 z^2) \right),$$

where the maximum density

$$n_0 = N \left(\frac{m}{2\pi k_B T} \right)^{3/2} \overline{\omega}^3$$

is obtained from normalisation. The approximate phase space density prior to condensation at the critical temperature $T = T_C$ is therefore given by

$$\text{PSD} = n_0 \Lambda_{dB}{}^3 = N \left(\frac{\hbar \overline{\omega}}{k_B T} \right)^3 = \zeta(3) \left(\frac{T_C}{T} \right)^3 ,$$

and thus $\text{PSD} = \zeta(3)$ at the Bose-Einstein phase transition.

The dependence of the ground state population on temperature for the simple relation Eq. 2.11 and for various scenarios of the more accurate expression Eq. 2.10 is shown in Fig. 2.1. The experimental parameters for the cigar-shaped Sussex BEC are as follows: The number of atoms is $N = 10^5$. The magnetic trapping potential is cylindrically symmetric with radial (axial) angular frequency $\omega_r = 2\pi \times 223\text{Hz}$ ($\omega_z = 2\pi \times 11\text{Hz}$) yielding a geometric mean frequency $\overline{\omega} = (\omega_r{}^2 \omega_z)^{1/3} = 2\pi \times 80\text{Hz}$.
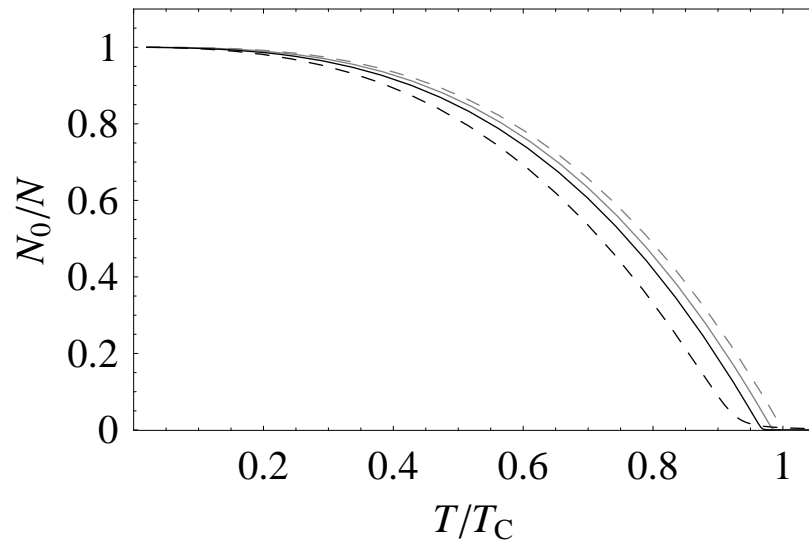
Figure 2.1: The relative number of atoms in the ground state as a function of temperature. The grey dashed line is the analytic high temperature (number) limit (Eq. 2.11). The black dashed line depicts $N = 10^3$ atoms in a spherical trap with $\overline{\omega} = 2\pi \times 80\text{Hz}$. The grey and black solid lines correspond to $N = 10^5$ atoms in spherical ($\overline{\omega} = 2\pi \times 80\text{Hz}$) and cylindrical ($\omega_r = 2\pi \times 223\text{Hz}$, $\omega_z = 2\pi \times 11\text{Hz}$) trapping potentials respectively. The critical temperatures predicted by Eq. 2.11 for $N = 10^3$, 10^5 are $T_C = 37$ and $171\,\text{nK}$.

2.2   Quantum mechanics

2.2.1   Models of BEC spatio-temporal evolution

The defining equation for many quantum mechanical derivations is the single-particle time-dependent
Schrödinger equation:

$$\left(-\frac{\hbar^2\nabla^2}{2m} + U(\mathbf{r}, t)\right)\Psi(\mathbf{r}, t) = i\hbar\frac{\partial}{\partial t}\Psi(\mathbf{r}, t),\qquad(2.13)$$

where $|\Psi(\mathbf{r}, t)|^2$ is the (normalised) atomic probability distribution ($\int|\Psi(\mathbf{r}, t)|^2\, d^3r = 1$) and $U(\mathbf{r}, t)$
describes the potential the atom inhabits. When the potential U is independent of time, one obtains the
time-independent Schrödinger equation:

$$\left(-\frac{\hbar^2\nabla^2}{2m} + U(\mathbf{r})\right)\psi(\mathbf{r}) = E\,\psi(\mathbf{r}) = \hbar\omega\,\psi(\mathbf{r}),\qquad(2.14)$$

where E is the total (kinetic+potential) atomic energy, and with $\Psi(\mathbf{r}, t) = \psi(\mathbf{r})\,e^{-i\omega t}$.

Let us now turn to the case of an N atom bosonic ensemble. In most experimental situations there
are two contributions to the atomic potential energy: $U(\mathbf{r}, t) = U_{ext}(\mathbf{r}, t) + U_{int}(\mathbf{r}, t)$, where U_{ext} is the
(external) magnetic trapping potential and U_{int} is the potential created by atomic interactions. Magnetic
traps used in experiments typically have the cylindrically symmetric harmonic form:

$$U_{ext}(r, z) = \frac{m\omega_r^2}{2}\left(r^2 + \eta^2 z^2\right),\qquad(2.15)$$

where $\eta = \omega_z/\omega_r$ is the ratio of axial to radial angular magnetic trapping frequencies. The description
of the potential due to atomic interactions is more complex. If the potential at time t on an atom at $\mathbf{r}$ due
to another atom at position $\mathbf{r}'$ is $V(\mathbf{r} - \mathbf{r}', t)$, then using the probability distribution interpretation of Ψ
it is plausible that the interaction potential at position $\mathbf{r}$ due to N non-localised wave-like atoms with a
quantum mechanical atomic density distribution $n(\mathbf{r}, t) = N\,|\Psi(\mathbf{r}, t)|^2$ will have the form:

$$U_{int}(\mathbf{r}, t) = N\int d^3r'\,\Psi^\dagger(\mathbf{r}', t)\,V(\mathbf{r} - \mathbf{r}', t)\,\Psi(\mathbf{r}', t).\qquad(2.16)$$

The form of U in this wave-function interpretation is the same as the field theoretical form, except in
quantum field theory $\sqrt{N}\,\Psi$ is replaced by the boson field annihilation operator $\hat{\Psi}$. Eq. 2.16 only consid-
ers two-body interactions, as three- and many-body collisions are relatively rare in a weakly interacting
sample like the gaseous Bose-Einstein condensate.

Given the potential energy term $U(\mathbf{r}, t)$, one can calculate the full Hamiltonian of a system of N
interacting bosonic atoms [9]:

$$\hat{H} = \int d^3r\,\hat{\Psi}^\dagger(\mathbf{r}, t)\left(-\frac{\hbar^2\nabla^2}{2m} + U_{ext}(\mathbf{r}, t) + \frac{1}{2}U_{int}(\mathbf{r}, t)\right)\hat{\Psi}(\mathbf{r}, t),\qquad(2.17)$$

where the second-quantised boson field creation and annihilation operators are $\hat{\Psi}^\dagger$ and $\hat{\Psi}$ respectively. A
discrete version of Eq. 2.17 has been evaluated directly using quantum Monte Carlo techniques [122],
however computational considerations limit calculations to atom numbers of around 10^4.

In the limit of large mean atom number, $\langle N \rangle$, the relative quantum-mechanical fluctuations in the number of atoms become negligible. The creation and annihilation operators, as well as the number operator $\hat{N} = \int d^3r \, \Psi^\dagger \Psi$, can be split into a 'mean-field' term, and a small fluctuating term which can be treated as a perturbation. This is known as the mean-field approximation. The annihilation operator can be expressed as $\hat{\Psi}(\mathbf{r}, t) = \sqrt{\langle N \rangle} \Phi(\mathbf{r}, t) + \hat{\varepsilon}(\mathbf{r}, t)$, where $\sqrt{\langle N \rangle} \Phi(\mathbf{r}, t) = \langle \hat{\Psi}(\mathbf{r}, t) \rangle$ is the mean-field multi-atom probability 'wave-function.' The operator $\hat{\varepsilon}$ describes the system's quantum fluctuations.

The mean-field approximation is perhaps more familiar in the context of photons: Φ is analogous to the coherent, classical, wave-like behaviour of a laser beam, whereas $\hat{\varepsilon}$ accounts for the quantum nature of the laser in its photon number fluctuations. Thus the wave-function Φ contains the essence of the coherent, matter-wave nature of a Bose-Einstein condensate.

The time-evolution of the wave-function Φ is given by [123]

$$i\hbar \frac{\partial}{\partial t} \Phi(\mathbf{r}, t) = \left(-\frac{\hbar^2 \nabla^2}{2m} + U_{ext}(\mathbf{r}, t) + \int d^3r' \, \Phi^\dagger(\mathbf{r}', t) \, V(\mathbf{r} - \mathbf{r}', t) \, \Phi(\mathbf{r}', t) \right) \Phi(\mathbf{r}, t). \qquad (2.18)$$

In the absence of atomic interactions, the time-independent ground-state mean-field wavefunction of a BEC confined in a cylindrically symmetric magnetic trap is given by the analytic function

$$\Phi(\mathbf{r}, t) = \left(\frac{m \omega_r \eta^{1/3}}{\pi \hbar} \right)^{3/4} \exp\left(-\frac{m \omega_r}{2\hbar}(r^2 + \eta z^2) - i(2 + \eta)\omega_r t \right), \qquad (2.19)$$

which has a spatial aspect ratio $\sqrt{\eta}$ between the major and minor axes of the ellipsoid. This can be contrasted with the equivalent thermal density distribution,

$$n_T(\mathbf{r}) = N \Phi_T(\mathbf{r})^2 = N \left(\frac{m \omega_r \eta^{1/3}}{2\pi k_B T} \right)^{3/2} \exp\left(-\frac{m \omega_r^2}{2k_B T}(r^2 + \eta^2 z^2) \right), \qquad (2.20)$$

which has the aspect ratio η.

Returning to the case of an interacting BEC, we consider atoms with an atomic scattering length a determined by the two-body scattering problem [119]. For a cold, relatively dilute, atomic ensemble like BEC, a consists almost entirely of the scattering length due to s-wave collisions, a_s. The short-range, 'hard-sphere' interactions of a cold, weakly-interacting Bose gas enable us to use the approximation:

$$V(\mathbf{r} - \mathbf{r}', t) = \xi \, \delta(\mathbf{r} - \mathbf{r}', t) = \frac{4\pi \hbar^2 a}{m} \delta(\mathbf{r} - \mathbf{r}', t), \qquad (2.21)$$

making Eq. 2.18 considerably more tractable. Under some circumstances Eq. 2.21 is equivalent to the Born approximation, however our use of Eq. 2.21 will also be valid outside the Born approximation's range of validity [9, 123]. To date, the most accurate determination of the ^{87}Rb scattering length for collisions between atoms in the $|F, m_F\rangle = |2, 2\rangle$ ground state at temperature $1\,\mu$K is $a = (104.5 \pm 2.5)a_0$ [124].

Substituting Eq. 2.21 into Eq. 2.18 leads to the time-dependent Gross-Pitaevskii equation (a nonlinear Schrödinger equation):

$$i\hbar\frac{\partial}{\partial t}\Phi(\mathbf{r},t) = \left(-\frac{\hbar^2\nabla^2}{2m} + U_{ext}(\mathbf{r},t) + N\xi|\Phi(\mathbf{r},t)|^2\right)\Phi(\mathbf{r},t). \tag{2.22}$$

In the case of a static potential this results in the time-independent equation

$$\mu\,\phi(\mathbf{r}) = \left(-\frac{\hbar^2\nabla^2}{2m} + U_{ext}(\mathbf{r}) + N\xi|\phi(\mathbf{r})|^2\right)\phi(\mathbf{r}), \tag{2.23}$$

with the time-dependent solution $\Phi(\mathbf{r},t) = \phi(\mathbf{r})\,e^{-i\mu t/\hbar}$, where μ is the chemical potential of the condensate.

In the limit of high N, it can be shown that the relative contribution of the kinetic energy term (K.E. $\propto \nabla^2\Phi$) in the Gross-Pitaevskii equation becomes negligible [118] – the magnetic and inter-atomic potential energy dominate the chemical potential. In this situation one may take the 'Thomas-Fermi' approximation [118], by neglecting the kinetic energy term in Eqs. 2.22, 2.23. The time-independent ground state solution for the quantum ensemble is then adequately described by the simple density distribution:

$$n(\mathbf{r}) = N\phi(\mathbf{r})^2 = \max\left(\frac{\mu - \frac{m\omega_r^2}{2}(r^2 + \eta^2 z^2)}{\xi}, 0\right). \tag{2.24}$$

The distribution is thus an inverted paraboloid with maximum extents in the radial and axial directions

$$r_{max} = \frac{1}{\omega_r}\sqrt{\frac{2\mu}{m}} \qquad \text{and} \qquad z_{max} = r_{max}/\eta \tag{2.25}$$

respectively, yielding an atomic cloud aspect ratio η. Normalisation of the distribution leads to the relation

$$\mu = \frac{\hbar\omega_r\eta^{1/3}}{2}\left(15Na\sqrt{\frac{m\omega_r\eta^{1/3}}{\hbar}}\right)^{2/5},$$

which links the chemical potential μ to the number of atoms and the strength of the magnetic trap.

The Sussex BEC of $N = 10^5$ atoms is well inside the Thomas-Fermi regime, as can be seen in Fig. 2.2 which shows the good agreement between the ground-state density distribution predicted by the Gross-Pitaevskii equation and the Thomas-Fermi approximation. The Gross-Pitaevskii solution was calculated by Dr. Boshier using the method of Ref. [125], in which the ground state wavefunction is determined by propagating a trial wavefunction through imaginary time. The trial wavefunction will be composed of a mixture of eigenstates of the condensate, $\Phi_{trial}(\mathbf{r},0) = \sum_{i=0}^{\infty}a_i\phi_{\mu_i}(\mathbf{r})$, and propagation in imaginary time ensures that after a suitable time delay the dominant term of $\Phi_{trial}(\mathbf{r},-it) = \sum_{i=0}^{\infty}a_i\phi_{\mu_i}(\mathbf{r},0)e^{-\mu_i t/\hbar}$ is that of the lowest chemical potential (i.e. μ_0) which corresponds to the ground eigenstate of the system.
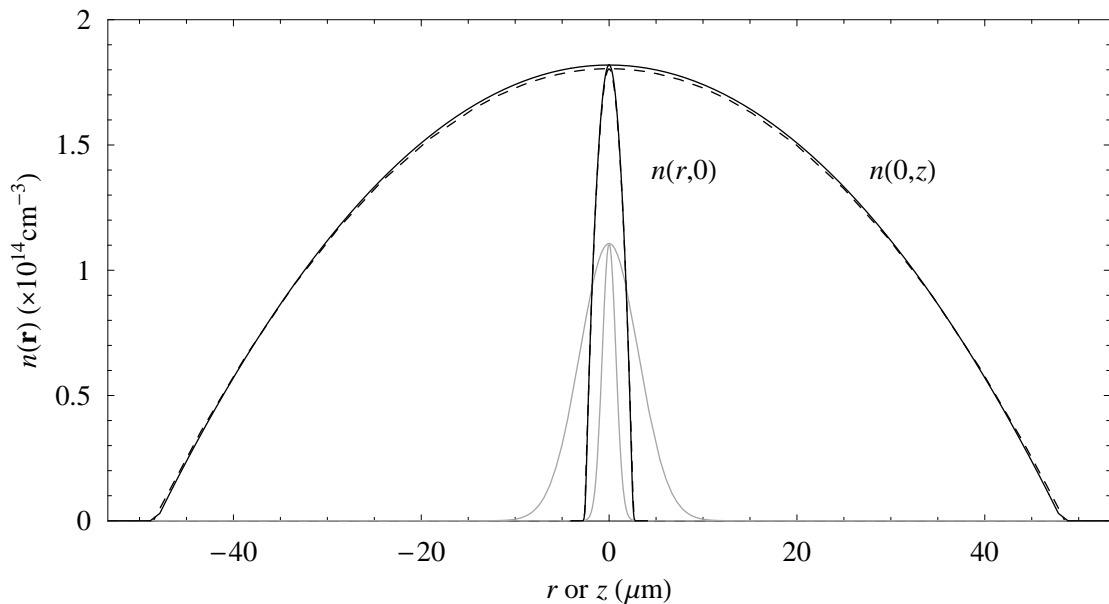
Figure 2.2: The ground-state radial $(n(r,0))$ and axial $(n(0,z))$ density profile of the Sussex BEC ($N = 10^5$, $\omega_r = 2\pi \times 223\,\text{Hz}$, $\omega_z = 2\pi \times 12\,\text{Hz}$) as predicted by the Gross-Pitaevskii equation (black) and Thomas-Fermi approximation (dashed). The equivalent density distribution profiles (divided by 100) for a non-interacting condensate are shown in grey.

2.2.2 Expansion and 'bouncing' in the Thomas-Fermi regime

In Ref. [85] Castin and Dum consider a method for calculating the evolution of BECs in time-dependent trapping potentials. The method is valid in the Thomas-Fermi regime and two derivations of the model were discussed – one classical and one quantum-mechanical – both yielding the same result. The classical case will be considered here, due to its relative simplicity.

Given the potential energy (internal+external) of a BEC with density distribution $n_t(\mathbf{r}, t)$, and omitting the kinetic energy (Thomas-Fermi approximation) one determines the classical force equation

$$\mathbf{F}(\mathbf{r}, t) = -\boldsymbol{\nabla}\left(U_{ext}(\mathbf{r}, t) + \xi\, n_t(\mathbf{r}, t)\right). \tag{2.26}$$

where $U_{ext}(\mathbf{r}, t)$ is an externally applied potential. If the external potential generates a force variation which is spatially odd (along the orthogonal axes x, y, z) about the centre of mass ($\mathbf{r}_0 = (x_0, y_0, z_0)$, i.e. if

$$
\begin{aligned}
\mathbf{F}_{ext}(x, y, z) - \mathbf{F}_{ext}(x_0, y_0, z_0) &= \mathbf{F}'_{ext}\big((x - x_0), (y - y_0), (z - z_0)\big) \\
&= -\mathbf{F}'_{ext}\big(-(x - x_0), (y - y_0), (z - z_0)\big) \\
&= -\mathbf{F}'_{ext}\big((x - x_0), -(y - y_0), (z - z_0)\big) \\
&= -\mathbf{F}'_{ext}\big((x - x_0), (y - y_0), -(z - z_0)\big)
\end{aligned}
$$

and the initial density distribution is an even function of the components of $\mathbf{r} - \mathbf{r}_0$ then the equation of

motion for an atom of mass m at the centre of mass of the falling cloud (gravity is in the $-y$ direction) is given by the solution $\mathbf{r_0}(t)$ of:

$$m\frac{d^2\mathbf{r_0}}{dt} = -\boldsymbol{\nabla} U_{app}(\mathbf{r_0}, t) - (0, mg, 0) - \underbrace{\xi\,\boldsymbol{\nabla} n(\mathbf{r_0}, t)}_{=0}, \tag{2.27}$$

where U_{app} refers to an applied magnetic potential. One then assumes that the trajectory of any particle within the cloud, relative to the centre of mass, is given by

$$(\mathbf{R}(t) - \mathbf{r_0}(t))_i = \lambda_{r_i}(t)(\mathbf{R}(0) - \mathbf{r_0}(0))_i = \lambda_{r_i}(t)R_i(0), \tag{2.28}$$

if one chooses $\mathbf{r_0}(0) = \mathbf{0}$. The BEC is held in a stable magnetic trap prior to perturbation at $t = 0$, and is therefore subject to the initial conditions $\lambda_{r_i}(0) = 1$, $\left.\frac{d\lambda_{r_i}}{dt}\right|_{t=0} = 0$.

The atomic cloud will expand, maintaining its overall shape, but with the x, y, z dimensions changing size as a function of time. Given an initial density distribution $n(\mathbf{r})$, this yields a time-varying spatial density distribution

$$n_t(\mathbf{r}, t) = \frac{1}{\lambda_x(t)\lambda_y(t)\lambda_z(t)}\, n\!\left(\frac{x - x_0(t)}{\lambda_x(t)}, \frac{y - y_0(t)}{\lambda_y(t)}, \frac{z - z_0(t)}{\lambda_z(t)}\right). \tag{2.29}$$

For any atomic trajectory $\mathbf{R}(t)$ the following relation therefore holds:

$$n_t(\mathbf{R}(t), t) = \frac{1}{\lambda_x(t)\lambda_y(t)\lambda_z(t)}\, n(\mathbf{R}(0)). \tag{2.30}$$

Comparison of Eqs. 2.29 and 2.30 yields $R_i(0) = \frac{r_i - r_{0_i}(t)}{\lambda_{r_i}(t)}$ and in particular $\frac{\partial R_i(0)}{\partial r_i} = 1/\lambda_{r_i}(t)$, so that

$$\begin{aligned}
\frac{\partial n_t(\mathbf{R}(t), t)}{\partial r_i} &= \frac{1}{\lambda_x(t)\lambda_y(t)\lambda_z(t)} \frac{\partial n(\mathbf{R}(0))}{\partial R_i(0)} \frac{\partial R_i(0)}{\partial r_i} \\
&= \frac{1}{\lambda_{r_i}(t)\lambda_x(t)\lambda_y(t)\lambda_z(t)} \frac{\partial n(\mathbf{R}(0))}{\partial R_i(0)}.
\end{aligned} \tag{2.31}$$

The difference of Eq. 2.26 evaluated at $\mathbf{r} = \mathbf{r_0}(t)$ and $\mathbf{r} = \mathbf{R}(t)$ removes the centre-of-mass motion and reduces to

$$\begin{aligned}
m\frac{d^2(\mathbf{R} - \mathbf{r_0})_i(t)}{dt^2} &= mR_i(0)\frac{d^2\lambda_{r_i}}{dt^2} \\
&= -\left.\frac{\partial U_{app}(\mathbf{r}, t)}{\partial r_i}\right|_{\mathbf{r} = \mathbf{R}(t)} + \left.\frac{\partial U_{app}(\mathbf{r}, t)}{\partial r_i}\right|_{\mathbf{r} = \mathbf{r_0}(t)} - \frac{\xi}{\lambda_{r_i}(t)\lambda_x(t)\lambda_y(t)\lambda_z(t)} \frac{\partial n(\mathbf{R}(0))}{\partial R_i(0)}.
\end{aligned} \tag{2.32}$$

We now consider a time-dependent magnetic potential U_{app} comprised of two components: a term centred on the origin generated by the original (harmonic) magnetic trap coils, and another harmonic term generated by magnetic coils centred at position $\mathbf{r_c}(t)$ with angular trap frequencies $\Omega_{r_i}(t)$ (where $\Omega_{r_i}(0) = 0$). The applied magnetic potential therefore has the form:

$$U_{app}(\mathbf{r}, t) = \frac{m}{2}\sum_{i=1}^{3}\left(\omega_{r_i}(t)^2 r_i{}^2 + \Omega_{r_i}(t)^2(\mathbf{r} - \mathbf{r_c}(t))_i{}^2\right), \tag{2.33}$$

which has the gradient

$$\frac{\partial U_{app}(\mathbf{r}, t)}{\partial r_i} = m \left(\omega_{r_i}(t)^2 r_i + \Omega_{r_i}(t)^2 (\mathbf{r} - \mathbf{r_c}(t))_i \right).$$

(2.34)

Note that if the potential U_{app} has linear spatial terms about the centre of mass then the force $\mathbf{F}_{app} = -\boldsymbol{\nabla} U_{app}$ will only be altered by a constant vector. This constant vector disappears when we subtract out the centre-of-mass motion (i.e. Eq. 2.27 still holds). Linear gradients in the applied magnetic potential therefore only alter the centre-of-mass motion of the atomic cloud, without changing the shape of the cloud (as harmonic potentials will be seen to do).

Substitution of the Eq. 2.34 into Eq. 2.32 leads to

$$R_i(0) \frac{d^2 \lambda_{r_i}}{dt^2} = - \left(\omega_{r_i}(t)^2 + \Omega_{r_i}(t)^2 \right) (\mathbf{R} - \mathbf{r_0}(t))_i - \frac{1}{m} \frac{1}{\lambda_{r_i}(t) \lambda_x(t) \lambda_y(t) \lambda_z(t)} \frac{\partial n(\mathbf{R}(0))}{\partial R_i(0)}.$$

(2.35)

From our knowledge of the initial density distribution $n(\mathbf{r})$ (Eq. 2.24), and once again employing Eq. 2.28, we arrive at:

$$R_i(0) \left(\frac{d^2 \lambda_{r_i}(t)}{dt^2} + \left(\omega_{r_i}(t)^2 + \Omega_{r_i}(t)^2 \right) \lambda_{r_i}(t) - \frac{\omega_{r_i}(0)^2}{\lambda_{r_i}(t) \lambda_x(t) \lambda_y(t) \lambda_z(t)} \right) = 0.$$

(2.36)

The fact that the cloud scaling parameters $\lambda_{r_i}(t)$ are independent of the initial position within the cloud $(\mathbf{R}(0))$ means that it is a valid assumption to model the cloud evolution in this manner. The ability to simply rescale the cloud dimensions, whilst the cloud essentially retains its original shape, is peculiar to the case of a harmonic potential.

'Bouncing' in a locally harmonic potential

Although it will be shown later that the form of the magnetic potential used in our bouncing experiments (Eq. 3.55) is not harmonic, the local force experienced by atoms about the centre-of-mass motion will be harmonic to second order. The linear spatial terms of the magnetic potential simply alter the centre-of-mass motion of the falling cloud, and the harmonic terms lead to changes in the shape of the cloud according to Eq. 2.36. For modelling the experiment we approximate the centre-of-mass motion by the path taken by an atom released at $\mathbf{r} = \mathbf{0}$ in a potential of the form given in Eq. 3.55.

The beauty of Eq. 2.36 is that complete information of the cloud evolution can be determined from three simple coupled ordinary differential equations, without requiring any knowledge of the centre-of-mass motion of the cloud, or performing the highly computationally intensive task of solving the time-dependent three-dimensional Gross-Pitaevskii equation. Although the model is limited to locally harmonic potentials, one can experimentally generate three-dimensional potentials which are essentially harmonic over a large region, allowing the possibility of focusing BECs or using them to provide colli-mated atomic beams. Further discussion of the model will ensue in section 5.3.

BEC ballistic expansion

The temporal evolution of the width parameters of an initially cylindrically symmetric BEC during ballistic expansion can be determined directly from Eq. 2.36. In this case the coupled differential equations simplify to

$$\frac{d^2\lambda_r(t)}{dt^2} = -\frac{\omega_r(0)^2}{\lambda_r(t)^3\lambda_z(t)} \qquad \frac{d^2\lambda_z(t)}{dt^2} = -\frac{\omega_z(0)^2}{\lambda_r(t)^2\lambda_z(t)^2}, \qquad (2.37)$$

yielding (for $\eta \ll 1$) the approximate analytic solutions [85]

$$\lambda_r(t) = \sqrt{1 + \omega_r(0)^2 t^2}$$

$$\lambda_z(t) = 1 + \eta^2\left(\omega_r(0)t\arctan(\omega_r(0)t) - \tfrac{1}{2}\ln(1 + \omega_r(0)^2 t^2)\right), \qquad (2.38)$$

where $\eta = \omega_z(0)/\omega_r(0)$. This model will be used to describe the ballistic expansion of the Sussex BEC in section 5.1. In the limit of large t, $\lambda_r(t) \to \omega_r(0)t$ and $\lambda_z(t) \to \frac{\eta^2\omega_r(0)\pi}{2}t$.

Comparison with the relation $\langle x_i(t)^2\rangle \to k_B T t^2/m$, given that the average value of $\langle x_i(t)^2\rangle$ for the time-dependent Thomas-Fermi density distribution (Eqs. 2.24, 2.37) is

$$\langle x_i(t)^2\rangle = \frac{1}{5}x_{i_{max}}(t)^2 = \frac{1}{5}x_{i_{max}}(0)^2\lambda_{x_i}(t)^2,$$

leads to the BEC 'release' temperatures in the radial and axial directions:

$$T_r = \frac{m}{5k_B}(r_{max}(0)\omega_r(0))^2 \qquad T_z = \left(\frac{\eta\pi}{2}\right)^2 T_r. \qquad (2.39)$$

'Bouncing' in an arbitrary magnetic potential

We briefly summarise a method for modelling the evolution of a 'bouncing' atomic cloud in more complicated magnetic potentials. As the BEC atomic cloud ballistically expands, the density drops and the inter-atomic repulsion term in the Gross-Pitaevskii equation becomes negligible. The evolution of the atomic density will initially follow the cloud expansion of Eq. 2.38. Then *provided* the density of the cloud remains low and the dimensions of the cloud are always much greater than the thermal de Broglie wavelength, one can approximate the evolution of the density by tracking classical atomic trajectories under an applied time-dependent magnetic field. These trajectories can be calculated using the magnetic forces described in section 3.2.

Simulation of the ballistic expansion of an N atom condensate can be made using M atoms with random initial position vectors $\{\mathbf{r}_1(0), ..., \mathbf{r}_M(0)\}$ which follow trajectories

$$\mathbf{r}_i(t) = (x_i(0)\lambda_r(t), y_i(0)\lambda_r(t) - gt^2/2, z_i(0)\lambda_z(t)),$$

until magnetic perturbations are applied.

In order to obtain initial position vectors weighted according to the Thomas-Fermi density distribution (Eq. 2.24), the density distribution is scaled to the spherically symmetric form: $n(R) \propto (1 - R^2)$,

where $R \in [0, 1]$, $(X, Y, Z) = R(\sin(\phi)\cos(\theta), \sin(\phi)\sin(\theta), \cos(\phi))$ are scaled cartesian co-ordinates and $(x, y, z) = (r_{max}X, r_{max}Y, z_{max}Z)$. We may then pick θ, ϕ isotropically over the spherical distribution by randomly selecting a value for $\theta = \theta_r$ in the interval $\theta_r \in [0, 2\pi)$, and choosing a value for $\cos(\phi) = c_\phi$ in the interval $c_\phi \in [-1, 1]$, with $\sin(\phi) = +\sqrt{1 - c_\phi{}^2}$. It remains to pick a random value of R weighted according to the density distribution. The volume weighted density $R^2 n(R)$ is integrated, yielding $P(R) = (R^3/3 - R^5/5)$, a monotonically increasing function with range $0 \leq P(R) \leq 2/15$ on the domain $R \in [0, 1]$. By randomly picking a value $P(R) = P_R$ from the interval $P_R \in [0, 2/15]$ and numerically inverting $P_R = R^3/3 - R^5/5 = P(R_{random})$, weighted random R values can be obtained.

This model can be used for comparison with the simpler model for 'bouncing' in a locally harmonic magnetic potential. It is stressed once again that this model is no longer valid in regimes where gradients in the density of the atomic cloud are high, for example if the cloud comes to a focus during its trajectory. This will be discussed further in Chapter 5.

Chapter 3

Reaching BEC: the theory

This chapter will deal with the theory behind the various mechanisms which are used to experimentally create Bose-Einstein condensation. The main topics covered are laser cooling, trapping and imaging as well as magnetic trapping and evaporative cooling. Each subject has a brief introduction and historical overview, followed by experimentally useful mathematical derivations.

Laser cooling and trapping (and in particular the 'magneto-optical trap' (MOT)) have enabled the creation of atomic gases with high density and extremely low temperature. These low temperature atomic clouds have revolutionised the field of atomic physics and led to improvements in a variety of precision measurements. Laser-cooled atoms have been used in highly accurate atomic clocks and gravity sensors. In this thesis laser cooled atoms will mainly be used in order to achieve a large 'head start' on the road to BEC, exploiting their relatively high phase space density.

In section 3.1.3 a simple model for optimising the collection efficiency in a MOT is explained, with a simplification to the calculation method of the original model. Further increase in the number (and lifetime) of the trapped atoms can be achieved with a 'double' MOT, and it is shown that a common technique used to transfer atoms between MOTs can be simplified. Mechanisms used to lower the temperature and increase the density of MOTs will then be discussed. The laser cooling section concludes with a discussion of absorption imaging, a technique which will be used to determine quantitative information about various properties of the atomic cloud.

Due to the inherent limitations on the density and temperature which can be attained by laser cooling the atoms must be transferred into a magnetic trap. Section 3.2 introduces the concept of magnetic trapping and briefly describes the limitations of 'quadrupole' magnetic traps. Derivations of common forms of magnetic trap potential are given, and a novel generalisation of the 'time-orbiting potential' magnetic trap. Atoms can be compressed in a magnetic trap, and changes to various parameters of the trapped atoms (particularly the phase space density and elastic collision rate) under sudden/adiabatic compression are considered.

The chapter concludes in section 3.3 with a discussion on evaporative cooling, the final technique needed to enhance the phase-space density of magnetically trapped atoms in order to attain BEC. The principles of radio-frequency evaporative cooling are covered, followed by a simple analytic model for evaporative cooling in the vein of Refs. [126, 127], which is contrasted with the more precise analytic theory of Refs. [128, 129]. Evaporation efficiency is first considered in the context of 'runaway' evaporation, and the evaporative cooling section ends with the topic of completely time-dependent evaporation trajectories as a means of obtaining optimal evaporation efficiency.

3.1 Laser cooling, trapping and imaging

As early as the seventeenth century it was postulated that light could exert pressure on matter – Kepler speculated that comet tails pointed away from the sun due to light pressure. Although in this circumstance light plays very little role, an experiment by Frisch [130] in 1933 left little doubt that light could in fact exert force on matter. He observed the deflection of a beam of sodium atoms by light resonant with a sodium energy level transition. Much larger effects can be observed today, as the advent of narrow-linewidth tunable lasers [131] in the 1970s made it possible to apply forces on atoms 10,000 times stronger than gravity.

With each photon absorption an atom will recoil with an impulse $\Delta \mathbf{p} = m\mathbf{v}_{recoil} = \hbar\mathbf{k}$, where m is the atomic mass, $\mathbf{k} = \frac{2\pi}{\lambda}\hat{\mathbf{k}}$, $\hat{\mathbf{k}}$ is the unit vector in the photon's direction of propagation and $\lambda = c/\nu$ is the wavelength of the light. The recoil velocity for the ^{87}Rb atoms used in our experiments is $v_{recoil} = 5.9$ mm/s. The time-averaged impulse applied to the atom by spontaneously emitted photons is zero [132] due to the random and symmetric nature of this kind of emission. The time-averaged acceleration on an atom in a laser beam is thus:

$$\langle \mathbf{a} \rangle = \frac{\hbar\mathbf{k}R(I,\nu)}{m},\qquad(3.1)$$

where R is the rate at which an atom absorbs photons.

The rate at which a two-level atom absorbs (and spontaneously emits) photons of light is given by the Lorentzian absorption profile [133, 134]:

$$R(I,\nu) = \frac{\Gamma}{2}\frac{I/I_S}{1 + I/I_S + (2\Delta/\Gamma)^2} = \frac{\Gamma}{2}\frac{I/I_S}{1 + I/I_S + (2\Delta_\nu/\Gamma_\nu)^2},\qquad(3.2)$$

where $\tau = 1/\Gamma$ is the excited state lifetime, ($\Gamma = 2\pi\,\Gamma_\nu$ is the full-width half maximum (FWHM) of the Lorentzian: in Rb $\Gamma_\nu = 6.07$ MHz), $\Delta_\nu = \frac{\Delta}{2\pi} = \nu - \nu_0$ is the detuning of the light frequency ($\nu = \frac{\omega}{2\pi}$) with respect to the frequency of the atom's electronic transition ($\nu_0 = \frac{\omega_0}{2\pi}$), I is the light intensity, $I_S = I\Gamma^2/(2\Omega^2) = 1.67$ mW/cm^2 is the saturation intensity (Sec. 4.1.3, App. C), and Ω is the Rabi frequency which is related to the atom's dipole moment. The maximum acceleration an ^{87}Rb atom can feel in a laser beam is thus (from Eqs. 3.1, 3.2): $\langle a_{max} \rangle = \frac{\hbar k\Gamma}{2m} = 1.1 \times 10^5$ m/s^2.

3.1.1   Doppler cooling

In 1975 Hänsch and Schawlow [135] proposed a mechanism by which lasers could be used to cool atoms. Laser light with angular frequency ω in the lab frame will be Doppler-shifted to $\omega' = \omega - \mathbf{k} \cdot \mathbf{v}$ for an atom travelling at velocity $\mathbf{v}$. A two-level atom positioned in a counter-propagating laser beam pair along the x direction will therefore feel an approximate time-averaged acceleration [134]:

$$a_x = \frac{\hbar k \Gamma}{2m} \left(\frac{I/I_S}{1 + I_{tot}/I_S + (2(\Delta_\nu - kv_x)/\Gamma_\nu)^2} - \frac{I/I_S}{1 + I_{tot}/I_S + (2(\Delta_\nu + kv_x)/\Gamma_\nu)^2} \right), \quad (3.3)$$

where I_{tot} is the total light intensity. The velocity-dependent nature of the acceleration is depicted in Fig. 3.1, and the acceleration has a first-order Taylor expansion of the form $a_x = -\alpha\, v_x$ – i.e. a damping, or cooling force for *red* laser detunings ($\Delta_\nu < 0$). For blue laser detunings ($\Delta_\nu > 0$) the Doppler acceleration cause heating.
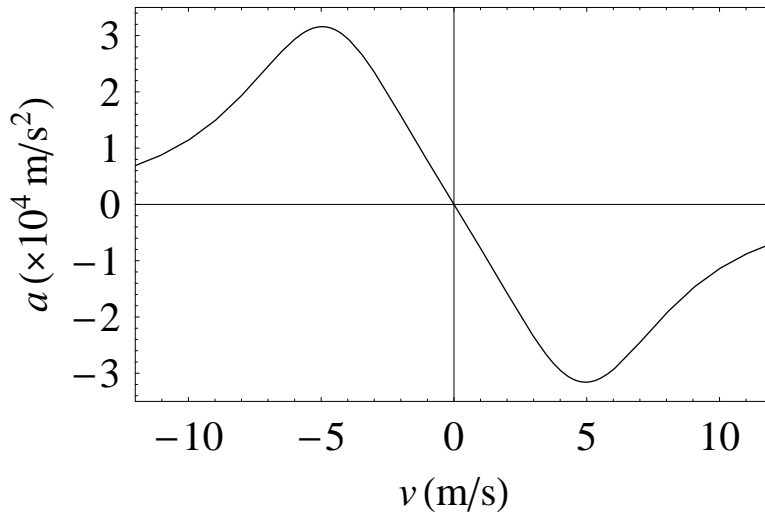
Figure 3.1: The velocity-dependent acceleration in optical molasses with Γ, k, and m as for rubidium, $I/I_S = 1$, $I_{tot} = 2I$, and $\Delta = -\Gamma$.

The ability to cool atoms in one dimension with red-detuned laser light is readily extended to three dimensions [132, 136]. N equal intensity laser beams are used with propagation vectors, $\{\mathbf{k}_1, ..., \mathbf{k}_N\}$ that span 3D space and add to zero ($\sum_{i=1}^{N} \mathbf{k}_i = \mathbf{0}$). The most common experimental configuration is comprised of three orthogonal counter-propagating laser beam pairs. The damping nature of the force is reflected in the common nomenclature for the cooling scheme: 'optical molasses.'

The viscous forces of optical molasses cool the atoms until a balance is struck with the fluctuating heating force due to the stochastic nature of photon absorption and emission. This leads to the Doppler temperature [132, 134]:

$$T_D = \frac{\hbar \Gamma}{4k_B} \frac{1 + I_{tot}/I_S + (2\Delta/\Gamma)^2}{-2\Delta/\Gamma},$$

which has a low-intensity $(I_{tot} \ll I_S)$ minimum of

$$T_D = \frac{\hbar \Gamma}{2 k_B} \tag{3.4}$$

at $\Delta = -\Gamma/2$. For both rubidium isotopes the Doppler temperature is $T_D = 145\,\mu\text{K}$. The Doppler temperature was initially thought to be the lowest temperature achievable with laser cooling.

The experimental realisation of laser cooling in the 1980s revolutionised the field of atomic physics. Lasers were used to slow an atomic beam in 1982 [24], and the first three-dimensional laser cooling — to temperatures around the sodium Doppler temperature $T_D = 240\,\mu\text{K}$ — was achieved in 1985 [11].

3.1.2 Magneto-optical trapping

In 1987 a quadrupole magnetic field, $\mathbf{B} = B_1(-\frac{x}{2}, -\frac{y}{2}, z)$, and appropriately circularly polarised laser beams were combined with optical molasses, making it possible to *trap* as well as cool atoms in a magneto-optical trap (MOT) [12]. Optical molasses and the magneto-optical trap can be compared as follows: in optical molasses the linear Doppler effect is used to cause a velocity-dependent pressure imbalance in counterpropagating laser beam pairs, whereas in a MOT this pressure imbalance is spatially-dependent and a result of the linear Zeeman effect. Moreover the MOT retains the velocity-dependent optical molasses damping forces, creating cold *and* dense atomic samples. Fig. 1.3 depicts the orientation of the magnetic coils and circularly polarised laser beams used in a MOT.

The simplest model for MOT operation uses a four-level atom comprised of a ground state $|F, m_F\rangle = |0, 0\rangle$ with degenerate excited states $|F', m_{F'}\rangle = |1, -1\rangle, |1, 0\rangle, |1, 1\rangle$ (Fig.3.2). The quantum number F refers to the total atomic (electronic+nuclear) angular momentum, and m_F refers to the projection of F onto the quantisation axis. The Zeeman shift alters the energies of the excited states, and the associated frequency for transitions from the ground state to the $|F', m_{F'}\rangle$ energy level changes from ν_0 to $\nu_0' = \nu_0 + \frac{\mu_B}{h} g_{F'} m_{F'} B$, where $\mu_B/h = 1.4\,\text{MHz/G}$, B is the magnetic field magnitude, and g_F is the Landé g-factor (section 3.2). In a one-dimensional example (the results generalise readily to three [136]), we consider atoms travelling along the x axis, where the magnetic field $B(x) = -\frac{B_1}{2} x$ varies linearly. The case $B_1 > 0$ will be considered, allowing direct comparison with Fig. 1.3.

Before proceeding, the sense of the circularly polarised light must be defined. The convention used here is that the quantisation axis at a given point in space is defined to be the direction of the local magnetic field. The polarisation of a laser beam at position $\mathbf{r}$ is independent of the light's direction of propagation (i.e. $\mathbf{k}$), and depends solely on the motion of the light's electric field vector around the local magnetic field. If the light's electric field vector $\mathbf{E}_L(\mathbf{r}, t)$ oscillates parallel to the local magnetic field $\mathbf{B}(\mathbf{r})$ (i.e. $\mathbf{E} \times \mathbf{B} = 0$) then the light is π-polarised. If $\mathbf{E}_L(\mathbf{r}, t)$ is always in the plane perpendicular to $\mathbf{B}(\mathbf{r})$, then the light is σ polarised. In particular, if one looks down on the 'arrow' of the $\mathbf{B}$ field vector and $\mathbf{E}_L$ traces out a circle in a clockwise (anti-clockwise) fashion, then this is σ^- (σ^+) polarised

light. The polarisations σ^-, π and σ^+ form a basis set for the polarisation description of coherent light sources, like lasers. The different polarisations drive different energy level transitions: σ^-, π and σ^+ photons drive transitions of the form $\Delta m_F = -1, 0, +1$ respectively.

From Fig. 1.3 it can be seen that for atoms on the x axis the laser propagating in the $-x$ direction is solely σ^- polarised for $x > 0$, but σ^+ polarised for $x < 0$. In fact all six laser beams have the property that along their propagation axis they are σ^- polarised as they approach the origin ($\mathbf{r} = 0$), and σ^+ polarised after they pass the origin. A description of how MOT spatial forces arise is given in Fig. 3.2.
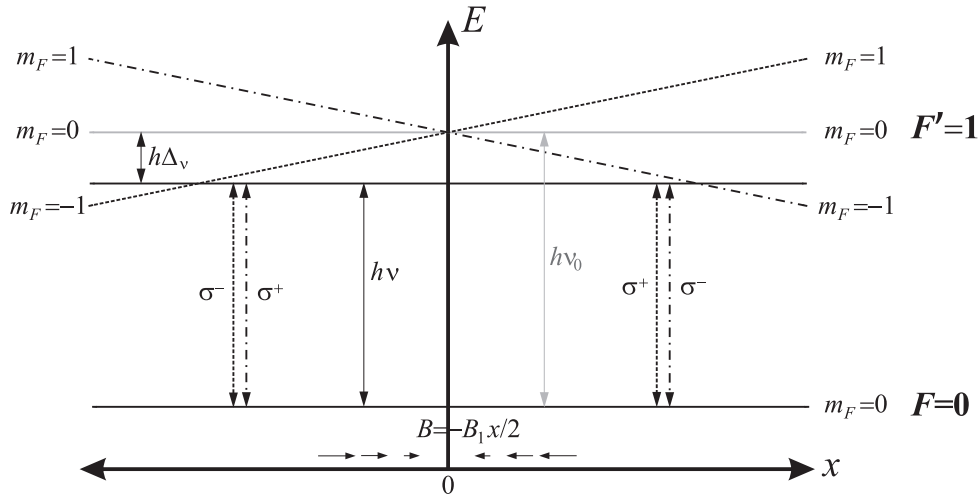
Figure 3.2: One-dimensional MOT energy level scheme. The laser beam travelling in the $+x$ direction is σ^- polarised when $x < 0$, and σ^+ polarised when $x > 0$ (as indicated by the dashed arrows). The energy difference between the laser frequency (ν) and the energy level (dashed) to which the $+x$ laser beam can drive atoms, increases as x increases. Therefore (Eq. 3.2) the acceleration from the $+x$ laser (in the $+x$ direction) gets stronger as x becomes more negative. Similarly the laser beam travelling in the $-x$ direction (represented by dot-dashed lines) creates an increasing acceleration in the $-x$ direction as x become more positive. The spatially-dependent force generated by the $\pm x$ beam pair is therefore restoring for red laser detunings ($\Delta_\nu < 0$).

Quantitative information about the spring constant of the Doppler trapping force can be obtained by substituting $\nu_0' = \nu_0 \pm \frac{\mu_B}{h} g_{F'} \frac{B_1}{2} x$ into Eq. 3.1 for the acceleration contributions of the $\pm x$-travelling laser beams.

The importance of the field of laser cooling was acknowledged in the 1997 Nobel physics prize, and the topic has been extensively reviewed by the Laureates [137, 138, 139], and others [140, 141, 142, 143]. Over twenty different atoms (and recently molecules), in a variety of isotopes have now been cooled and trapped [143, 144], however most work has focused on the alkali metal atoms. The alkali metals are particularly amenable to laser cooling as their energy level scheme is relatively simple and the required

laser wavelengths lie in a spectral region where commercial laser sources are readily available.

In an alkali metal there are two ground state F levels $(F(I, J = \frac{1}{2}) = I - \frac{1}{2}, I + \frac{1}{2})$ and four excited state F levels reached by the D2 transition $(F'(I, J = \frac{3}{2}) = I - \frac{3}{2}, I - \frac{1}{2}, I + \frac{1}{2}, I + \frac{3}{2})$, where J and I are the quantum numbers for total electronic and nuclear angular momentum, respectively. Each F level has $2F + 1$ magnetic sublevels $m_F = -F, -F + 1, ..., F$. In rubidium the ground and excited state levels that we will be interested in are the $5p^2S_{2/2}$ and $5p^2P_{3/2}$ states respectively. The energy transition that links these states is called the D2 line. The energy levels for the two isotopes of rubidium (^{85}Rb, for which $I = 5/2$ and ^{87}Rb $(I = 3/2)$) with their frequency separations are shown in Figs. B.1 and B.2.

The selection rules for light absorption on the D2 line are: $\Delta F = 0, \pm 1$ and $\Delta m_F = 0, \pm 1$. The two transitions (per Rb isotope) of the form $\Delta F = \Delta m_F = m_F = 0$ are forbidden. For alkali metals the energy levels which are equivalent to the $F = 0 \rightarrow F' = 1$ cooling transition discussed in the 1D MOT model, are $F = I + \frac{1}{2} \rightarrow F' = I + \frac{3}{2}$. A laser red-detuned from this transition is referred to as the 'trap laser.' Because of the selection rules an atom excited to $F' = I + \frac{3}{2}$ can only decay to $F = I + \frac{1}{2}$, however trap laser light is also capable of driving transitions to the $F' = I + \frac{1}{2}$ level. This transition occurs at a lower rate if the red detuning of the laser with respect to the $F' = I + \frac{3}{2}$ level is relatively small compared to the blue detuning of the laser with respect to the $F' = I + \frac{1}{2}, I + \frac{1}{2}$ levels. Unfortunately any transition to $F' = I - \frac{1}{2}$ or $F' = I + \frac{1}{2}$ is capable of decaying to the $F = I - \frac{1}{2}$ ground state. All transitions from the $F = I - \frac{1}{2}$ state have a very large detuning compared to the trap laser and are driven at a very low rate.

Therefore with trap laser light on its own, atoms all eventually accumulate in the ground $F = I - \frac{1}{2}$ state and effectively cease interacting with the trap laser – laser cooling and trapping stop. For this reason a 'repump' laser tuned to the $F = I - \frac{1}{2} \rightarrow F' = I + \frac{1}{2}$ transition is overlayed with the trap laser beams. The repump laser repopulates the $F = I + \frac{1}{2}$ ground state upon which laser cooling operates.

Experiments with MOTs initially involved collimated atomic beams generated in ovens. A single laser beam propagates in the opposite direction of the atomic beam, and radiation pressure is used to slow the atoms. As the atoms slow down their changing Doppler shift takes them out of resonance with the laser beam, preventing further cooling. One can compensate for this effect by either sweeping the frequency of the laser ('chirped' cooling [26, 27, 28]) or altering the atomic energy levels along the atomic beam path with a spatially-varying magnetic field (Zeeman slowing [24, 25]). The slowed atomic beams were used as a source of cold atoms with which to load MOTs.

Realisation that substantial numbers of atoms could be collected from an uncooled atomic beam, led to the development of the vapour cell MOT in 1990 [145]. MOTs can be characterised by their 'capture velocity,' v_C. Any atoms travelling into the MOT beam intersection region with speeds below the capture velocity can be slowed and captured. Typical MOT capture velocities of $v > 10$m/s cover a small, but significant fraction of the Boltzmann distribution. The relative simplicity and low cost of the vapour cell

MOT led to the proliferation of laser-cooling apparatuses around the globe, to the extent that MOTs are sometimes employed as (non-trivial) undergraduate atomic physics experiments [146].

3.1.3   MOT atom number

A simple one-dimensional model can be used to give an estimate of the number of atoms that can be captured in a vapour cell MOT [147]. The model for the capture velocity both here and in the original paper [147] is numerical, however the capture velocity developed here is subject to some initial analytical manipulation.

Substituting $a_x = \frac{dx}{dt}\frac{dv_x}{dx} = v_x\frac{dv_x}{dx}$ into Eq. 3.3 and integrating, leads to the relation:

$$\Gamma v\left(48\frac{k^4 v^4}{\Gamma^4} + 40\frac{k^2 v^2}{\Gamma^2}(1 + I/I_S - 4\Delta^2/\Gamma^2) + 15(1 + I/I_S + 4\Delta^2/\Gamma^2)^2\right) = \frac{120I\hbar k^2\Gamma\Delta}{mI_S}(x - K),$$
(3.5)

where K is an integration constant. The single laser beam intensity I is used instead of I_{tot} for loading, as during the capture process an atom mainly interacts with a single laser beam. If laser beams of diameter D are used, then K can be determined by setting $v = 0$ at $x = D/2$ – i.e. $K = D/2$. As Eq. 3.5 is a quintic in v, it must be inverted numerically to determine the capture velocity $v = v_C$ at $x = -D/2$. For the parameters of our 'high' pressure rubidium MOT ($D = 2.3$ cm, $I/I_S = \frac{1}{6}I_{tot}/I_S = \frac{1}{6}6.1/1.67$, $\Delta = -13$ MHz) this gives a capture velocity of $v_C = 20$ m/s.

The rate equation which determines vapour cell MOT loading as a function of time (ignoring collisional loss within the MOT [148]) is:

$$\frac{dN}{dt} = R - N/\tau,$$
(3.6)

where N is the number of atoms, R is the loading rate of alkali metal from a uniform thermal background gas, and $1/\tau$ is the rate at which collisions from thermal background atoms can knock atoms out of the MOT. The solution of Eq. 3.6 has the exponential form:

$$N(t) = N_0(1 - e^{-t/\tau}) \qquad t \geq 0,$$
(3.7)

where the number of atoms in the MOT at times $t \gg \tau$ is $N_0 = R\tau$.

The loss rate can be expressed:

$$1/\tau = 1/\tau_{Rb} + 1/\tau_X = n_{Rb}\sigma_{Rb}v_{Rb} + n_X\sigma_X v_X,$$

where n is the atom number density of the background gas, σ is the collision cross-section and $v = \sqrt{\frac{8k_B T}{\pi m}}$ is the velocity of the gas relative to the MOT atoms ($v_{MOT}/v \approx 0$). The subscripts Rb and X separate the contributions to the loss rate from rubidium vapour, and those due to other background species.

The loading rate R can be determined by considering the flux of rubidium atoms through a surface of area A in the plane $\phi = \pi/2$ (spherical coordinates will be used for the derivation). The flux of atoms with velocity components v_n normal to the surface in the range $0 < v_n = v\cos(\phi) < v_C$ can be determined using the Boltzmann velocity distribution $P(v) = \frac{1}{\pi^{3/2}v_T{}^3}e^{-v^2/v_T{}^2}$, where $v_T = \sqrt{2k_BT/m}$. The rubidium flux through the area A is then:

$$R = n_{Rb}A\overline{v_n} = n_{Rb}A \int_0^{2\pi}d\theta \int_0^{v_C}dv \int_0^{\pi/2}d\phi \; v^2 \sin(\phi)(v\cos(\phi))P(v) \tag{3.8}$$

$$\approx n_{Rb}A\frac{v_C{}^4}{4\sqrt{\pi}v_T^3}, \qquad v_C \ll v_T. \tag{3.9}$$

The total number of atoms trapped in a MOT with a spherical trapping region of area $A = \pi D^2$ is therefore:

$$N_0 = R\tau = \frac{\pi D^2}{8\sigma_{Rb}}\left(\frac{v_C}{v_T}\right)^4 \frac{1}{1 + \frac{n_X\sigma_X m_{Rb}}{n_{Rb}\sigma_{Rb}m_X}}. \tag{3.10}$$

As the loss and decay processes both depend on the rubidium density, the only dependence N_0 has on n_{Rb} is in relation to the density of other background species. In a vacuum where the background vapour is mainly Rb ($n_{Rb} \gg n_X$) the MOT is said to be in the 'rubidium dominated' regime. In this regime the number of atoms in the MOT is at a maximum and is independent of the background pressure.

Rubidium has two isotopes, and so it is expected that in each case N_0 will be weighted by the relative isotopic abundance 72% ^{85}Rb : 28% ^{87}Rb – i.e. for the same MOT parameters a factor of 2.6 times more ^{85}Rb atoms should be collected than ^{87}Rb. In practice there are additional MOT loss mechanisms which are based on ground-state hyperfine changing collisions, or excited state collisions within the MOT. These loss mechanisms can have a marked isotopic difference [148]. In our case this has worked in favour of the isotope which is used for BEC production, ^{87}Rb, and we experimentally observe only ≈ 1.5 times the number of ^{85}Rb atoms relative to an ^{87}Rb MOT.

The simple two-level model discussed in this section has some limitations, mainly in the absolute number of atoms, although trends are predicted well. With a constant scaling factor, the theory and experiment are in good agreement. A more complicated model – with an average over magnetic sub-levels for various paths through the capture regions – can be used, however it gives similar results to the two-level model [147] (except of course when predicting dependence of the MOT number on magnetic field).

In a rubidium dominated MOT we still need a value for the background rubidium collision cross section in order to obtain quantitative information from Eq. 3.10. The original vapour cell MOT paper [145] gave an estimate $\sigma_{Cs} = 2 \times 10^{-13}$ cm^2 using a model which employed the MOT lifetime (τ) and the (ideal gas) density determined from the pressure ($n = \frac{P}{k_BT}$) :

$$\sigma = \frac{1}{n\tau v} = \frac{1}{\tau P}\sqrt{\frac{8}{\pi}mk_BT}.$$

Using the pressure and lifetime measurements of Ref. [149], the cross-section $\sigma_{Rb} = 2 \times 10^{-13}\,\text{cm}^2$ is determined. It should be stressed that pressure measurements in high vacuum can be relatively inaccurate however. In Ref. [147] theoretical data had to be scaled by a factor 3.3 before agreement with experiment could be reached.

For the experimental data parameters mentioned earlier in this section, our model therefore yields an ^{87}Rb atom number of $N = 1.3 \times 10^8$, a factor 7.5 times lower than the experimental result (Sec. 4.1.3) of $N = 1 \times 10^9$. The theoretical variation of the MOT atom number as the MOT parameters alter about their usual settings is depicted in Fig. 3.3.
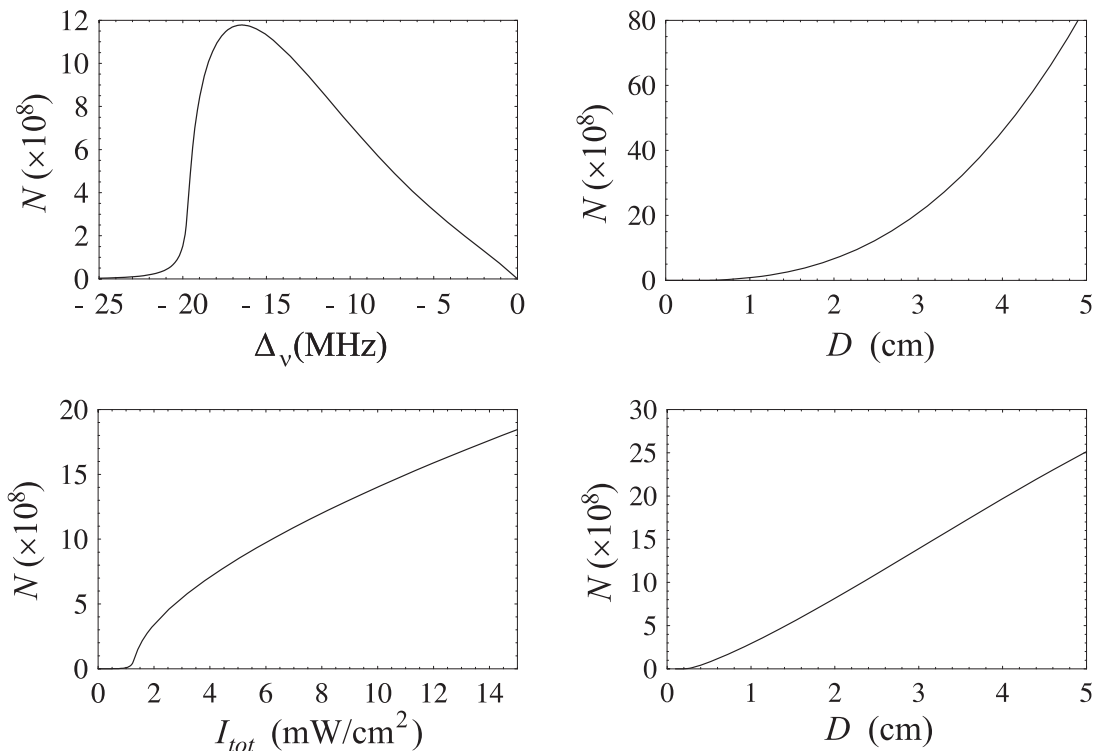
Figure 3.3: The theoretical ^{87}Rb MOT atom number variation with MOT parameters. In the first three images one of the parameters $D = 2.3\,\text{cm}$, $I_{tot} = 6.1\,\text{mW/cm}^2$, $\Delta = -13\,\text{MHz}$ is varied while the others are held constant. The final image shows how the number of atoms increases with D, for constant total laser power.

One reason that more atoms were captured in the MOT than expected could be our value for the area of the trapping region. Some experimental results in Sec. 4.1.4 suggest that trapping also occurs outside the 6-beam intersection region.

3.1.4   The double MOT

Although the vapour cell MOT is relatively simple to build in comparison to a MOT loaded by an atomic beam slower, this comes at the price of a smaller total number of atoms. Because of the high loss in the

number of atoms during the evaporative cooling phase of BEC production it is important to have a large number of atoms in the MOT. The various experimental schemes for increasing atom number will be discussed in Sec. 4.1.1 and at Sussex we chose the relatively simple 'double MOT' system.

In a rubidium-dominated vapour cell MOT the number of atoms is independent of the Rb pressure. The *rate* at which these atoms are loaded is proportional to pressure however, and relatively high pressures yield a fast fill time. Fast loading rates are useful for rapid experimentation, but high pressure is incompatible with evaporative cooling in a magnetic trap because trap lifetimes need to be on the order of a minute.

The idea behind the double MOT is to spatially separate the loading and storage MOTs. Atoms are rapidly accumulated in a 'high' pressure (HP) MOT and transferred into a 'low' pressure (LP) MOT. This has the advantage of rapidly loading atoms into a region which yields a long lifetime, plus the longer lifetime of the LP MOT means that it can collect multiple loads from the HP MOT. One wins both in terms of the trap lifetime and number of atoms.

If the HP MOT has a lifetime τ_{HP} and loading rate R, then if these atoms are continually loaded, with efficiency η into an LP MOT with lifetime τ_{LP} then from Eq. 3.6 one arrives at the relation:

$$N_{LP} = (\eta R)\tau_{LP} = \eta N_{HP}\frac{\tau_{LP}}{\tau_{HP}}. \tag{3.11}$$

This relation holds as long as the HP MOT atoms are transferred at time intervals $t < \tau_{HP}$. It is possible to create high lifetime ratios $\left(\frac{\tau_{LP}}{\tau_{HP}} > 100\right)$ by connecting the HP and LP MOT vacuum chambers with a relatively low conductance transfer tube and pumping the LP end with a higher throughput vacuum pump. At Sussex (Fig. 4.8) the HP end has no vacuum pump at all. The HP MOT chamber is therefore pumped through the transfer tube, however there is also a pumping contribution from the walls of the stainless steel vacuum chamber due to the long sticking time of rubidium on stainless. Neglecting the latter form of pumping the background pressure in each vacuum chamber is determined by the conductance from the respective MOTs to the vacuum pump.

Pressure ratio

The conductance (both MOTs chambers are well into the molecular flow regime) of a cylindrical tube with diameter d and length l $(d \gtrsim l)$ is given by [150]:

$$C = \frac{1}{3}\sqrt{\frac{\pi k_B T}{2m}}\frac{d^3}{l}\left(1 - \frac{3d}{l}\ln(2l/d) - \frac{91}{96}\frac{d}{l}\right) \text{ m}^3/\text{s}. \tag{3.12}$$

The path from the HP MOT to the $20\,\text{L/s}$ vacuum pump consists of a tube with dimensions $d = 1.6\,\text{cm}$, $l = 15\,\text{cm}$, and so the conductances for the main background gas species (hydrogen and rubidium) are $C_{H_2} = 9.8\,\text{L/s}$ and $C_{Rb} = 1.5\,\text{L/s}$. The connecting tube from the LP MOT to the vacuum has dimensions $d = 3.5\,\text{cm}$, $l = 20\,\text{cm}$, and hence conductances $C_{H_2} = 67\,\text{L/s}$, $C_{Rb} = 10\,\text{L/s}$.

The pumping speed for each MOT is given by the relation $1/S = 1/S_{pump} + 1/C$. The ratio of pumping speeds for a given atomic species in the LP and HP MOT then determine the pressure ratio for this species in the two MOT chambers. For hydrogen this is $P_{HP}/P_{LP} = S_{LP}/S_{HP} = 2.3$, and for ^{87}Rb it is $P_{HP}/P_{LP} = 4.8$.

In practice the conductance for rubidium is considerably lower than predicted, as the alkali metal atoms have a very long 'sticking time' on stainless steel compared to glass [151, 152]. The HP MOT has a rubidium source, and this MOT is observed to operate in the rubidium dominated regime. Thus the lifetime of the HP MOT is mainly due to rubidium, in contrast with the LP MOT with a background of hydrogen, due to the low conductance of rubidium through the transfer tube. In short, the pressure ratio is relatively difficult to calculate (as it varies with the amount of Rb present in the HP MOT) and is best measured experimentally. The MOT lifetimes give an upper estimate on pressure, as MOT lifetime is proportional to pressure in regimes where the time constant is not shortened by two-body or light-assisted collisions. Typical experimental lifetimes in the HP MOT cover the range $\tau_{HP} = 3\,\mathrm{s} \to 25\,\mathrm{s}$, depending on the rubidium pressure in the HP MOT chamber. The fill time in the LP MOT ranges from $\tau_{LP} = 30\,\mathrm{s}$ to $\tau_{LP} = 50\,\mathrm{s}$ and has only a slight dependence on the HP MOT rubidium pressure.

Transfer

The mechanism which is most commonly used for transferring atoms from one MOT to the other is light pressure. A laser beam propagating in the direction of the LP MOT illuminates the HP MOT atoms, and the atoms accelerate according to Eq. 3.1. As long as the atoms are not accelerated past the capture velocity of the LP MOT, then they will be trapped after transfer.

The atomic acceleration can be modelled using the term for a single laser from Eq. 3.3. This, unlike the case of two counter-propagating beams, can be solved analytically for $v(x)$ in a similar manner to Sec. 3.1.3.

For every photon momentum recoil the atom receives from absorbing a photon from the 'push' laser (in the $+x$ direction, say) it will also spontaneously emit a photon in a random direction. After absorbing M photons an atom's mean x velocity will be $\overline{v_x} = M v_{recoil} = M\hbar k/m$. The atom will also undergo a random walk in momentum space for the M spontaneously emitted photons. This is identical to Brownian motion, and one can calculate that in the limit of large M, for isotropically emitted photons, the velocity distribution of an ensemble of atoms is given by [153, 132]:

$$P(v_x, v_y, v_z) = A e^{-\frac{(v_x - \overline{v_x})^2 + v_y^2 + v_z^2}{2\langle \Delta v^2 \rangle}}, \tag{3.13}$$

where A is a normalisation constant and

$$\sqrt{\langle \Delta v^2 \rangle} = \sqrt{\frac{M}{3}} v_{recoil}.$$

The HP MOT cloud will be considered as a point source as its dimensions are much smaller than the transfer tube. The initial velocity spread of the MOT atoms due to their temperature T (i.e. $\langle \Delta v_{x_i}^2 \rangle = \frac{k_B T}{m}$) will add in quadrature with the velocity spread due to the push laser beam. This modifies Eq. 3.13 by changing the parameter $\langle \Delta v^2 \rangle$ to:

$$\langle \Delta v^2 \rangle = \frac{M}{3} v_{recoil}^2 + \frac{k_B T}{m}.$$

The approximate relative angular spread of the pushed atoms is therefore given by $P(\theta) \approx e^{-\theta^2/(2\overline{\theta}^2)}$ where

$$\overline{\theta} = \frac{\sqrt{\langle \Delta v^2 \rangle}}{\overline{v_x}} = \sqrt{\frac{v_{recoil}}{3\overline{v_x}} + \frac{k_B T}{\overline{v_x}^2 m}},$$

which decreases with the mean velocity of the pushed atoms.

Some double MOT systems rely on gravity to transfer the atoms between MOTs, however this requires an additional cooling stage, and works best with the heaviest stable alkali metal, caesium, because it can be cooled to lower temperatures. In our vacuum system the HP MOT and LP MOT are separated by a horizontal distance 45 cm and as light pressure can be used to quickly accelerate the atoms to $\overline{v} \approx 20$m/s, the atoms only fall 2.5mm during transfer. This is reduced to a quarter of the fall if the atoms are given a slight upward trajectory. Gravity can therefore be neglected from calculations.

The line of sight from the HP MOT centre to the LP MOT capture region (assumed to be a sphere with dimensions of the laser beam diameter $D = 23$ mm) is unobstructed by the transfer tubes. This means that the fraction of pushed atoms arriving in the MOT capture region is:

$$\eta = \frac{\int_0^{\theta_{LP}} \theta P(\theta)\, d\theta}{\int_0^\infty \theta P(\theta)\, d\theta} = 1 - e^{-\theta_{LP}^2/(2\overline{\theta}^2)}, \tag{3.14}$$

where $\theta_{LP} \approx \frac{1.15\,\text{cm}}{45\,\text{cm}} = 0.026$. With an HP MOT temperature of $300\,\mu$K and a push velocity $v_C = 17$ m/s this leads to a transfer efficiency of $\eta = 78\%$.

High efficiency (80%) push beam transfer of ^{87}Rb has been achieved in the past by optically pumping the atoms and using a magnetic transfer tube [33]. The above calculation demonstrates that this additional complication is in fact unnecessary. Relatively low transfer efficiencies of $\eta = 25\%$ have been measured for our push-beam-only system, however this appears to be due to the beam profile (containing a bright central spot) of the LP MOT laser beams. A new laser has yielded much higher transfer efficiency for the same beam power.

Greater MOT lifetime ratios could be achieved in future by placing a constriction in the transfer tube. The angular acceptance of a tube scales like $\theta \propto d/l$, whereas the conductance scales like $\theta \propto d^3/l$. A constriction in the 1.6 cm$\phi \times 15$ cm tube with a hole of diameter 5 mm and of length 4 cm would not obstruct the line of sight to the LP MOT capture region, but would lead (using the simple conductance calculation) to pressure ratios of $P_{HP}/P_{LP} = 16$ for hydrogen and $P_{HP}/P_{LP} = 45$ for rubidium. This might increase the total number of atoms in the LP MOT by a factor of 10.

3.1.5   Below the Doppler limit

In a 1988 experiment with optical molasses in sodium, the idea of the Doppler temperature (Eq. 3.4) was shattered when temperatures were observed six times colder than the sodium Doppler temperature $T_D = 240\,\mu$K [13]. These low temperatures were attained in situations where the magnetic field was low $B < 100\,$mG (i.e. the earth's field must be cancelled). The laser detuning at which the effect was observed, $\Delta_\nu = -2\Gamma_\nu$, was considerably larger than the optimum detuning ($\Delta_\nu = -\Gamma_\nu/2$) predicted by Doppler theory.

It wasn't long before new theories developed to explain this new phenomenon, and the topic was extensively covered in a special issue of *Journal of the Optical Society of America B* [14]. The new effects were the result of the multiple level structure of 'real' atoms as opposed to the simple two-level Doppler approach. The extra cooling mechanisms rely on the spatial variation of light polarisation and AC stark shift due to laser optical standing waves.

Perhaps the most commonly cited cooling mechanism, dubbed the 'Sisyphus effect' after the Greek myth of a man forever climbing hills, can be explained in one dimension in a standing wave generated by two linearly polarised laser beams with orthogonal polarisation axes. As one travels along the standing wave the total polarisation varies from σ^+ to σ^- and back on a scale of half the light wavelength. This causes spatial variation in the light shifts experienced in the ground level of an atoms ground state. For an $F \to F' = F + 1$ atomic transition, the largest negative AC Stark shifts are experienced by the $|F, m_F\rangle = |F, \pm F\rangle$ ground states in red-detuned $\sigma^\pm$ polarised laser light. If an atom in the light field moves away from a potential minimum in the light shift, optical pumping processes preferentially drive the atom from ground states with low light shifts back to those with large light shifts. Atoms thereby lose potential energy from their total energy, and are cooled. Because of the relative small 'light' shifts in the energy of ground state atoms, this cooling mechanism is most noticeable for atoms travelling at quite low velocities. In optical molasses atoms will be pre-cooled using the Doppler mechanism, before sub-Doppler forces can take effect.

Another important sub-Doppler cooling mechanism is the motion-induced orientation effect. In one dimension this occurs in the standing wave of counter-propagating circularly polarised laser beam pairs like those shown in Fig. 1.3. The light of the standing wave is linearly polarised, with an orientation that rotates along the axis of the beam pair. A moving atom observes a rotating light polarisation and in the rotating frame which follows the polarisation axis an extra inertial term is added to the hamiltonian of the atom. This term takes the form $V = kvJ_z$, and this perturbation causes an asymmetric mixing of the ground state sub-levels in a way that promotes preferential light absorption from the laser beam toward which the atom moves. Quantitative details of these sub-Doppler cooling mechanisms can be found in Refs. [154],[155].

The local polarisation of the light field generated by the six MOT laser beams varies spatially in a complex manner, however it is possible to quantitatively identify polarisation gradients which yield both Sisyphus and induced orientation sub-Doppler cooling mechanisms [132, 156]. The final temperatures created by both mechanisms are similar and in the limit of low laser intensity I and large laser detuning $\Delta_\nu = \nu - \nu_0$ the temperature has the form $T \propto I/|\Delta_\nu|$. Sub-Doppler mechanisms work particularly well for the heaviest stable alkali metals, rubidium and caesium, due to the large spacing of their hyperfine energy levels. This allows large laser detuning from a given energy level without driving transitions to other levels.

The sub-Doppler mechanisms still have an inherent limit on the lowest temperature which can be reached: the recoil temperature. If an atom is capable of absorbing light then it is always possible for it to have a momentum of at least one photon recoil. This corresponds to a 'recoil' temperature of:

$$T_R = \frac{\hbar^2 k^2}{k_B m},$$
(3.15)

(sometimes defined to be half this value). In practice most sub-Doppler cooling experiments obey the temperature law:

$$T = T_0 + AI/|\Delta_\nu|,$$

where T_0 and A are constants that depends on the atomic species. Typically the lowest temperature is around $T_0 = 10 T_R$ (in Rb $T_0 = 4\,\mu$K [157]).

Polarisation gradient cooling mechanisms occur directly in MOTs, but only in MOTs with quite small atom numbers and hence small cloud size, as this prevents atomic trajectories entering regions of high magnetic field [158, 159]. For this reason the magnetic field of large MOTs must be turned off before sub-Doppler cooling in optical molasses can occur.

Although there are mechanisms which can be used to circumvent the recoil temperature, namely velocity-selective coherent population trapping (VSCPT) [160] and Raman cooling, these processes have often resulted in low atomic densities, unconducive to the pursuit of BEC. Significant increases in phase-space density have been seen from Raman cooling in an optical dipole trap [107, 108], however the goal of an all-optical BEC remains elusive. For this reason the addition of an unnecessary (and relatively complicated) Raman cooling stage is omitted from the Sussex experimental BEC creation process.

3.1.6 Dark and compressed MOTs

Because increases in phase-space density (PSD) due to decreases in the atomic temperature are curtailed by the recoil limit, attempts were made to increase the PSD of atomic clouds by increasing their density. The most common mechanisms used are the 'dark' [16] or 'compressed' [19] MOT. These techniques are commonly used on most BEC experiments (Table 1.1), however we have not employed them in order to simplify the BEC creation process. Their description here will therefore be fairly brief.

As well as the normal restoring force in a MOT, two other forces become important as the number of atoms increases. One is the absorption force [15], which occurs because laser beams drop in intensity as they pass through a MOT due to light absorption. In a counter-propagating laser beam pair, the light at the edge of the atomic cloud from the incoming laser beam will be more intense than the beam which has already passed through the cloud. The imbalance in radiation pressure from the absorption force acts to compress the cloud.

The reradiation force [15, 161] occurs because as well as the direct laser light, atoms can also absorb the light spontaneously emitted by neighbouring atoms. This force acts like a Coulombic repulsion term due to the $1/r^2$ nature of the re-radiated light intensity. The reradiation and absorption forces have a very similar form [162, 159], and as the reradiation force depends on σ_R (the cross-section for absorption of re-radiated light) and the absorption force depends on σ_L (the cross-section for direct absorption of laser light) the approximate total force is proportional to $(\sigma_R - \sigma_L)$. This difference is always positive, and so the combined absorption and reradiation forces act to expand the cloud against the MOT restoring forces. This limits the attainable density in MOTs [15, 162, 163, 164, 165, 166, 167], and also raises the temperature of MOTs with large number of atoms by the law $T \propto N^{1/3}$ [168, 169, 170, 171, 172].

One way to counter-act this density-limiting effect is to create a hole in the repump laser light in the MOT formation region. With a population p in the laser cooled $F = I + 1/2$ ground state, on average only this fraction of atoms interact with the laser light. The spring constant in the MOT therefore drops by a factor p, but since the reradiation force depends on p^2 then the combined effect is to compress MOTs which contain large number of atoms (for which the reradiation force dominates). This is a spatial dark MOT (DMOT) – similar effects can be achieved by rapidly dropping the intensity or changing the detuning of the repump laser after a MOT has been loaded (temporal DMOT) [16, 17, 18].

For the alkali metals with large hyperfine energy intervals (Rb, Cs), repump light is utilised less often and so it takes more time to 'depump' the atoms into the non-interacting $F = I - 1/2$ ground state. This can be improved by using a 'forced' DMOT, which involves using a laser beam tuned to the either of the $F = I + 1/2 \rightarrow F' = I \pm 1/2$ transitions to actively pump $F = I + 1/2$ atoms into the $F = I - 1/2$ state.

Compressed MOTs (CMOTs) [19, 173] work by further red-detuning the laser beams (to decrease the reradiation force) and ramping up the MOT quadrupole magnetic field. This stops the loading process, but allows the MOT to be compressed.

3.1.7   Absorption imaging

It is important to be able to experimentally determine the density and temperature of atomic clouds. This section covers methods for determining quantitative information about these and other parameters.

If near-resonant low intensity 'probe' laser light is shone through a cloud of atoms, the atoms absorb part of the light and re-radiate it spontaneously. The shadow formed in the laser beam can then be imaged through a lens system onto a CCD camera. Suppose the imaging beam propagates along the $-x'$ axis of an x', y', z' cartesian co-ordinate system. Then if the incident probe beam intensity I_{in} is low ($I_{in} \ll I_S$) a cloud will absorb light according to Beer's law [131]:

$$I_{out} = I_{in} \exp\left(-\sigma_L \int_{x'_{min}}^{x'_{max}} n(u, y', z') \, du\right), \tag{3.16}$$

where σ_L is the cross section for light absorption, n is the number density of the atomic cloud, and x'_{min}, x'_{max} denote the extent of the cloud along the x' axis. Experimentally one obtains $I_{in}(y', z')$ and $I_{out}(y', z')$ by recording two CCD images – one with and one without atoms.

Atomic number and density

Given the scattering rate for the probe light (Eq. 3.2) it is relatively straightforward to show that the cross section for light absorption is

$$\sigma_L = h\nu \frac{\Gamma}{2} \frac{1/I_S}{1 + I/I_S + 4\Delta^2/\Gamma^2} = \frac{A}{1 + I/I_S + 4\Delta^2/\Gamma^2}, \tag{3.17}$$

where ν is the laser's frequency, and I_S is the saturation intensity (App. C) for the $|F, m_F\rangle = |I + 1/2, I + 1/2\rangle \rightarrow |F', m'_F\rangle = |I + 3/2, I + 3/2\rangle$ transition. In rubidium $A = 2.90 \times 10^{-13} \, \mathrm{m}^{-2}$ and $I_S = 1.67 \, \mathrm{mW/cm}^2$. This saturation intensity is used because in the experiment the probe light is circularly (σ^+) polarised with respect to a small ($\approx 1G$) bias field which is applied along the probe beam's propagation axis during imaging. Atoms are optically pumped into the $|F, m_F\rangle = |I + 1/2, I + 1/2\rangle$ ground state relatively quickly, and from there the only σ^+ transition is the one described above. The imaging probe light will also be used for optical pumping (Sec. 4.2.2). In our experiment the probe laser intensity is $I = 300 \, \mu\mathrm{W/cm}^2$.

Quantitative information about the atomic cloud can then be obtained by processing the images $I_{in}(y', z')$ and $I_{out}(y', z')$ to determine the 'two-dimensional' atomic density distribution:

$$n_{2D} = \int n(u, y', z') \, du = \ln\left(\frac{I_{in}(y', z')}{I_{out}(y', z')}\right) \frac{1}{\sigma_L}. \tag{3.18}$$

The total number of atoms, N, can then be found by integrating $n_{2D}(y', z')$ over y', z'. The optical density of the atomic cloud is given by $\mathrm{OD} = \ln\left(\frac{I_{in}(y',z')}{I_{out}(y',z')}\right)$.

In most experimental circumstances the atomic distribution fits a model which assumes a Gaussian spatial distribution:

$$n(x, y, z) = n_0 \exp\left(-\left(\frac{x^2}{2\,\sigma_x^2} + \frac{y^2}{2\,\sigma_y^2} + \frac{z^2}{2\,\sigma_z^2}\right)\right), \tag{3.19}$$

where

$$n_0 = \frac{N}{(2\pi)^{3/2}\,\sigma_x\,\sigma_y\,\sigma_z}. \tag{3.20}$$

In our experiment, limitations with optical access have led us to perform absorption imaging at an angle of $60°$ with respect to the cylindrically symmetric magnetic trap (Sec. 3.2) (z) axis, and the transformation from the xyz (magnetic trap frame) to the $x'y'z'$ (imaging frame) is:

$$x' = x \cos(\theta) - z \sin(\theta) \quad y' = y \quad z' = x \sin(\theta) + z \cos(\theta), \tag{3.21}$$

where $\theta = 30°$. Fig. 4.16 depicts the imaging geometry.

The two-dimensional projection of a Gaussian atomic density distribution into the imaging ($y'z'$) plane is also Gaussian, with modified width parameters:

$$\sigma_{y'} = \sigma_y, \qquad \sigma_{z'} = \sqrt{\sigma_z{}^2 \cos^2 \theta + \sigma_x{}^2 \sin^2 \theta}. \tag{3.22}$$

Gaussian fits to images of the atomic cloud yield the maximum value of n_{2D}, as well as $\sigma_{y'}$, $\sigma_{z'}$. The number of atoms in the atomic cloud can then be given by:

$$N = \max(n_{2D}(y', z')) \, 2\pi \, \sigma_{y'} \, \sigma_{z'}.$$

Determination of the maximum atomic density, n_0, requires the depth of the atomic cloud, however this cannot be ascertained without invoking the cloud's spatial symmetries.

In the case of our low pressure MOT and optical molasses (Secs. 4.1.3, 4.1.6), the atomic cloud is assumed to be cylindrically symmetric about the y' axis: i.e. $\sigma_{x'} = \sigma_{z'}$. The magnetic trap (Sec. 4.2) has a more well-defined potential than the MOT, as it is not affected by spatial variations in light intensity, and in the magnetic trap $\sigma_x = \sigma_y$. The magnetic trap's cylindrical symmetry is then used to obtain the axial width of the trapped cloud:

$$\sigma_z = \frac{\sqrt{\sigma_{z'}{}^2 - \sigma_{y'}{}^2 \sin^2 \theta}}{\cos^2 \theta}. \tag{3.23}$$

The three width parameters σ_x, σ_y, σ_z, can therefore be obtained for both MOTs and magnetic traps. The density of atoms is then given by Eq. 3.20.

Temperature

It is necessary to make data acquisitions at at least two different times during a MOT's ballistic expansion to determine the temperature of the MOT/molasses. The ballistic evolution of the Gaussian cloud's $i = x, y, z$ width parameter after releasing the MOT cloud at $t = 0$ takes the form [174, 173]:

$$\sigma_i{}^2(t) = \sigma_{i_0}{}^2 + \frac{k_B T_i}{m} t^2, \tag{3.24}$$

where σ_{i_0} is the initial width of the distribution along the i axis. Given atomic widths, σ_{i1}, σ_{i2} at times t_1, t_2 respectively, the temperature is thus:

$$T_i = \frac{m}{k_B} \frac{\sigma_{i2}{}^2 - \sigma_{i1}{}^2}{t_2{}^2 - t_1{}^2}.$$

The temperature can also be obtained from the slope of the ${\sigma_i}^2(t)$ vs. t^2 graph.

The well-defined initial geometry of the magnetic potential allows the magnetic trap temperature to be determined from a single image of the atomic cloud at any time during ballistic expansion. Given the trap's axial and radial frequencies, ν_r, ν_z, one finds for $\nu_i = \nu_r, \nu_z$ [174, 163]:

$$\sigma_i{}^2(t) = \frac{k_B T_i}{m(2\pi\nu_i)^2} + \frac{k_B T_i}{m} t^2 \quad \rightarrow \quad T_i = \frac{m}{k_B} \frac{\sigma_i{}^2(t)}{t^2 + \frac{1}{(2\pi\nu_i)^2}}. \tag{3.25}$$

For atomic distributions in thermal equilibrium the temperatures along the three trap axes are equal (although deviations may occur during trap compression or anisotropic RF evaporation).

Collision rate

A parameter which will be useful in the following paragraphs is the density-weighted density: $\langle n \rangle = \frac{\int n^2(\mathbf{r})\, d^3 r}{\int n(\mathbf{r})\, d^3 r}$, and for a Gaussian density distribution $\langle n \rangle = \frac{n_0}{2\sqrt{2}}$.

The elastic collision rate in an isotropic gaseous medium is defined $\gamma = n\,\sigma_{el}\,\langle v_{rel} \rangle$ where σ_{el} is the (temperature and magnetic field dependent) elastic collision cross-section, and $\langle v_{el} \rangle$ is the average relative velocity between atoms. For a thermally uniform medium, with non-uniform spatial distribution, the spatially averaged elastic collision rate is:

$$\begin{aligned} \gamma_{el} = \langle\gamma\rangle &= \sigma_{el} \frac{\int n^2(\mathbf{r})\, v_{rel}\, d^3 r}{\int n(\mathbf{r})\, d^3 r} \\ &= \langle n \rangle\, \sigma_{el}\, \langle v_{rel} \rangle \\ &= \frac{n_0 \sqrt{3 k_B T}}{2\sqrt{m}}\, \sigma_{el}\, \langle v_{rel} \rangle, \end{aligned} \tag{3.26}$$

where the rms average relative velocity between atoms is $\langle v_{rel} \rangle = \sqrt{6 k_B T/m}$. The collision rate can therefore be determined from the measurements of density and temperature described above, given the elastic collision cross-section σ_{el}.

At the low atomic temperatures used in this experiment s-wave elastic collisions are dominant, and the elastic s-wave cross section takes the form [175]:

$$\sigma_{el} = \frac{8\pi a^2}{1 + k^2 a^2}, \tag{3.27}$$

where $k = \frac{2\pi}{\lambda_{deB}}$, $\lambda_{dB} = h/\sqrt{2\pi m k_B T}$ is the thermal de Broglie wavelength, and a is the scattering length. The scattering length of ^{87}Rb at $1\,\mu$K is (Sec. 2.2.1) $a = (104.5 \pm 2.5)a_0$. Therefore the approximation $\sigma_{el} \approx 8\pi a^2 = 7.7 \times 10^{-12}\,\mathrm{cm}^2$ is valid in the low temperature limit $ka^2 \ll 1$, i.e. $T \ll \frac{h^2}{(2\pi)^3 m k_B a^2} = 29\,\mu$K, and the approximation $\sigma_{el} \approx 8\pi k^2$ is valid when $T \gg 29\,\mu$K. A full derivation of Rb cross-sections for various hyperfine states and temperatures is given in Ref. [124]. This yields a total elastic cross-section between ^{87}Rb atoms in the $|2, 2\rangle$ ground state which is approximately constant at $\sigma_{el} \approx 8\pi a^2 = 7.7 \times 10^{-12}\,\mathrm{cm}^2$ for temperatures $0 < T < 300\,\mu$K.

The simple relations $n_0 \propto \frac{N}{\overline{\sigma}^3}$, $T \propto \overline{\sigma}^2$, where $\overline{\sigma}$ is the geometric mean of the cloud width parameter, can be used to show that the collision rate has the form:

$$\gamma_{el} \propto \frac{N}{\overline{\sigma}^2} \propto \max(n_{2D}), \tag{3.28}$$

where n_{2D} is the 'height' distribution (Eq. 3.18) of a processed CCD image for a fixed laser detuning. The signature of runaway evaporation (Sec. 3.3.3) is therefore equivalent to observing an increase in image 'height' as evaporation proceeds.

Phase space density

This parameter can also be determined from our temperature and density relations, and the phase space density (PSD) is given by (Eq. 1.1):

$$\text{PSD} = n_0 \left(\frac{h}{\sqrt{2\pi m k_B T}} \right)^3. \tag{3.29}$$

The equivalent form of the scaling law Eq. 3.28 for phase space density is:

$$PSD \propto \frac{\max(n_{2D})}{\overline{\sigma}^4}.$$

A caution

Limitations to absorption imaging will now be considered, in the vein of Ref. [41]. The refractive index $\mathcal{N}$ of an atom has a real and complex part. As well as absorption within the atomic cloud (due to $\text{Im}(\mathcal{N})$) the real part of the refractive index (given by the Kramers-Kronig relation $(\text{Re}(\mathcal{N}) - 1) = -\frac{2\Delta}{\Gamma}\text{Im}(\mathcal{N})$ causes refraction which makes the atomic cloud act like a lens. The imaginary part of the refractive index causes diffraction.

The spatial intensity drop in a laser beam as it propagates in the x' direction through a medium with refractive index $\mathcal{N}(x', y', z')$ is

$$\ln(I_{out}/I_{in}) = -2k \int \text{Im}(\mathcal{N}(u, y', z'))\, du \;\; (= -\sigma_L \int n(u, y', z')\, du), \tag{3.30}$$

yielding the relation

$$\text{Im}(\mathcal{N}) = 2\pi\sigma_L n(\mathbf{r}')/\lambda. \tag{3.31}$$

The dependence of the refractive index near an atomic resonance is depicted in Fig. 3.4.

The spatial advance X' in the wavefronts of the electric field of the probe beam due to the atomic medium is then:

$$X'(y', z') = -\int (\text{Re}(\mathcal{N}(u, y', z')) - 1)\, du = -\frac{\Delta}{k\Gamma} \ln(I_{out}/I_{in}),$$
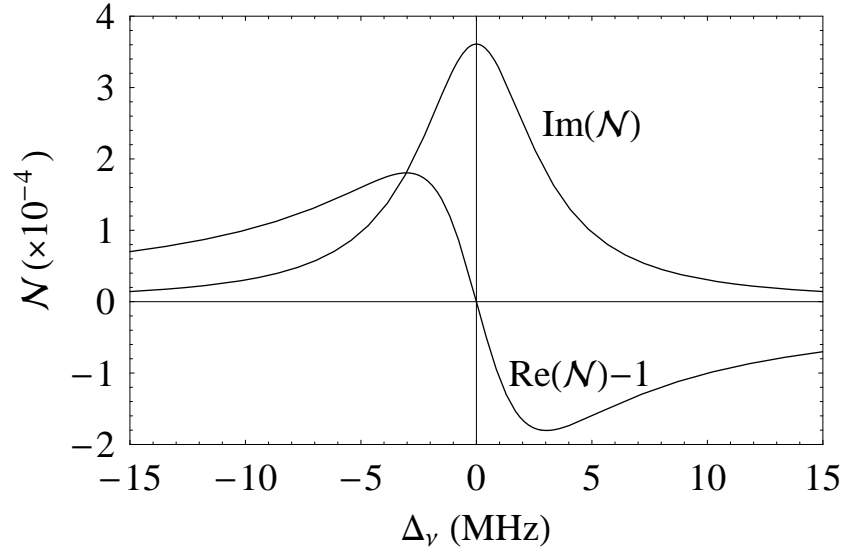
Figure 3.4: The frequency dependence of the refractive index near an atomic resonance. The imaginary part of the refractive index for rubidium (at density $n = 10^{10}$ cm^{-3}) was determined using the light cross-section parameters in Sec. 3.1.7. The real part of the refractive index follows from the Kramers-Kronig relation.

and the cloud of atoms can be treated as a lens with focal lengths (negative for a convex lens) determined by the curvature of the light wave-fronts:

$$f_{y'} = 1/\left(\frac{\partial^2 X(y',z')}{\partial y'^2}\right), \qquad f_{z'} = 1/\left(\frac{\partial^2 X(y',z')}{\partial z'^2}\right).$$

For a Thomas-Fermi atomic distribution (Eq. 2.24), the light absorption will have the radial (most tightly confined) intensity profile

$$\ln(I_{out}/I_{in}) = \ln(I_{out}/I_{in})|_{\mathbf{r}=0}\left(1 - (r/r_{max})^2\right)^{3/2},$$

yielding the radial focal length

$$f_r = \frac{r_{max}{}^2 k\Gamma}{3\Delta \ln(I_{out}/I_{in})|_{\mathbf{r}=0}}.$$

Assuming the cloud widths in the y', z' directions are $2R_{y'}$ and $2R_{z'}$, then the refracted light will be deflected by an angle $\theta_i \approx R_i/f_i$ in the $i = y'$, z' directions. It is possible for the refraction angle to be greater than the angle due to diffraction ($\theta_{D_i} = \frac{\lambda}{4R_i}$), however as long as the imaging system collects all diffracted and refracted light quantitative imaging can still be obtained [41]. It is therefore important to use laser light exactly on resonance, or far from resonance to prevent distortion of the imaged cloud due to diffraction effects. The cloud's focal length has the dependence $f \propto \text{sign}(\Delta)$ (i.e. the atomic cloud acts like a convex lens for blue-detuned light).

With our present experimental imaging system (Sec. 4.1.4) the acceptance angle of the imaging lens is $\theta = \sin^{-1}(1.15\,\text{cm}/11.25\,\text{cm}) = 0.102\,\text{rad}$. The minimum observable diffraction-limited atomic

cloud radius is therefore $R = \frac{\lambda}{4\theta} = 2\,\mu$m. We use resonant imaging, but fluctuations in the laser frequency about ν_0 due to the laser linewidth ≈ 1 MHz will still (Fig. 3.4) create time-varying lensing effects within the cloud due to refraction. The refraction limited cloud radius for a laser detuning of 1 MHz and a typical central optical depth $\ln(I_{out}/I_{in})|_{\mathbf{r}=0} = -3$ is

$$r_{max} = \frac{3\Delta \ln(I_{out}/I_{in})|_{\mathbf{r}=0}}{\theta k \Gamma} = (-)2\,\mu\text{m}.$$

The atomic cloud must be allowed to ballistically expand for a sufficiently long time ($t \approx 10$ ms) that the BEC size increase and density drop allow quantitative information about the cloud to be obtained. Although imaging should not be limited by the calculated refraction and diffraction limits, the discrete nature of the CCD camera image limits the resolution of the image. The magnification ($M = 0.8$) of the imaging system leads to a resolution of $\Delta y' \times \Delta z' \approx 15.8\,\mu$m $\times 7.8\,\mu$m, determined by the CCD camera pixel size ($12.6\,\mu$m $\times 6.25\,\mu$m). In the experiment we observe an imaging limit in the radial direction of $r_{max} = 35\,\mu$m (Fig. 5.3) which could be due to the poor optical quality of the quartz windows through which the absorption imaging laser beam must pass (Fig. 3.5). The fact that an object with $35\,\mu$m radial width closely corresponds with the object width ($31.5\,\mu$m in the y direction) leading to an image which covers two CCD camera pixels also suggests the possibility that the image of the BEC is centred on the edge of two pixels, or that 'cross-talk' exists between adjacent pixels of the CCD camera.

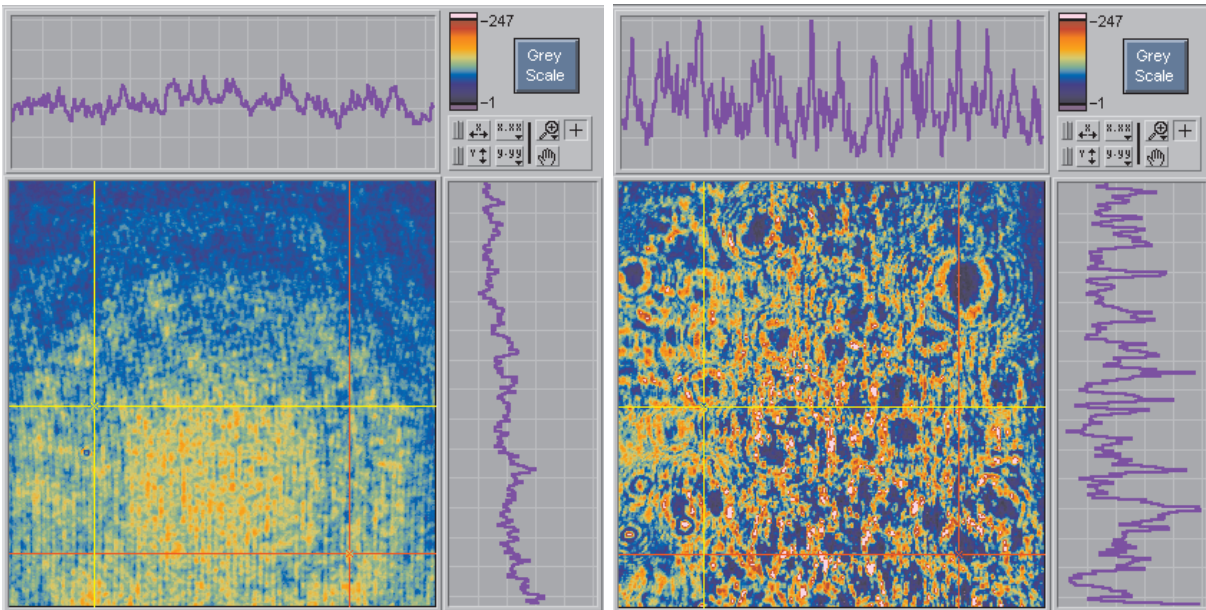Figure 3.5: The optical quality of the quartz vacuum cell windows through which the absorption imaging laser light passes. The image to the left is the intensity profile of the probe laser beam after spatial filtering, without the vacuum cell in the beam path. The image to the right indicates the probe beam's spatial intensity profile after passing through the two relatively low-quality 3mm thick quartz windows.

3.2 Magnetic trapping

Magnetic fields were first employed to manipulate atoms in the well-known experiments of Stern and Gerlach in 1921 [176, 177]. These experiments were necessarily performed with thermal atomic and molecular beams, yielding small angular deflections (due to the short interaction time with the magnetic fields) that were highly dependent on the longitudinal velocity spread of the atoms. With the advent of laser cooling, small clouds of atoms with very narrow velocity spreads became available, enabling high precision magnetic manipulation and confinement of cooled atomic samples [102]. In this section the magnetic forces felt by atoms will be derived, then applied to the technique of magnetic trapping. Magnetic forces also allow other forms of atomic manipulation, namely reflection and focusing, which will be discussed in both theoretical and experimental contexts in chapter 5.

Atoms may also be trapped optically, with minimal scattering of photons, in a dipole trap. The dipole trap (Sec. 1.4) was first construed theoretically in 1980 [84], and realised experimentally in 1986 [104]. Unlike the MOT the dipole trap does not cool the atoms, however it has the advantage that there is only a very small fluctuating heating force, allowing further atomic cooling by other mechanisms. Dipole traps have the advantage that they do not perturb the atoms to the same extent as magnetic traps, but although there have been advances toward the goal of obtaining a BEC by all-optical means [108], this goal has so far remained elusive. It was for this reason, and because the necessary high power lasers used in dipole traps were not in keeping with the aim of a relatively simple BEC experiment, that we chose the path of magnetic trapping.

3.2.1 Atom–magnetic field interaction

The Hamiltonian for a ground state alkali metal atom in a magnetic field $\mathbf{B}$ is given in the basis of the total electronic ($\mathbf{J}$) and nuclear ($\mathbf{I}$) angular momentum states $|J, m_J; I, m_I\rangle$ by:

$$\hat{H} = \frac{A_{HFS}}{I + 1/2} \mathbf{I} \cdot \mathbf{J} - \boldsymbol{\mu} \cdot \mathbf{B}, \tag{3.32}$$

where $\frac{A_{HFS}}{I+1/2}\mathbf{I} \cdot \mathbf{J}$ is the ground state hyperfine interaction, A_{HFS} is the hyperfine splitting ($A_{HFS}/h = 3036$ MHz for ^{85}Rb, $A_{HFS}/h = 6835$ MHz for ^{87}Rb) and $\boldsymbol{\mu}$ is the atom's magnetic moment.

The magnetic moment has the form:

$$\boldsymbol{\mu} = -(\mu_B g_J \mathbf{J} + \mu_N g_I \mathbf{I}), \tag{3.33}$$

where g_J and g_I are the Landé g-factors of the total electronic and nuclear momentum respectively. The rubidium nuclear g-factors are $g_I = 1.353$ for ^{85}Rb (for which $I = 5/2$) and $g_I = 2.751$ for ^{87}Rb ($I = 3/2$). The total electronic momentum ($\mathbf{J} = \mathbf{L} + \mathbf{S}$) g-factor for both isotopes can be determined

from the total orbital ($\mathbf{L}$) and spin ($\mathbf{S}$) angular momenta through the relation:

$$g_J = \frac{3J(J+1) - L(L+1) + S(S+1)}{2J(J+1)}.$$

The ground state of the D2 transition $5p^2S_{2/2}$ ($J = 1/2, L = 0, S = 1/2$) has $g_J = 2$ and the excited state $5p^2P_{3/2}$ ($J = 3/2, L = 1, S = 1/2$) has $g_J = 4/3$.

With a magnetic field of magnitude $B = |\mathbf{B}|$ along the z axis, Eq. 3.32 leads to the Zeeman-shifted Hamiltonian:

$$\hat{H} = A_{HFS}(I_z J_z - I_+ J_- - I_- J_+) + \mu_B(g_J J_z + \frac{\mu_N}{\mu_B} g_I I_z)B, \tag{3.34}$$

where J_+, J_-, I_+, I_- are the raising and lowering angular momentum ladder operators for $\mathbf{J}$, $\mathbf{I}$. The ladder operators generate off-diagonal terms in the Hamiltonian. The Hamiltonian, Eq. 3.34 can be diagonalised for a given alkali metal atom. The resulting magnetic field dependence of the ^{87}Rb ground state energy levels can be seen in the Breit-Rabi plot of Fig. 3.6.
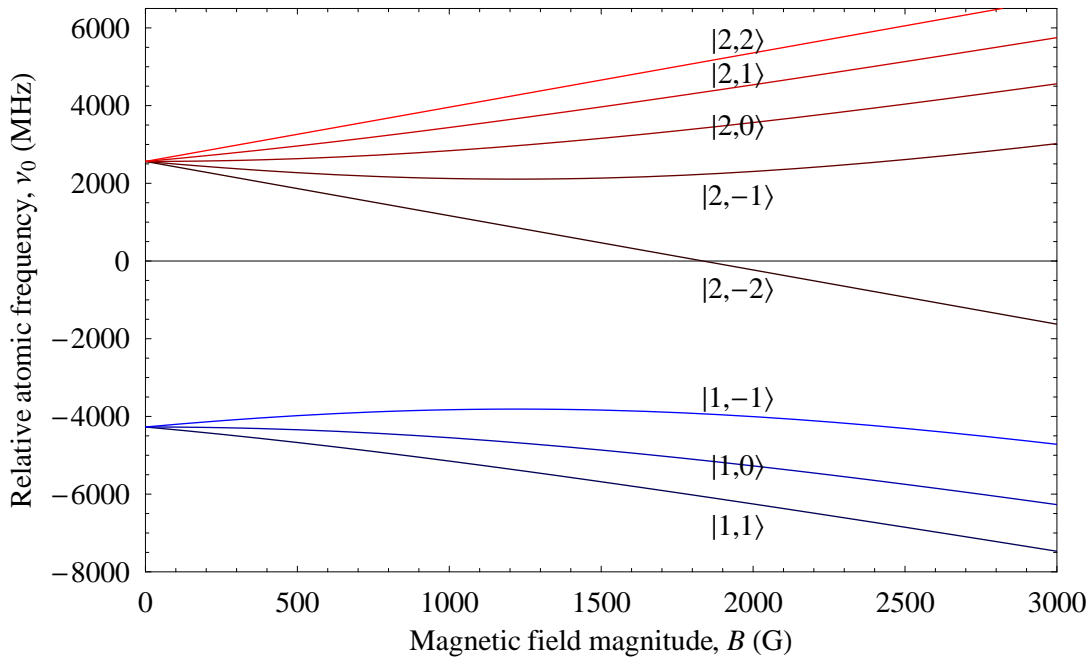
Figure 3.6: The ground state Breit-Rabi diagram for ^{87}Rb. Ground states are labelled by the $|F, m_F\rangle$ level they correspond to at low B fields (when the Hamiltonian is diagonal in F).

For low magnetic fields ($B < 300\,\mathrm{G} = 0.03\,\mathrm{T}$) the ground state Hamiltonian is approximately diagonal in the basis of the total atomic angular momentum quantum vector $\mathbf{F} = \mathbf{J} + \mathbf{I}$. In a low magnetic field the relative energy of the two degenerate F ground levels sets $|F = I - 1/2, m_F\rangle$, $|F = I + 1/2, m_F\rangle$ become:

$$E_{|F=I-1/2, m_F\rangle}(B) = E_{I-1/2} + \mu_B g_F m_F B$$

$$E_{|F=I+1/2, m_F\rangle}(B) = E_{I-1/2} + A_{HFS} + \mu_B g_F m_F B,$$

where

$$g_F = \frac{g_J\big(F(F+1) + J(J+1) - I(I+1)\big) + \frac{\mu_N}{\mu_B}g_I\big(F(F+1) - J(J+1) + I(I+1)\big)}{2F(F+1)}.$$

As $\mu_N \ll \mu_B$, g_F values in the two alkali metal ground state F levels ($I, J = 1/2, F = I \pm 1/2$) are approximately

$$g_F = \frac{\pm 2}{2I + 1}$$

(i.e. $g_F \approx \frac{\pm 2}{2I+1}$ and so $g_F = \pm 1/3$ in ^{85}Rb, $g_F = \pm 1/2$ in ^{87}Rb).

The above derivation is valid for constant magnetic fields. If an atom moves in a spatially varying magnetic field $\mathbf{B}(\mathbf{r})$, then the result $U \propto |\mathbf{B}|$ holds as long as the atoms's motion is adiabatic – i.e. if the frequency at which the atom's magnetic moment precesses about the magnetic field (the Larmor frequency, $\nu_L = \mu_B g_F m_F B/h = g_F m_F \times (1.4\text{MHz/G})$) is much greater than the frequency with which the magnetic field rotates about the atom in its local frame. This is usually the case for cold atoms except in regions where $B \approx 0$.

The form of the potential energies (monotonically increasing) for ground states with $g_F m_F > 0$ means that they are attracted toward low B fields (these are the weak field seeking states). Similarly states with $g_F m_F < 0$ are strong field seeking. The ^{87}Rb ground state hyperfine levels $F = 1$ and $F = 2$ have total momentum g-factors $g_F \approx -1/2, +1/2$ respectively (states $|F, m_F\rangle = |1, -1\rangle, |2, 1\rangle, |2, 2\rangle$ are weak-field seeking in low magnetic fields). The ^{85}Rb ground state hyperfine levels $F = 2$ and $F = 3$ have total momentum g-factors $g_F \approx -1/3, +1/3$ respectively (states $|F, m_F\rangle = |2, -2\rangle, |2, -1\rangle, |3, 1\rangle, |3, 2\rangle, |3, 3\rangle$ are weak-field seeking in low magnetic fields).

Adiabatically moving weak-field seeking atoms will be attracted to local spatial minima in the magnetic field. This allows atoms to be magnetically trapped in suitable fields, and the form of these magnetic fields will be covered later in this section. Strong field seeking atoms are attracted to local maxima in the magnetic field. Unfortunately spatial maxima in static magnetic fields are forbidden by Maxwell's equations [178], however it is possible to trap strong field seeking atoms in a time-varying magnetic field with an AC trap [179, 180, 181]. Such AC traps have the advantage that hyperfine changing atomic collisions are energetically forbidden in samples of atoms stored in the lowest energy strong-field seeking states. AC magnetic traps have the marked disadvantage that their potential is much shallower than a DC magnetic trap at similar currents.

The Breit-Rabi diagram for the excited state $5\text{p}^2\text{P}_{3/2}$ has been omitted, because the excited state is mainly of use when probing the atoms with D2 light. All of our experimental absorption imaging is done in magnetic fields $B < 1\,\text{G}$ at which the Zeeman splitting is in the linear regime. The closer proximity of the excited state energy levels (at the level of $100\,\text{MHz}$) compared to the ground state level splitting (a few GHz) means that non-linear excited state Zeeman effects become important at fields $B > 5\,\text{G}$.

Given the form of the atomic response to an applied magnetic field, it remains to determine the magnetic field and its magnitude which arise from various experimental coil configurations. Details of various magnetostatic traps are presented in Ref. [182].

3.2.2 Magnetic fields from circular and rectangular coils

The magnetic field from a current-carrying wire can be determined using the Biot-Savart law:

$$d\mathbf{B} = \frac{\mu_0 \mathcal{I}}{4\pi} \frac{d\mathbf{l} \times (\mathbf{r} - \mathbf{r}')}{|\mathbf{r} - \mathbf{r}'|^3}, \tag{3.35}$$

where the magnetic field $d\mathbf{B}$ at the point $\mathbf{r}$ is generated by a current element at position $\mathbf{r}'$ with current $\mathcal{I}$ and length $d\mathbf{l}$. In the common units of magnetic trapping (the Gauss, $1\text{G} = 10^{-4}\,\text{T}$, and the centimeter), the proportionality constant in Eq. 3.35 is $\frac{\mu_0}{4\pi} = \frac{1}{10}\,\text{GcmA}^{-1}$. These units will be used throughout this section.

For a segment of wire along the z axis with length $2c$ (having ends at the positions $(0, 0, \pm c)$), carrying a current $\mathcal{I}$ in the $+z$ direction one can integrate Eq. 3.35 to obtain the magnetic field:

$$\mathbf{B} = \frac{\mathcal{I}}{10(x^2 + y^2)} \left(\frac{-(z - c)}{\sqrt{x^2 + y^2 + (z - c)^2}} + \frac{z + c}{\sqrt{x^2 + y^2 + (z + c)^2}} \right) (-y, x, 0). \tag{3.36}$$

Although such a current carrying wire segment isn't physical, a closed path of current line segments is. In particular, pairs of rectangular coils will be of interest in the experimental chapter. The magnetic field generated by a pair of N turn rectangular 'Helmholtz' coils (with the dimensions and current sense depicted in Fig. 3.7) has a Taylor expansion about the origin of

$$\mathbf{B} = \frac{8N\mathcal{I}}{5} \frac{ab(a^2 + b^2 + 2c^2)}{(a^2 + \boxed{c^2})(b^2 + c^2)\sqrt{a^2 + b^2 + c^2}} (0, 0, 1) \tag{3.37}$$

to first order (only even order terms exist). The second order terms of the expansions are omitted for brevity.

The magnetic field Taylor expansion for an N turn rectangular 'anti-Helmholtz' coil pair is

$$\mathbf{B} = \frac{16N\mathcal{I}}{5} \frac{abc}{(a^2 + b^2 + c^2)^{3/2}} \left(-B_{1x}x, -B_{1y}y, (B_{1x} + B_{1y})z \right) \tag{3.38}$$

to second order, where $B_{1x} = \frac{2b^2 + 3(a^2 + c^2)}{(a^2 + c^2)^2}$, $B_{1y} = \frac{2a^2 + 3(b^2 + c^2)}{(b^2 + c^2)^2}$.

Integration of the Biot-Savart law for circular loops and arcs does not result in an analytic expression, however the field can be expressed in elliptic integrals, which are built-in functions for many mathematical computation packages. The (cylindrically symmetric) magnetic field in cylindrical polar co-ordinates due to a circular current loop of diameter d centred in the $z = 0$ plane is [183]:

$$\begin{aligned}
\mathbf{B}(r, z) &= (B_r(r, z), B_z(r, z)) \\
&= \frac{N\mathcal{I}}{5\sqrt{(r + d/2)^2 + z^2}} \left(\left[-K[G(r, z, a)] + \frac{(d^2/4 + r^2 + z^2)E[G(r, z, a)]}{(r - d/2)^2 + z^2} \right] \frac{z}{r}, \right. \\
&\qquad \left. K[G(r, z, a)] + \frac{(d^2/4 - r^2 - z^2)E[G(r, z, a)]}{(r - d/2)^2 + z^2} \right).
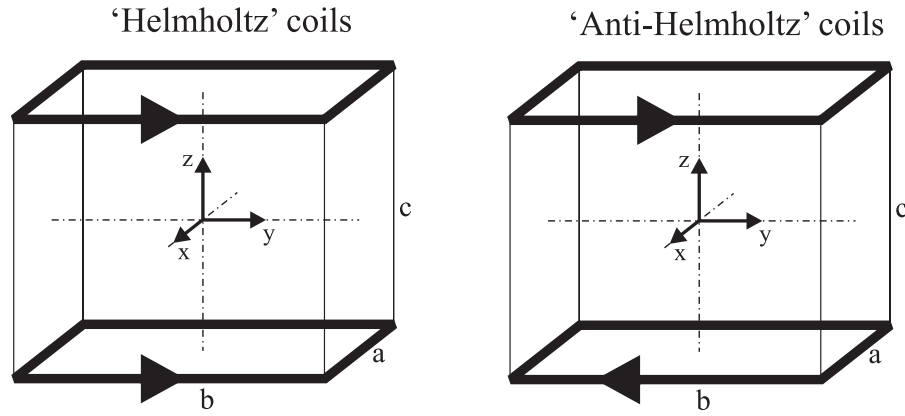\end{aligned} \tag{3.39}$$

Figure 3.7: Rectangular 'Helmholtz' and 'anti-Helmholtz' magnetic field coils, with dimensions as indicated.

where $G(r, z, a) = \frac{2\,dr}{(r+d/2)^2+z^2}$ and the functions E and K refer to the corresponding E and K elliptic integrals $E[m] = \int_0^{\pi/2} \left(1 - m\sin^2\theta\right)^{1/2} d\theta$, $K[m] = \int_0^{\pi/2} \left(1 - m\sin^2\theta\right)^{-1/2} d\theta$. These are sometimes defined in a slightly different manner [184].

The magnetic field along the axis of a circular current loop *is* analytic however, namely $B_z(0, z) = \frac{2\pi N\mathcal{I}}{5}\frac{d^2}{(d^2+4z^2)^{3/2}}$. The on-axis magnetic field Taylor expansion from a cylindrically symmetric system of constant current coils can in fact be used to determine the magnetic field Taylor expansion over all space. This extension is made using Maxwell's equations, and the fourth order cylindrically symmetric magnetic field has the form:

$$\mathbf{B}(r, z) = B_0(0, 1) + B_1\left(-\tfrac{r}{2}, z\right) + \tfrac{B_2}{2}\left(-rz, z^2 - \tfrac{r^2}{2}\right) + \tfrac{B_3}{6}\left(\tfrac{3r^3}{8} - \tfrac{3r^2 z}{2}, z^3 - \tfrac{3r^2 z}{2}\right)$$
$$+ \tfrac{B_4}{24}\left(\tfrac{3r^3 z}{2} - 2rz^3, z^4 - 3r^2 z^2 + \tfrac{3r^4}{8}\right), \tag{3.40}$$

where $B_n = \left.\frac{\partial^n B_z}{\partial z^n}\right|_{(0,0)}$.

For two coils of diameter d, separated by a distance s (Fig. 3.8) there are two forms of the magnetic field. When the coils carry current in the same sense, then they are often loosely called 'Helmholtz' coils, and their magnetic field Taylor expansion has the even symmetric form:

$$B_1 = B_3 = 0, \;\; B_0 = \tfrac{4\pi N\mathcal{I}d^2}{5(d^2+s^2)^{3/2}}, \;\; B_2 = \tfrac{48\pi N\mathcal{I}d^2(4s^2-d^2)}{5(d^2+s^2)^{7/2}},$$
$$B_4 = \tfrac{576\pi N\mathcal{I}d^2(d^4-12d^2 s^2+8s^2)}{(d^2+s^2)^{11/2}}. \tag{3.41}$$

'True' Helmholtz coils obey the additional restriction that the magnetic field is spatially constant to fourth order. From the Taylor expansion this clearly occurs when the coil separation has the form $s = d/2$. In the case of square rectangular coils $(a = b)$ the 'true' Helmholtz coils are formed when $c = 0.5445a$.

The two coils of an 'Anti-Helmholtz' pair carry currents in opposite senses. Their magnetic field has

'Helmholtz' coils   'Anti-Helmholtz' coils
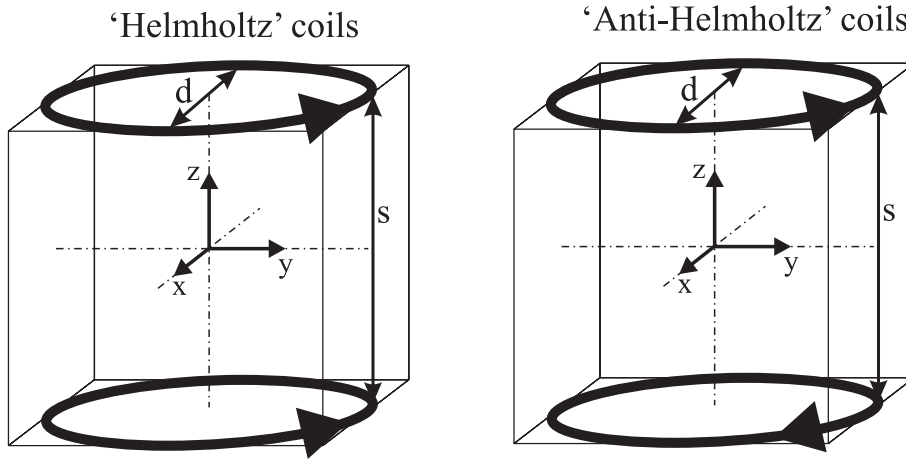
Figure 3.8: Circular 'Helmholtz' and 'anti-Helmholtz' magnetic field coils, with separation s and diameter d.

the odd symmetric form:

$$B_0 = B_2 = B_4 = 0, \ B_1 = \frac{24\pi N \mathcal{I} d^2 s}{5(d^2 + s^2)^{5/2}}, \ B_3 = \frac{96\pi N \mathcal{I} d^2 s (4s^2 - 3d^2)}{(d^2 + s^2)^{9/2}}, \tag{3.42}$$

which is linear to fifth order when $s = \sqrt{3}d/2$ (the 'true' anti-Helmholtz configuration). For square rectangular coils $(a = b)$ the 'true' anti-Helmholtz configuration is reached when $c = 0.9458a$.

It is worth noting that if all of the dimensions of a magnetic field coil system are scaled down by a factor f, then the nth order co-efficients in the Taylor series of the magnetic field will increase by a factor $1/f^{n+1}$.

3.2.3 Quadrupole trap

To first order all square and circular 'Anti-Helmholtz' coil pairs generate a field of the form $\mathbf{B}_{quad}(\mathbf{r}) = B_1(-\frac{x}{2}, -\frac{y}{2}, z)$ (Fig. 1.3) which is known as a quadrupole field. The first atomic magnetic trap in 1985 [185] employed a quadrupole magnetic trap loaded from a laser-slowed atomic beam. The potential energy of a ground state atom in a quadrupole magnetic field is:

$$U(x, y, z) = \mu_B g_F m_F B_1 \sqrt{\frac{x^2}{4} + \frac{y^2}{4} + z^2}, \tag{3.43}$$

i.e. a three dimensional 'conical' potential.

Although quadrupole traps have a very simple geometry and provide strong confinement to atomic samples they have a major drawback – magnetically trapped atoms can 'leak' out of regions where the magnetic field approaches zero. In section 3.2.1 it was mentioned that the magnetic trapping potential can only be considered proportional to the magnitude of $\mathbf{B}$ if the atomic motion through a spatially varying field is adiabatic. A simple estimate for the trap region in which non-adiabatic spin-flips (or 'Majorana

transitions') occur [20, 102] in a magnetic trap can be made by considering an atom with speed V on a trajectory in the $z = 0$ plane which takes it to a minimum distance R away from the the magnetic field zero. The magnetic field precesses around the atom in its local frame with a maximum rate of change $\omega = 2\pi\nu = V/R$. Spin flips into untrapped magnetic quantum states $g_F m_F \leq 0$ can occur when the Larmor frequency $\nu_L = \frac{\mu_B g_F m_F B_1 R}{2h}$ satisfies the condition $\nu_L \lesssim \nu$. This leads to an ellipsoidal region over which loss occurs, and the relative loss rate from the magnetic due to spin flips can then be found given the temperature of the atoms and strength of the magnetic field gradient B_1.

The loss rate due to spin flips would not have been catastrophic in itself, however trap loss is greatest for the coldest atoms – precisely the atoms we wish to keep in order to attain high phase space densities. As the atomic cloud size decreases during evaporative cooling (Sec. 3.3) relative trap loss rates continue to grow and quickly thwart any attempts to start runaway evaporation to BEC.

The problem of spin-flip loss at zeroes in the magnetic trapping potential can be solved by using magnetic traps with non-zero spatial minima in the magnetic field magnitude (or by 'plugging' the hole near the magnetic field zero with an optical dipole beam [39]). The two forms of entirely magnetic traps which have been used to evaporatively cool atomic samples to the BEC phase transition are the time-orbiting potential (TOP) and Ioffe-Pritchard (IP) trap. These will be discussed in sections 3.2.4 and 3.2.5 respectively.

3.2.4 Time-orbiting potential trap

The time-orbiting potential (TOP) magnetic trap is based on a quadrupole field. The 'hole' in the trap at $B = 0$ is made to vary with time by displacing the trap with an applied field vector

$$\mathbf{B}_{bias}(x, y, z, t) = B_{bias}(\sin(\omega_\phi t)\cos(\omega_\theta t), \sin(\omega_\phi t)\sin(\omega_\theta t), \cos(\omega_\phi t)),$$

which rotates about a sphere of constant magnitude B_{bias}. The bias field is generated experimentally by applying oscillating currents to orthogonal pairs of Helmholtz coils. Only two-dimensional bias fields have been used experimentally so far, in the two configurations: $\omega_\phi t = \pi/2$ [29] (the bias field rotates in a circular path through the $z = 0$ plane) and $\omega_\theta = 0$ [73] (confined to the $y = 0$ plane, say).

As the 'hole' in the magnetic trap at $\mathbf{B}_{quad} + \mathbf{B}_{bias}(t) = \mathbf{0}$, i.e.

$$\mathbf{r}_{hole}(t) = \frac{B_{bias}}{B_1}(2\sin(\omega_\phi t)\cos(\omega_\theta t), 2\sin(\omega_\phi t)\sin(\omega_\theta t), -\cos(\omega_\phi t)), \qquad (3.44)$$

changes position with time, then the atoms in the magnetically trapped cloud attempt to 'chase' it, due to their weak-field seeking nature. As long as the magnetic trap frequencies (Eq. 3.48) are much smaller than the frequency at which the bias field rotates, then the atoms will instead be confined at the centre of the time-averaged magnetic potential. The other provision for TOP operation is that the bias field cannot rotate faster than the Larmor frequency (ν_L), to ensure that the atomic motion is still adiabatic.

The time averaged potential is obtained by taking the Taylor expansion of $B = \sqrt{\mathbf{B} \cdot \mathbf{B}} = \sqrt{B_{bias}^2 + X}$ where X includes the time and position dependent terms of the field and $X = 0$ at $\mathbf{r} = 0$. The second order Taylor expansion has the form $B = B_{bias} + \frac{X}{2} - \frac{X^2}{8B_{bias}}$. Collecting together all terms of spatial order less than three, and omitting spatial terms which time-average to zero, the magnitude of the magnetic field is

$$B = B_{bias} + \frac{B_1{}^2}{8B_{bias}} \left(\left[1 - \sin^2(\omega_\phi t) \cos^2(\omega_\theta t)\right] x^2 + \left[1 - \sin^2(\omega_\phi t) \sin^2(\omega_\theta t)\right] y^2 \right.$$
$$\left. + 4\left[1 - \cos^2(\omega_\phi t)\right] z^2 \right). \qquad (3.45)$$

When $\omega_\phi/\omega_\theta$ is not a rational number the trajectory of the field zero traces out a path which covers an ellipsoid.

For most values of ω_ϕ, ω_θ the time average of the potential in Eq. 3.45 has the harmonic form:

$$B = B_{bias} + \frac{B_1{}^2}{32B_{bias}} \left(3x^2 + 3y^2 + 8z^2\right). \qquad (3.46)$$

The special two-dimensional cases $\omega_\phi t = \pi/2$ and $\omega_\theta = 0$ yield potentials of the form:

$$B = B_{bias} + \frac{B_1{}^2}{16B_{bias}} \left(x^2 + y^2 + 8z^2\right),$$

$$B = B_{bias} + \frac{B_1{}^2}{16B_{bias}} \left(x^2 + 2y^2 + 4z^2\right)$$

respectively.

Although 3D TOP traps have not been implemented experimentally as yet, they are suggested in this thesis as an interesting prospect for future research. The main advantage of a 3D TOP however, would be that the evaporation surface is three-dimensional, unlike the two-dimensional evaporation surface of 2D TOPs. This would enhance the efficiency of evaporative cooling in the TOP, particularly in the low-temperature regime. They also have the advantage that the trapping potential is closer to the isotropic case. Traps with isotropic potentials are particularly easy to model theoretically, as spherical symmetry reduces many properties to one-dimensional problems.

The Hooke's law relation, where a spring constant k results in a harmonic potential $U = \frac{k}{2}x^2$, yields an oscillation frequency of $\omega = 2\pi\nu = \sqrt{k/m}$ where m is the mass of a particle. Comparison of the TOP potential energy

$$U = \mu_B g_F m_F B = \mu_B g_F m_F \left(B_0 + \frac{B_{2x}}{2}x^2 + \frac{B_{2y}}{2}y^2 + \frac{B_{2z}}{2}z^2\right) \qquad (3.47)$$

with Hooke's law gives the 'trap frequencies' which are often used to describe how tight a magnetic trap is. The trap frequency in the x_i direction is thus:

$$\nu_{x_i} = \frac{1}{2\pi} \sqrt{\frac{\mu_B g_F m_F B_{2x_i}}{m}}. \qquad (3.48)$$

where B_{2x_i} is the magnetic field curvature in the direction x_i. For the case of ^{87}Rb atoms in the $|2,2\rangle$ ground state Eq. 3.48 becomes $\nu_{x_i} = 1.276\sqrt{B_{2x_i}}$ when the magnetic field curvature is measured in units of G/cm^2. Typical experimental trapping frequencies are given in Table 1.1. Ioffe-Pritchard magnetic traps (see below) are also harmonic to second order and their trap frequencies can be characterised in this manner.

In the discussion so far we have neglected gravitational effects, which are particularly important for heavier atomic species. The main effect of gravity is to cause a vertical displacement in the centre of the atomic cloud with respect to the centre of the magnetic trapping potential. If gravity is in the $-y$ direction, the equilibrium point is displaced Δy where

$$-k_y\,\Delta y = -m\omega_y{}^2\,\Delta y = mg \quad \Rightarrow \quad \Delta y = -\frac{g}{(2\pi\nu_y)^2}. \tag{3.49}$$

As well as the magnetic field curvature, the gravitational displacement of the cloud therefore depends on both the mass m and the m_F quantum number. To minimise gravitational sag, magnetic traps are usually oriented with their strongest trapping frequency in the gravity direction.

The formation of a magnetic trap with a double potential minimum would be very interesting as it allows the formation of two condensates. It can be shown however, that regardless of the time-dependent motion of a bias field $\mathbf{B}(t)$ it is impossible to obtain a TOP trap with negative spatial curvature in any direction.

Interesting variants of the time-orbiting potential trap that create tighter and more stable confinement using rotating *quadrupole* fields are discussed in Ref. [186].

3.2.5 Ioffe-Pritchard configuration

Unlike the TOP magnetic trap the Ioffe-Pritchard (IP) [21, 22] magnetic trap is a static trap. Although there are a large variety of magnetic coil configurations (Table 1.1) which can be used to generate an IP field, the form of the magnetic field is essentially the same in all cases and will be discussed below. The non-zero minimum in the magnitude of the IP magnetic field prevents non-adiabatic spin flips within the magnetic trap.

The 'traditional' form of IP trap is comprised of a pair of circular (or square) 'Helmholtz' coils as well as four long wires equi-distant from each other, and equi-distant from the symmetry (z) axis of the Helmholtz pair. The four long wires have the property that adjacent wires have opposite currents. The Helmholtz coil pair will generate a second-order magnetic field (Eq. 3.40):

$$\mathbf{B}(x,y,z) = B_0\,(0,0,1) + \frac{B_2}{2}\left(-xz, -yz, z^2 - \frac{x^2+y^2}{2}\right). \tag{3.50}$$

Depending on the Helmholtz pair coil spacing, the sign of B_2 can be altered. The magnitude of the magnetic field due to this coil pair alone has the property that the magnetic potential is confining in the

axial direction precisely when it causes repulsion in the radial direction (and vice versa).

The four wires generate a two-dimensional quadrupole magnetic field (to fourth order):

$$\mathbf{B}(x, y, z) = B_1(-x, y, 0). \tag{3.51}$$

A good approximation for the magnitude of the magnetic field generated by the combination of fields from the four wires and the Helmholtz pair is therefore

$$B = \sqrt{\left(B_0 + \frac{B_2}{2}\left(z^2 - \frac{x^2 + y^2}{2}\right) \right)^2 + B_1{}^2(x^2 + y^2)}. \tag{3.52}$$

This yields a magnetic field magnitude with a harmonic, cylindrically symmetric, second order Taylor expansion

$$B = B_0 + \frac{B_{2r}}{2}(x^2 + y^2) + \frac{B_{2z}}{2}z^2,$$

where the radial and axial curvatures of the field magnitude are $B_{2r} = \frac{B_1{}^2}{B_0} - \frac{B_2}{2}$ and $B_{2z} = B_2$ respectively. This expansion is valid as long as $r = \sqrt{x^2 + y^2} \lesssim \sqrt{2}B_0/B_1$. In general the IP potential has a hyperbolic radial cross-section at constant z – parabolic when $r \lesssim \sqrt{2}B_0/B_1$ and linear when $r \gtrsim \sqrt{2}B_0/B_1$.

It is therefore possible to create strong radial confinement by decreasing the level of the bias field B_0, and this can be achieved experimentally using a coil system which creates strong axial field curvature (and necessarily a constant axial bias field) plus another coil system with a comparable bias field and much lower (or negative) axial curvature oriented in the opposite direction. These coils which generate the cancelling field will henceforth be called the IP 'bias' coils. Experimental bias coils typically lower the magnetic field minimum to the level $B_0 \approx 1\,\mathrm{G}$ – low enough to create tight confinement, but large enough to greatly reduce the rate of non-adiabatic spin flips. Cigar-shaped atomic clouds form in these compressed IP traps in contrast to the slightly flattened ellipsoidal clouds formed in TOPs.

Cloverleaf

The first IP trap was similar to the 'traditional' IP trap (a circular coil pair generate an axial curvature, with the constant field cancelled by a circular bias coil pair), however the four wires in the $\pm z$ direction were replaced by a combination of four anti-Helmholtz coil pairs, as depicted in Fig. 3.9. The advantage of this 'cloverleaf' configuration is the high degree of optical access to the trapped atomic cloud. The 2D quadrupole field from the 'cloverleaf' coils has a complicated Taylor expansion for the B_1 gradient term, and the general case is omitted for brevity. If one considers the specific geometry $d = a/\sqrt{2}$, $s = a$ however, then the gradient scales with a as

$$B_1 = \frac{1.52N\mathcal{I}}{a^2}.$$

This can be contrasted with the gradient due to four infinitely long wires centred on the axes of the cloverleaf coil pairs, namely

$$B_1 = \frac{5N\mathcal{I}}{8a^2}.$$
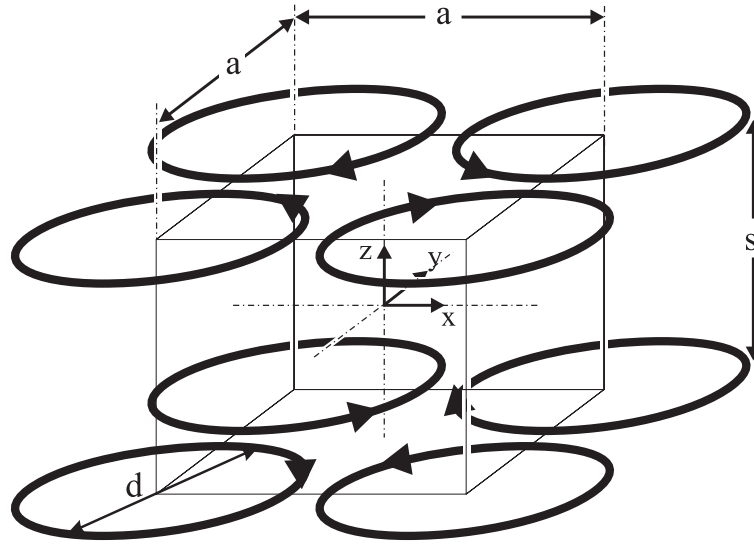
Figure 3.9: IP 'cloverleaf' magnetic field coils, comprising 4 pairs of 'anti-Helmholtz' coils (with spacing s, diameter d) with axes centred on a square of side length a. Adjacent coil pairs have the opposite current sense.

IP baseball

Another IP variant is the baseball coil, which was chosen for experiments at Sussex. Although the optical access to the magnetic trap is more limited than the cloverleaf, it has the advantage that axial curvature and radial confinement are all provided by a single coil, rather than ten. An extra pair of bias coils are used to lower the constant axial field term B_0 and increase the magnetic trap's radial confinement.

The baseball coil is named after the seam which runs around the edge of a baseball. A variety of geometries exist [182], however the simplest is formed from four semi-circular arcs. This 'circular' baseball coil is depicted in Fig. 3.10. 'Rectangular baseball' coils have a similar geometry (Fig. 3.10) but are comprised of line segments. In the limit $c \gg a$ the rectangular baseball has a field equivalent to the four current carrying wires of the 'traditional' IP magnetic trap.

Using the dimension $a = 2r$ to allow easier comparison of the two forms of baseball coil, the magnetic parameters for an N turn circular baseball coil carrying a current $\mathcal{I}$ are

$$B_0 = \frac{2\sqrt{2}N\mathcal{I}}{5a}, \qquad B_1 = \frac{2N\mathcal{I}}{a^2}, \qquad B_2 = \frac{8\sqrt{2}N\mathcal{I}}{5a^3}. \tag{3.53}$$

Circular baseball coil   Rectangular baseball coil

Figure 3.10: Geometry of the IP 'baseball' magnetic field coil in circular and rectangular configurations.
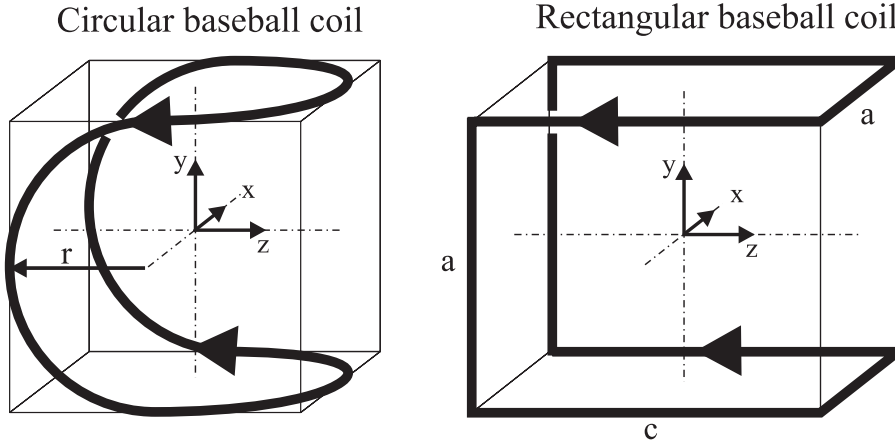
The equivalent parameters for rectangular coils are

$$B_0 = \frac{8N\mathcal{I}a^2}{5(a^2+c^2)\sqrt{2a^2+c^2}}, \qquad B_1 = \frac{8N\mathcal{I}(4a^4c+3a^2c^3+c^5)}{5a^2(a^2+c^2)^2\sqrt{2a^2+c^2}},$$
$$B_2 = \frac{64N\mathcal{I}(-5a^6+11a^4c^2+18a^2c^4+6c^6)}{5(a^2+c^2)^3(2a^2+c^2)^{5/2}}. \tag{3.54}$$

The magnetic trap at Sussex was a combination of the two forms of baseball coil – a rectangular baseball with rounded corners. The dimensions of the 9-turn coil are given in Fig. 4.17. A good approximation to the coil is a rectangular coil with dimensions $a = 4.5$ cm, $c = 5.5$ cm – complete integration of the Biot-Savart for the nine individual coil windings (comprised of line segments and quarter-circles current sources) yields magnetic field constant, gradient and curvature terms which differ only at the $5-10\%$ level. Given the correct geometry of a coil the largest source of error in magnetic field calculation is the average dimensions d of the coil – the magnetic field curvature scales as $1/d^5$.

At the maximum current of 216 A the Sussex baseball coil generates an IP field with parameters $B_0 = 165$ G, $B_1 = 180$ G/cm, $B_2 = 60$ G/cm^2. A fraction ($\approx 10\%$) of any current in the baseball goes through the bias coil as well (Sec. 4.2.3) and this mainly affects the uncompressed IP trap bias field – changing it to $B_0 \approx 150$ G.

The relevant parameters for the Sussex *compressed* Ioffe-Pritchard baseball+bias magnetic trap are $B_0 = 1.04$ G, $B_1 = 180$ G/cm and $B_2 = 70$ G/cm^2. These parameters yield trapping frequencies $\nu_r = 225$ Hz and $\nu_z = 11$ Hz, in good agreement with the experimentally measured radial frequency of the trap ($\nu_r = 223$ Hz). The gradient and curvature were calculated, however the net bias field B_0 is the difference of two large magnetic fields and is best obtained experimentally from the base frequency of evaporative cooling (Sec. 3.3.1).

The form of the IP potential given in equation Eq. 3.52 is a reasonable approximation to the full magnetic field magnitude generated by IP magnetic coils, and its cylindrical symmetric nature will be
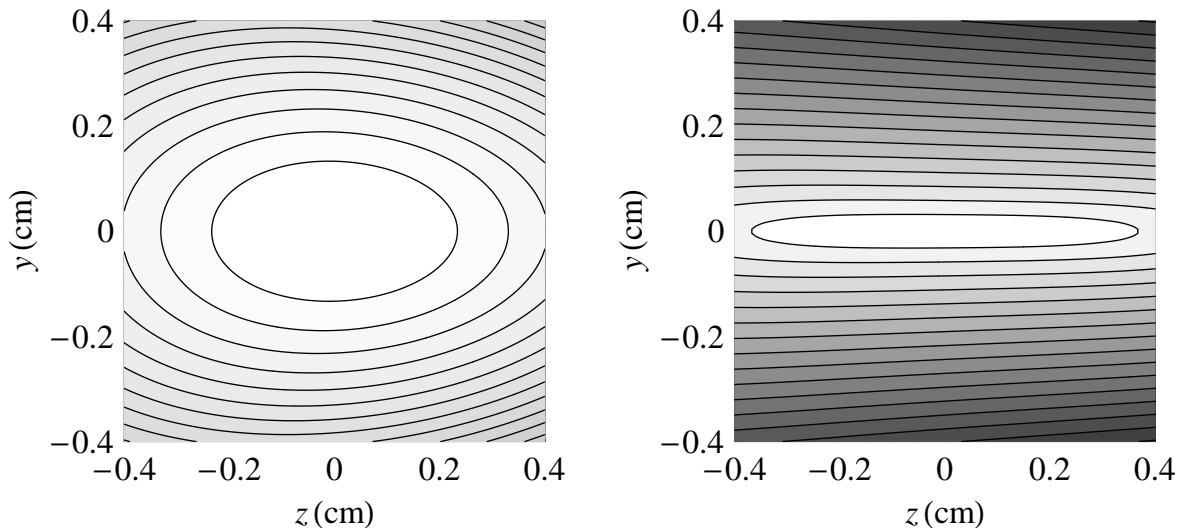
Figure 3.11: The magnetic field contours of the Sussex IP trap in the uncompressed (left) and compressed (right) configurations. The contour intervals are three times smaller in the uncompressed contour plot, but equivalent grey-scale shading is used for both plots.

advantageous later in the thesis for simplifying calculations. There are second order terms in the x and y magnetic field components that have been neglected in this treatment however, and the more exact magnitude of the second-order magnetic field (for the Sussex IP geometry) is:

$$B = \sqrt{\left(B_0 + \frac{B_2}{2}\left(z^2 - \frac{x^2 + y^2}{2}\right)\right)^2 + \left(B_1 x - \frac{B_2 xz}{2}\right)^2 + \left(B_1 y - \frac{B_2 yz}{2}\right)^2}. \qquad (3.55)$$

Graphical depictions of the magnetic potential for the Sussex IP trap are shown in Figs. 3.11, 3.12. An interesting feature of the magnetic field magnitude of Eq. 3.55 is that it does not have an even symmetry in z. This will be important in chapter 5 when we consider magnetic 'bouncing' in an IP potential, as atoms at y values below the magnetic field minimum will be imparted momentum in the $-z$ direction.

3.2.6 Compression

If the strength of the the spring constants in a harmonic magnetic trap are jumped rapidly (non-adiabatically) from the initial spring constant k_i to the final value k_f (e.g. by changing the magnetic coil current from $\mathcal{I}_i$ to $\mathcal{I}_f = \frac{k_f}{k_i}\mathcal{I}_i$) then the change in temperature is

$$\frac{T_f}{T_i} = \frac{1}{2}\left(1 + \frac{k_f}{k_i}\right).$$

This can be derived by considering the average initial potential (U_i), kinetic (K_i) and total $(E_i = U_i + K_i)$ energy of an atom in a magnetic trap. If the spring constant is suddenly increased, then the potential energy changes to $U' = \frac{k_f}{k_i}U_i$. The new total energy $E' = U' + K_i$ gets redistributed between kinetic
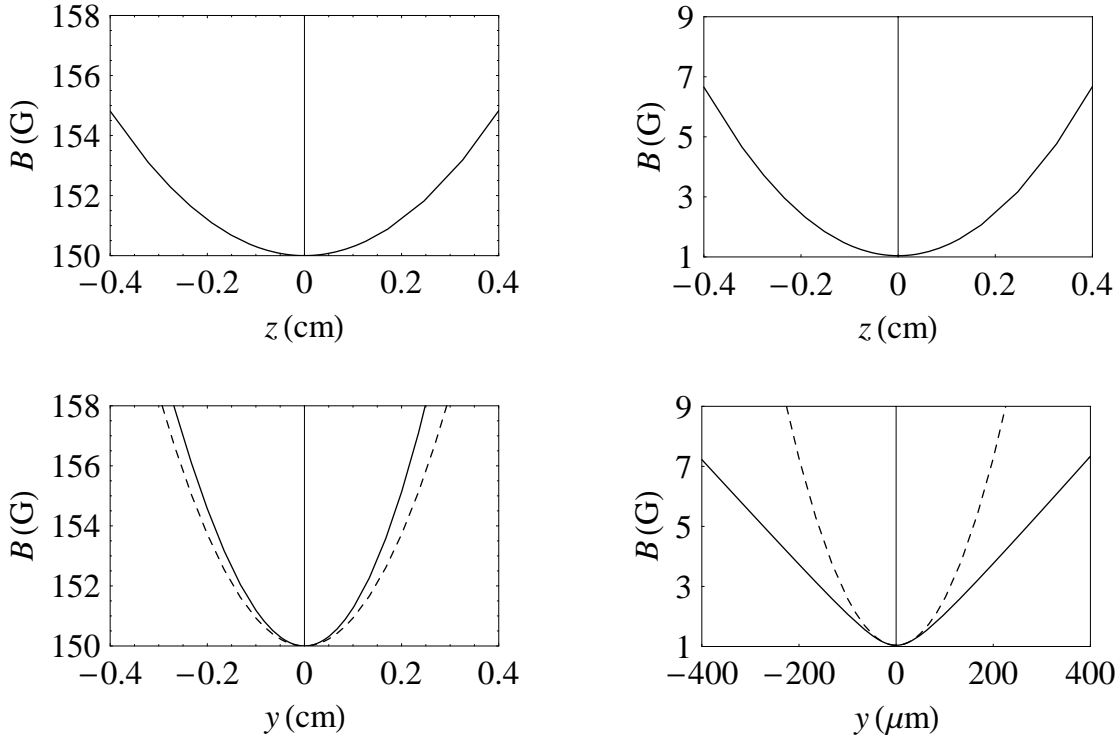
Figure 3.12: The magnetic field magnitude along the z (top images) axis in the uncompressed (left) and compressed (right) IP configurations with the maximum current of $216\,\text{A}$. Note the change in magnetic bias, B_0. The lower images depict corresponding images of the magnetic field magnitude along the y axis in the uncompressed (left) and compressed (right) IP magnetic trap. Note the change in y scale.

and potential terms as the distribution thermalises until $E_f = E'$ and then $E_f = 3k_B T_f = 2U_f = 2K_f$ in a harmonic trap. The sudden change in temperature leads to a change in density $(n \propto (k/T)^{3/2})$:

$$\frac{n_f}{n_i} = \left(\frac{1}{2} \left(1 + \frac{k_i}{k_f} \right) \right)^{-3/2} .$$

If the rate of change of the trapping frequencies ν_{x_i} is slow enough to obey the relation [173]

$$\frac{d\nu_{x_i}}{dt} \ll \min(\nu_{x_i}{}^2, \gamma_{el}{}^2),$$

where γ_{el} is the elastic collision rate in the atomic cloud (Sec. 3.1.7) then the compression becomes adiabatic. By integrating over a sequence of infinitesimal non-adiabatic changes in the spring constant $k_i = k$, $k_f = k + dk$, the temperature and density increases in the adiabatic regime are obtained:

$$\frac{T_f}{T_i} = \sqrt{\frac{k_f}{k_i}},$$

$$\frac{n_f}{n_i} = \left(\frac{k_f}{k_i} \right)^{3/4} .$$

As well as the temperature and density, the change in the elastic collision rate ($\gamma \propto nT^{1/2}$) and phase space density (PSD $\propto nT^{-3/2}$) can be computed. A graphical summary of the change in atomic parameters during adiabatic and non-adiabatic compression is given in Fig. 3.13. Importantly, it is impossible to increase the phase space density of a trapped atomic cloud by modifying the strength of their potential in a time-dependent manner whilst retaining the potential's overall shape [187].
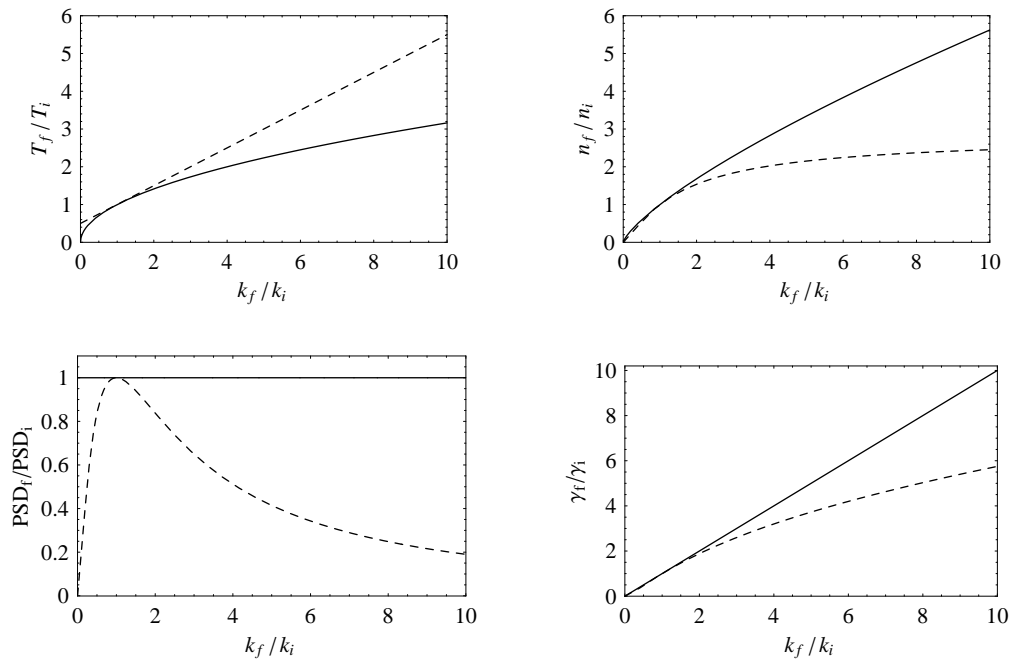
Figure 3.13: The change in various atom trap parameters (temperature T, density n, phase space density (PSD), elastic collision rate (γ)) in a harmonic trap when the trap spring constant is ramped adiabatically (solid curves) or suddenly (dashed curves) from an initial value k_i to k_f.

Full derivations of the parameter changes during non-adiabatic/adiabatic compression of a complete Ioffe-Pritchard potential (Eq. 3.52) can be made in a similar manner. The average kinetic energy of an atom is again $K = \frac{3}{2}k_B T$, and the spatial distribution is given by the Boltzmann distribution

$$n(\mathbf{r}) \propto e^{-\frac{U_{IP}(\mathbf{r})}{k_B T}},$$

where in this case $U_{IP}(\mathbf{r})$ is the potential energy distribution arising from Eq. 3.52. The potential energy for an atom in the trap is therefore

$$U = \frac{3}{2}k_B T \left(\frac{2 + 5\frac{k_B T}{U_0}}{2 + 3\frac{k_B T}{U_0}} \right)$$

where $U_0 = \mu_B m_F g_F B_0$ is the potential energy at the centre of the trap. In the limit $U_0 \gg k_B T$ the atoms observe a trap which is essentially harmonic ($U = \frac{3}{2}k_B T$) and in the opposite limit the trap potential is linear in the two radial directions and harmonic in the axial direction:

$$U = \frac{2}{3}(3k_B T) + \frac{1}{3}\left(\frac{3}{2}k_B T\right) = \frac{5}{2}k_B T.$$

The equations for the scaling of atomic parameters during Ioffe-Pritchard compression are more complex than in the harmonic case, and while the 'sudden' compression is analytic the adiabatic case must be evaluated computationally. However, in most experimental circumstances the Ioffe Pritchard (IP) magnetic trap at Sussex can be considered harmonic, with the greatest deviation occurring in the compressed trap before evaporative cooling is initiated.

An interesting effect inside an IP potential is that the phase-space density of trapped atoms can be made to increase slightly [188]. If the cloud is radially compressed in the IP potential (by lowering the bias field), the shape of the potential changes and hot atoms can sample anharmonic regions of the trapping potential. An extreme example of the effect of trap deformation on the phase-space density was observed in a combined magnetic and optical trap by Stamper-Kurn *et al.* [51].

3.3 Evaporative cooling

The final step on the path to BEC at Sussex was made using the technique of radio-frequency (RF) evaporative cooling.

Evaporative cooling is a process whereby the temperature of a distribution of atoms is lowered by selectively removing the hotter atoms from the distribution and allowing the remaining atoms to rethermalise. In 1985 it was proposed that evaporatively cooling would be a good technique to efficiently cool trapped atoms to the Bose-Einstein phase transition [189].

Ideally it is theoretically possible to wait a sufficiently long time until *all* of the energy in the system is redistributed into a single atom. If this atom is evaporated, a huge drop in atomic temperature results. Unfortunately the reality is that by this time no atoms would be left as cold atomic ensembles, which are optically or magnetically trapped in a vacuum, have a finite lifetime due to trap losses from collisions with relatively hot background atoms. The interplay of rethermalising elastic ('good') collisions, and 'bad' collisions due to inelastic collisions arising within the sample and from background atoms, are critically important in determining the efficiency of evaporative cooling.

We begin with an explanation of RF evaporative cooling. Section 3.3.2 will describe the dynamical theory of evaporative cooling, and this is followed in Sec. 3.3.3 by a discussion of 'runaway' evaporation. The topic is reviewed in Ref. [190].

3.3.1 RF evaporative cooling

In section 3.2.1 it was shown that for atoms trapped in spatially varying magnetic fields the Zeeman perturbation of the $|F, m_F\rangle$ ground state energy level is given by

$$\Delta E = \mu_B m_F g_F B(\mathbf{r}),$$

where $B(\mathbf{r})$ is the local magnitude of the magnetic field vector. In a Ioffe-Pritchard magnetic trap the magnetic field vector has a relatively uniform (i.e. axial) direction throughout the trapped atomic cloud, and its magnitude obeys Eq. 3.52.

An oscillating AC magnetic field applied perpendicular to the trap's magnetic field vector is capable of driving σ^+ and σ^- (i.e. $|F, m_F\rangle \to |F, m_F \pm 1\rangle$) ground state atomic transitions, if the frequency ν_{RF} of the oscillating magnetic field obeys the relation

$$h\nu_{RF} = \mu_B g_F B(\mathbf{r}). \tag{3.56}$$

In Ioffe-Pritchard traps (like ours) this corresponds to an ellipsoidal 'evaporation surface' around the centre of the magnetic trap. In a 2D TOP trap the evaporation surface at a fixed time is also ellipsoidal, centred on the zero in the magnetic field. As the magnetic field zero rotates, the time-averaged evaporation surface in a 2D TOP trap is therefore toroidal. The evaporation surface and the atomic cloud are displaced by the gravitational sag of the cloud (Eq. 3.49). This can lead to changes in the evaporation dynamics when the cloud width in the gravity direction approaches the gravitational sag.

At the evaporation surface $\Delta m_F = \pm 1$ transitions are driven in the magnetically trapped atoms, transferring atoms near this surface into states which are no longer weak field seeking and are therefore lost from the magnetic trap. As well as being spatially selective, the evaporation surface is also energy selective - only atoms with sufficient total energy are capable of climbing the magnetic potential high enough to reach the evaporation surface. Evaporation can be approximated by assuming that all atoms in the $|F, m_F\rangle$ sublevel with total energy $E \geq h m_F(\nu_{RF} - \nu_0)$ above $E_0 = h m_F \nu_0 = \mu_B g_F m_F B_0$ (the potential energy of atoms at the magnetic field minimum) are lost from the magnetic trap.

The first experiments on RF evaporative cooling of cold alkali metal atoms [191, 20] were made shortly before the first experimental observations of Bose-Einstein condensation.

3.3.2 Evaporation dynamics

As evaporation progresses atoms are lost from the trap and the temperature drops. The cloud becomes smaller as there are fewer high energy atoms – one must therefore dynamically alter the evaporation surface with time. It is useful to determine the optimal evaporation trajectory – obtaining the largest increase in phase space density with the minimal loss of atoms. The model used here requires the assumption of an energy-independent elastic collision cross-section σ_{el} (see Sec. 3.1.7) and 'sufficient ergodicity' (a phase-space distribution that depends only on energy) [128].

The temperature weighted atomic energy distribution is given by:

$$P(\epsilon) = A\rho(\epsilon)e^{-\epsilon}, \tag{3.57}$$

where $\epsilon = \frac{E}{k_B T}$, $\rho(\epsilon)$ is the energy density of states for a given spatial potential distribution $U(\mathbf{r})$, and A

is a normalisation constant. The case of a harmonic potential $\rho(\epsilon) \propto \epsilon^2$ will be considered here, although all results can also be derived for other power-law potentials and the complete Ioffe-Pritchard potential [128].

The dynamics of the evaporation are determined by the evaporation parameter η. All atoms with energy $\epsilon > \eta$ are lost from the magnetic trap. If η is held constant then as the temperature drops the corresponding evaporation energy $E_{evap} = \eta k_B T$ decreases with it. A trapped cloud of atoms subjected to evaporative cooling has an energy distribution which can be approximated by a truncated Boltzmann distribution [128] ($P(\epsilon) = 0$ for $\epsilon > \eta$). The relative number of atoms in the ensemble compared to that prior to truncation is

$$f_< = \frac{\int_0^\eta P(\epsilon)\, d\epsilon}{\int_0^\infty P(\epsilon)\, d\epsilon} = 1 - \frac{\Gamma(3, \eta)}{\Gamma(3)}, \tag{3.58}$$

where the incomplete gamma function is given by $\Gamma(x, \eta) = \int_\eta^\infty t^{x-1} e^{-t}\, dt$, and $\Gamma(n) = \Gamma(n, 0) = (n-1)!$. In the interest of simplicity the approximation $f_< \approx 1$ will be made in the following discussion. The validity of this approximation will be shown later.

After each atom has had, on average, four atomic collisions the truncated energy distribution rethermalises. The rethermalisation rate is therefore defined $\gamma_{th} = \gamma_{el}/4$, where the elastic collision rate γ_{el} is assumed to be temperature-independent (a good approximation for cold ^{87}Rb – Sec. 3.1.7). After the rethermalisation process all atoms with redistributed energy $\epsilon > \eta$ are lost. Assuming $f_< \approx 1$ then the rethermalised distribution will have an approximate fractional loss of population [126]

$$\frac{\Delta N}{N} = -\frac{\int_\eta^\infty P(\epsilon)\, d\epsilon}{\int_0^\infty P(\epsilon)\, d\epsilon} = -\frac{\Gamma(3, \eta)}{2!}$$

after a time $t = 1/\gamma_{th}$.

This leads to the rate equation [127]:

$$\frac{1}{N}\frac{dN}{dt} = -\frac{\gamma_{el}}{4}\frac{\Gamma(3, \eta)}{2!} - \frac{1}{\tau_{loss}}, \tag{3.59}$$

where the lifetime τ_{loss} characterises losses from the trapped atomic cloud due to collisions with background gas species and from inelastic collisions within the trapped cloud. If we ignore the latter form of loss (two- and three-body losses, which have a square and cube dependence on the atomic density n respectively), an assumption that it is valid over most of the evaporation trajectory, the loss rate is constant and proportional to the background vacuum pressure.

A result similar to Eq. 3.59 can be obtained for the relative rate of energy loss within the trap

$$\frac{1}{E}\frac{dE}{dt} = -\frac{\gamma_{el}}{4}\frac{\int_\eta^\infty \epsilon P(\epsilon)\, d\epsilon}{\int_0^\infty \epsilon P(\epsilon)\, d\epsilon} - \frac{1}{\tau_{loss}} = -\frac{\gamma_{el}}{4}\frac{\Gamma(4, \eta)}{3!} - \frac{1}{\tau_{loss}} \tag{3.60}$$

which is linked to the temperature via the relation $\frac{dE}{E} = \frac{dN}{N} + \frac{dT}{T}$.

The solutions for the number and temperature of atoms in a magnetic trap as a function of time are therefore:

$$N(t) = N_0 \exp(-\alpha_N t/\tau_{loss}) \qquad T(t) = T_0 \exp(-\alpha_T t/\tau_{loss}), \qquad (3.61)$$

where

$$\alpha_N = \frac{\gamma_{el}\tau_{loss}}{4}\frac{\Gamma(3,\eta)}{2!} + 1 \qquad \alpha_T = \frac{\gamma_{el}\tau_{loss}}{4}\left(\frac{\Gamma(4,\eta)}{3!} - \frac{\Gamma(3,\eta)}{2!}\right).$$

From the time-dependence of N and T it is then straightforward to determine the time evolution of other properties of the magnetically trapped cloud, namely the density $n \propto N/T^{3/2}$, elastic collision rate $\gamma_{el} \propto N/T$, and phase space-density PSD $\propto N/T^3$. In this simple model, all parameters $X = N/T^b$ have an exponential time dependence of the form $X = X_0 e^{-\alpha_X t/\tau_{loss}}$, where $\alpha_X = \alpha_N - b\alpha_T$. Therefore $\alpha_n = \alpha_N - \frac{3}{2}\alpha_T$, $\alpha_\gamma = \alpha_N - \alpha_T$, $\alpha_{\mathrm{PSD}} = \alpha_N - 3\alpha_T$ and all properties of the atomic cloud depend solely on the values of the parameters $\gamma_{el}\tau_{loss}$ and η.

3.3.3 Runaway evaporation

Because evaporation is essentially an exponential process it is critical to have a large enough value of $\gamma_{el}\tau_{loss}$ that the parameter α_{PSD} is negative, as the phase-space density will then rapidly *grow* rather than decay. In fact the condition for efficient evaporative cooling is more stringent than this, as the criterion $\alpha_{\mathrm{PSD}} < 0$ may be satisfied when $\alpha_\gamma > 0$. In the treatment so far we have treated γ_{el} as a constant for simplicity, yet to first approximation the collision rate also varies exponentially with time. If the collision rate exponentially decays then the state $\alpha_{\mathrm{PSD}} > 0$ is quickly reached, preventing further phase space density enhancement. The condition on self-sustaining or 'runaway' evaporation is therefore $\alpha_\gamma < 0$. This is a function of the evaporation parameter η and the ratio of 'good' elastic collisions to 'bad' collisions $\gamma_{el}\tau_{loss}$ (see Fig. 3.14).

The threshold for runaway evaporation, where the elastic collision rate remains constant, occurs when $\alpha_\gamma = \alpha_N - \alpha_T = 0$ in which case the relative decrease in atom number with time is equivalent to the relative decrease in temperature. For every factor of ten loss in N and T there is therefore a corresponding increase of 100 in PSD, and $10\sqrt{10}$ in n. Magnetically trapped atomic clouds which lie within the runaway regime can be cooled with much higher evaporation efficiencies.

In the Sussex compressed magnetic trap (using the ^{87}Rb elastic collision cross-section $\sigma_{el} = 5.4\ 10^{-12}\ \mathrm{cm}^{-2}$ [192]) the initial collision rate (Table 4.1) is $\gamma_{el} \approx 20\,\mathrm{Hz}$ and the lifetime of the trapped cloud is $\tau_{loss} = 70\,\mathrm{s}$. This yields $\gamma_{el}\tau_{loss} = 1400$ – the magnetic trap should be well into the regime where runaway-evaporation can be obtained. The experimental evaporation trajectory has a relatively constant collision rate however (Fig. 1.1), with increases in the collision rate only occurring after an initial evaporation period. This implies that our evaporation process could be optimised somewhat, which could be related to inaccuracies in initial trap temperature measurements due to the anharmonic nature
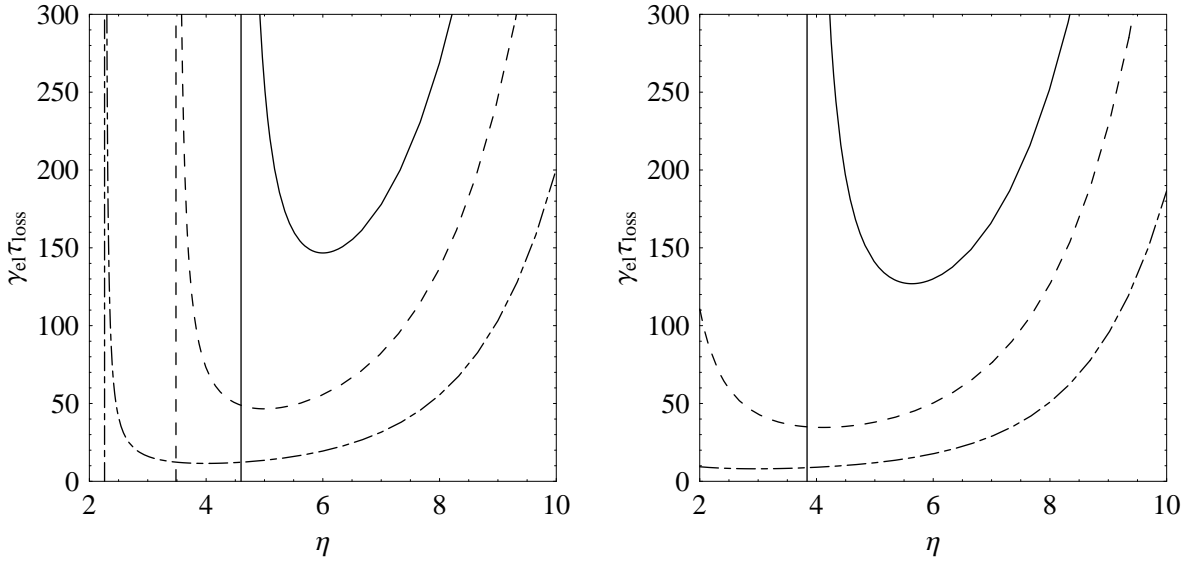
Figure 3.14: Parameter enhancement thresholds in evaporative cooling. The left graph uses the simple model discussed in the text, whereas the right image uses the more complete model of Refs. [128, 129]. The agreement between the two models is strongest for $f_< \approx 1$ (i.e. for large η). Solid curves indicate the runaway evaporation boundary $\alpha_\gamma = 0$, whereas dashed and dash-dotted curves correspond to the boundaries $\alpha_n = 0$ (density enhancement) and $\alpha_{\mathrm{PSD}} = 0$ (phase-space density enhancement) respectively. For atomic clouds with a 'good' to 'bad' collision ratio $\gamma_{el}\tau_{loss} \lesssim 150$ it is impossible to obtain sustainable increase in the elastic collision rate and thereby sustainable enhancement of the density or phase space density. Vertical lines correspond to the low η limits of the respective evaporation parameter boundaries, if they exit.

of the IP trap for relatively hot atoms. The magnetic trap compression phase may not be sufficiently adiabatic, leading to a 'settling down' phase during initial evaporation.

Optimisation of the evaporation efficiency K occurs when the maximal relative PSD increase occurs for a given relative atom number loss [193] i.e. by maximising

$$\frac{dK}{K} = -\frac{d(\mathrm{PSD})}{\mathrm{PSD}} \bigg/ \frac{dN}{N} = 3\frac{\alpha_T}{\alpha_N} - 1. \tag{3.62}$$

With $\gamma_{el}\tau_{loss} = 1400$, K is maximised for $\eta \approx 8$. Interestingly, this predicts an evaporation efficiency $K \approx 4$ – a PSD increase of 4 orders of magnitude for every factor of 10 loss in atoms – in contrast to the experimental result $K \approx 2$ (Fig. 1.1).

The evaporation trajectory can be linked to the applied RF magnetic field via the relation

$$E = \eta k_B T = \frac{3}{2}k_B T + (\mu_B g_F m_F (B - B_0) = h m_F (\nu_{RF} - \nu_0)),$$

yielding

$$\nu_{RF} = \nu_0 + \left(\eta - \frac{3}{2}\right)\frac{k_B}{h m_F}T,$$

and the radio frequency trajectory has the same form of exponential decay as the temperature (the time constant is $\tau_{RF} = \tau_{loss}/\alpha_T$), with a base RF frequency $\nu_0 = \frac{\mu_B g_F}{h} B_0$.

Given the parameters of our initial magnetically trapped sample of ^{87}Rb $|F, m_F\rangle = |2, 2\rangle$ atoms (Table 4.1, $B_0 = 1.04\,\text{G}$), the simple evaporation model predicts optimal RF parameters for $\eta = 8$ of $\nu_0 = 0.73\,\text{MHz}$, $\nu_{RF}|_{t=0} = 38\,\text{MHz}$, $\tau_{RF} = 7\,\text{s}$. The agreement with the experimentally optimised initial RF trajectory (Sec. 4.3) is correct at the level of a factor of 2.

3.3.4 Temporal variation of evaporation parameters

As runaway evaporation progresses the collision rate increases and soon the evaporation trajectory alters in a manner faster than an exponential. This can be seen by allowing for a time-varying elastic collision rate in Eqs. 3.59, 3.60. As $\gamma_{el} \propto N/T$ we have

$$\frac{1}{N}\frac{dN}{dt} = -\frac{\gamma_{el}}{4}\frac{NT_0}{TN_0}\frac{\Gamma(3,\eta)}{2!} - \frac{1}{\tau_{loss}} \qquad \frac{1}{T}\frac{dT}{dt} = -\frac{\gamma_{el}}{4}\frac{NT_0}{TN_0}\left(\frac{\Gamma(4,\eta)}{3!} - \frac{\Gamma(3,\eta)}{2!}\right). \quad (3.63)$$

These coupled differential equations have an analytic solution, which must be inverted numerically to obtain the time evolution of N and T depicted in Fig. 3.15.
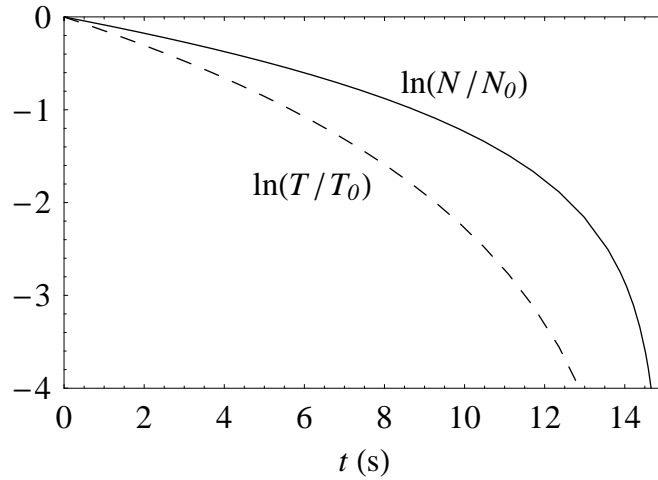
Figure 3.15: Temporal evolution of N and T in a magnetic trap with time-varying collision rate (Eqs. 3.63). The model parameters used are those of the Sussex initial compressed magnetic trap: $\gamma_{el} = 20\,\text{Hz}$, $\tau_{loss} = 70\,\text{s}$ and $\eta = 8$. The required RF evaporation trajectory $(\nu_{RF} - \nu_0)(t)$ has the same dependence as the temperature.

The present experimental RF trajectory was found by optimising the parameters for three exponential trajectories with adjustable decay time constants and base frequencies (Sec. 4.3). The combined RF sequence has a log dependence similar to that of Fig. 3.15. Both the simple (constant γ_{el}) and time-varying collision rate models suggest that further optimisation of the experimental evaporation efficiency should be possible in future however.

Because the optimal evaporation parameter η varies during the evaporative cooling process, efficiency can be further enhanced using a evaporation model which allows for the time variation of η [194, 193]. The path of greatest global evaporation efficiency is obtained for the trajectory which locally maximises the efficiency parameter K (Eq. 3.62) [193]. In regimes where the 'sufficient ergodicity' criterion is no longer valid, e.g. the two-dimensional evaporative cooling in a time-orbiting potential (TOP) magnetic trap (Sec. 3.2.4, it is necessary to model evaporation using Monte Carlo techniques [195, 196]. Cross-dimensional rethermalisation after partial evaporation in a TOP trap can be used as a technique for experimentally determining temperature-dependent elastic collision cross-sections.

Chapter 4

BEC creation: the experiment

This chapter will outline the experimental parameters and techniques which were used at Sussex University to create a Bose-Einstein condensate, highlighting simplifications which can be made to the system. The layout will closely follow that of the preceding theoretical chapter – a section on laser cooling, trapping and imaging will be followed by sections on magnetic trapping and evaporative cooling.

Laser cooling requires reliable, highly stable lasers. A new, simple, type of diode laser construction is described. The lasers are easily assembled from commercial components (with minimal additional machining) and perform at a level comparable with traditional designs. The mechanisms used to stabilise the frequency of the lasers will also be detailed.

Another necessity for a good laser cooling system is an ultra high vacuum chamber. The Sussex vacuum system has the advantage that low pressures are essentially maintained by a single low-throughput ion pump. Two magneto-optical traps (MOTs) are created in the two differentially pumped chambers of the vacuum apparatus. A simple mechanism is used to transfer atoms from the 'high' pressure MOT to the low pressure end using light pressure alone. The atoms are then cooled in 'optical molasses' (without the added complication of a preceding 'dark' or 'compressed' MOT phase) and optically pumped into a magnetically trappable quantum state. The laser section concludes with a description of the implementation of absorption and fluorescence imaging, enabling the acquisition of quantitative information about the cold atomic clouds.

The Ioffe-Pritchard 'baseball' coils which are used to magnetically trap the atoms after the optical pumping stage are described at the beginning of section 4.2. A highly stable current source is required for the magnetic field coils, and our simple, inexpensive and relatively low power stabilisation scheme is explained.

A short final section on the experimental implementation of evaporative cooling within the magnetic trap also includes a description of the computer control system which controls the entire BEC creation process. The chapter concludes with the first experimental realisation of Bose-Einstein condensation in

the UK.

4.1   Laser cooling, trapping and imaging

4.1.1   The laser system

Why diode lasers?

Probably the most vital ingredient for a good MOT is a stable, well-behaved laser. The efficiency of laser cooling can vary considerably over the frequency range of one atomic linewidth [147]. In rubidium the D2 $(5s\,^2S_{1/2} \rightarrow 5p\,^2P_{3/2})$ optical transition in the stable ^{85}Rb and ^{87}Rb isotopes has a linewidth of $\Gamma_\nu = 6.07$ MHz [4], and hence the MOT lasers must necessarily be stable at the level of 1 MHz for effective laser cooling. This can be contrasted with the much larger frequency of the rubidium D2 transition of $\nu = 384.2$ THz $(\lambda_0 = 780.2$ nm vacuum wavelength) [143].

The two types of laser typically used to trap atoms at this wavelength are the diode and the Ti:sapphire laser. Whilst the latter generates a large amount of power $(P \approx 1$ W$)$, it is a considerably more expensive option. Tapered amplifiers [197, 198] based on laser diode technology are also able to generate large $(P \approx 0.5$ W$)$ powers, but are again rather expensive and require an additional 'master' laser for single-frequency operation.

The output of a Ti:sapphire laser, split into six relatively large $(4$ cm diameter) beams was used by Gibble *et al.* to create a caesium MOT containing $N = 4 \times 10^{10}$ atoms [199]. Laser diodes at 780 nm are able to generate powers of around 50 mW, and with 23 mm diameter laser beams 15 mW still suffices to capture $N > 10^9$ atoms in both rubidium and caesium MOTs [23, 147] and a double MOT [23, 181, 200] system based on laser diodes is capable of producing approximately the same number of atoms as a single MOT controlled with a high power laser [23]. Similar atom numbers can also be attained using a zero-crossing σ^- Zeeman slower [24, 25] with laser intensities of around $I/I_S = 10$ to load a MOT [16]. Thus all three MOT loading schemes discussed here are capable of yielding an atom number of a few 10^{10} atoms which at present constitutes the experimental upper limit on MOT population.

A single MOT with large beams has the disadvantage that electrical wires for magnetic trapping cannot be brought into close proximity of the atoms, and it also has a long loading time. Zeeman slowers are relatively large devices that are expensive and technically more demanding to build and optimise. A diode laser based double MOT system is therefore the cheapest and arguably the simplest method of producing a large number of laser cooled atoms in a MOT designed for magnetic trapping in extra high vacuum systems, and was therefore used in this work. The double MOT laser system and locking mechanisms will be discussed first, followed by the vacuum and optical set-ups.

Laser design

A 'bare' laser diode typically has a linewidth of ≈ 100 MHz, and would be unsuitable for laser cooling. However it is possible to make the output of the laser narrower by employing frequency-selective feedback from an external grating and/or etalon. Various schemes are discussed in Ref. [201]. The linewidths of such extended-cavity diode lasers are typically < 1 MHz which is certainly adequate for laser cooling. The linewidth reduction is due to changes in the laser cavity's effective length and output facet reflectivity [202], for example due to mechanical or thermal instabilities.

Considerable time was spent investigating various diode laser assemblies, and the details of our final diode laser design can be found in Appendix A (Ref. [203]). We found this design to be simple, cheap and reliable. A photo of the laser design is shown in Fig. 4.1.
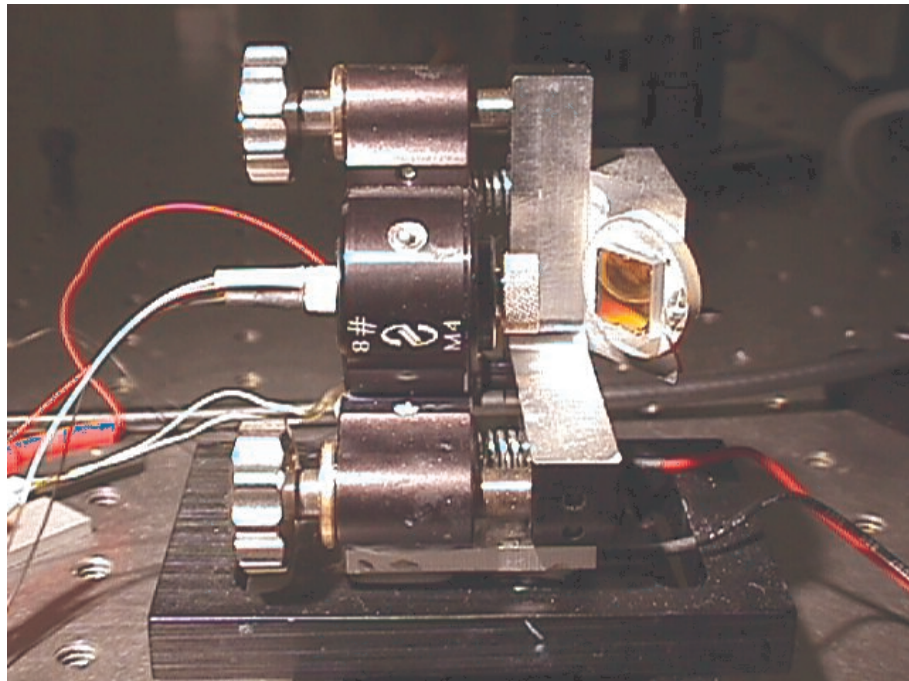
Figure 4.1: The mirror-mount diode laser design.

Laser stabilisation

In order to stabilise the frequency of a laser, it is necessary to have some kind of frequency-dependent signal, (here the photodiode current from a saturated absorption spectrum) which can be used to provide feedback to the laser. For each isotope of Rb, the D2 line has 3 atomic transitions ($\Delta F = -1, 0, 1$) for each of the ground level 5 s hyperfine states (see appendix B). The proximity of absorption lines within each of these four groups of three transitions (≈ 100MHz) means that saturated absorption spectroscopy [201, 204] must be used to obtain narrow absorption features on the scale of the natu-

Figure 4.2: Theoretical Doppler-broadened absorption spectrum of the rubidium D2 line. Vertical solid lines indicate the centre frequencies of atomic transitions and dashed lines correspond to crossover peaks. Dashed curves indicate the contribution to absorption from individual $F \rightarrow F'$ atomic transitions – weighted by the relative Rb abundances ($72\,\%\,^{85}$Rb : $28\,\%\,^{87}$Rb [1]), hyperfine population distributions and transition strengths.

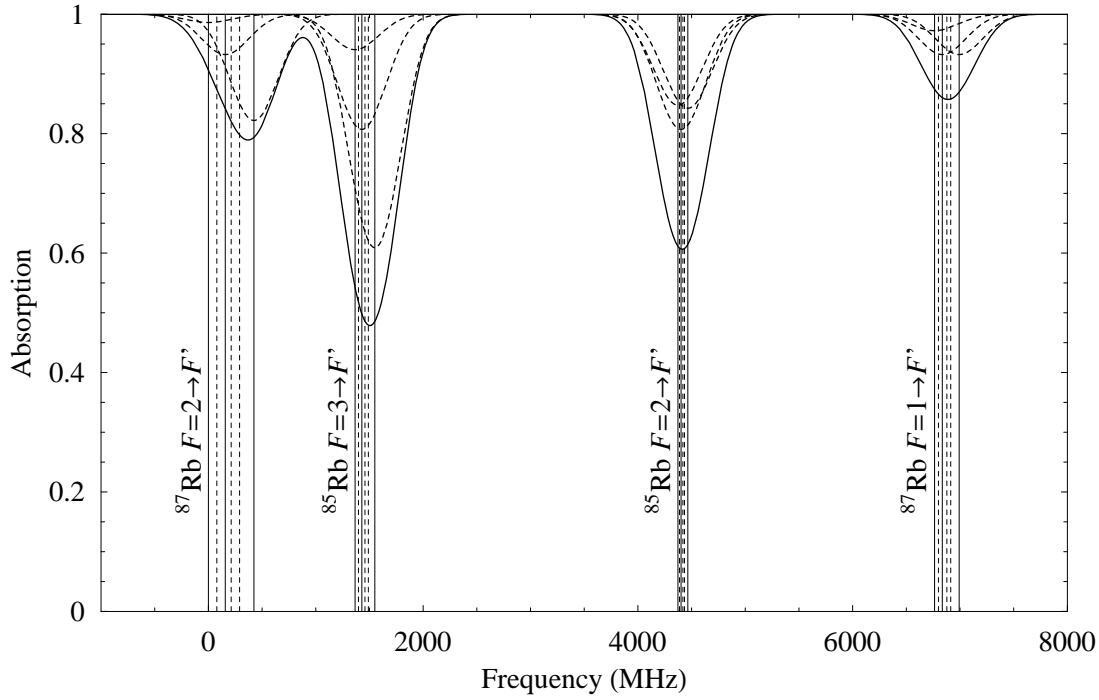ral linewidth ($\Gamma_\nu = 6.07\,$MHz), and resolve these transitions from their overlapping Doppler-broadened ($\approx 500\,$MHz) absorption profiles. Each group of three saturated absorption spectral features at atomic transition frequencies $\{\nu_1,\ \nu_2,\ \nu_3\}$ has a corresponding set of three spectral features known as cross-over peaks [204] at the frequencies $\{\frac{\nu_1+\nu_2}{2},\ \frac{\nu_1+\nu_3}{2},\ \frac{\nu_2+\nu_3}{2}\}$.

The saturation absorption spectrometer used for the trap laser is shown in Fig. 4.3. The benefits of this design are that it creates large peaks at the frequencies used for locking, and that it makes it easy to trap either of the two Rb isotopes. The saturation absorption set-up used for the repump laser is detailed in Fig. 4.5, whereas Figs. 4.4 and 4.6 depict experimental rubidium saturated absorption spectra of the 'trapping' and 'repumping' transitions respectively.

The photodiode signal from a saturated absorption spectrometer gives us a 'map' of the laser frequency which we can then use as an error signal in a feedback loop. A laser frequency that is too low can be corrected by either increasing the extension of the diffraction grating piezo-electric transducer (PZT) or decreasing the laser diode current(appendix A). Opposite measures have to be taken if the laser frequency is too high. Thus if the photodiode response is monotonic with laser frequency, an op-amp based integrator can be used to provide feedback to the laser diode current and/or the PZT voltage, ensuring the
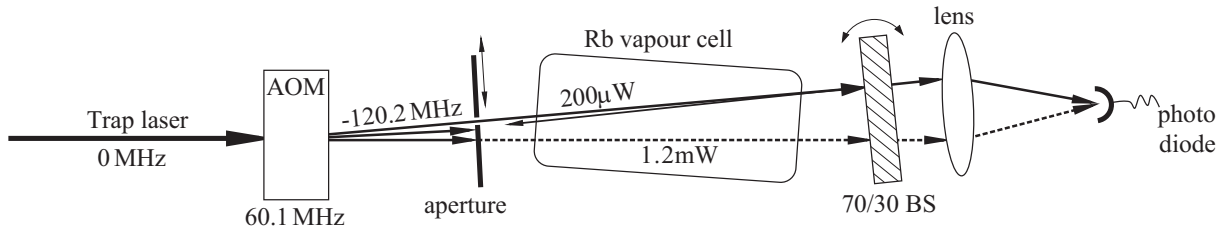
Figure 4.3: The trap laser saturated absorption spectrometer. Solid arrows indicate the laser beam paths for trapping the ^{87}Rb isotope, using the (down-shifted) second order beam of the acousto-optic modulator (AOM [205]). When trapping ^{85}Rb the zeroth order beam (dashed arrow) is required instead. In this case the aperture and beamsplitter (BS) must be adjusted accordingly and a neutral density (ND) filter is used to lower the laser intensity. As the laser beam is not focused into the AOM only a fraction of the incident beam passes into the AOM crystal. The second order laser beam therefore has an apertured beam profile, and in this case $200\,\mu$W correspond to $16\,$mW/cm^2 (cf. Fig. 4.5). The experimental saturated absorption spectra for the trapping light of the two Rubidium isotopes are shown in the following figure.

photodiode voltage (and therefore laser frequency) is locked to a particular level. However, this 'offset' lock will cause frequency drifts if the laser is susceptible to intensity fluctuations, and moreover the trap laser lock-point would be near a turning point in the photodiode signal.

For this reason we take the derivative of the photodiode signal. The derivatives of saturated absorption peaks are dispersion curves, which have a linear response to laser frequency near the centre of the absorption line. An integrator can therefore be used to lock the laser to zeroes in the derivative signal, corresponding to the tops of absorption peaks. In practice the derivative of the photodiode signal is taken using a lock-in amplifier: a frequency modulation, small ($\approx 1\,$MHz) compared to Γ_ν, is applied to the laser frequency used in the saturated absorption spectrometer. A demodulator then takes the product of the applied modulation and the modulation on the photodiode signal. This gives a signal proportional to the derivative of the saturated absorption signal, which can then act as the error signal for an integrator.

The trap laser saturated absorption beam (frequency down-shifted, cf. Fig. 4.3) is locked to the ^{87}Rb $F = 2 \rightarrow F' = 1, 3$ cross-over peak, or the zeroth order AOM beam is locked to the ^{85}Rb $F = 3 \rightarrow F' = 2, 4$ cross-over peak. The trap laser is therefore locked to a frequency which is red-detuned $\approx 92\,$MHz from the main cooling transition ($F = 2 \rightarrow F' = 3$ in ^{87}Rb, $F = 3 \rightarrow F' = 4$ in ^{87}Rb) regardless of the rubidium isotope. Part of the trap laser light later passes through an AOM, up-shifting the frequency by 78.6 MHz. This light is red-detuned $\approx 13\,$MHz from the cooling transition and provides the trapping light for both the high pressure and low pressure MOTs (see Subsection 4.1.3). The repump laser is either locked to the peak of the ^{87}Rb $F = 1 \rightarrow F' = 2$ transition, or the ^{85}Rb $F = 2 \rightarrow F' = 3$ transition.

Rubidium 87, $F = 2 \rightarrow F' = 1,\, 2,\, 3$ **Rubidium 85**, $F = 3 \rightarrow F' = 2,\, 3,\, 4$
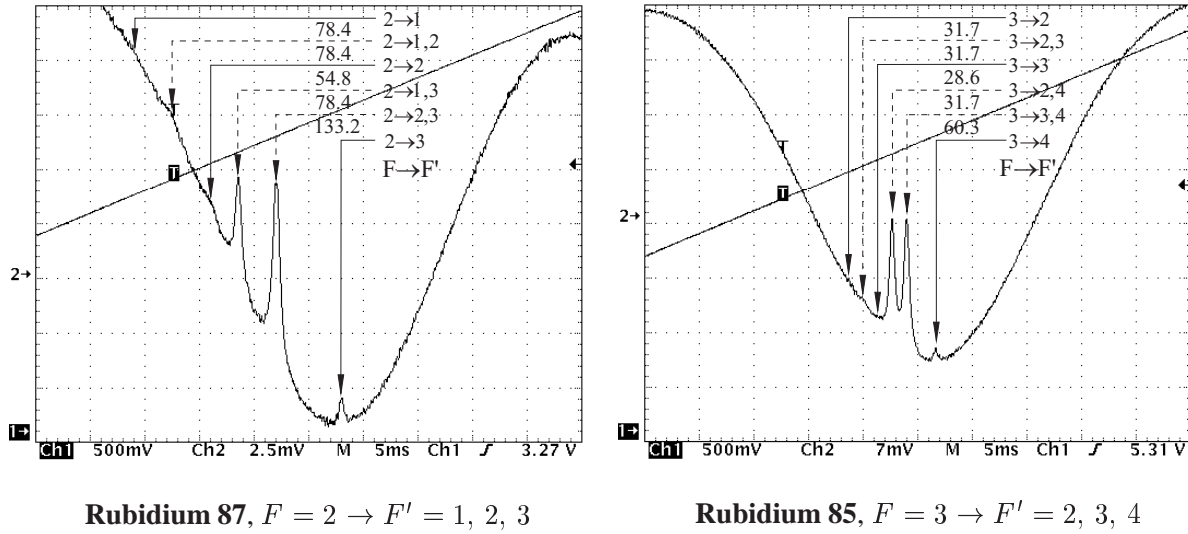
Figure 4.4: Experimental saturated absorption spectrum of the ^{87}Rb (left) and ^{85}Rb (right) 'trapping' transitions (16 averages). The diagonal trace is the piezo-electric transducer (PZT) voltage divided by 100. Arrows indicate $F \rightarrow F'$ transitions and dashed arrows correspond to cross-over peaks. Frequency splittings between peaks are in MHz and are calculated from the A and B coefficients of Ref. [2]. The relative sizes of saturation features are partly determined by oscillator strengths, however optical pumping also has a significant effect.
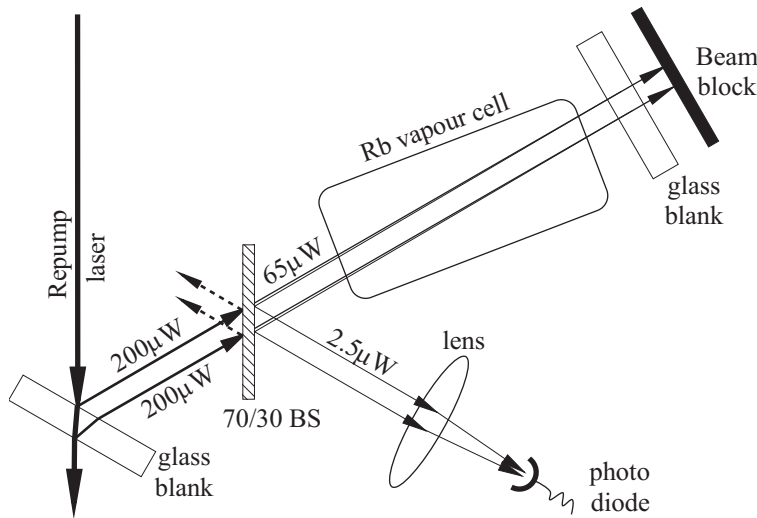
Figure 4.5: The repump laser saturated absorption spectrometer. This differs from the trap laser spectrometer shown in Fig. 4.3 due to a need to resolve the more closely spaced spectral features of the repumping lines. Light with a low intensity is used, to reduce power broadening, and the gain of the photodiode is increased accordingly (a factor of 30 greater than in the trap laser spectrometer). The position of the photodiode prevents it from seeing retro-reflected light from the MOTs. Intensities can be determined from the correspondence of $200\,\mu$W with 3.5 mW/cm^2. Saturated absorption spectra for the repumping light of the two Rb isotopes are shown in the following figure.

**Rubidium 85**, $F = 2 \rightarrow F' = 1, 2, 3$ **Rubidium 87**, $F = 1 \rightarrow F' = 0, 1, 2$
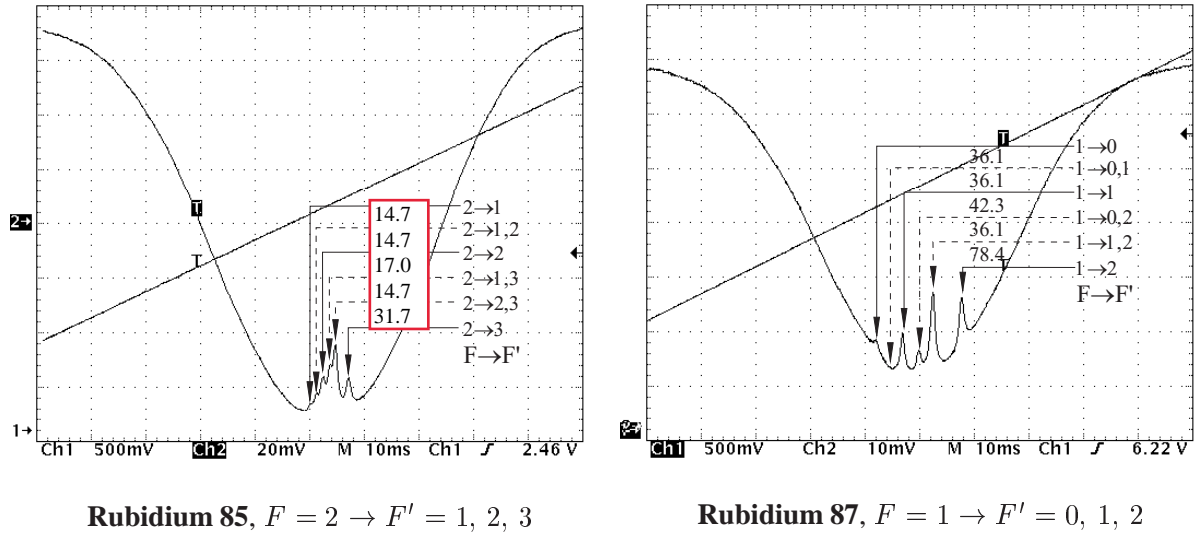
Figure 4.6: Experimental saturated absorption spectrum of the ^{85}Rb (left) and ^{87}Rb (right) 're-pump' transitions (16 averages), notation as in Fig. 4.4.

An electronic cross-over was used in the feedback loop of the integrator, in order to separate the fast and slow frequency components of the feedback. High frequency feedback is applied to the laser diode current due to its fast frequency response, but limited mode-hop free tuning range. Low frequency response is applied to the voltage of the PZT.

The circuits for both the integrator and lock-in were optimised considerably before arriving at the final designs described in Appendix D. Printed circuit boards (PCBs) of these designs were created (in *QuickRoute* 3.6) to facilitate production. For locking, a modulation at $50\,\mathrm{kHz}$ is usually applied to the laser diode current, however reasonable locking can also be achieved by modulating the PZT at $1\,\mathrm{kHz}$.

Our optimised lock-in/integrator combination has demonstrated a high level of stability, enabling continuous lock periods of several days.

Other saturated absorption spectrometer designs were investigated prior to those shown in Figs. 4.3 and 4.5, and their drawbacks will be briefly discussed. A pump-probe type arrangement with a reference beam and differential amplifier was used initially, however this spectrometer was found to be unnecessarily complicated. Rather than modulate the frequency of the laser diode directly through the current or PZT, attempts were made to apply external frequency modulation via a double-passed AOM, or by using various circularly polarised laser beams and an oscillating magnetic field. However, the AOM technique produced an unwanted phase offset due to amplitude modulation of the laser beam, and the Zeeman modulation resulted in an offset as well as an asymmetric dispersion signal in the derivative. This may have been caused by optical Zeeman pumping, as well as by disturbances due to the earth's magnetic field. All of these problems are avoided with the simple laser locking set-up described in this section.

It is worth mentioning a recently published Zeeman-effect based spectroscopic technique by Corwin *et al.* [206] which has the benefits of fast tuning, extremely stable locking and a relatively simple and inexpensive set-up. It has the disadvantage of susceptibility to drift when the offset lock-point is altered from zero, however it could well be an interesting prospect for a future laser lock system.

AOM control

Three acousto-optic modulators (AOMs [205]) are currently employed in the BEC experiment: an *ISOMET* 1205-603F for the trap laser saturated absorption spectrometer, and two *NEC* C8217A's were used for frequency-shifting the two laser beams used for trapping and pushing/pumping/probing. The *NEC* AOMs are primarily used as very fast optical shutters for the trap and push/pump/probe laser beams. We discuss our RF set-up which provides the necessary precise control, at timing levels of a few μs, over the radio-frequency (RF) waves used to create the traveling sound wave in the AOM crystals. The RF set-up we adopted for the *NEC* AOMs is depicted in Fig. 4.7.
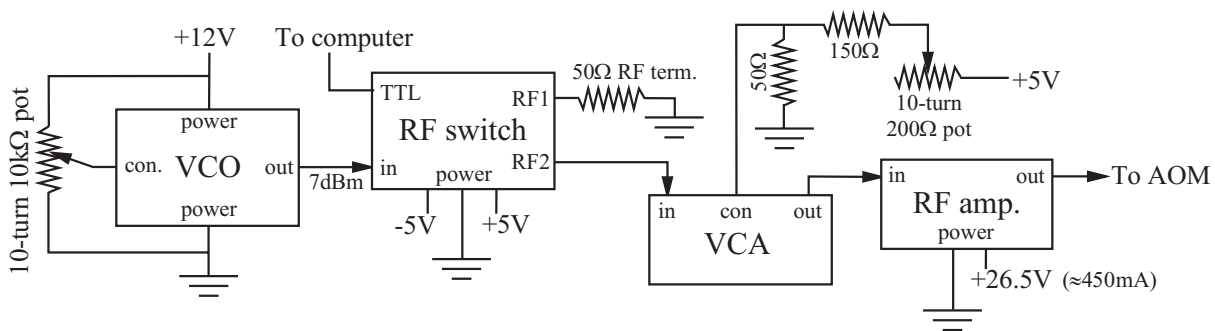
Figure 4.7: The RF set-up for the NEC AOMs. The voltage-controlled oscillator (VCO), RF switch and voltage-controlled attenuator (VCA) are all from *Mini Circuits* (the ZOS-150/ZOS-100, ZYSWA-2-50DR and ZAS-3 respectively). The amplifier is home-made and employs a *Motorola* CA2832C 2 W wideband linear RF amplifier chip in the configuration recommended in its specifications. The RF switch is quite sensitive to the accuracy of the ± 5 V power input voltage, which affects the maximum attainable attenuation.

The voltage-controlled attenuators (VCAs) were initially used alone, without RF switches, however they yield a lower attenuation, have a relatively slow ($\approx 20\,\mu$s) switching speed and a variable voltage must be applied to the VCA's control port. For this reason RF switches were employed: yielding switching speeds of < 100 ns, attenuation of 50 dB and TTL logic control. The VCAs are now used solely to provide continuous control over the output RF power to maximise the AOM diffraction efficiency. The additional RF attenuation that would be possible with combined VCA and RF switch control is not necessary because another limitation affects the total attenuation of the first order laser beam – scattering of light within the AOM crystal itself.

As the intensity of light from the first order AOM beam used in the trap laser saturated absorption set-up is held constant, a simplified RF system is sufficient. It consists solely of a *Tenma* 72-585 (highly stable at the level of $10\,\text{kHz}$!) variable RF frequency generator and a *Motorola* CA2832C 2 W wideband linear RF amplifier.

In order to achieve high efficiency Bragg diffraction into the 1st order AOM beams, the laser light was focused ($f = 40\,\text{cm}$) to a waist inside the AOM crystal, and the thin axis of the laser beam (observed just before the focusing lens) was oriented parallel to the propagation direction of the standing wave within the AOM crystal. This made a narrower distribution of $\mathbf{k}$ vectors within the crystal, and conversion efficiencies of $80\,\%$ could be attained for $780\,\text{nm}$ light at RF frequencies of $80 - 100\,\text{MHz}$ (cf. $90\,\%$ efficiency for a focused $633\,\text{nm}$ HeNe laser beam).

One problem encountered with the AOMs was that a short period of time ($\approx 2\,\text{s}$) was required for the first order laser beam position and intensity to stabilise when the RF power was first turned on. This appears to be a thermal effect in the AOM crystal, and fortunately did not disrupt the experiment. Any problems of this nature could be solved by turning the AOM RF power back on after the shutters used for magnetic trapping (see below) have closed.

Shutter control

Due to scattering of light within the AOM crystal, the first order beam from an AOM cannot be extinguished completely with RF attenuation alone. However since even very small amounts of resonant laser light can degrade magnetic trap lifetimes [127, 134], by transferring atoms into quantum states that are not magnetically trapped, mechanical shutters are used in conjunction with the AOMs to enable complete light extinction.

We used two commercial shutters from *Newport* (the 846HP, with $3\,\text{ms}$ switching speed) as well as some home-made shutters which were based on an *RS* 352-907 latching solenoid, a spring, and a *Thorlabs* optical base ($10\,\text{ms}$ switching speed). Short ($\approx 5 - 10\,\text{ms}$) pulses of current are used to toggle the shutter position. Stronger pulses are required to fire the more robustly built home-made shutters. The circuit used to drive the magnetic shutters is depicted in Fig. D.5. It converts rising/falling edges of a TTL signal into bi-directional current pulses, enabling computer control of the shutters.

The main disadvantage of the mechanical shutters was their effect on the laser frequency. Two layers of Sorbothane sheet (particularly in the case of the home-made shutters) were required to help damp the shutters' mechanical effect on the lasers, however it was still necessary to wait $\approx 30\,\text{ms}$ after firing the shutters before the laser frequencies stabilised.

4.1.2   The vacuum system

Another important requirement for a MOT used to create Bose-Einstein condensation is a good extra high vacuum (XHV) system [150]. The lifetime of atoms in magnetic traps typically must be greater than one minute in order to achieve BEC, and this corresponds to background pressures of $P < 10^{-11}$ torr. For this reason care must be taken during the cleaning, assembling and baking of the vacuum system. We obtain a very low pressure, essentially maintained by a single low-throughput ion pump, in a relatively simple vacuum apparatus. A major advantage of the set-up is the compact nature of the vacuum chamber.

The surfaces of all vacuum components were handled only when necessary, and then with latex gloves. The cleaning procedure used for vacuum components was as follows:

- Soak overnight in *Decon* (vacuum compatible detergent)

- Place in ultrasonic bath for one hour in *Decon*

- Rinse thoroughly to remove *Decon*, first with tap water and finally with distilled water

- Soak overnight in distilled water

- Ultrasonic cleaning for one hour in distilled water

- Ultrasonic cleaning for one hour in new distilled water

- Dry (if possible under an infra-red lamp)

- Soak overnight in methanol

- Ultrasonic cleaning for one hour in methanol

- Ultrasonic cleaning for one hour in new methanol

- Dry (if possible under an infra-red lamp)

The vacuum system was then assembled as depicted in Fig. 4.8. All connections are made with *Conflat* knife-edge seals and copper gaskets. It is useful to apply anti-seize compound to the exterior nuts and bolts, aiding future removal, however it should be used with caution as even small residues of grease within the vacuum chamber will limit ultimate pressures to $\approx 10^{-6}$ torr.

The vacuum pumps used on the double MOT are a 20 L/s *Varian* Star-cell 919-0235 (ferrite magnet), and an *SAES* GP 50 Sorb-AC non-evaporable getter (NEG) pump. The nude ionisation gauge was a *Varian* UHV-24 and had a maximum sensitivity of 2×10^{-11} torr. The double MOT (Sec. 3.1.4) has a high pressure (HP) and low pressure (LP) MOT, and the pressure difference results from the different pumping rates of the two chambers due to the respective conductances they present to the vacuum pumps (Sec. 3.1.4). The transfer tube presents a markedly different conductance for rubidium than for other gaseous species however, due to the long sticking time of rubidium on stainless steel [151].

The system needs to be 'roughed' (rough pumped) to pressures below 10^{-6} torr before the ion pump and NEG pump can be activated. The vacuum system was roughed using a *Varian* V-250 turbo pump,
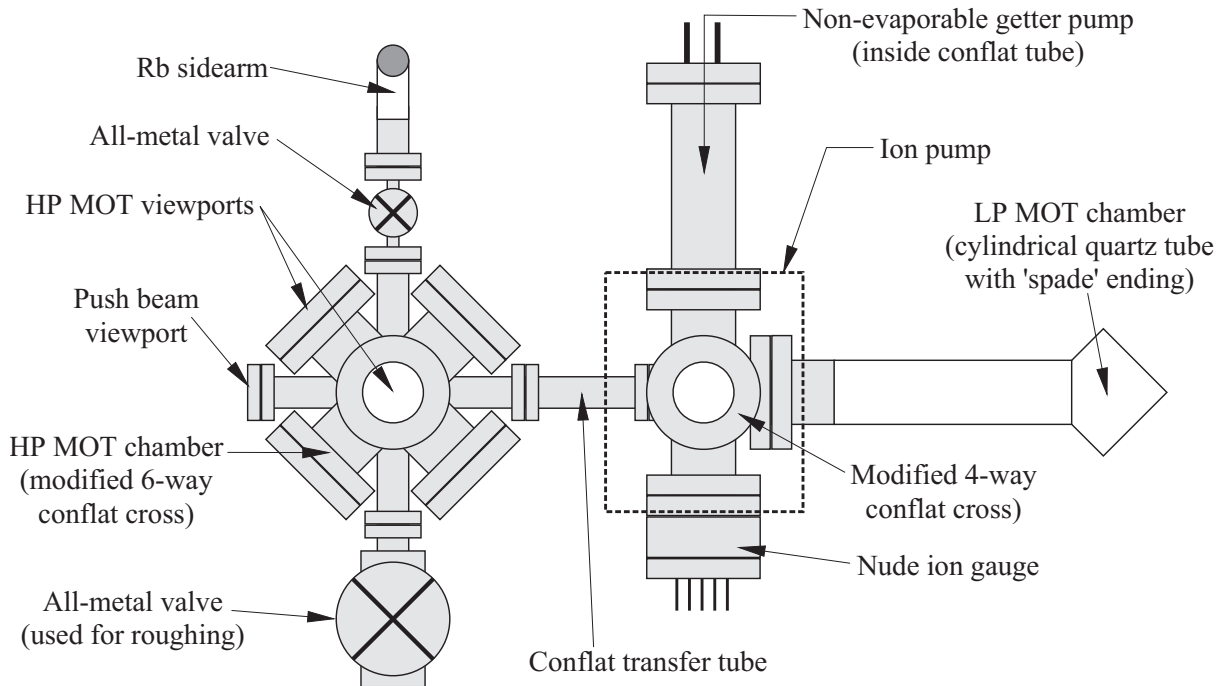
Figure 4.8: The vacuum system. The MOT viewports (like most of our *Conflat* components) are from *Caburn* but were anti-reflection (AR) coated at *CVI* for normally-incident 780 nm light.

backed by a *Varian* 949-9425 diaphragm pump. The diaphragm/turbo pump system was chosen to allow an oil-free vacuum environment. Although the diaphragm backing pump has a relatively high base pressure (0.3 torr) compared to a rotary pump, turbo pump base pressures of around $10^{-8} - 10^{-9}$ torr were still attainable. A fan was needed to prevent the turbo pump overheating.

During roughing, the vacuum system was connected to the turbo pump by a flexible metal bellows. Just before the turbo pump, an ion gauge and residual gas analyser (RGA) were used to monitor the total pressure as well as the relative pressures of the various gaseous species within the vacuum. The RGA was a useful leak-checker.

Outgassing from a vacuum chamber depends in a highly non-linear way on the temperature of its walls. For this reason it is wise to raise a vacuum chamber's temperature ('bake' it) at temperatures as high as possible. In this way outgassing times can be dropped from decades to days, enabling low pressures to be reached in a relatively fast time. The ultimate limit to the temperature attainable within our system was determined by the ferrite magnet used in the ion pump $(\text{T} < 350^\circ\,\text{C})$, and also by the glass-to-metal seal of the LP MOT chamber (*Caburn* quote $\text{T} < 350^\circ\,\text{C}$, whereas *Kurt J. Lesker* quote $\text{T} < 400^\circ\,\text{C}$).

An oven was made to enclose the vacuum system. This allowed the temperature of the entire system to be raised evenly – an effect difficult to achieve with heater tape! Once again, due to the non-linearity of

outgassing with temperature, the final pressure may be limited by a small area within the vacuum system that was at a lower temperature. The oven was a critical factor in obtaining our low base pressure.

The oven consisted of an insulated metal box containing $3\,\text{kW}$ of infra-red heater elements, a thermocouple, and a temperature control circuit. During the bake glass surfaces were covered with aluminium foil, and the temperature was raised slowly over the course of two hours in order to allow a more uniform thermal expansion. The vacuum system was then baked at 270° C (the oven's maximum temperature) for 50 hours. All vacuum components between the turbo and the vacuum system, but outside the oven, were also baked at this temperature. When the hot pressure dropped below 10^{-6} torr the ion pump and NEG were activated. It is also important to degas the nude ion gauge.

Due to an oversight with the housing of the NEG pump, its conductance is very low and it pumps the vacuum system at only a tenth of the speed of the ion pump (cf. the NEG's nominal pumping speed of $> 100\,\text{L/s}$). The ion pump is only rated at $20\,\text{L/s}$, and therefore it is rather surprising that we have been able to achieve such low pressures (an ion gauge reading of 2×10^{-11} torr (the gauge's limit) and a magnetic trap lifetime of $70\,\text{s}$) without the need for vacuum pumps with speeds above $100\,\text{L/s}$, which are commonly used on other BEC experiments. With a new NEG housing even lower pressures may well be possible.

The main species that is outgassed from the walls of the vacuum chamber toward the end of baking is hydrogen. Pre-baking the system in air at 350° C allows a golden oxide layer to form on any stainless steel surfaces [173], which helps slow this outgassing rate. This process did not appear to be necessary in this experiment, however this may be relevant for future attempts at reaching lower pressures.

The rubidium metal used to load the HP MOT is situated in a sidearm (Fig. 4.8). It is, of course, rather important to have the sidearm valve closed during baking. A drawback encountered with the rubidium sidearm was that it requires regular heating (every few days) with a heatgun to maintain the Rb vapour pressure level in the HP MOT chamber. Using alkali metal dispensers ('getters') would alleviate this problem by allowing reproducible amounts of Rb vapour to be generated in a few minutes. In a 'getter' alkali salts are reduced to alkali metal vapour when current is passed through them. Getters have now been successfully used at XHV in a BEC experiment [35], and 'home-made' isotopically enriched potassium getters have also recently been demonstrated [207].

4.1.3   The double MOT

The layout

With operational, lockable lasers and a good vacuum system, the remaining step in the building of a double MOT [23] is to combine the lasers and vacuum together with a large array of optics and other paraphernalia. Simplicity, durability and precision were the design criteria, and the trap and repump laser

beams for *both* MOT systems are derived from only two low power lasers. Figure 4.9 depicts the main features of the set-up.

Periscopes were used to raise the height of the horizontal laser beams emerging from the diode laser boxes to ≈ 10 cm above the table and to ensure the laser beam was polarised in the horizontal plane (p-polarised with respect to subsequent horizontal plane optics). This is the required polarisation for the anamorphic prisms, and it also yielded good splitting ratios with our *Melles Griot* plate beam-splitters. Non-polarising beam-splitter cubes were used when it was important to split laser beams evenly into two perpendicular equal intensity beams.

The beam splitting periscopes were used partly to split laser light into two beams with an intensity ratio of 2:1, and partly to raise the light in the horizontal MOT beams to a height of 20 cm above the *TMC* optical table. The beamsplitters were carefully aligned, to ensure that counter-propagating laser beams had equal intensities (at the 5% level) to minimise drift velocities within molasses, and improve sub-Doppler [13, 154, 155] cooling.

The beam intensities in the MOTs were measured using the photodiode head of a powermeter. The 0.45 cm^2 circular detector was irradiated by each beam and the maximum power was recorded. For the HP trapping (repumping) beams this yielded: $I_x = 0.82\,(1.84)$ mW/cm^2, $I_y = 1.29\,(2.31)$ mW/cm^2, $I_z = 0.93\,(2.49)$ mW/cm^2. The corresponding intensities for the LP MOT were: $I_x = 0.82\,(0.44)$ mW/cm^2, $I_y = 0.89\,(1.00)$ mW/cm^2, $I_z = 0.58\,(0.40)$ mW/cm^2. The total trap (repump) intensities $I_{tot} = 2(I_x + I_y + I_z)$ in the HP and LP MOT were $I_{tot} = 6.1\,(8.8)$ mW/cm^2, $I_{tot} = 4.6\,(3.7)$ mW/cm^2 respectively.

A $\lambda/2$ waveplate rotates the polarisation of the trapping light by $45°$, shortly before the trapping beam enters a -40 dB *Isowave* I-80-T4 optical isolator (which rotates the polarisation back to p-plane). As described in section 4.1.1, the frequency of each laser diode is controlled by feedback from the 3 cm external cavity created by the laser diode, and a diffraction grating (Appendix A). If other cavities are formed (e.g. between the laser diode and one of the retroreflecting MOT mirrors) then the laser diode will be sent a conflicting frequency-selective signal. This unwanted optical feedback is removed with the optical isolator [205]. The most obvious symptom of optical feedback is when the saturated absorption spectrometer indicates a sudden substantial decrease in the laser's mode-hop free tuning range. We find that the quality of the MOT does not critically depend on the degree to which the repump laser is retro-reflected, and the (relatively expensive) optical isolator is therefore omitted from the repump laser set-up.

Melles Griot anamorphic prism pairs are used to expand the diode lasers' beam profiles from elliptic to circular. The trapping laser beams for the LP and HP MOTs then have separate beam expanders to control beam size and collimation. For each MOT, individual laser beam paths back to the beam expander were kept approximately the same length to aid collimation. A pinhole was initially used at the focus of the HP MOT beam expander, to spatially filter the laser beam. With equal intensity laser beams,

Figure 4.9: The double MOT optical set-up. Note that the trap laser and repump laser provide the trapping and repumping light for it both the high pressure (HP) and low pressure (LP) MOTs. The trap laser also provides laser beams used for pushing the atoms, as well as pumping/probing.

approximately equal numbers of atoms were trapped with rough or smooth laser beam profiles. This rather surprising result is due to the remarkable insensitivity of MOTs to a variety of optical parameters [145]. As spatial filtering lowers the light intensity (and hence the MOT loading efficiency) our MOTs are normally operated without filters.

The laser beams in a MOT must have particular circular polarisations (Fig. 1.3). This is achieved by passing a linearly-polarised laser beam through a $\lambda/4$ waveplate, with its fast axis rotated $45°$ with respect to the laser polarisation, before it enters the MOT cell. As one looks along the beam path towards the MOT, in the direction of propagation, then the two waveplates on the axis of the MOT quadrupole coils must be rotated $45°$ clockwise (say) with respect to the laser polarisation, whereas the other waveplates must be rotated anticlockwise. In the case of the HP MOT, where three of the laser beams are retroreflected to provide the remaining three MOT beams, the orientation of the waveplates next to the retro-mirrors can in fact be arbitrary and still generate the requisite polarisation. The reason that six individual laser beams (rather than the three retro-reflected beams) are used in the LP MOT is that this MOT is designed to have a very high atom number. When a MOT contains a large number of atoms shadows in the laser beam occur due to absorption, resulting in strong intensity imbalances in retro-reflected systems. Such intensity imbalances degrade sub-Doppler cooling in optical molasses [159].

After setting the waveplate geometry it only remains to determine the sense with which current should be supplied to the anti-Helmholtz coils used to generate the spherical quadrupole MOT magnetic field. This can be quickly found by trial and error. The (axial) magnetic field gradient of the 'anti-Helmholtz' coils (Sec. 3.2.2) in both the HP and LP MOTs is typically $B_1 \approx 10$ G/cm (cf. Ref. [147]). The coils were designed with low power dissipation and fast switching speeds $\tau < 1$ ms in mind.

Each HP MOT anti-Helmholtz coil has 54 turns, an inductance of $360\,\mu$H and a resistance of $0.35\,\Omega$. They are 80 mm in diameter and separated by 55 mm. The currents in the HP coils were 3.2 A (upper) and 2.8 A (lower). Separate currents were used to shift the MOT to the vertical centre of the HP MOT cell as a 3 G stray magnetic field (probably from the ion pump or a weld) operated vertically. The LP MOT coils had 75 turns, a diameter of 60 mm, a separation of 84 mm, and a resistance of $0.36\,\Omega$. The total current was 3.65 A. The LP MOT coils must be switched off simultaneously, and they were therefore operated in series with a single power supply. The lower coil was placed in parallel with a $1\,\Omega$ resistor in order to lower the MOT centre. A high power resistor was used to decrease magnetic geometry changes due to thermal resistance deviations. The total inductance of the LP anti-Helmholtz coil pair is $480\,\mu$H.

In the rubidium-dominated regime (Sec. 3.1.3) the Rb pressure in the HP vacuum chamber does not affect the total number of atoms trapped, however it does affect the HP MOT loading time constant, τ_{HP} (Sec. 3.1.4). When τ_{HP} became too long and double MOT performance was decreased, the sidearm valve was opened and Rb vapour was transferred into the HP MOT by heating the sidearm with a heatgun. The amount of vapour added can be monitored using a photodiode to detect its level of fluorescence in the

MOT laser beams.

After the laser beams for the LP MOT are aligned and locked, the optics are in place, the anti-Helmholtz coils are on, and there is Rb vapor in the HP vacuum chamber, a MOT will form. A charged coupled device (CCD) camera image of the MOT can be seen in Fig. 4.10. The viewing angle is in the direction of the LP MOT chamber, through the viewport used to transfer ('push') atoms from the HP MOT to the LP MOT.
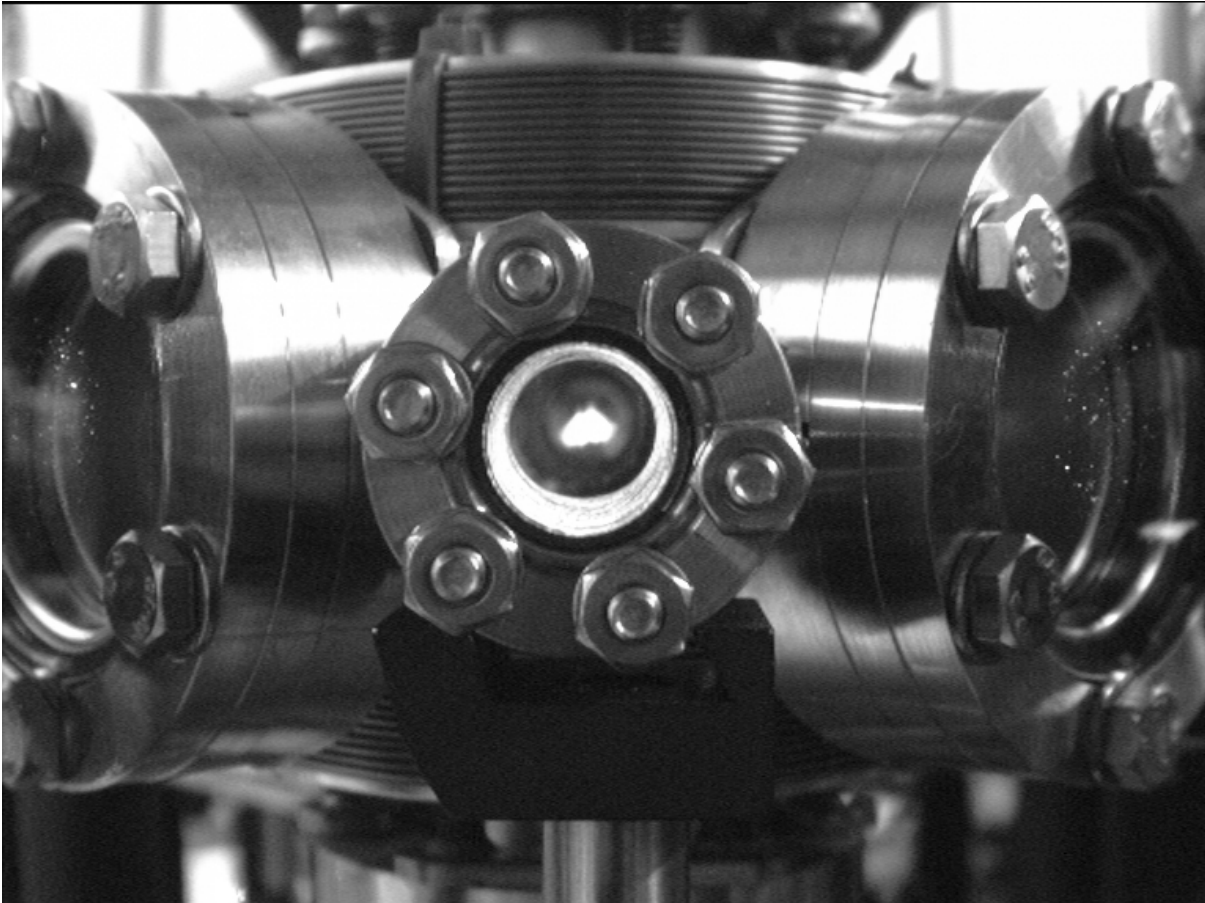

Figure 4.10: A 'push-beam's eye view' of the fluorescence from the high pressure (HP) MOT. The MOT contains about 10^9 ^{87}Rb atoms.

Atom number

It is useful to be able to measure the atom number and fill characteristics of a MOT for optimisation purposes. These properties can be determined by measuring the MOT fluorescence with a photodiode. A large area ($r = 5.5\,\text{mm}$) photodiode could be placed at the push beam viewport, $d = 95\,\text{mm}$ from the HP MOT, for this purpose (it must be removed during double MOT operation). The MOT can therefore be considered as a point source, emitting light isotropically. Given that the energy of a photon is $E = hc/\lambda$, the approximate photon absorption (and emission) rate in light with intensity I_{tot}
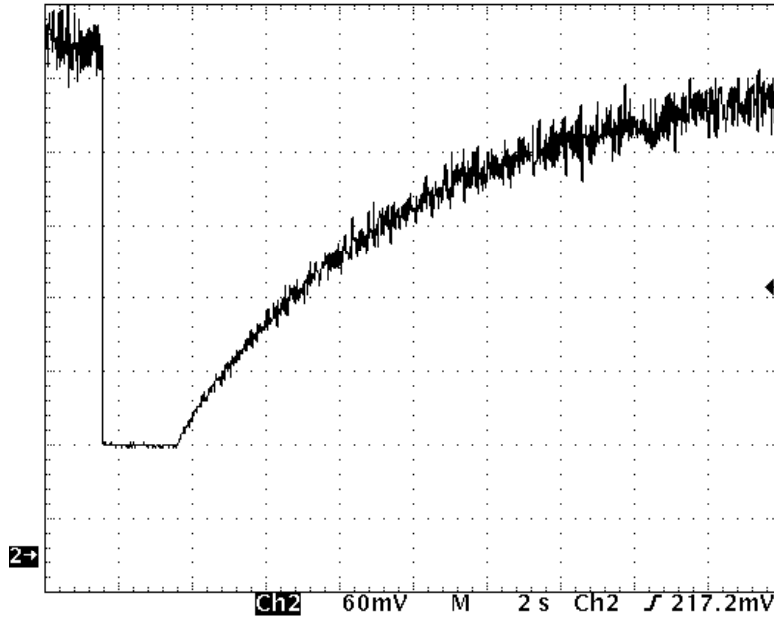
Figure 4.11: A MOT's fluorescent light can be collected on a photodiode to determine the number of atoms, N, in the MOT. An experimental exponential 'fill curve' of N as a function of time (Eq. 3.7) is shown for ^{87}Rb atoms in the HP MOT. Here $N_{HP} = 1.0 \times 10^9$, and the HP MOT loading time constant is $\tau_{HP} = 7.3$ s. The rapidly falling signal at $t = 1.6$, s indicates where the MOT is emptied by turning off the magnetic quadrupole field. The MOT begins to fill again at $t = 3.6$, s when the MOT magnetic field is turned back on.

$(I_{tot_{HP}} = 6.1 \, \mathrm{mW/cm^2}$, $I_{tot_{LP}} = 4.6 \, \mathrm{mW/cm^2})$ is $R \approx \frac{\Gamma}{2} \frac{I_{tot}/I_S}{1 + I_{tot}/I_S + 4\Delta^2/\Gamma^2}$ [134], the relative solid angle of light reaching the photodiode is $\frac{\Omega}{4\pi} \approx \frac{r^2}{4d}$ and that the detection efficiency of the photodiode is $\eta = 0.47 \, \mathrm{A/W}$, then one determines the number of atoms in the MOT to be:

$$N = \frac{4\pi}{\Omega} \frac{2\lambda}{hc\Gamma} \frac{1 + I_{tot}/I_S + 4\Delta^2/\Gamma^2}{I_{tot}/I_S} \frac{i}{\eta}, \tag{4.1}$$

where i is the current measured in the photodiode. The photodiode current is amplified by an op-amp with feedback resistance $R = 1 \, \mathrm{M\Omega}$ yielding an output voltage $v = iR$. This voltage is used to measure N and its variation with time. Under normal (HP and LP) MOT operating conditions $\Delta/\Gamma = -13 \, \mathrm{MHz}/6.07 \, \mathrm{MHz}$, and so $N_{HP} = 3.3 \times 10^6$ atoms/mV, and $N_{LP} = 4.2 \times 10^6$ atoms/mV. The main sources of error are the measurement of laser intensity, and the applicable saturation intensity – the atom number should be correct at the 20% level however. A typical HP MOT fill curve is shown in Fig. 4.11.

Quotes of the saturation intensity in Eq. 4.1 vary widely in the literature. Each allowed D2 rubidium transition has a separate saturation intensity, I_S (Tables C.1, C.2). The total light field at the intersection of the MOT's six laser beams is a mixture of polarisations [132], and all allowed near-resonant transitions will be driven. One possibility is to assume an isotropic population distribution over the m_F levels, and
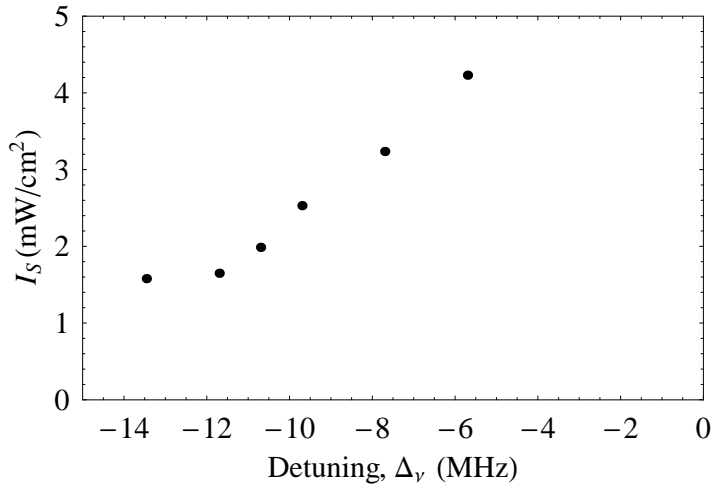
Figure 4.12: The experimentally measured average saturation intensity, I_S, in the ^{87} Rb HP MOT as a function of the detuning, Δ.

find the average I_S from the inverse of the average relative strength of all $F = 2 \rightarrow F' = 3$ transitions ($F = 3 \rightarrow F' = 4$ for ^{85}Rb). This yields $I_S = 3.80\,\text{mW/cm}^2$ for ^{85}Rb and $I_S = 3.49\,\text{mW/cm}^2$ for ^{87}Rb (cf. Ref. [146]), however this does not agree with experiment.

One can determine I_S by collecting atoms in a MOT, then toggling the light intensity rapidly between two values I_1 and I_2 (the experiment was performed with $I_1 \approx I_S/2$). The ratio of MOT fluorescence is given by:

$$\frac{F_1}{F_2} = \frac{I_1}{I_2}\frac{1 + I_2/I_S + 4\Delta^2/\Gamma^2}{1 + I_1/I_S + 4\Delta^2/\Gamma^2}, \tag{4.2}$$

and experimental measurements of F_1 and F_2 thus determine the remaining parameter I_S. The fill/decay processes in the MOT are very small on time scales of $10\,\text{ms}$, and the total atom number is assumed to remain essentially the same if the light intensity is altered with a $10\,\text{ms}$ period square wave. The results of this experiment, at a variety of detunings, are shown in Fig. 4.12.

An experiment was also performed at $\Delta = -13\,\text{MHz}$ with constant intensity and a small $(0.5\,\text{MHz})$ square modulation on the detuning, yielding $I_S = 1.70\,\text{mW/cm}^2$. It appears that there are strong optical pumping effects in MOTs operating with large detuning, and the atoms mainly populate the larger $|m_F|$ levels, in agreement with Refs. [163, 166]. The average I_S [146, 147] is now rarely used and the saturation intensity of the strongest atomic transition is commonly employed [157, 163, 166, 173, 199]. Any MOT calculations discussed in this thesis use the saturation intensity of the strongest Rb D2 line: $I_S = 1.67\,\text{mW/cm}^2$ (Appendix C). For a more accurate determination of the number of atoms the method described in Ref. [199] can be used, which is independent of the saturation intensity as well as laser polarisation, intensity and detuning.

Initial measurements of the MOT number yielded values around $N \approx 10^7$ ^{85}Rb atoms. This atom

number was rather low, given our MOT beam parameters [147], and we therefore replaced the double MOT vacuum chamber with a different, smaller, single MOT vacuum system for comparison. This system used Rb alkali metal dispensers (getters) to generate Rb vapour. With this vacuum cell 50 times more atoms were collected, and we surmised that the relative pressure of Rb in the HP MOT chamber of the vacuum system was too low. Subsequent, more intense, heating of the sidearm proved this to be the case, and HP MOT atom numbers of $N = 10^9$ are now typical. This heating may have helped to outgas the sidearm.

Measurements of the dependence of a MOT's fluorescence, F, versus a variety of trap parameters were carried out with the getter vacuum system, using ^{85}Rb atoms. The number of atoms, N, can be determined from F, given the intensity and detuning of the trapping light (Eq. 4.1). In situations where beam diameters or the quadrupole magnetic field are varied F is directly proportional to N, otherwise N must be determined using Eq. 4.1. In summary (Fig. 4.13, cf. Fig. 3.3 and Ref. [147]): N increased with the square of laser beam diameter, and displayed an approximately bell-shaped dependence with detuning and axial magnetic field gradient (centred at maxima of -15 MHz and 14 G/cm respectively). The atom number displayed a notably similar dependence on the trap and repump laser beam diameters: quadratic, but saturating as the beam's maximum diameter of 23 mm was approached. The MOT fluorescence was linear with trap beam power (intensity), implying that the number of atoms saturated as trap power increased. These results can be compared with the theoretical model described in Sec. 3.1.3.

The big push

With an operational HP MOT, it was then possible to 'push' the atoms down the transfer tube to the LP MOT. The push laser beam was aligned to pass through the centre of the HP MOT, along the transfer tube and a few millimetres above the centre of the LP cell (to prevent the push light affecting the LP MOT, and also to give the atoms a slight upwards trajectory). A lens with a focal length equivalent to the HP-LP MOT separation can be used to focus the push light, causing a smaller spread in atomic transverse velocity, and the narrow beam waist in the LP MOT chamber helps prevent LP MOT interaction with the push beam. In practice we rarely use the lens. A useful parameter when considering the photon scattering rate (and thereby acceleration) during the push pulse is the velocity at which the atom's frequency is Doppler-shifted by one atomic linewidth: i.e. $kv = \Gamma \Rightarrow v = \lambda\Gamma_\nu = 4.6$ ms^{-1}.

Resonant light is used for the push beam, and the atoms are rapidly accelerated to velocities of 17 m/s (Fig. 4.14). The longitudinal velocity distribution of the pushed atoms was studied using the fluorescence signal of the atoms as they passed through a 5 mm wide, 25 mm high laser probe beam (consisting of trap and repump light) in the cylindrical section of the quartz LP MOT cell $d = 29.5$ cm from the HP MOT. To achieve good signal to noise, the detection photodiode must be kept away from reflections off the cell,
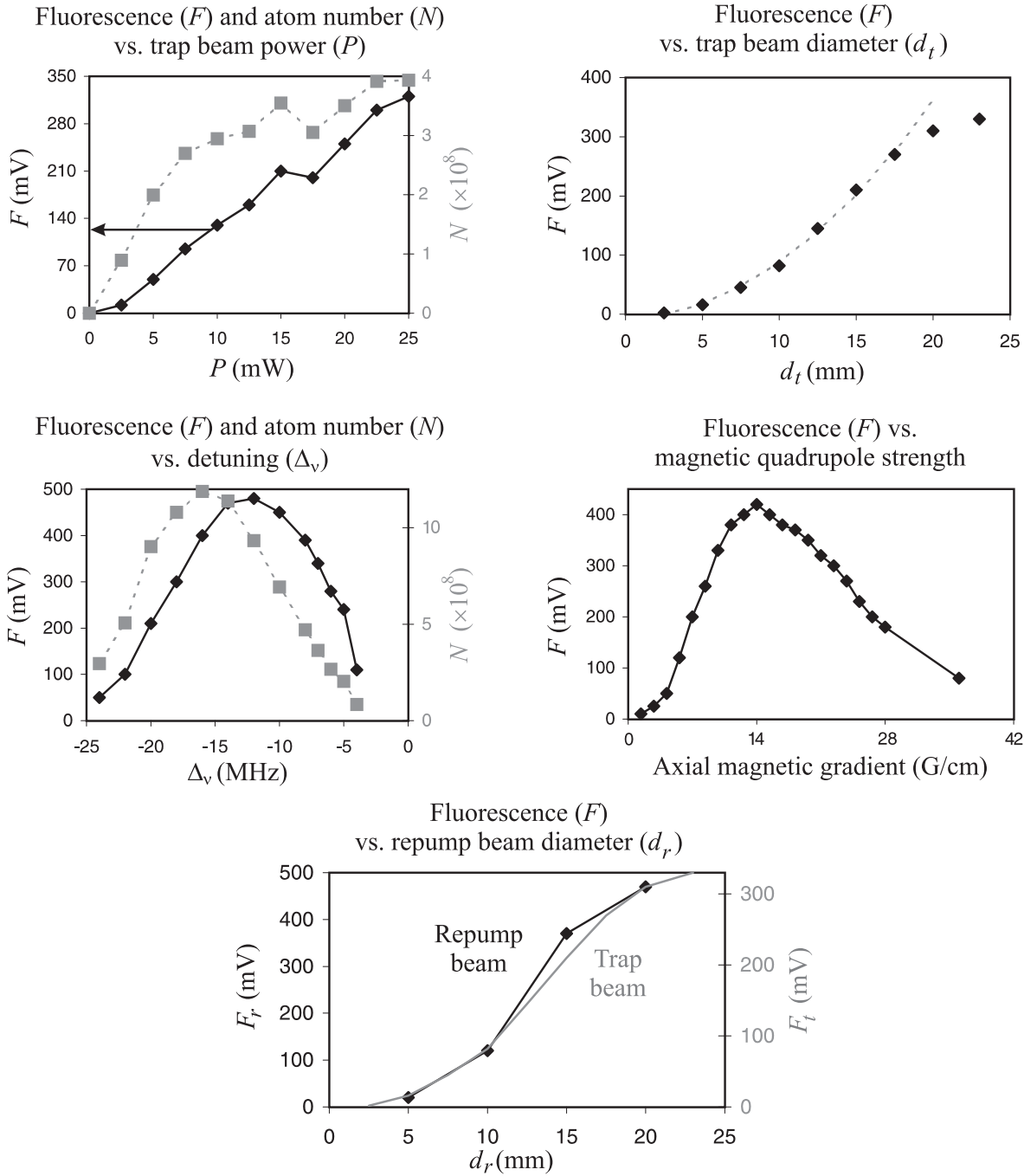
Figure 4.13: The dependence of ^{85}Rb MOT fluorescence, F, and atom number, N, versus a variety of MOT parameters. The lasers and photodiode position of the double MOT were used, however the double MOT chamber was replaced by a small getter-loaded single MOT vacuum chamber and anti-Helmholtz coils. Most measurements were taken at a detuning of $\Delta = -8\,\text{MHz}$, and the maximum HP MOT trap laser power was $25\,\text{mW}$ (cf. the present HP MOT settings of $\Delta = -13\,\text{MHz}$, $11\,\text{mW}$). The maximum intensity was $I_{tot} = 10.5\,\text{mW/cm}^2$. The beam diameter was varied by aperturing the MOT's Gaussian laser beams. In the final figure the dependence of the fluorescence with trap beam diameter is included for comparison.

and a $10\,\text{M}\Omega$ photodiode amplifier feedback resistor was used. The fluorescence signal vs. time, $S(t)$, must be processed to find the velocity distribution, as atoms only fluoresce for a period of time inversely proportional to their velocity.

The velocity distribution and the total number of atoms are given by

$$n(v) \propto \frac{S(d/v)}{v} \quad \text{and} \quad N \propto \int_0^\infty n(v)dv.$$

Fig. 4.14 depicts the atomic longitudinal velocity distribution after a variety of push-pulse durations. Note the wide velocity spread. If the transverse velocity width was also large it would certainly account for the low transfer efficiency. The data in Fig. 4.14 was taken with push beam parameters ($I_{push} < 30\,\text{mW/cm}^2$, $\Delta = +8\,\text{MHz}$) different to those currently used ($I_{push} = 46\,\text{mW/cm}^2$, $\Delta = 0\,\text{MHz}$). Transfer efficiency to the LP MOT improved with red push beam detunings and longer push pulses. Atoms transferred horizontally at a mean velocity of $v = 17\,\text{m/s}$ will fall $4.2\,\text{mm}$ under gravity as they traverse the $50\,\text{cm}$ distance from the HP to the LP MOT. If the atoms are given a slight upwards velocity, this deviation from a straight line can be reduced by a factor of 4 to $1.1\,\text{mm}$.

It may be interesting in future to study the transverse velocity distribution of the pushed atoms using absorption imaging (see below), at the end of the quartz LP MOT cell where the MOT forms. This would give a better idea of why the transfer efficiency is low.

The present LP MOT loading sequence (for optimised N_{LP}) is as follows:

- Trap: Turn the trapping beam AOM on, and load the HP MOT for $80\,\text{ms}$.

- Push: Turn off the trapping beams, and turn on the push beam AOM for $0.15\,\text{ms}$.

- Wait: Turn off the push beam and wait an additional $1.31\,\text{ms}$ for the HP atoms to clear the HP MOT beams on their journey to the LP MOT.

This sequence is repeated until the required number of atoms accumulates in the LP MOT. Fig. 4.15 depicts a typical LP MOT multiple loading fill curve, and an LP MOT decay curve. Note that during the 'push' and 'wait' phases of loading *both* the LP and HP MOT have no confinement, as their trapping beams are both derived from the same AOM (Fig. 4.9). This leads to an additional loss rate in the LP MOT that would be removed if separate control of the LP and HP MOT intensity were implemented. The number of atoms captured in the LP MOT appears to be quite critical on the laser intensity, and separate trap lasers for the HP and LP MOTs would probably rectify this.

The HP MOT quadrupole coils are left on during the push and wait phases, and although this will lead to optical pumping, this does not affect the LP MOT transfer efficiency of $25\,\%$. Magnetic forces from the coils are at the same level as gravity, however the atoms only have $2 - 3\,\text{ms}$ to interact with the anti-Helmholtz coils before they are in the transfer tube. Previous double MOT schemes have relied
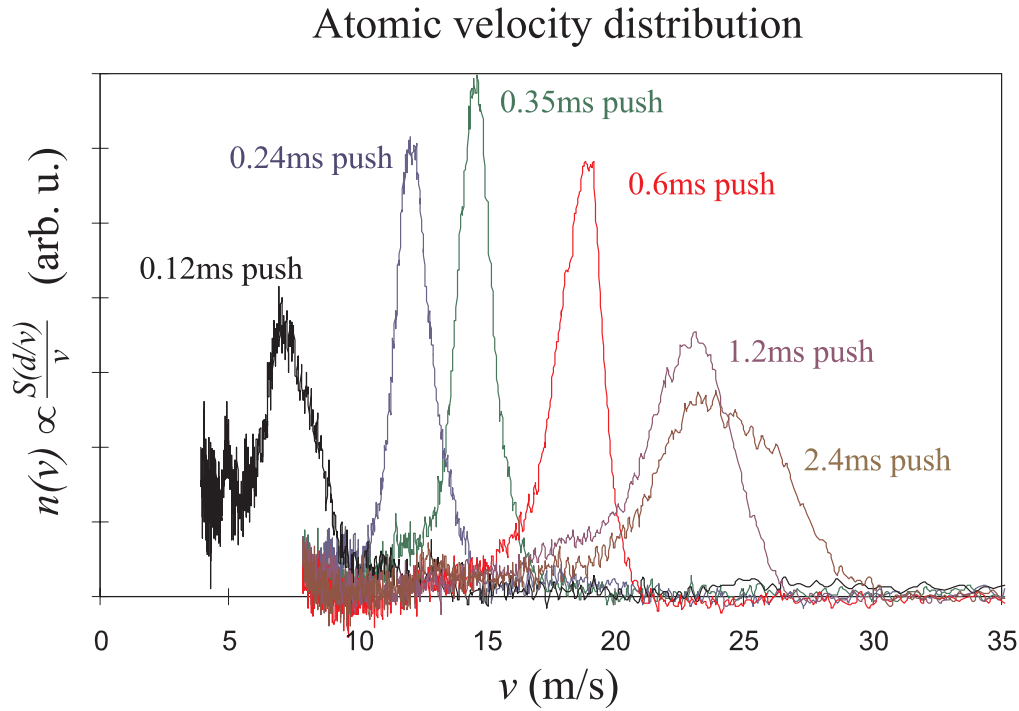
Atomic velocity distribution

Figure 4.14: The longitudinal velocity distribution, $n(v)$, of 'pushed' ^{85}Rb atoms as the push pulse length is varied. The total numbers of atoms transferred to the LP MOT chamber as the push pulse duration increases are $N = 4.2, \ 8.4, \ 9.9, \ 9.8, \ 12.3, \ 13.0$ (arbitrary units). Although more atoms reach the LP cell as the push duration is increased, the number of atoms captured in the LP MOT reaches a maximum with $0.4\,$ms push pulses. The capture velocity of the LP MOT is therefore $v_C \approx 17\,$m/s.

on preparing atoms in a weak field seeking state, and magnetically guiding them along the transfer tube [23]. We have managed to avoid this additional complication - perhaps at the cost of transfer efficiency.

Transfer efficiency was found to be lower than expected from theory (Sec. 3.1.4), and this may have been due to the rough push beam profile (the beam is not spatially filtered) causing an uneven acceleration across the HP MOT cloud. The transfer efficiency dropped greatly when large clouds of atoms were transferred (i.e. when a long 'fill' phase was used), possibly due to an increased pushed cloud transverse velocity due to the increase in temperature often seen in MOTs with a large number of atoms [168, 169]. The optical thickness of the MOT may also have been an issue. If multiple emissions and absorptions of individual photons occur within the atomic cloud, then the transverse heating rate would be significantly increased. Transfer should be improved to a small extent by using repump light overlapped with the push beam, however we found no significant difference if only the MOT repump light was used.

It is useful to estimate the average number of trap light photons that are absorbed in a MOT before an atom decays into the lower ground hyperfine state and needs to be repumped. This can be found by calculating the relative transition rates from the $F_g = I + 1/2$ ground state to the excited levels
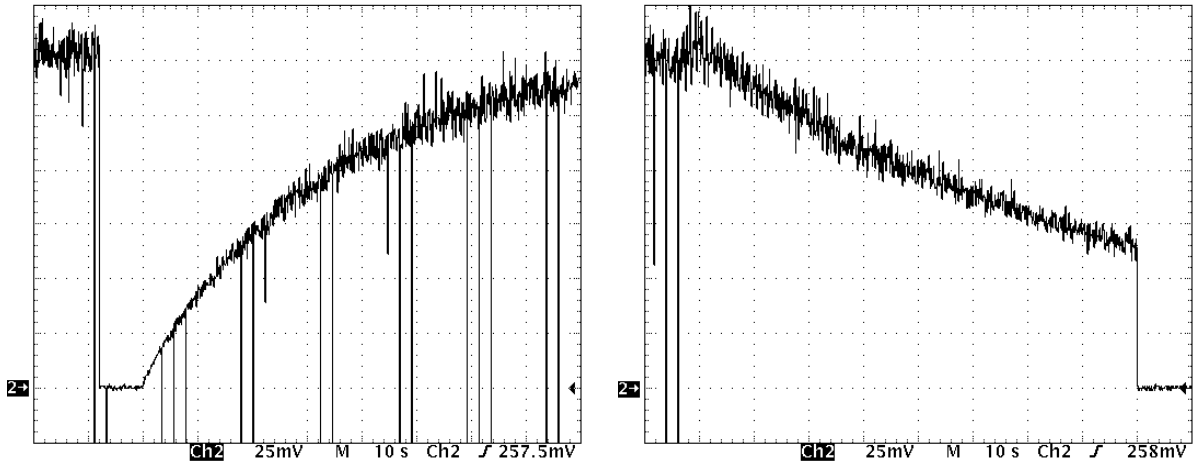
Figure 4.15: Typical ^{87}Rb LP MOT fluorescence fill (left) and decay (right) curves. The number of atoms and decay lifetime for the LP MOT (Eq. 3.7) are $N_{LP} = 6.5 \times 10^8$, $\tau_{LP_{fill}} = 33$ s. The vertical lines in the LP MOT fill curve indicate when the LP MOT light is turned off whilst atoms are 'pushed' from the HP to the LP MOT during loading (the trapping light for the two MOTs is derived from the same laser beam). When multiple loading of the ^{87}Rb LP MOT is halted ($t = 10$ s in the right image), one observes the decay of atoms from the MOT. The decay time constant is $\tau_{LP_{decay}} = 92$ s. Fill/decay curve departures from the exponential form of Eq. 3.7 can occur due to collisional losses within a MOT [164, 148].

$F_e = I + 1/2, I + 3/2$ with Eq. 3.2, given $I_{tot} \approx 5$ mW/cm^2, $\Delta = -13$ MHz. On average $\frac{3}{4}(2 + 1/I)$ repump photons must be absorbed (App. C) before the atom is repumped from the $F_g = I - 1/2$ to the $F_g = I + 1/2$ ground state. This means that the average number of trap photons absorbed per repump photon is 32 for ^{85}Rb and 157 for ^{87}Rb.

4.1.4 Temperature diagnostics and imaging

The temperature is an important parameter necessary for the determination of phase space density. The MOT temperature was initially measured using the release and recapture [13, 134] technique. However we found the model did not fit well with our experimental results - the atoms appeared to be trapped even after they had left the common intersection of all 6 MOT beams (conventionally defined as the MOT re-trapping region). This was true regardless of whether the MOT coils were on during free-fall or not – i.e. it was not a magnetic trapping effect – and the extra re-capture was probably from the region described by the union of the 6 MOT beams.

A more reliable and direct temperature measurement was implemented by observing the ballistic expansion of the MOT cloud with time. This relies on careful triggering of the camera involved, and short observation light pulses to provide a snapshot of the moving atoms: $t_{exposure} < 1$ ms $\ll t_{expansion} \approx t_{CCDframe} = 40$ ms. As the RS 185-3091 CCD camera we used could not be triggered externally,

the computer control program employed for imaging was synchronised with the camera. This ensured that the short imaging light pulse did not fall in the CCD's 2 ms 'dead period' (when the CCD is neither integrating, nor reading out) and also that the correct odd/even frame (i.e. that which contains the imaging light pulse) is read into the computer's frame-grabber.

This camera/computer synchronisation is also important because it is sometimes useful to observe the behaviour of the atomic cloud shortly after the atoms have been in a MOT. In any CCD frame where the MOT has been operating, the image will be completely dominated by the MOT, rather than the signal from the imaging light pulse. It is therefore useful in such circumstances to have the MOT trapping phase finish at the end of a frame, so that the imaging pulse writes on a 'clean slate' in the next frame. This is not entirely true however, as the CCD camera retains a 'ghost' image of the previous frame, particularly if the signal was large. In these situations it is useful to use a (*Newport*) shutter in front of the camera. The shutter alone cannot limit the exposure time (one on/off cycle is ≈ 8 s), however it can be synchronised to open very shortly before the imaging pulse arrives.

The *Labview* computer control program that operated the BEC experiment was developed and documented solely by Dr. Malcolm Boshier. Section 4.3.1 gives a description of the hard and software used to implement the computer-controlled operation of the experiment.

The CCD camera had a response approximately proportional to the square root of intensity. Experimental measurements of the camera's intensity response were used to generate a look-up table, ensuring that the CCD's processed output was directly proportional to intensity, with no offset. This was essential for obtaining correctly dimensioned images of the atoms, and for accurate absorption imaging. The camera's automatic shutter must be switched off, to ensure reproducible exposure times.

Fluorescence imaging

The lens system for imaging was designed to have low aberration and a relatively low magnification, allowing atoms to be accurately studied throughout the BEC creation process (Fig. 1.2). An $f = 5$ cm lens doublet was placed ≈ 10 cm away from the LP MOT cloud and the CCD camera was placed in the lens' image plane. The two $f = 10$ cm plano-convex lenses were placed with the curved surfaces facing each other, as ray-tracing calculations predicted low image distortion for this lens configuration.

Atoms were collected in the MOT, then released into darkness for variable amounts of time. An image can then be formed by pulsing on the MOT laser beams again for ≈ 1 ms. Given the dimensions of the CCD pixels ($6.25 \, \mu$m $\times$ $12.6 \, \mu$m) and the magnification of the lens system ($M = 0.80(1)$), it is then possible to calibrate the size of these fluorescence images. The integrated signal over the CCD array gives a relative measure of atom number, N, which must be compared with a calibrated photodiode in order to obtain absolute measurements of N.

The imaging process is destructive, and so in order to obtain measurements of the time evolution of an atom cloud it is necessary to repeat the data acquisition sequence (MOT fill/release/image) several times.

Absorption imaging

In this situation a circularly polarised, collimated $I = 300\,\mu\text{W/cm}^2$ probe laser beam (derived from the push beam) is sent through the atomic cloud. A magnetic field is also applied along the beam's direction of propagation (Sec. 3.1.7). A shadow of the atomic cloud is formed in the beam, which is imaged onto the CCD camera through the same lens system used for fluorescent imaging. In this way both imaging techniques can be employed, as required. The advantage of absorption imaging over fluorescence imaging is that much shorter imaging pulses can be used (we typically use $8\,\mu\text{s}$ pulses of probe light), giving a very clear temporal snapshot of the atomic cloud. Also, as most of the imaging light which interacts with the atoms is used to form the image (unlike fluorescence imaging) this allows much greater signal to noise, particularly in the case of very small clouds (like BECs).
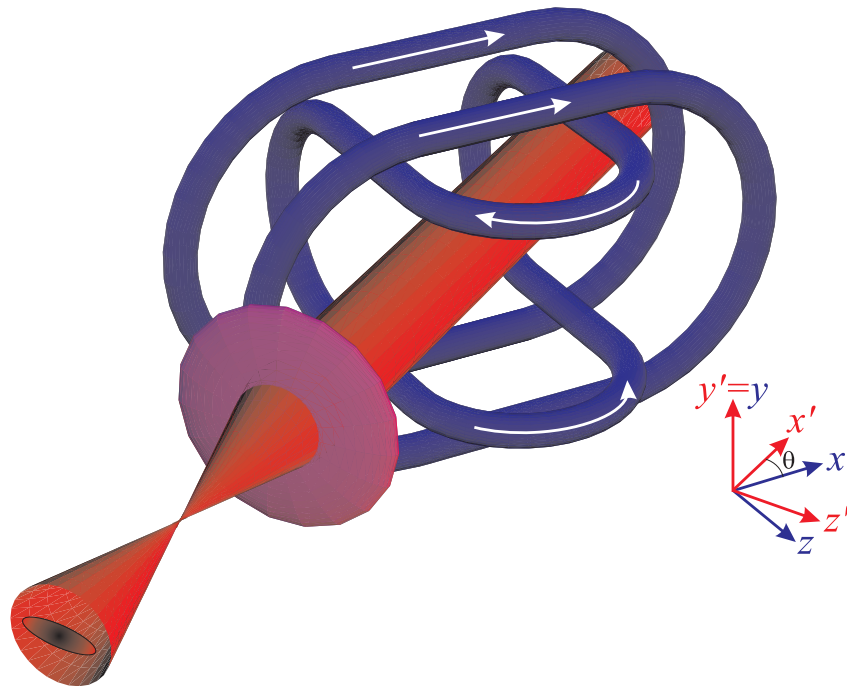

Figure 4.16: Schematic of the Sussex absorption imaging set-up. The probe laser beam is indicated in red, and the blue coils represent the Sussex Ioffe-Pritchard magnetic baseball trap (Sec. 4.2.3). The probe laser passes through the atomic cloud, creating a shadow in the beam which is imaged through the lens system onto a CCD camera.

In order to obtain quantitative information about the atomic cloud one must take two images (one with and one without atoms) and the relative absorption signal can then be interpreted to yield the atomic cloud

dimensions, as well as the atom number, density, temperature, collision rate and phase space density (Sec. 3.1.7). Due to thermal effects from the magnetic field coils (Sec. 4.2.3), which heat the LP MOT cell windows, it is important to acquire these two images from sequential CCD frames.

The probe laser beam is also used for optical pumping (Sec. 4.2.2). When optically pumping or imaging the atoms it is useful to have a uniform intensity distribution across the laser beam. For this reason the beam was spatially filtered, by passing it through a pinhole. Unfortunately when the resulting smooth beam is passed through the quartz LP MOT cell, the poor optical quality of the cell results in an output beam with intensity fluctuations greater than a factor of two (Fig. 3.5). Fortunately absorption imaging is quite forgiving, as only relative intensity fluctuations are measured, and clear images of the atomic cloud are obtained.

Experimental data from the ballistic expansion of small, cold thermal clouds was used as a mechanism with which to calibrate the magnification of the imaging camera. Comparison of the parabolic atomic centre-of-mass motion with the expected $y = -\frac{g}{2}t^2$ led to the magnification factor $M = 0.80\,(\pm 1\%)$.

Like fluorescence imaging, absorption imaging is also destructive, and in future it may be prudent to employ other, non-destructive, imaging techniques to observe the MOT and/or BEC. This would allow several images to be taken from the same experimental run – quite useful for accumulating data, when each run of the experiment usually lasts over a minute. Non-destructive imaging also reduces inevitable shot-to-shot errors. Three non-destructive imaging techniques have already been employed successfully by other groups: dark-ground imaging [41, 208], phase-contrast imaging [44, 208] and phase-contrast polarisation imaging [61].

4.1.5   Feeding forwards

Various procedures in the production of a BEC require changes to the trap laser frequency. The AOMs which are used in the trapping and push/probe/pump beams are primarily used as shutters, and their frequency is never altered as this would change the MOT laser beam alignment. In fact, with the long beam paths used in the LP MOT one must be careful not to let the trapping beam AOM frequency drift at the level of a few $100\,\mathrm{kHz}$. Here various methods which could be used for adjusting the laser frequency are discussed, before the method we settled on at Sussex is described.

One method for adjusting the laser frequency is the use of a double-passed AOM beam. In this case the laser beam is subjected to two Bragg diffractions in opposite directions within the AOM crystal and the output beam's direction is insensitive to AOM frequency. Such a scheme often results in lower laser beam powers.

It is also possible to alter the trap laser frequency by changing the frequency of the AOM in the

saturated absorption spectrometer (Fig. 4.3). With an appropriate lens after the AOM (or using a double-passed AOM) it is possible to build a spectrometer based around a beam whose direction is independent of AOM frequency. The problem then is that when one changes the frequency of the AOM, the servo circuit used to lock the laser may not be able to compensate for the sudden change in AOM frequency.

For this reason a 'feed-forward' was built to quickly inject small amounts of current into the laser diode, altering its frequency. It turned out that the passive stability of the laser frequency was sufficiently good $(1\,\text{MHz}$ drift in $200\,\text{ms})$ that it was not actually necessary for the laser to remain locked throughout the frequency excursion. The AOM frequency was therefore kept constant, and the feed-forward worked by simultaneously breaking the laser lock and injecting current to the laser diode. The lock was re-established after the laser was returned to its initial frequency.

The breaking of the lock was achieved by placing a digital switch (DG201ACJ) in two of the connections between the lock-in and integrator: the modulation connection, and the lock-in output to integrator input connection. A single TTL signal from the computer drives both switches, with a 'HI' signal opening the switches.

Current was injected into the diode using the 'scan' input of the integrator (see Fig. D.1). A $40\,\text{k}\Omega$ resistor was placed in series between the scan input and a multiplex (4-state analogue outputs set by trimpots and driven by two digital lines (Sec. 4.3.1)) signal from the computer in order to reduce the feed-forward's sensitivity. A feed-forward multiplex signal of $+5\,\text{V}$ now corresponds to an SDL laser frequency shift of $-280\,\text{MHz}$. The frequency responses of the two diodes we have used are $-300\,\text{MHz/mA}$ for the SDL-5401 and $-500\,\text{MHz/mA}$ for the *Hitachi* HL7851G.

When using the integrator's scan input (and for stable locking) it is important to set the gain of the high frequency feedback on the integrator's cross-over, to ensure the laser frequency has a flat response to all feedback frequencies. This can be achieved by observing an xy-mode oscilloscope plot of a linear region of the saturated absorption photodiode signal vs. a modulation applied to the 'scan' port of the integrator. The linear scope trace should remain the same as the modulation frequency is increased. Another test for appropriate cross-over gain is to apply a square pulse to the scan port - a corresponding square pulse in the photodiode signal should result, and this is also true when using the feed-forward.

For stable, adjustable laser frequencies over periods longer than $100\,\text{ms}$ it would be necessary to keep the laser locked, and adjust the AOM frequency and scan input simultaneously. This could be implemented quite easily and would also improve frequency stability for short periods of time as well.

4.1.6 Optical Molasses

Optical molasses is a process often used to lower the temperatures of a MOT into the sub-Doppler regime. The process is very sensitive to magnetic fields, and efficient molasses requires the residual field to be less

than 100 mG [134]. For this reason the MOT's quadrupole magnetic field must be switched off (at least for large MOTs [158, 159]), and additional magnetic coils must be used to cancel the earth's magnetic field. In theory this could be achieved with one pair of Helmholtz coils in the appropriate direction, but at various times in the BEC experiment it is necessary to generate fields in other directions. Three orthogonal pairs of Helmholtz bias coils were therefore centred around the LP MOT cell. The axes of the coils corresponded with axes of the LP MOT laser beams, as this facilitates drift-velocity cancellation (see below).

The rectangular coils were wrapped around a frame made from aluminium and perspex, preventing the flow of eddy currents in the frame during rapid switching of the magnetic fields. This is also a useful feature of the quartz LP MOT cell. Quartz has another advantage over stainless steel, as stainless chambers often generate strong magnetic perturbations near welds. In addition, quartz allows transmission of the RF field that will later be used for evaporative cooling.

The rectangular magnetic coils are not, strictly speaking, Helmholtz coils, in that although they produce a relatively constant magnetic field the second derivative of the magnetic field at the centre of a coil pair is non-zero (Sec. 3.2.2). The cuboid geometry chosen for the three coil pairs was mainly for simplicity, with side lengths large enough that the remnant magnetic field curvature is still small (< 60 mG/cm^2 for a 3 G field). 'Genuine' square Helmholtz coils have a spacing corresponding to ≈ 0.545 times the side length of the square, and the three pairs of frames would therefore be rather impractical. A cuboid coil frame was chosen instead of a cube in order to avoid the cylindrical stem of the LP MOT cell (Fig. 4.9).

The coils were designed to have a relatively low inductance ($L \propto N^2 d$ where N is the number of turns and d is the coil side length) compared to resistance, to ensure that the 'natural' time constant of the coils $\tau = L/R$ was smaller than a millisecond and hence facilitate fast switching speeds. Another factor considered was the need to generate large fields with minimal power consumption. The relevant parameters of the x, y and z pairs of Helmholtz bias coils are as follows (resistances and inductances for coil pairs in series):

- x (red) coils: 17 cm $\times$ 27.5 cm, 16 cm separation, $2.1\,\Omega$, 1.31 mH, 3 A $\equiv 5.3$ G

- y (black) coils: 16.5 cm $\times$ 27 cm, 19 cm separation, $2.0\,\Omega$, 1.04 mH, 3 A $\equiv 4.3$ G

- z (green) coils: 18.5 cm $\times$ 23 cm, 22.6 cm separation, $1.8\,\Omega$, 0.98 mH, 3 A $\equiv 3.5$ G.

Each coil has 30 turns.

The coil-driver design that controls the current in each Helmholtz bias pair is depicted in Appendix D. The design is based on an integrator, controlling a MOSFET that limits the flow of current through the coils. The relatively simple set-up enables extra voltage across the coils' power supply to be used to effectively shorten the 'natural' time constant of the coils, τ. The one caution with increasing the constant voltage of a coil's supply is that there is of course a limit to the power a MOSFET can dissipate.

Each coil-driver's adjustable gain resistor was set as high as possible whilst preventing oscillation. The 'set' voltage for each x, y, z bias coils (and the LP MOT coil) was provided by a separate multiplex (Sec. 4.1.5, 4.3.1) signal from the computer. The current of each coil could then be rapidly ($\approx 0.5\,\mathrm{ms}$) set to three (plus $0\,\mathrm{V}$) adjustable values.

In preparation for optical molasses, state 1 of the multiplex signal for each x, y, z bias coil pair was adjusted in turn, whilst observing the LP MOT's background magnetic field with a Gaussmeter. In this way the total magnetic field was nulled to $< 30\,\mathrm{mG}$. Molasses could subsequently be observed by loading the LP MOT and then rapidly turning off the LP MOT coils. This removes the MOT's spatial confinement, however the molasses damping force is still very strong. The atomic cloud could be observed slowly expanding on time scales of half a second. If counterpropagating laser beams in the LP MOT have different intensities and/or the magnetic field in the direction of a counterpropagating beam pair is non-zero then the imbalance in radiation pressure results in a molasses drift velocity [209]. There is a magnetic field, for a given intensity imbalance, at which the drift velocity is zero. One can therefore adjust the magnetic field along each beam pair (the MOT must be observed from two camera angles) until the molasses drift velocity is zero. If the intensity imbalances are small enough then the magnetic field at which this occurs enables sub-Doppler temperatures.

Altering the frequency of the trap laser during molasses allows the optimisation of the molasses final temperature. At large detunings the final molasses temperature is proportional to laser intensity, and inversely proportional to detuning [154, 155, 210, 157]. Thus with sufficiently well-spaced atomic hyperfine levels one only needs to optimise the detuning. Larger MOT clouds require a longer time to reach their equilibrium molasses temperature, due to optical thickness. We find that if $\approx 10^9$ MOT atoms are exposed to $\Delta_\nu = -30\,\mathrm{MHz}$ detuned molasses for $5\,\mathrm{ms}$, then their temperature drops to $40\,\mu\mathrm{K}$. A balance must be struck between the final temperature of the atoms, the number of atoms remaining, and the decrease in density due to atomic diffusion during optical molasses.

Both density and temperature are important as one approaches BEC (Eq. 1.1). In MOTs without spatial/temporal dark MOTs (DMOTs) [16] which reduce the density-limiting reradiation force [15], it is often customary to operate a compressed MOT (CMOT [19, 173]) stage before molasses, to increase the MOT's density. This involves red-detuning the trap laser, and ramping up the MOT magnetic field. We find that the added complication of either the ^{87}Rb (depumped) DMOT [16, 17, 18] or CMOT were unnecessary to obtain BEC, however either technique could be used in future to improve the number of Bose condensed atoms.

4.2   Magnetic trapping

4.2.1   Quadrupole magnetic trap

The first experiments on magnetically trapping neutral atoms were performed with quadrupole coils [185]. Preliminary experiments were also performed at Sussex using the quadrupole geometry, due to its simplicity. Small ($32\,\mathrm{mm}$ diameter, $40\,\mathrm{mm}$ separation) 55 turn anti-Helmholtz coils were employed to provide the quadrupole field for the LP MOT, and these coils could then be 're-used' as magnetic trapping coils. The coils generated an axial field gradient of $10\,\mathrm{G/cm/A}$, and could be operated at $8\,\mathrm{A}$ for a minute or so. Atoms were multiply loaded into the LP MOT, molasses was applied, and then the trap laser light was switched off whilst the quadrupole field was simultaneously ramped up. Only the atoms in weak field seeking states (Sec. 3.2.1) are magnetically trapped. The atoms leaving the MOT/molasses are in the upper ground hyperfine state ($F = 3$ for $^{87}\mathrm{Rb}$, $F = 2$ for $^{87}\mathrm{Rb}$). If there is a uniform population distribution across the m_F levels, then one expects a weak field seeking population of $43\,\%$ in $^{85}\mathrm{Rb}$ and $40\,\%$ in $^{87}\mathrm{Rb}$. This agreed very well with the magnetic trap capture efficiency we measured when atoms were released from optical molasses, however the efficiency was only $27\,\%$ ($^{85}\mathrm{Rb}$) when atoms were captured directly from a MOT. The MOT had a tendency to pump atoms into the strong field seeking states.

During magnetic trapping it soon became clear that the shutters used to complete the trap laser light extinction were highly important: leaving the shutters open drastically decreased the magnetic trap lifetime. Even the broadband light from a $40\,\mathrm{W}$ incandescent desklamp, $1\,\mathrm{m}$ away from the magnetic trap has sufficient light in the narrow rubidium absorption line at $780\,\mathrm{nm}$ to empty the trap in a few seconds. This is because a single photon can optically excite an atom, which will then quickly spontaneously decay. After this decay process the majority of atoms return to a ground state which is not magnetically trapped and are therefore lost from the trap.

4.2.2   Optical pumping

Optical pumping is a process whereby one increases the population of atoms in particular quantum states. For magnetic trapping we wish to enhance the population of weak field seeking states. In particular, the $^{87}\mathrm{Rb}$ $|2, 2\rangle$ state is the weak field seeking state with the highest magnetic moment, and it therefore allows the strongest magnetic confinement. Atoms are transferred to the $|2, 2\rangle$ state from other $|2, m_F\rangle$ magnetic sublevels through the absorption of appropriate σ^+ circularly polarised photons. An atom in $|2, m_F\rangle$ absorbing a σ^+ photon can be excited to the state $|(F' = 1, 2, 3), m_F + 1\rangle$, if it exists (Fig. B.2). Once excited, the atom will then decay to the ground state $|(F = 1, 2), m_F, \rangle$, $|(F = 1, 2), m_F + 1, \rangle$, or $|(F = 1, 2), m_F + 2, \rangle$ (depending on the emitted photon polarisation, and with relative rates given in

Table C.1) by spontaneously emitting a photon.

We optically pump on the $F = 2 \rightarrow F' = 2$ σ^+ transition, because when the atom reaches the 'dark' ground state $|2, 2\rangle$ further σ^+ light absorption is forbidden. This prevents unnecessary heating, as each D2 line photon absorption/emission imparts a 6 mm/s recoil to a rubidium atom. The disadvantage of cooling on this transition is that (compared to $F = 2 \rightarrow F' = 3$ pumping) the repump laser is very important, as 50 % of the excited atoms will decay to the $F = 1$ ground level. In our experiment the mixed polarisation combined MOT repump light is used during optical pumping, and so each repump absorption will have a random $(\delta m_F = -1, 0, 1)$ effect on the atom's ground state m_F level. This could be rectified if σ^+ polarised repump light were overlayed with the pump beam. Another improvement to the scheme would be to add a retro-reflecting mirror (or high reflectance beamsplitter) to the pumping beam – the time-averaged impulse imparted to an atom by optical pumping photons would then be low. Retro-reflected optical pumping would necessitate the added complication of separate imaging and pumping laser beams however.

The source of the optical pumping light is the 'pump/probe' laser beam (Fig. 4.9) which is also used for absorption imaging. During optical pumping a 1 G magnetic field was applied (using State 2 of the multiplex signal for the x, y, z bias coils) along either direction of the pump laser beam's axis of propagation. The **B** vector with the smallest angle to the Baseball coil's (Sec. 4.2.3) axial field vector was chosen, as this improves transfer efficiency into the magnetic trap by decreasing Majorana flops during the rapid baseball field switch-on period. With the correct sense of pump beam circular polarisation, transfer efficiency into the ground state $|2, 2\rangle$ reached 75 %. The atoms are optically pumped for 0.5 ms, as longer pumping times yield noticeable atomic heating with no improvement in transfer efficiency. In a weak harmonic magnetic trap (unlike the quadrupole trap) alkali metal weak-field seeking spin states with different $|m_F|$ values can be distinguished as they form clouds at different vertical positions due to their respective gravitational sags (Eq. 3.49).

4.2.3 Baseball and bias coils

The main disadvantage of a quadrupole magnetic trap is that although it provides tight confinement, it has a 'hole' in it (Sec. 3.2.3). This causes the coldest atoms to leak out (which is not very helpful for reaching BEC). There are a variety of ways to circumvent this problem and obtain BEC (Table 1.1), however the most common magnetic traps used in BEC production are the time-averaged orbiting potential (TOP) trap [20] and the Ioffe-Pritchard (IP) [21, 22] trap. Reservations about the low loading efficiency and confinement of the TOP [40] have, to some extent, been dispelled by demonstrations of large condensate formation in a TOP trap [211]. The decision at Sussex was to build an IP style magnetic trap however, as in both IP and TOP geometries high currents are required, but with an IP trap it is not necessary to produce

and synchronise large AC magnetic fields. There are a variety of IP styles to chose from, however the 3-coil geometry of the baseball with bias configuration appeared (and proved to be) exceptionally stable and relatively simple to implement.

A large number of amp-turns are required for the magnetic trap, as the forces involved for a given current are much weaker than in magneto-optical trapping. One must therefore dissipate large amounts of power, and at present the most efficient way to remove heat from the magnetic coils is to exploit the combined water and electrical current carrying capabilities of copper tubing. This is best achieved with a small number of turns and large current, which also prevents the unpleasant combination of high voltages and water. Our IP magnetic coil system is similar to that of Ref. [173] however some simplifications and reduction of the magnetic noise have been made.

Standard $3.2\,\text{mm}$ ($1/8$ inch) outside diameter ($1.7\,\text{mm}$ inside diameter) annealed copper refrigeration tubing was used for the 9-turn Ioffe-Pritchard (IP) baseball and the two 3-turn IP bias coils. The coils were designed to be as small as possible, constrained by the shape of the quartz LP MOT vacuum chamber. Nine turns were used in the baseball coil to minimise the resistance and inductance of the coil, aid water cooling efficiency, and because additional turns have a low relative contribution to the magnetic field curvature ($B_2 \propto 1/r^3$ where r is a coil dimension).

The geometry of the baseball and bias coils are shown in Figs. 4.17 and 4.18 respectively. The copper tubing was electrically insulated with appropriate lengths of $4.8\,\text{mm}$ heatshrink tubing. Shaped wooden formers were created on which to wind the coils.

Although the coils were relatively stable after formation, small globs of epoxy and a few cable ties were used to prevent the coils losing their new shape. It appears that the coils are sufficiently mechanically stable without encasing them in epoxy (cf. [173]). The coils were observed through a traveling telescope whilst the current was pulsed on, and no motion was seen at the level of $100\,\mu$m.

The current for the coils was supplied by two constant voltage *Sorensen* SSD 5-225 $5\,$V, $225\,$A, switching power supplies operated in series. These were remarkably robust, and had some rather useful automatic cut-out capabilities. The built-in cooling fan was removed from each supply unit housing and placed externally, near the air intake port. This removed almost all mechanical vibration in the power supplies, in order to prevent vibration of the IP coils through the connection leads. The power spectrum of the *Sorensen* supply's voltage noise is shown in Fig. 4.19.

The coil current was measured using *Honeywell* CSNR-161 closed loop, Hall effect current sensors. This enabled non-invasive accurate current readings with little thermal drift, $\pm 0.1\,\%$ linearity and a high ($150\,$kHz) frequency response. The high frequency response is important for providing fast feedback to a current stabilisation mechanism. With a $\pm 15\,$V power supply and a $33\,\Omega$ sense resistor the sensors could measure currents of up to $250\,$A, with a nominal output of $3.3\,$V$/100\,$A.

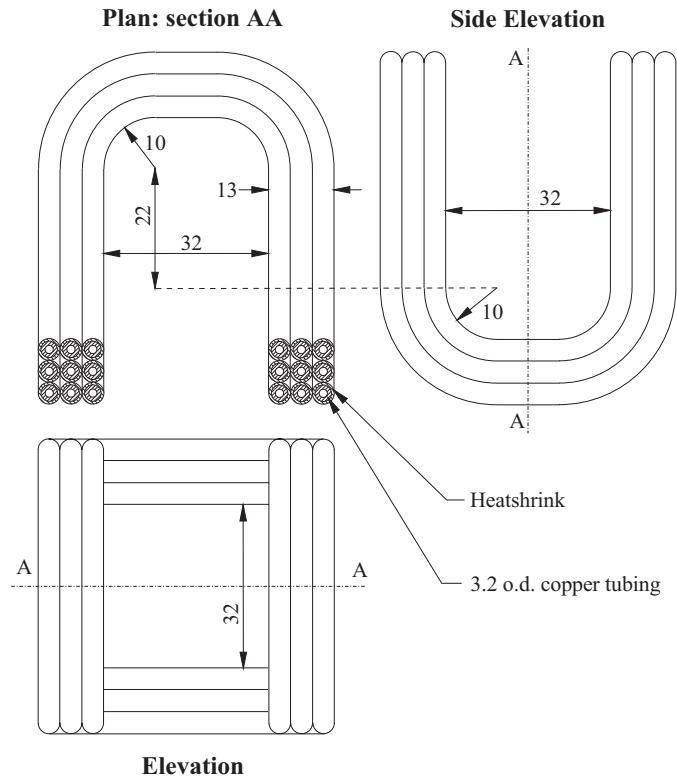The current in the coil circuit was regulated with simple water-cooled MOSFET banks. A straight-

Figure 4.17: The 9-turn Ioffe-Pritchard baseball magnetic field coil. All dimensions are in mm. At $216\,\mathrm{A}$ the IP baseball coil generates an axial bias field of $167\,\mathrm{G}$, a radial gradient of $180\,\mathrm{G/cm}$ and an axial curvature of $58\,\mathrm{G/cm^2}$. The coil has an inductance of $L_{BB} = 8\,\mu\mathrm{H}$, and a room temperature resistance with (without) leads of $0.015\,\Omega$ $(0.011\,\Omega)$.
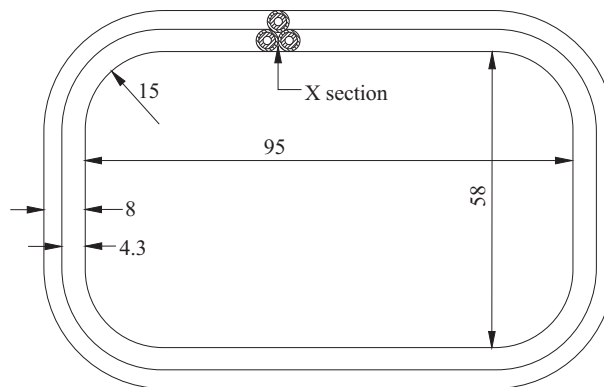

Figure 4.18: The dimensions used for the two 3-turn IP bias magnetic field coils. The wide dimension of the coils was limited by the quartz LP MOT cell. With an average coil separation of $30\,\mathrm{mm}$, the bias coils produce a $158\,\mathrm{G}$ axial bias field at $216\,\mathrm{A}$ and an axial curvature of $-8\,\mathrm{G/cm^2}$ (i.e. the bias curvature increases the baseball curvature). The IP bias coils have a total series inductance of $L_{Bias} = 3\,\mu\mathrm{H}$, and a room temperature resistance with (without) leads of $0.010\,\Omega$ $(0.007\,\Omega)$.
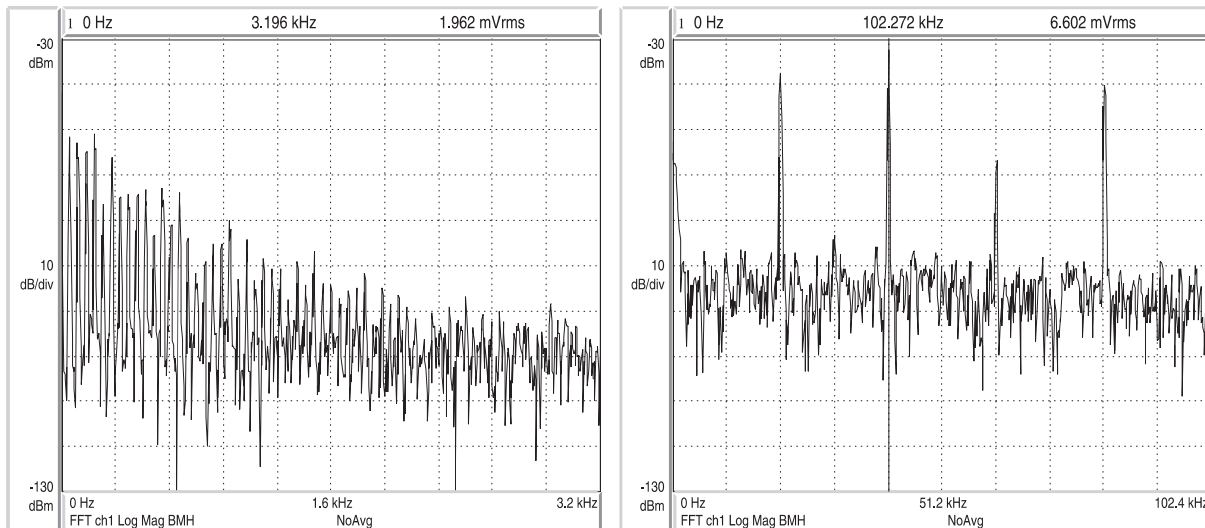
Figure 4.19: The power spectrum of the high current power supply's voltage noise. There are some line frequency harmonics, however most of the noise is at harmonics of the operating frequency of the *Sorensen* switching supplies. There is $6\,$mV of rms ripple on the $5\,$V DC voltage.

forward control circuit is used, essentially a modified integrator circuit, and the schematic is shown in Fig. 4.20. The MOSFETs used in this instance have to deal with rather heavy-duty powers: $10\,$V $\times$ $250\,$A $= 2.5\,$kW. The IP baseball MOSFET bank consists of 20 BUK456-60H $60\,$V, $60\,$A, $150\,$W MOS-FETs with the drains (sources) bolted onto both surfaces of a $12.5\,$mm $\times$ $19\,$mm ($12.5\,$mm $\times$ $12.5\,$mm) cross-section copper bar. The IP bias MOSFET bank is similar, but uses 10 MOSFETs. The drain of each MOSFET is connected to the tab of their TO-220 package, where all the heat is generated. The copper bars used for the drain of the MOSFET banks were therefore water-cooled with two passes of $3.2\,$mm o.d. copper tube recessed and soldered into the bars.

The BUK456-60H MOSFET is now obsolete, although the PHP125NO6T $55\,$V, $75\,$A, $187\,$W MOS-FETs actually perform better anyway, and will be used in future. The on-state resistance of a BUK456-60H (PHP125NO6T) MOSFET is $0.02\,\Omega$ ($8\,$mΩ) yielding a total IP baseball FET bank on-state resistance of $1\,$mΩ ($0.4\,$mΩ), with a corresponding value of $2\,$mΩ ($0.8\,$mΩ) for the IP bias FET bank.

A $30\,$cm long water-cooled piece of stainless steel pipe (R_{pipe} in Fig. 4.20) is used as a series resistor in order to lower the power dissipated in the MOSFET banks. A $10\,$kΩ resistor was placed across the common gate-source of each MOSFET bank, ensuring automatic shut-down if their connection to the current controlling circuit was broken. Thick ($> 1\,$cm^2 cross-sectional area) copper cable was used for any non water-cooled electrical connections. Due to the low resistance of the circuit care must be taken to ensure contact resistances are small.

The water used in the FET banks and coils was provided through lengths of 6 mm diameter nylon hose. Initial problems with insufficient flow rate were rectified by connecting a high conductance dis-
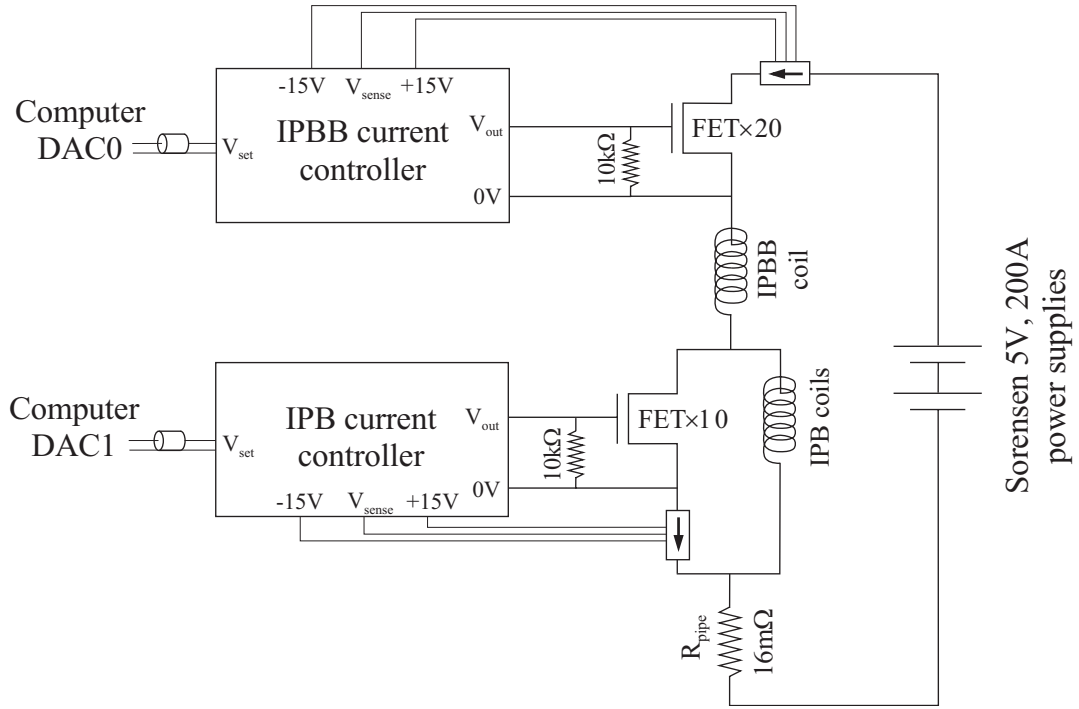
Figure 4.20: The Ioffe-Pritchard baseball (IPBB) and bias (IPB) coil control circuit.

tribution pipe directly to the lab's main water supply. The water pressure is now $40\,\text{PSI}$ and does not alter significantly when flow is initiated. The omission of a booster pump for raising the water pressure helps prevent mechanical vibration in the system. The flow rate in the baseball coil was $260\,\text{mL/min}$, and in the bias coils (which were water-cooled in parallel) it was $780\,\text{mL/min}$. Given the specific heat of water, $4.2\,\text{J/g/K}$ and the resistances of the coils, the temperature change across the baseball (bias) coils at $216\,\text{A}$ is calculated to be $\Delta T = 38^\circ\,C\ (8^\circ\,C)$, which agrees well with experiment. The flow rate in the MOSFET banks is $880\,\text{mL/min}$, however in this case the contact length of the cooling pipe with the heat source is much shorter, and heat is not extracted as efficiently. The relatively high temperature rise in the baseball coil did not seem to increase the outgassing of the quartz MOT chamber, although this could be an issue if there were good thermal contact between the coils and the cell [173].

The simple circuit used to control the MOSFET banks which regulate currents in the IP baseball and bias coils is shown in Appendix D. The design is similar to the coil-driver used for the x, y, z and LP MOT coils (Fig. D.6). The most significant difference is that the two DAC outputs (Fig. 4.27) which are used to set the IP baseball and bias currents must first be passed through a differential amplifier, otherwise the AC noise on the DAC outputs became much higher than in the specifications $(< 200\,\mu\text{V})$. Each coil controller had a separate $\pm 15\,\text{V}$ low-noise floating power supply, to allow two stable 'zeroes' in the coil circuit. The controllers could alter coil currents in $<\ 1\,\text{ms}$ and the ratio of rms AC current noise (sensor reading: $<\ 400\,\mu\text{V}$ rms) to DC current (sensor reading: 7.3 V) was better than 5×10^{-5}.
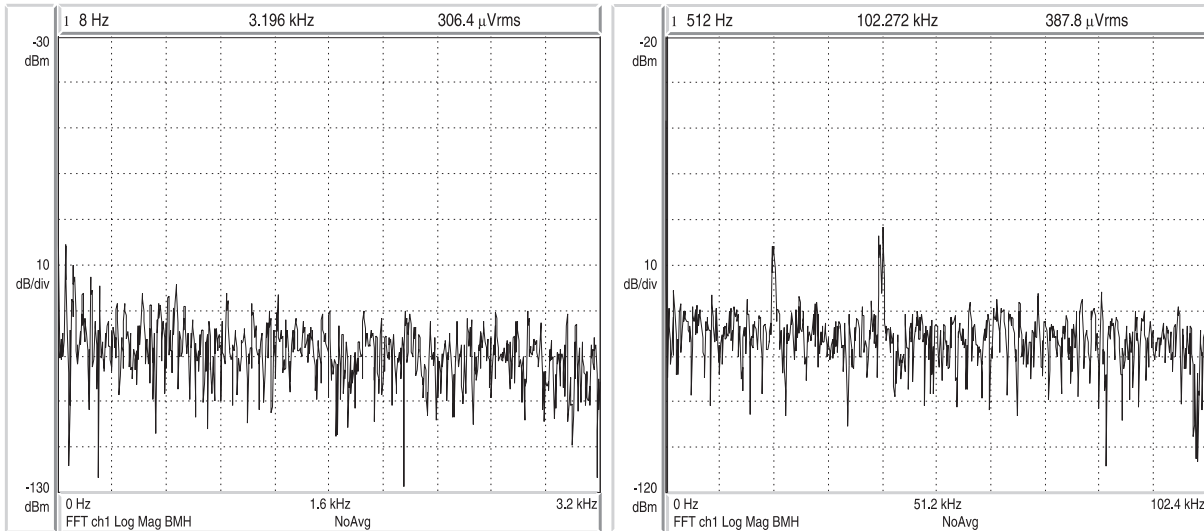
Figure 4.21: The power spectrum of the Ioffe-Pritchard series current noise. The spectrum up to frequencies of 20 kHz is essentially flat, indicating good suppression of the line noise seen in Fig. 4.19. The two spikes indicate harmonics of the *Sorensen* switching supply's operating frequency. Current noise levels approach the background level of the spectrum analyser. Measurements with a 1 MHz bandwidth HP34401A multimeter (calibrated for sub-mV AC operation) confirm the current sensor's 5×10^{-5} upper limit on relative rms current noise.

The power spectrum of the current noise is shown in Fig. 4.21.

Given the output voltage of the DAC controlling the IP baseball MOSFET bank, V_{DAC}, the response of the total current was measured to be $I_{tot} = (29.9 V_{DAC} - 1.75)$ A. The maximum setting the coils were operated at was $V_{DAC} = 7.3$, yielding a total series current of $I_{tot} = 216$ A. The *Sorensen* power supplies were capable of generating higher currents, however when the drain-source voltage across the IP baseball FET bank dropped considerably below 2 V it became difficult to maintain current stability.

The power supply and control circuit discussed above have decreased current noise to levels 20 times lower than those of Ref. [173], with particular improvement at 100 Hz levels where unwanted parametric heating [70] of the magnetic trap can occur. Our coils have fewer windings than those of Ref. [173], however they would still yield a comparable magnetic field if the dimensions were scaled down slightly. Magnetic field curvature, an important characteristic of an IP trap, scales with the inverse cube of dimension and so the inner coil windings are the most important. A decrease in R_{pipe} would lead to a higher maximum current and if the windings of the baseball coil were electrically connected in series, but cooled in parallel [173], they could be cooled much more efficiently although at the expense of simplicity.

4.2.4 Operation of the Ioffe-Pritchard trap

After the LP MOT has been loaded, the atoms have been cooled in molasses, and the atoms are optically pumped, the magnetic trap is turned on. The MOSFET bank controlling the IP bias coils is left fully open, allowing $> 85\,\%$ of the current to flow through the FET bank rather than the IP bias coils. The IP baseball coil controller is primed by its DAC input for $0.4\,\mathrm{ms}$ at $9.9\,\mathrm{V}$, to allow a rapid turn-on of the IP baseball FET bank (this allows for the finite response time of the current-controlling integrator). The IP baseball DAC voltage is then dropped to $2.6\,\mathrm{V}$, setting the initial coil current to $76\,\mathrm{A}$. At this point the cylindrically symmetric magnetic potential's radial and axial trapping frequencies are approximately $\nu_r = 10\,\mathrm{Hz}$, $\nu_z = 6\,\mathrm{Hz}$.

Mode-matching and slosh prevention

The quadrupole magnetic trap has the useful property that the magnetic fields for the MOT and magnetic trap are provided by the same coils. In the case of the IP magnetic trap however, the MOT and baseball coils are separate. With careful relative positioning of the coils it is possible for the respective centres of the magnetic fields from the two systems to coincide at the level of a millimetre or two. This means the centre of the IP trap could be displaced from the MOT by a few MOT diameters. Loading the harmonic IP trap off centre will apply a restoring force to the atomic cloud, and the atoms will obtain a centre-of-mass 'sloshing' motion with an amplitude equivalent to their initial displacement from the trap centre. This leads to unwanted heating, and loss of phase-space density.

For this reason the MOT is formed whilst the x, y, z bias coils (Sec. 4.1.6) are in their third multiplex state (state 1 is for molasses, state 2 for optical pumping). The position of the MOT can be altered by up to $5\,\mathrm{mm}$, and in this way it can be made to coincide with the centre of the IP magnetic trap. The atoms loaded into the IP trap were observed at various times, from two separate camera angles. These measurements provide information about the trapping frequencies in the IP trap and also allow the minimisation of 'sloshing' effects. The MOT cloud was then moved to the spatial centre of the sloshing oscillation. The oscillation amplitudes along the three orthogonal trapping axes were reduced to below $200\,\mu\mathrm{m}$.

As well as 'sloshing' it is also possible to excite 'breathing' modes in the magnetic trap. This occurs when the initial atomic cloud size does not match the equilibrium cloud size in the magnetic trap $\sigma_{x_i} = \sqrt{k_B T / \kappa_{x_i}}$ where T is the atomic temperature, and κ_{x_i} is the magnetic trap's spring constant along the x_i axis). Breathing usually occurs when there is bad mode-matching (PSD loss due to sudden compression discussed in Sec. 3.2.6), however no significant breathing effects were observed in the experiment.

Compression and release

After loading the atoms into a centred, mode-matched magnetic trap, the atoms are compressed by linearly ramping the IP baseball DAC voltage from 2.6 V, to 7.3 V over the space of 2 s. While this occurs the DAC controlling the IP bias coils is ramped from 4 V to -0.5 V, at which time the IP baseball and bias coils are completely in series and carry a current of 216 A. The radial and axial trap frequencies are then $\nu_r = 223$ Hz and $\nu_z = 11$ Hz respectively. Fig. 4.22 demonstrates the speed with which the IP coils are switched on, and the compression ramps for the IP baseball and IP bias coil currents are shown in Fig. 4.23.
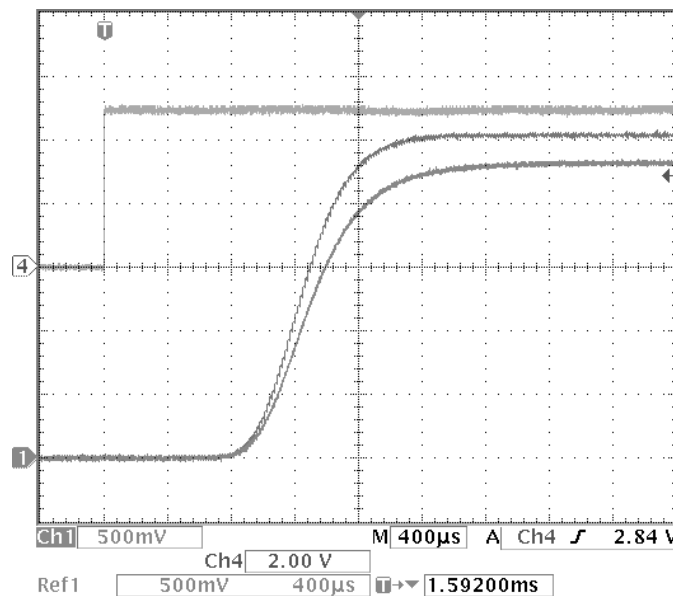

Figure 4.22: The initiation of magnetic trapping. The square edge indicates the start of the DAC pattern which controls the IP baseball and bias coils. The other traces indicate the currents sensed in the IP baseball coil (upper trace) and the MOSFET bank in parallel with the IP bias coils (lower trace). 1 V $\equiv 30$A.

The magnetic trap must be switched on quickly, to ensure that the atomic cloud does not expand significantly during loading as this would increase the potential energy of the atoms and thus heat the trap. It is also important to be able to switch off the magnetic trap quickly on time scales corresponding to the trap frequencies, to prevent involving the atoms in a decompression phase before release.

There are two obvious ways in which to turn off the current in the IP coils. Firstly (case 1), the IP bias FET bank can be left closed and the total current switched using the IP baseball FET bank. One might instead think (case 2), that opening up the IP bias FET bank will cause part of the series current to flow through that channel. This is not the case however, and eddy currents flow around the IP bias coil/IP bias FET bank circuit, *increasing* the current flowing through the IP bias coils relative to the IP baseball coils.
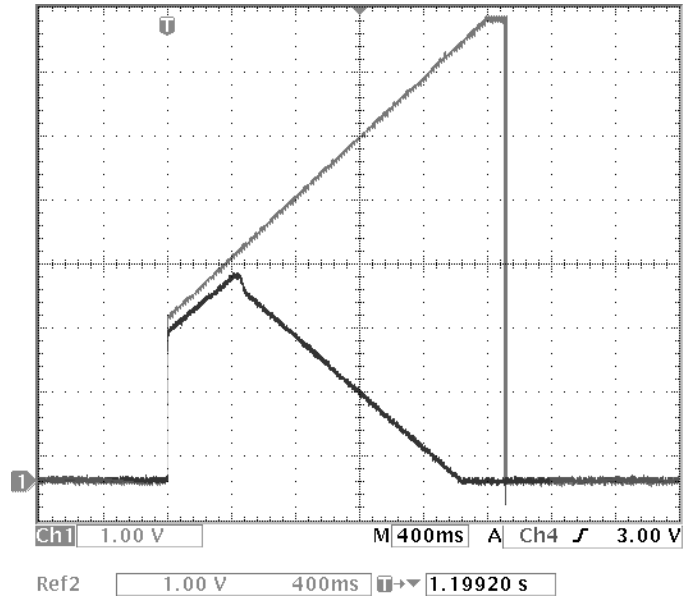
Figure 4.23: The 'adiabatic' compression of the magnetic trap. The rising trace indicates the current in the IP baseball coil, whereas the falling trace represents the fraction of the total current *not* passing through the IP bias coils. After compression the IP baseball and bias coils operate in series.

Unfortunately similar eddy currents driven by back emfs can also occur in case 1, as the MOSFETs used for the IP bias FET bank contain a built-in reverse-biased diode.

A graphical depiction of the switching speed in these two cases is shown in Fig. 4.24. The negative current through the IP bias MOSFET bank is indicative of eddy currents in the IP bias coil/IP bias FET bank circuit. Thus the current in (and therefore magnetic field from) the IP bias coils can be greater than in the IP baseball coil, enabling unwanted Majorana spin flips (Sec. 3.2.3). Spin flips in a rapidly released magnetically trapped cloud may not be evident during expansion, but they quickly become apparent when one uses the Stern-Gerlach force to 'bounce' these atoms off a magnetic mirror.

When operated in series the IP baseball and bias coils yield a remnant axial bias magnetic field of $B_0 \approx 11$G (Sec. 4.2.5), and it is necessary to lower this value in order to get tight magnetic confinement for efficient evaporative cooling . A shim resistor in parallel with the IP baseball or bias coils (cf. [173]) could have been used for trimming the relative size of the IP bias and baseball axial magnetic fields. One of the reasons we chose not to do this was to prevent the formation of eddy currents, which limited the switching times seen in Ref. [173] to > 1 ms. Although eddy currents still occur in our circuit, these could easily be eliminated using a slightly longer ($\approx 300\,\mu$s) turn-off ramp. In practice eddy currents do not appear to cause spin flips if we turn the current off with the IP bias MOSFET bank closed (case 1).
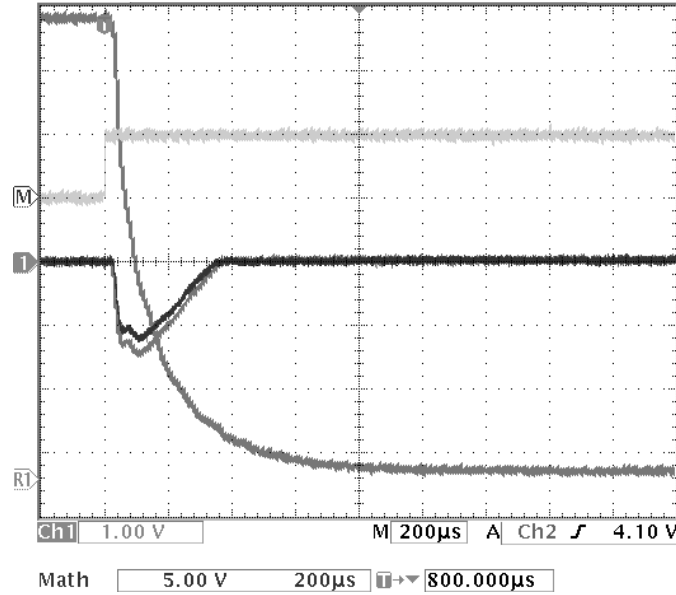
Figure 4.24: The magnetic trap turn-off. The square edge indicates the DAC signal to turn off the trap. The exponential trace is the IP baseball current, and the other traces are the current in the IP bias MOSFET bank. Of these, the black trace shows case 1, and the grey trace shows case 2. The data acquisition required a digital oscilloscope with a floating power supply, and differencing is performed to obtain the trigger pulse in Math mode. This prevents ground loops.

Noise control

The main reason for passing current, from the same power supply, through the IP baseball and bias coils in series is that in this situation the majority of magnetic noise in the opposing axial fields cancel [43, 173]. If the total series current is $I_{tot}(t) = \overline{I}(1 + n(t))$ (where $n(t)$ is a fluctuating noise term) and the corresponding bias fields of the IP baseball and IP bias coils are $B_{baseball}$ and B_{bias}, then the axial magnetic field constant term has the form: $B_0 = (B_{baseball} - B_{bias})(1 + n(t))$. Thus the noise level decreases in proportion to the net bias field. This is the other reason we chose not to use a shim resistor in parallel with the IP baseball or bias coils: in this case the high frequency noise passes through the resistive load, and low frequency noise passes through the inductive load, limiting the circuit's series noise cancellation properties at high frequencies.

4.2.5   Extra bias coils

The disadvantage of our coil configuration (without a parallel shim resistor) was that it did not allow major alterations in the net axial bias field without changes in the trap's strength. Ideally the axial bias field in the fully compressed IP trap would be around $B_0 = 1 - 2\,\mathrm{G}$, however due to geometrical limitations our system had a bias field of $B_0 = 11.4\,\mathrm{G}$ (measured during RF evaporative cooling (Sec. 4.3)). This

limited the noise reduction from series IP coil operation to a factor of fifteen: certainly helpful, but it could be improved in future.

In order to lower the bias field, B_0, and to allow flexibility in its final value, 'extra' bias coils were made for the IP magnetic trap. Again, the main coil design criteria were simplicity, fast switching speed, and low power consumption. Each 12 turn coil was $20\,\mathrm{cm} \times 20\,\mathrm{cm}$ and the coils were separated by $6.5\,\mathrm{cm}$. The IP extra bias coils were made from 13 A wire, and had a series inductance of $180\,\mu\mathrm{H}$, with resistance $0.45\,\Omega$. A current of $8.4\,\mathrm{A}$ created the typical operating field of $10\,\mathrm{G}$, with a curvature of $-0.13\,\mathrm{G/cm}^2$. The switching time of the IP extra bias coils was considerably shorter than that of the IP baseball and bias coils, to help prevent spin flips in the atomic cloud during release.

The IP extra bias coils would ideally have been independently controlled with one of the computer's DAC outputs (Fig. 4.27), and the coil controller shown in Fig. D.7. However, the two available DAC outputs are used to control the IP bias and baseball coils. An inverting amplifier with offset (IAO, Fig. D.8) was therefore created in order to link control of the IP bias and extra bias coils to the same DAC output. A linearly increasing ramp of V_{DAC} led to linear current increases in both the IP bias and extra bias coils. Adjusting the gain and offset of the IAO allowed control of the IP trap's axial bias field, B_0.

Because the current through the IP bias FET banks was limited to zero with control voltages $V_{DAC} < 0\,\mathrm{V}$, the IAO could be used in conjunction with negative final IP bias V_{DAC} voltages to create variable IP extra bias currents during the IP compression stage. This allowed the removal of long term (week to week) fluctuations ($\Delta B_0 \approx 10\,\mathrm{mG}$) in the axial bias field of the magnetic trap.

4.2.6 Bounce coils

One additional pair of coils were used in our Bose-Einstein condensation experiments: Helmholtz 'bounce' coils. These were employed during the bouncing experiments to shift the centre of the IP magnetic trap. This provided control over the radius of curvature of the bouncing 'mirror.' They modify the y magnetic field component of an IP magnetic trap (Eq. 3.55) to $B_y = B_1 y - \frac{B_2 yz}{2} + B_{bounce}$ where B_{bounce} is a constant vertical magnetic field.

The 9 turn, $8.5\,\mathrm{cm}$ diameter Helmholtz bounce coils are separated by $9\,\mathrm{cm}$, have a series inductance of $15\,\mu\mathrm{H}$ and a resistance of $22\,\mathrm{m}\Omega$. The coils were made of the same copper tubing as the IP baseball and bias coils, however as they are only pulsed on for short duration, they are not water-cooled. The current is controlled by 10 paralleled PHP125NO6T MOSFETs with their drains and sources bolted to separate copper rods – also without water-cooling. Car batteries turned out to be an ideal current source for the coils, and two batteries in series could produce $500\,\mathrm{A}$ currents in the coils for up to $10\,\mathrm{ms}$.

In the 'bouncing' BEC experiment presented in section 5.3 the current in the Helmholtz bounce coils is $80\,\mathrm{A}$, producing a vertical field of $70\,\mathrm{G}$ with vertical curvature $B_{2y} = 9\,\mathrm{G/cm}^2$. As the quadrupole field
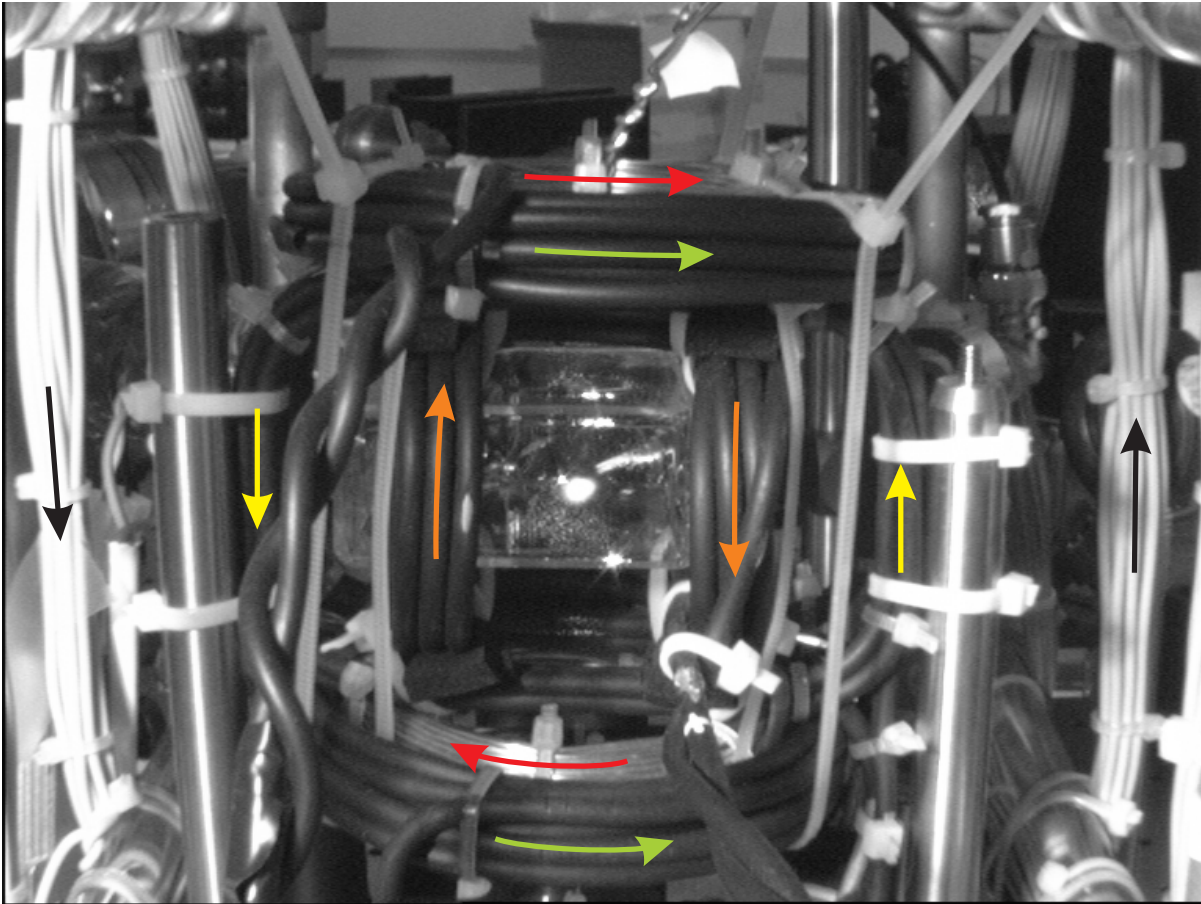
Figure 4.25: The LP MOT cell and magnetic field coils, with arrows indicating the normal direction of coil currents during operation. The view includes the LP MOT quadrupole coils (red arrows), Ioffe-Pritchard baseball (orange), bias (yellow) and 'extra' bias (black) coils, and the Helmholtz 'bounce' (green) coils.

of the IP trap during bouncing is $B_1 = 123\,\text{G/cm}$ (the bias current controller is set to $V_{DAC} = 5.0\,\text{V}$) the centre of the IP field is shifted $\approx 5.7\,\text{mm}$ upwards. The atoms fall $\approx 1.3\,\text{mm}$ before they experience the 'bounce' IP field and so we effectively drop the atoms from a height $h = R/5.4$, where R is the displacement of the atoms from the IP field centre and is equivalent to the 'mirror' radius of curvature in the x direction. A discussion of bouncing dynamics as the h/R ratio is altered is given in Ref. [102].

A $600\,\text{A}$ CSNJ481 *Honeywell* Hall effect sensor monitors the current in the Helmholtz bounce coils, and the circuit which drives the Helmholtz bounce coils is very similar to that of Fig. D.7. The main difference in the circuit is that the Helmholtz bounce coils are driven from a multiplex output, and therefore do not require the input differential amplifier. The other difference is that the resistor leaving the remaining differential amplifier's positive input is connected to an offset voltage ($V_{offset} \approx 1\,\text{V}$), rather than to zero. This ensures that the coils are only switched on by multiplex voltages greater than a volt, preventing accidental ignition. The sensor and double car battery set-up were designed with large currents in mind,

however these are now unnecessary and could be downgraded in line with a $200\,\mathrm{A}$ maximum current in future.

4.3 Evaporative cooling to BEC

After the magnetically trapped cloud of rubidium atoms was compressed, radio frequency (RF) evaporative cooling (Sec. 3.3) was applied to increase the phase space density (PSD) of the atoms past the BEC phase transition.

The two-turn RF coil was $25\,\mathrm{mm}$ in diameter and constructed from $1\,\mathrm{mm}$ diameter copper wire. Only two turns were used to keep the inductance of the RF coil to a minimum and the current was sensed through a $2.2\,\Omega$ resistor in series with the coil. The coil was placed $35\,\mathrm{mm}$ from the centre of the magnetic trap, oriented to induce a magnetic field perpendicular to the trapping axis (to drive $\Delta m_F = \pm 1$ magnetic transitions). The RF was supplied by a Stanford Research Systems (SRS) DS345 $30\,\mathrm{MHz}$ synthesized function generator, through co-axial cable with a sufficiently low ($< 100\,\mathrm{pF}$) capacitance.

The SRS synthesizer has a $50\,\Omega$ output impedance which was the dominant impedance of the coil circuit for frequencies $< 30\,\mathrm{MHz}$. With the synthesizer magnitude set to the typical value of $10\,\mathrm{V}$ peak-peak, $20\,\mathrm{V}$ peak-peak is actually generated as a $50\,\Omega$ termination is expected. The current in the coil is therefore $140\,\mathrm{mA}$ rms which creates a magnetic field of amplitude $B = 11\,\mathrm{mG}$ at the centre of the magnetic trap. The corresponding Rabi frequency at the trap centre is $8\,\mathrm{kHz}$ [212].

The RF frequency ramp used during evaporation was composed of three phases of exponential frequency modulation. In each of the three evaporation phases, the time-dependent RF frequency followed the form [173]:

$$\nu(t) = \nu_{base} + (\nu_{start} - \nu_{base})\exp(-t/\tau_{RF}), \quad 0 < t < \tau_{RF}\,\ln\left(\frac{\nu_{start} - \nu_{base}}{\nu_{stop} - \nu_{base}}\right). \quad (4.3)$$

Each phase of evaporation was optimised by observing the changes in the atomic cloud's collision rate and phase-space density as the evaporation parameters $\nu_{start}, \nu_{stop}, \nu_{base}$ and τ_{RF} were varied. By setting ν_{base} below the base frequency of the magnetic trap, ν_0, it is possible to generate an RF ramp that is 'faster' than an exponential. The evaporation parameters typically used in BEC production are shown in Fig. 4.26. During evaporative cooling the RF frequency is updated every $40\,\mathrm{ms}$. In future a decrease in this step size may be advantageous for the end phase of evaporation, when the collision rate rapidly increases. At present the step size is limited by software considerations.

Initial attempts at evaporation were performed without the additional IP extra bias magnetic field coils described earlier. In this situation the product of collision rate and lifetime was too low to obtain runaway evaporation and so the collision rate was observed to decrease with time. The additional compression of the IP extra bias coils raised the atomic collision rate to a level where evidence for runaway
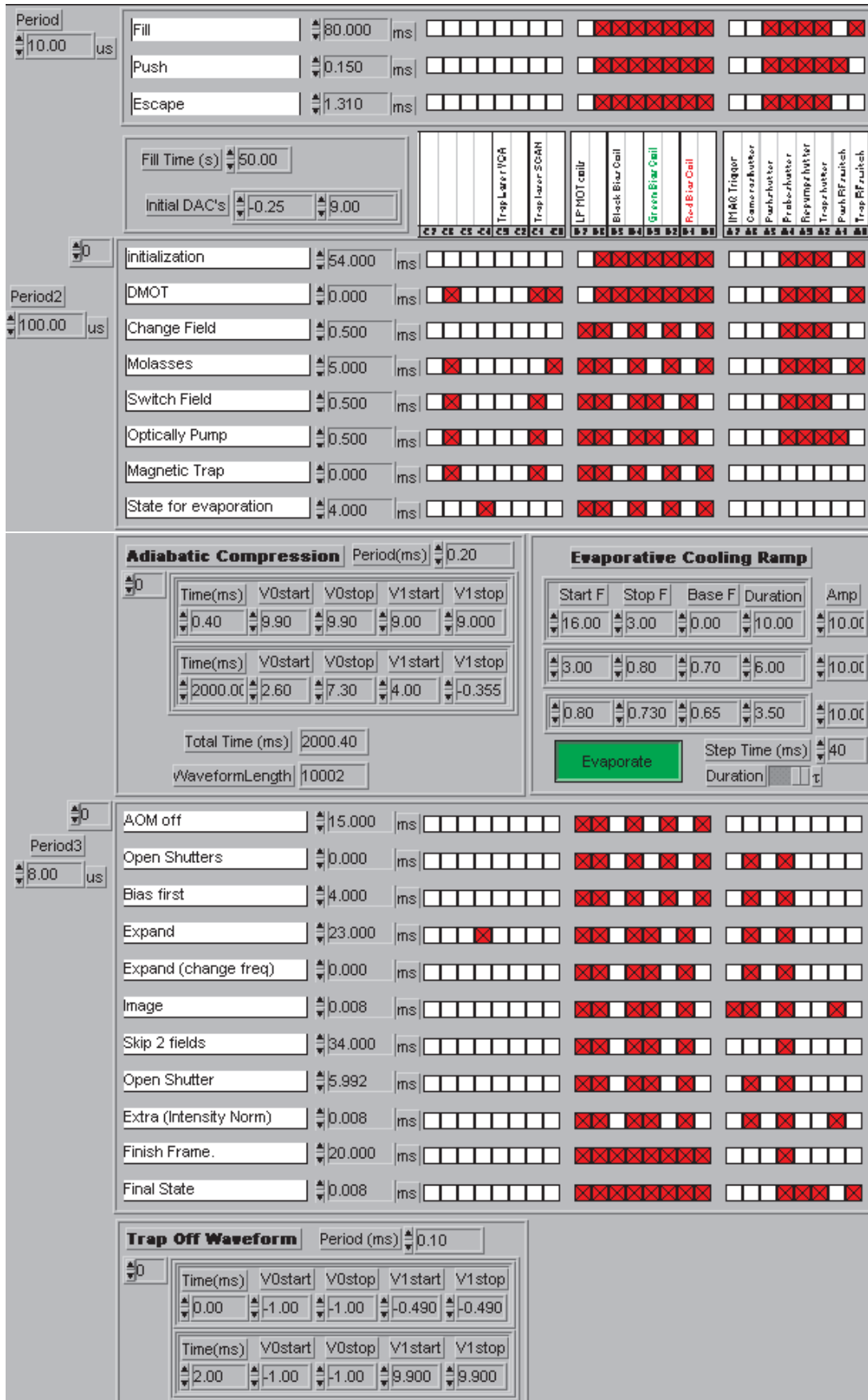
Figure 4.26: The Labview user-interface for the BEC program.

evaporation was obtained. The first Sussex Bose-Einstein condensate was observed on the same evening as the runaway signature.

4.3.1 Computer control and data acquisition

The computer uses four National Instruments (NI) boards to control the experiment, and these boards are controlled by NI's Labview software. Because the CCD camera used for imaging the BEC does not have an external trigger, the computer control program must be synchronised with the camera. To this end a sync separator chip can be used to trigger the PCI-DIO-32HS digital pattern generation board at the beginning of a camera frame (Fig. 4.27).
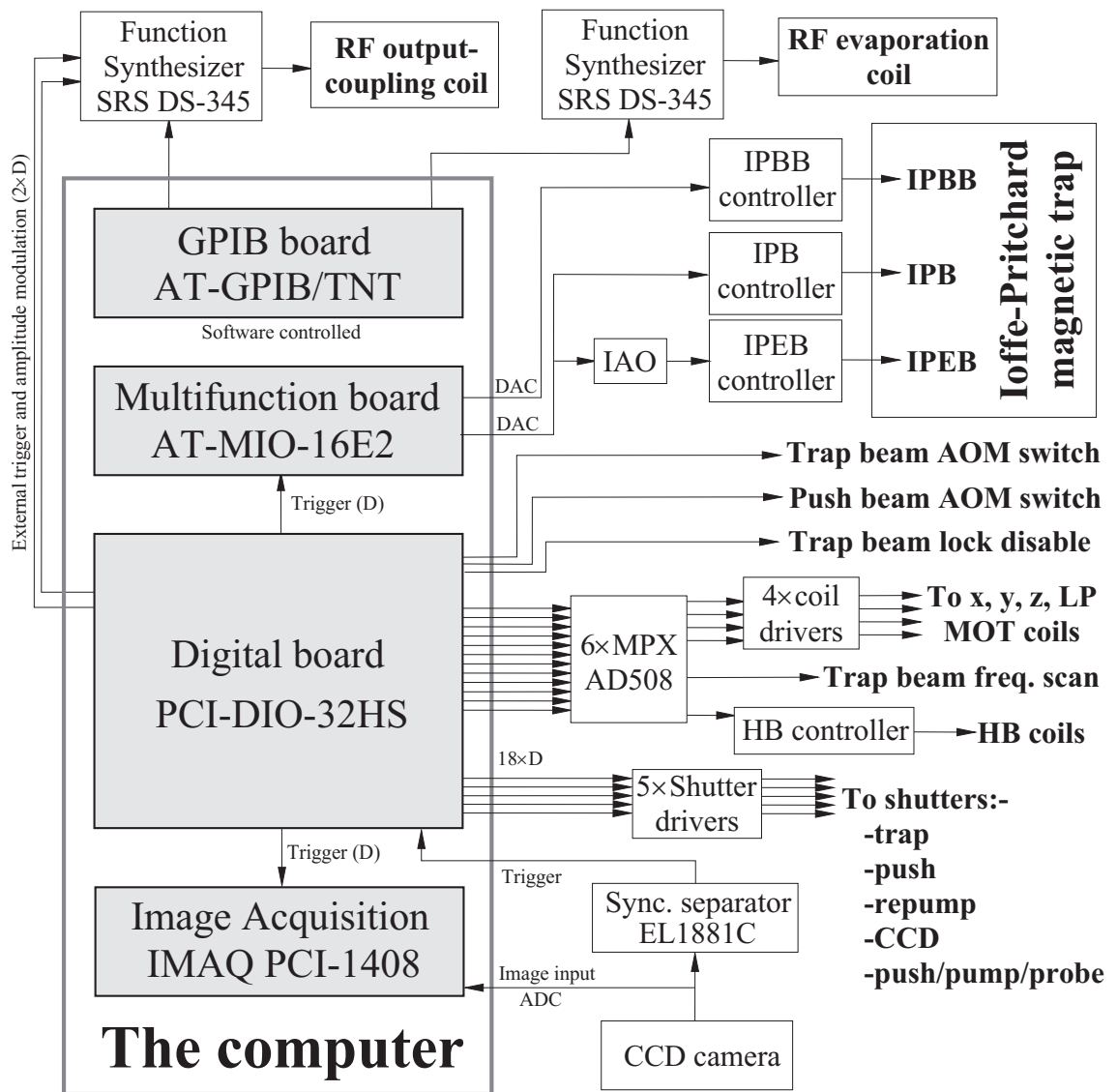
Figure 4.27: The computer control set-up. Abbreviations used: D=digital, DAC=digital to analogue converter, ADC=analogue to digital converter, MPX = multiplex (converts two digital lines into four adjustable analogue outputs), IPBB/IPB/IPEB=Ioffe-Pritchard baseball/bias/'extra' bias coils, HB = Helmholtz 'bounce' coils, IAO=inverting amplifier with offset.

When the experimental sequence is initiated, the digital board implements a time-varying pattern for the board's 20 digital outputs. Some outputs are used to trigger computer boards whilst other outputs control (either directly or through one of the control circuits in Appendix D) various shutters, AOM RF switches, and magnetic field coils. The digital pattern thus performs the multiple loading, optical molasses and optical pumping. As the AOMs and shutters close for magnetic trapping, the digital board sends a trigger to the AT-MIO-16E2 multifunction board. The multifunction board's digital-to-analogue converters (DACs) are used to control the Ioffe-Pritchard magnetic trap coils.

After the magnetic trap has been loaded and compressed, the GPIB board is triggered in software. This initiates RF evaporative cooling by controlling the SRS RF synthesizer. Upon completion of evaporative cooling the computer is synchronised with the CCD camera, and a new digital pattern is implemented. The final digital pattern releases the magnetic trap by sending a second trigger to the multifunction board. The pattern also triggers the IMAQ PCI-1408 board to grab the two consecutive frames from the CCD camera coinciding with the imaging laser pulses. A flow diagram of the way in which the computer interacts with the experimental hardware is shown in Fig. 4.27.

Typical settings for the digital and analogue pattern parameters are shown in Fig. 4.26. The image depicts the Labview program's user-interface.

A second Labview program, 'BECvideo,' was used for displaying the images acquired during an experimental run. The two frames acquired during absorption imaging (subsection 4.1.4) are processed according to Eq. 3.18, and this image is displayed in false-colour. BECvideo's Gaussian least-squares fitting sub-programs determine the optical depth and widths of the cloud: OD, $\sigma_{y'}$, $\sigma_{z'}$. Given the probe laser detuning and release time, this information enables the determination of the number (N), density (n), temperature (T), collision rate (γ), and phase-space density (PSD) of the magnetically trapped atoms (Sec. 3.1.7).
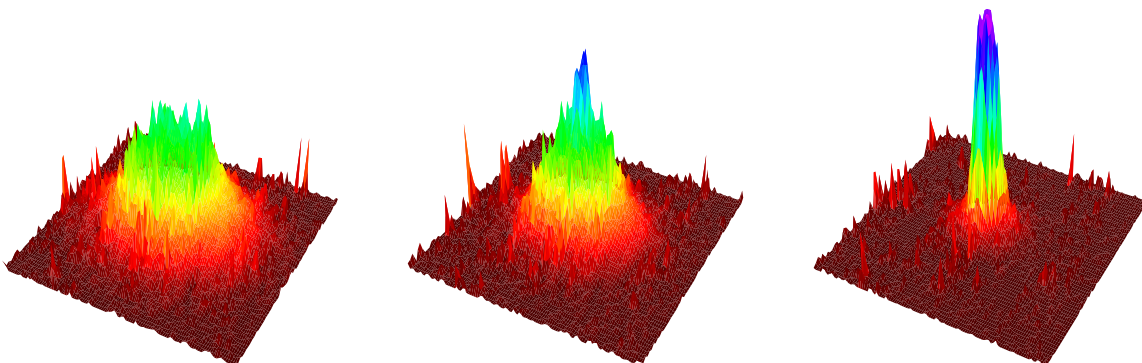

Figure 4.28: The formation of the Sussex Bose-Einstein condensate as the final RF frequency is lowered during evaporative cooling. Final RF frequencies are (left to right) $750\,\mathrm{kHz}$, $735\,\mathrm{kHz}$ and $720\,\mathrm{kHz}$.

Typical values of the atomic parameters obtained at various stages during the production of the Sussex Bose-Einstein condensate are shown in Table 4.1, and graphically in Fig. 1.1. The corresponding false colour images are depicted in Fig. 1.2 – the experimental data was taken shortly after the first production of Bose-Einstein condensation in the UK.

	N ($\times 10^8$)	$\langle n \rangle$ ($\times 10^{10}$ cm^3)	T (μK)	γ (Hz)	PSD
Rb sidearm vapour	N/A	0.3	293×10^6	500	4×10^{-18}
LP MOT	6	1.3	300	3	5×10^{-8}
Optical Molasses	5	0.44	40	0.4	3×10^{-7}
'Mode-matched' IP trap	3	0.44	45	0.4	2.5×10^{-7}
Compressed IP trap	2	7	550	20	5×10^{-8}
Evaporation phase 1	0.14	16	43	14	1×10^{-5}
Evaporation phase 2	0.016	364	1.3	53	5×10^{-2}

Table 4.1: Typical atomic parameters during the production of the Sussex BEC. Note the decrease in PSD during the 'adiabatic' magnetic trap compression. The efficiency of this process could be improved in future.

Chapter 5

Manipulating the BEC

The preceding chapters (3 and 4) have dealt with the theoretical and experimental techniques which were used to realise the Sussex Bose-Einstein condensate. In this chapter various experiments which were subsequently performed on the condensate will be discussed.

The first two experiments were undertaken in order to compare the behaviour of the Sussex condensate with other BECs and with theory. In one experiment the ballistic expansion of the BEC will be compared with a theoretical model discussed in the earlier chapter on the theory of Bose-Einstein condensation (Sec. 2.2.2). The other experiment determines the fraction of atoms in the condensate fraction as a function of the thermal atomic temperature. This experiment will also be compared with a theoretical model described earlier (Sec. 2.1).

In the final experiment, novel magnetic manipulation of the BEC will be performed in the form of magnetic 'bouncing.' A brief discussion of the spatial and temporal form of the magnetic potential will precede the experimental data. The data will then be compared with two simple theoretical models (Sec. 2.2.2). The dynamics of the bouncing atoms are demonstrated to be radically altered when the spatial curvature of the magnetic 'mirror' is varied.

5.1 Ballistic expansion of the BEC

5.1.1 Data processing

A variety of models have been used by different groups to model the condensate and non-condensate fractions of cold atomic clouds. This will be discussed in more detail in section 5.2, however the three density distributions used in BEC data analysis will be summarised here:

- the Gaussian distribution (Eq. 3.19)

$$n_G(\mathbf{r}) = \frac{N}{(2\pi)^{3/2}\sigma_x\sigma_y\sigma_z} \exp\left[-\left(\frac{x^2}{2\sigma_x{}^2} + \frac{y^2}{2\sigma_y{}^2} + \frac{z^2}{2\sigma_z{}^2}\right)\right]$$

- the 'Bose' distribution

$n_B(\mathbf{r}) = \frac{N}{\zeta(3)(2\pi)^{3/2}\sigma_x\sigma_y\sigma_z} \exp\left[g_{3/2}\left(-(\frac{x^2}{2\sigma_x{}^2} + \frac{y^2}{2\sigma_y{}^2} + \frac{z^2}{2\sigma_z{}^2})\right)\right]$

where g_n is the polylogarithm function of Sec. 2.1

- the Thomas-Fermi distribution (Eq. 2.24)

$n_{TF}(\mathbf{r}) = \frac{15N}{8\pi x_{max}y_{max}z_{max}} \max\left(1 - \frac{x^2}{x_{max}{}^2} - \frac{y^2}{y_{max}{}^2} - \frac{z^2}{z_{max}{}^2}, 0\right).$

The density distribution obtained from absorption imaging is integrated along the line of sight of the probe laser beam. By using the co-ordinate transformation into the $x'y'z'$ (imaging) frame (Eq. 3.21), and integrating along the absorption imaging beam axis (x'), one obtains the equivalent 'two-dimensional' density for each of these distributions:

$$n_{G2}(y', z') = \frac{N}{2\pi\sigma_{y'}\sigma_{z'}} \exp\left[-(\frac{y'^2}{2\sigma_{y'}{}^2} + \frac{z'^2}{2\sigma_{z'}{}^2})\right], \tag{5.1}$$

$$n_{B2}(y', z') = \frac{N}{\zeta(3)2\pi\sigma_{y'}\sigma_{z'}} \exp\left[g_2\left(-(\frac{y'^2}{2\sigma_{y'}{}^2} + \frac{z'^2}{2\sigma_{z'}{}^2})\right)\right], \tag{5.2}$$

$$n_{TF2}(y', z') = \frac{5N}{2\pi y'_{max}z'_{max}} \max\left(1 - \frac{y'^2}{y'_{max}{}^2} - \frac{z'^2}{z'_{max}{}^2}, 0\right)^{3/2}, \tag{5.3}$$

where the width parameters $\sigma_{y'}$ and $\sigma_{z'}$ are given in Eq. 3.22. The width parameters for the 2D Thomas-Fermi density have the same angular dependence as Eq. 3.22, i.e.

$$y'_{max} = y_{max}, \qquad z'_{max} = \sqrt{z_{max}{}^2\cos^2\theta + x_{max}{}^2\sin^2\theta}. \tag{5.4}$$

In the Sussex BEC experiment the viewing angle of the camera is $\theta = 30°$ because the probe laser optical access to the vacuum cell is constrained by the IP magnetic trap coils. In order to obtain a viewing angle along one of the magnetic trap axes it would be necessary to directly overlay the probe laser beam with the MOT laser beams. This could be done in future by placing polarising beamsplitters in front of the MOT quarter-wave plates – thus allowing light to be coupled into the MOT beam path, then coupled out again after passing through the vacuum cell.

5.1.2 The expansion data

Fig. 5.1 depicts the ballistic expansion of the BEC at 2 ms intervals. Note the anisotropic nature of the cloud expansion, a signature that this is a BEC and not a thermal atomic cloud. Anisotropic expansion also occurs for thermal atoms in the hydrodynamic regime, however the time dependence differs [70]. The three forms of 2D density distribution – Gaussian, Bose and Thomas-Fermi (Eqs. 5.1, 5.2, 5.3) – were fit to $\approx 260\,\mu$m $\times$ 260 μm regions of the experimental data, centred on the atomic cloud. Each fit had five free parameters: the optical depth of the cloud, two width parameters, and the co-ordinates of the cloud centre. Only single images were taken of the BEC's temporal flight – no averaging was used. The
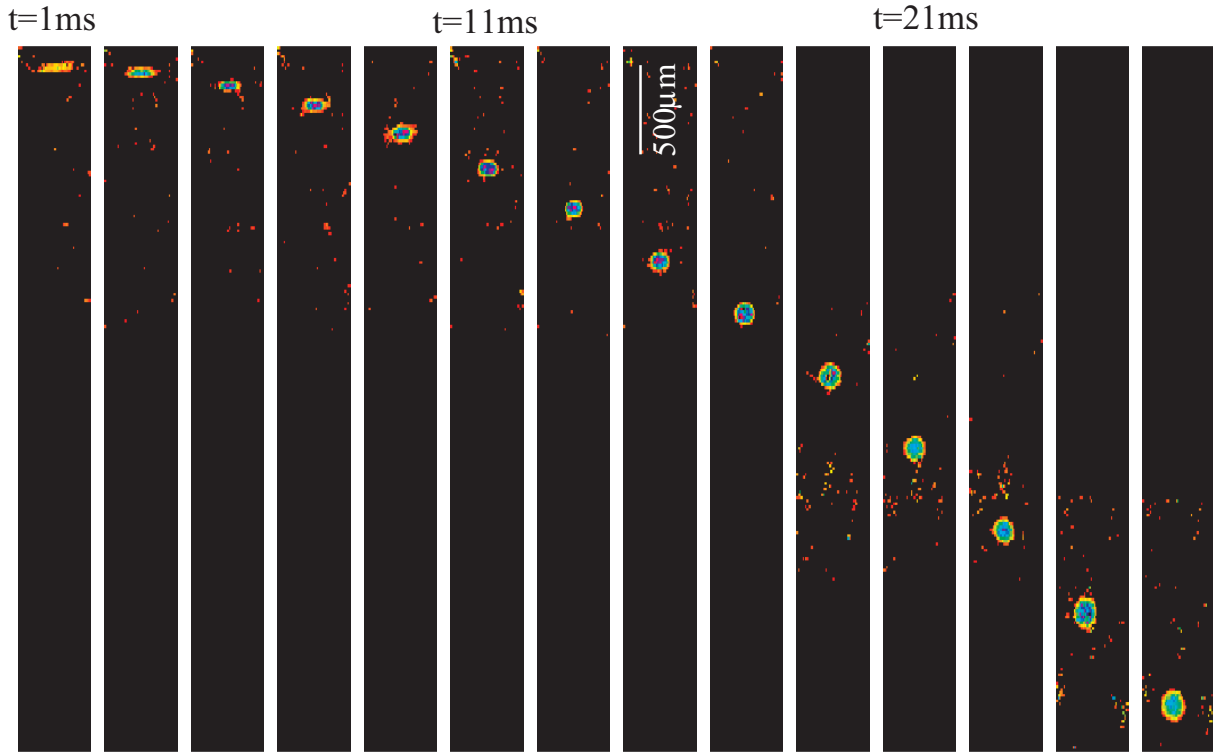
Figure 5.1: The parabolic trajectory of a BEC ballistically expanding under gravity. Each image is 4.5mm long, and a selection of the experimental data is shown here for times $t = 1, 3, 5, ..., 27$ ms after the BEC is released from the IP magnetic trap. The centre-of-mass motion of the falling BEC is used to calibrate the CCD camera magnification.

degree to which each fit agreed with the experimental data is discussed in Fig. 5.2. All further analysis in this section will be carried out using the Thomas-Fermi model.

Using the Thomas-Fermi fits to the data and assuming cylindrical symmetry, the axial ($z_{max} = \frac{\sqrt{z'_{max}{}^2 - y'_{max}{}^2 \sin^2 \theta}}{\cos \theta}$) and radial ($r_{max} = y'_{max}$) width parameters of the BEC can be determined as a function of expansion time. In Fig. 5.3 the fitted width parameters are contrasted with the theoretical evolution of the width parameters predicted by the Thomas-Fermi model (Eq. 2.36) namely

$$z_{max}(t) = z_{max}(0)\lambda_z(t), \qquad r_{max}(t) = r_{max}(0)\lambda_r(t).$$

The theoretical model assumes a condensate containing $N = 1.8 \; 10^5$ atoms is released from a magnetic trap with axial and radial frequencies $\nu_z = 11$ Hz and $\nu_r = 223$ Hz respectively.

The agreement between the theoretical and experimental BEC ballistic expansion is quite good, but only for expansion times $t > 10$ ms as the density of the atomic cloud is then low enough to allow quantitative determination of cloud width and optical depth parameters. Improvements to the imaging system would be necessary in order to obtain reliable data below this time limit. It is perhaps worth noting that experimental data points for times below $t < 10$ ms are omitted in the BEC ballistic expansion of
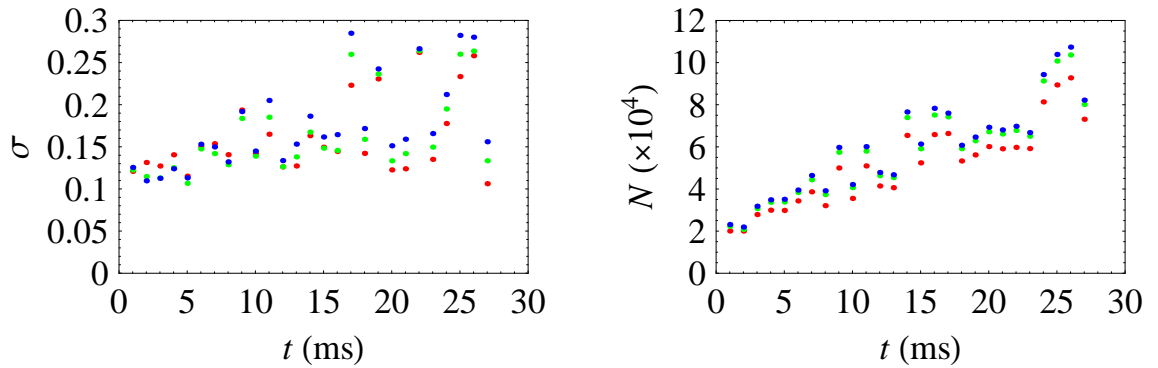
Figure 5.2: Analysis of the various fits to the BEC's ballistic expansion. The left image depicts the standard deviation of the fit to the data for the Gaussian (green), Bose (blue) and Thomas-Fermi (red) distributions. For comparison the typical 'height' of each 2D distribution is $OD_{max} \approx 2$. The three functions fit the data almost equally well, although the Thomas-Fermi model fits the best at large expansion times (when imaging errors are reduced). Further discussion of the applicability of various fits will be given in the next section. The right image represents the total number of atoms, derived from the fit, as a function of drop time. The number of atoms should stay constant – the departure may be an artifact of the imaging system (Sec. 3.1.7).
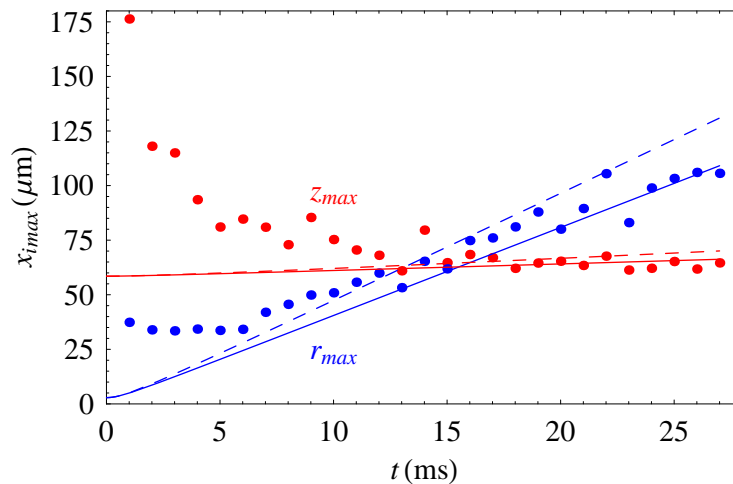

Figure 5.3: Time evolution of the BEC width parameters during ballistic expansion. Comparison of fitted experimental data (dots) and Thomas-Fermi theory (solid lines). Discrepancies arise at short time intervals when the BEC cloud is extremely dense, probably due to the limitations of the imaging system discussed in Sec. 3.1.7. The predicted time-evolution of the atomic cloud widths for a thermal distribution in the hydrodynamic regime [70] are also shown (dashed lines).

Ref. [70].

For more convincing evidence of the distinction in our BEC experiment between the Thomas-Fermi BEC and thermal hydrodynamic expansions, further data should be acquired (enabling the use of averaging) with an improved imaging system. Our (low magnification) imaging set-up does have one advantage over Ref. [70] in that the higher on-camera intensities lead to very short exposure times ($8\,\mu$s cf. $100\,\mu$s[70]). The width data therefore only requires processing at the $1\,\mu$m level to account for the blurring of the image as the atoms fall under gravity.

5.2   Ground state occupation

Several experiments have been performed on the temperature dependence of the relative ground state population in a Bose-Einstein condensate [31, 40, 64, 67]. Here the results of a similar experiment at Sussex are presented, and a summary of the various techniques of each BEC group is given to contrast the different experimental and data analysis schemes. The magnetic trap frequencies used by the different experimental groups can be obtained from Table 1.1.

In all cases the data are compared with theoretical models similar to that of Eq. 2.11. In the theory section (Sec. 2.1) we dealt with the case of a cloud with a constant total number of atoms N and considered the relative ground state occupation N_0/N as a function of the temperature normalised by the critical temperature for the BEC phase transition (i.e. T/T_C). In experimental condensate production the total number of atoms changes during the evaporation process – N is a function of the temperature T. By using a critical temperature T_C that is a function of N and plotting N_0/N versus $T/T_C(N)$ we may obtain experimental curves of the form shown in Fig. 2.1.

The first BEC ground state occupation experiment, at MIT [40], used experimental data obtained from absorption imaging an atomic cloud of $> 5 \; 10^6$ Na atoms after a $40\,$ms ballistic expansion. The imaging system had a $5\,\mu$m resolution. The normal (non-condensed, or 'thermal') fraction $f_{NC} = 1 - N_0/N$ of the atomic distribution was fit using the density distribution arising from a Bose velocity distribution $\propto g_{3/2}(\exp(-mv^2/(2k_BT)))$, where the function $g_{3/2}$ is defined in Sec. 2.1. The BEC fraction $f_{BEC} = N_0/N$ was fit using a 'parabolic' Thomas-Fermi density distribution. The relatively low density of the 'normal' fraction limited reliable temperature determination to condensate fractions $f_{BEC} < 0.5$. Agreement with the approximate temperature dependent ground state occupation (Eq. 2.11) was good, however a temperature fit factor was used.

The second experiment (at JILA) [31] used $> 5 \; 10^3$ ^{87}Rb atoms absorption-imaged with resonant light for $26\,\mu$s, $10\,$ms after they were released from their magnetic trap. The condensate fraction was fit with a 2D Gaussian distribution, and a separate Gaussian fit was made to the 'high-energy tail' of the thermal atomic fraction. The rationale behind this was that the high energy atoms spend most of their time

in the low-density weakly-interacting part of the atomic cloud, away from the centre of the magnetic trap, and can therefore be characterised by an ideal gas Maxwell-Boltzmann distribution. Accurate ground state occupation data could be obtained in this experiment for condensate fractions $f_{BEC} < 0.8$. Their fits yielded excellent agreement with theory, to the extent where finite temperature effects (Fig. 2.1) could be observed. Fits to the data yielded $T_C^{expt} = 0.94(5)T_C$ where the critical temperature in the limit of large atom number is given be Eq. 2.12.

Experiments at Texas [64] used $> 2 \ 10^5 \ ^{87}$Rb atoms absorption-imaged with $+9.5$ MHz detuned light for $50 \, \mu$s, 18ms after they were released from their magnetic trap. The atomic cloud was adiabatically expanded over a period of 2 s prior to its release. The imaging data was fit using the sum of two Gaussian distributions: one broad and symmetric, the other narrow and asymmetric. Results were obtained for $f_{BEC} < 0.4$, with a fitted transition temperature $T_C^{expt} = 0.96(15)T_C$.

The experiment at Yale [67] used $> 3 \ 10^4 \ ^{87}$Rb atoms absorption-imaged with up to four $16 \, \mu$s exposures of resonant light. The atoms were imaged 18 ms after their release from the magnetic trap, which had previously been adiabatically expanded for 0.4 s. The imaging system had a magnification of $M = 7.0 \pm 0.3$, with a measured resolution of $3.9(3) \, \mu$m. Their experimental data was fit using a combination of two Gaussian distributions and contrasted with the theoretical temperature-dependent BEC population predicted in Ref. [213]. Results were obtained for $f_{BEC} < 0.7$.

In our experiment $> 8 \ 10^4 \ ^{87}$Rb atoms were absorption-imaged with resonant light for $8 \, \mu$s, 23.2 ms after they were released directly from the magnetic trap. The imaging system had a magnification of $M = 0.80(1)$ determined from fits to the centre-of-mass motion of a ballistically expanding atomic cloud. A standard video camera was used. Three different types of fit were used for the thermal+condensate atomic cloud: Gaussian+Thomas-Fermi (Eq. 5.1+Eq. 5.3), Bose+Thomas-Fermi (Eq. 5.1+Eq. 5.3) and a bi-modal Gaussian distribution. Each fit had nine parameters – two co-ordinates for the centre of the bi-modal distribution, four cloud widths, two heights, and a constant to allow for the small shot-to-shot variations in the background level of the imaging system. The experimental RF evaporation sequence can be seen in Fig. 4.28 and a comparison of the different fits to the data is shown in Fig. 5.4. The experimental data suggests we can measure condensate fractions $f_{BEC} < 0.7$, and the experimental BEC transition temperature $T_C^{expt} = f_T T_C$ is discussed in Fig. 5.5.

The number of atoms in the condensate N_0 and non-condensate $N - N_0$ fraction of the atomic cloud can be determined from these fits. Using the fitted non-condensed (Gaussian or Bose) distribution and the methods of section 3.1.7, the temperature T of the atomic cloud can be calculated. The total number of atoms N and magnetic trap frequencies can then be used to determine the critical temperature T_C. Fig. 5.5 depicts how the ground state occupation N_0/N varies with the normalised temperature T/T_C in the Sussex experiment.

The results show that averaging several absorption images improves the signal-to-noise (the fits are
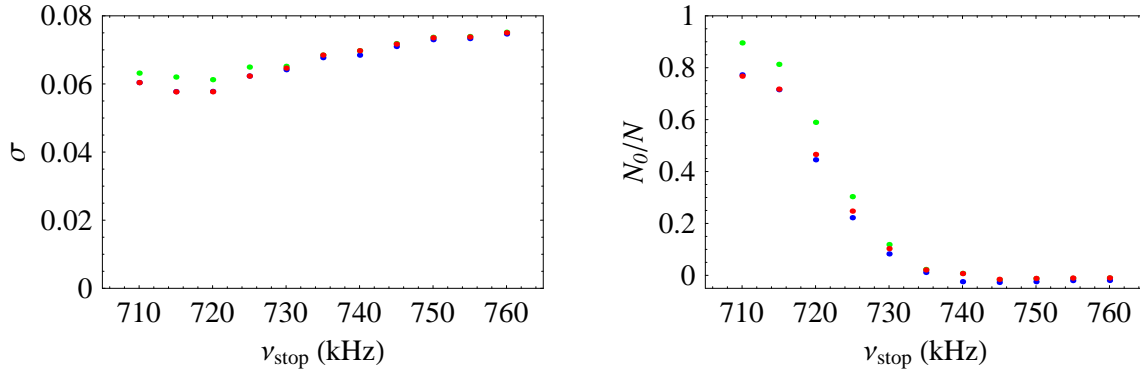
Figure 5.4: Fit standard deviation (left) and relative ground state occupation (right) for various fit distributions as a function of the final RF evaporation frequency, ν_{stop} (Eq. 4.3). Fits to the atomic thermal+BEC distribution were made using Gaussian+Thomas-Fermi (red), Bose+Thomas-Fermi (blue) and double-Gaussian (green) models. These bi-modal distributions were fit to the average of five $\approx 940\,\mu$m $\times$ $940\,\mu$m experimental absorption images (4 images for $\nu_{stop} = 710\,$kHz), neglecting points of 'infinite' optical density (OD) and those with OD < -0.3. Note the lower standard deviation compared to the un-averaged data of Fig. 5.2. Again the *type* of distribution in the fit made little difference to the fit residue, however the Gaussian+Thomas-Fermi and Bose+Thomas-Fermi distributions gave a consistently better fit.
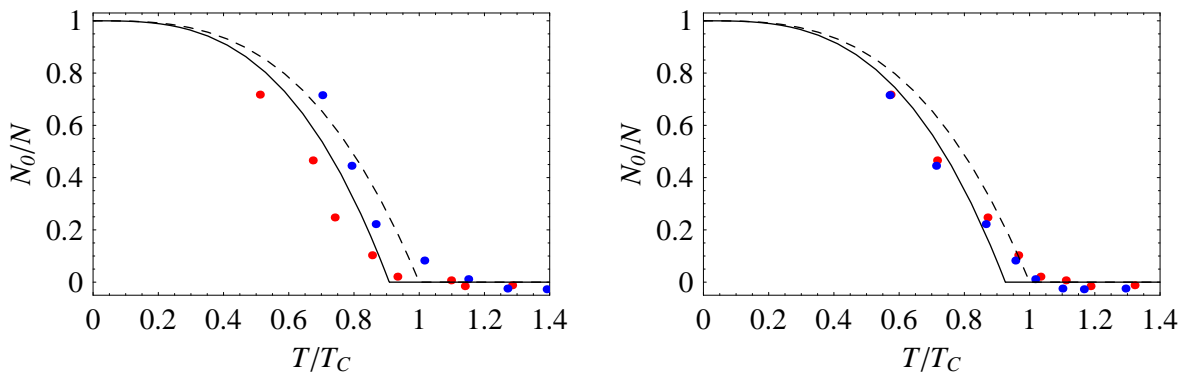

Figure 5.5: The temperature dependence of the BEC ground state occupation. The left image uses nine parameter bi-modal Gaussian+Thomas-Fermi (red) and Bose+Thomas-Fermi (blue) distributions fit to the experimental data enabling determination of both N_0/N and the temperature T/T_C. The right graph employs the atom numbers N and N_0 of the left figure, thus determining $T_C(N)$, however (cf. Ref. [31]) a Gaussian distribution is fit to the wings of the distribution (the central $\approx 250\,\mu$m $\times$ $250\,\mu$m section of each absorption image is omitted) in order to determine the temperature T. The experimental data is fit (bold curves) by a model based on Eq. 2.11 (dashed curves) i.e. $N_0/N = 1 - (T/(f_T T_C))^3$ where f is the fraction of the large-N critical temperature (Eq. 2.12) at which the phase transition occurs. The left image has $f_T = 0.91$ and the fit on the right yields $f_T = 0.93$. These values can be compared with those of Fig. 2.1.

not yet limited by systematics). Because the production time of a Sussex BEC is presently around two minutes from start to finish, averaging over several data points can become rather a long task. This could be improved by increasing the signal-to-noise of the camera using a cooled CCD camera, but at some expense (such cameras typically cost 100 times the price of the standard video camera used at Sussex). Employing an imaging system with greater magnification would also yield tighter measurements on the widths of the cloud, and it would be interesting to see closer comparisons with the theoretical predictions of Ref. [122] and [213].

In summary, fair agreement has been seen between the Sussex experiment and theoretical predictions of BEC evolution in both this and the preceding section, providing a useful benchmark with other experiments. Both the ballistic expansion and ground state population experiments would benefit by improvements to our imaging system and the size of the condensate however.

5.3 The 'bouncing' experiment

In the preceding sections experiments were performed to contrast the Sussex BEC with other BECs and with theory. In this section novel experiments are performed: a BEC is 'bounced' off a soft magnetic mirror. The history of the experimental 'bouncing' and focusing of atoms is briefly reviewed, followed by a description of the magnetic mirror and the bouncing experiments.

Several methods by which atoms can be manipulated were discussed in chapter 1 and are reviewed in Ref. [102]. Here we will mainly consider the particular atom-optical properties of reflection and focusing. Atoms can be focused by quantum reflection due to atom-atom interactions [100, 101], however the most commonly implemented tools with which to manipulate cold atoms are those which exploit the magnetic and dipole forces. The advent of laser cooling (and in particular the MOT) provided an ideal atomic source with which to study reflection, focusing and other forms of atom optics, using relatively simple experimental set-ups.

The first evidence of the reflection of cold (laser cooled) atoms off a mirror was observed with the evanescent wave mirror of Kasevich *et al.* [110] in 1990, not long after the realisation of the MOT in 1987. Mirrors and other atom-optical elements that employ the dipole force have the advantage that their potential can be quickly altered by changing the intensity or detuning of the laser beams used. A laser beam can also be spatially rastered using an AOM, and this technique was used to form a (time-averaged) dipole sheet with which a BEC has been reflected [112]. The disadvantage of the dipole force is that high intensity, far detuned light must be used in order to provide strong forces with minimal scattering of photons. As experiments are carried out in vacuum, the propagation direction of the laser beam may also fluctuate due to changes in the optical properties of the viewports.

Cold atoms may also be reflected due to magnetic interactions. The first magnetic mirror for cold

atoms was demonstrated by Roach *et al.* in 1995 [113]. Flat and curved mirrors have been created at Sussex using a variety of periodically magnetised magnetic recording media [113, 214, 215, 115, 102]. Such mirrors have a level of flatness equivalent to that of mirrors relying on the optical dipole force. Reflection of atoms off an array of permanent magnets was demonstrated by Sidorov *et al.* [216], and also micro-fabricated nickel mirrors [217].

So far only 'spatial' mirrors have been discussed – i.e. mirrors for which the potential is always 'on.' It is also possible to produce 'temporal' mirrors by pulsing on light or magnetic forces for limited periods of time. Whilst spatial interference effects can only be observed from spatial mirrors, temporal mirrors can readily be used for altering the temperature and density of atomic samples. Based on a similar principle [114] to the permanent magnetic mirrors, magnetic reflection of atoms from a current-carrying serpentine wire pattern has recently been demonstrated with laser-cooled atoms [218].

All of the magnetic atom-optical elements discussed so far have a magnetic field with a short spatial periodicity ($\lambda \approx 10 - 100\,\mu\text{m}$). As the magnitude of the field, and hence the magnetic potential, decay exponentially away from the field-generating surface on a length scale equivalent to this period, the interaction region of the atoms with the magnetic mirror is small. This is advantageous for producing a relatively 'hard' potential for reflection, where the atomic interaction distance with the magnetic field is much shorter than the distance the atoms drop before reaching the mirror. The disadvantage of such magnetic mirrors is that they must necessarily be placed inside a high vacuum system. While outgassing from the mirror can be reduced to a level that does not perturb MOT operation, this might cause difficulties in obtaining the much lower pressures required for BEC production.

The possibility of using a serpentine wire pattern, or simply two wires carrying opposite currents, with a sufficiently large period ($> 2\,\text{mm}$) to be placed near a viewport of the vacuum chamber was considered. Problems were calculated to arise if this 'soft' magnetic potential was used to manipulate BECs however, due to the potential's large spatial curvature. This curvature would cause the small and relatively dense BEC clouds to rapidly expand after bouncing and quickly become undetectable.

The idea then arose to employ the IP magnetic field used for magnetic trapping as a magnetic potential with which to reflect and focus the BEC. The IP field has the advantage that its curvature always causes focusing rather than defocusing of the atomic cloud. A one-dimensional magnetic lens has recently been demonstrated with cold atoms [219]. Their magnetic field is generated by a pair of 'Helmholtz' coils. The second order magnetic field magnitude at the centre of these coils can produce either radial or axial focusing of atomic clouds (but not both). Three dimensional atomic cloud focusing was employed earlier, in 1991, by Cornell *et al.* [181, 127] as a means of efficiently loading an AC magnetic trap.

Here we demonstrate one-dimensional focusing of a BEC using a magnetic potential that can be readily adapted to enable three-dimensional focusing. The viewing angle for absorption imaging makes

the main observations indirect, however clear agreement with theoretical models is shown, and future experiments with different viewing angles could provide important information regarding the creation of strong atomic focusing (for atom lithography) and the production of extremely cold, low density collimated atomic beams (which would, for example, increase the accuracy of atomic clocks).

5.3.1 The 'bouncing' potential

When the atoms are held in the Ioffe-Pritchard (IP) magnetic trap, during the final evaporation stage of BEC production, then the total confining potential (gravitational+magnetic) has the approximately cylindrically form shown in Fig. 5.6. The atomic cloud has a small gravitational sag (Eq. 3.49) of $dy = -5.0\mu$m with respect to the centre of the magnetic trap (which is used to define the co-ordinate system).
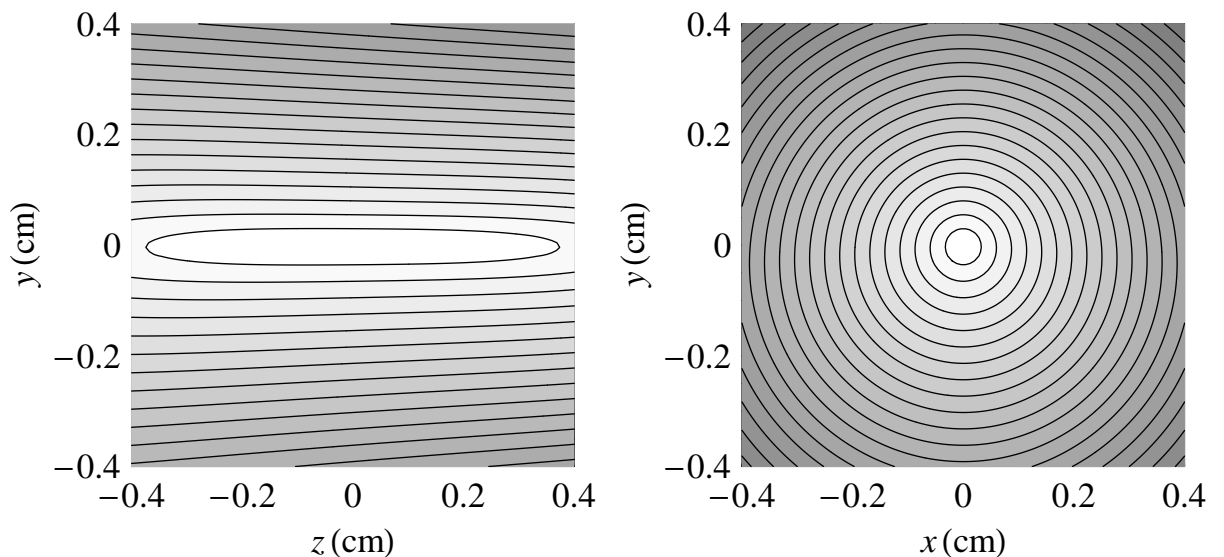

Figure 5.6: Contour plot of the full (magnetic+gravitational) potential seen by atoms bouncing off the standard IP potential. The IP trap is in the same compressed geometry used for evaporative cooling, however the current is only pulsed to 68% of its maximum value 216 A which is used for trapping. The left image depicts the $x = 0$ plane, whereas the right image depicts the $z = 0$ plane.

In the experiment the atoms are rapidly ($< 250\,\mu$s) released from the magnetic trap at $t = 0$ with an initial centre-of-mass position $(x, y, z) = (0, dy, 0)$. They then ballistically fall until $t = 15$ ms when the magnetic field is pulsed back on to 68% of its original strength (with the same magnetic geometry) for a period of 5 ms. The time it takes to switch on the coils (≈ 1 ms) is longer than the switch off time, and for subsequent calculations the coil current is assumed (for simplicity) to follow a square pulse in time between $t = 15.6$ ms and $t = 20$ ms, in close accordance with the mean pulse time and integrated current signal of the experimental current pulse. Larger coil currents could be used during bouncing if

the 'bounce' field is pulsed on for a shorter time.

After the atoms' $1.2\,\text{mm}$ vertical $(-y)$ fall under gravity, prior to the magnetic pulse, they enter a region of the IP potential which has six spatially varying Taylor expansion terms, to second order. Linear gradients in the potential y and z simply alter the centre-of-mass motion of the atomic cloud in these directions. A yz potential term generates a force which applies a torque to the atomic cloud in the yz plane. The three remaining terms are harmonic, acting along the x, y and z axes, which serve to focus the magnetic cloud.

By far the dominant harmonic term is the x curvature, as can be seen from the contour plots of Fig. 5.6. The radius of curvature of the magnetic mirror R_x along the x direction is equal to the height h from which the atoms are dropped. This is in fact on the edge of the stability region of bouncing regimes [102].

To illustrate different time-dependent bouncing regimes, one can consider the classical one-dimensional motion of atoms falling under gravity before reflection from a one-dimensional magnetic potential that is either linear or quadratic. In the linear case all atoms experience the *same* time-dependent forces. The centre-of-mass motion of the atomic cloud is therefore the only thing that alters (Fig. 5.7).
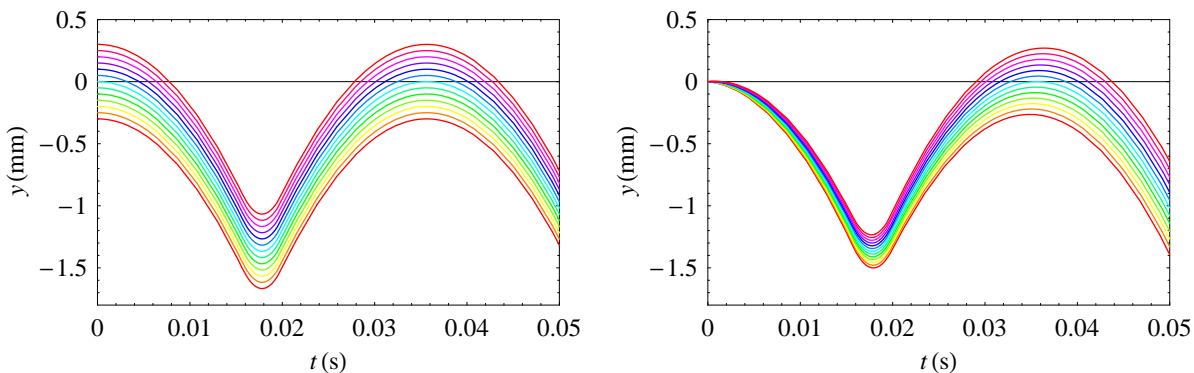

Figure 5.7: One-dimensional bouncing off a pulsed linear potential. Atoms with a spread of y positions (left image) and y velocities (right image) fall under gravity g from a drop height $h = 1.2\,\text{mm}$ (and hence a time $t_1 = \sqrt{2g/h}$) before being reflected by an upward constant force $F_y = \mu_B m_F g_F B_1 - g = \eta g$ pulsed on for a period $\tau = 2t_1\eta$. The parabolic atomic trajectories enable easy analytic tracking, and it is clear that the centre-of-mass motion of the atoms remains constant.

This can be contrasted with reflection from a parabolic magnetic potential. The force has a constant term (depending on the centre of the parabolic potential), as well as a linear contribution. The constant term produces the centre-of-mass motion of Fig. 5.7; however the linear term will produce atomic focusing. In one (and in fact in three) dimensions the atomic trajectory is again analytic, consisting of a parabolic flight under gravity followed by a sinusoidal trajectory during the magnetic 'bounce' pulse. If one removes the centre-of-mass motion then if an atom is released at time $t = 0$ from position y_0 with

velocity v_{y0}, the final velocity and position of the atom at time $t = t_1 + \tau + t_2$ after a bounce pulse with force $F_y = -m\omega_y^2 y$ from time $t = t_1$ to $t = t_1 + \tau$ are:

$$v_y = v_{y0}\cos(\omega_y\tau) - (y_0 + v_{y0}t_1)\sin(\omega_y\tau), \tag{5.5}$$

$$
\begin{aligned}
y(t) &= (y_0 + v_{y0}t_1)\cos(\omega_y\tau) + \frac{v_{y0}}{\omega_y}\sin(\omega_y\tau) + v_y t_2 \\
&= (y_0 + v_{y0}(t_2 + t_1))\cos(\omega_y\tau) + \left(\frac{v_{y0}}{\omega_y} - \omega_y t_2(y_0 + v_{y0}t_1)\right)\sin(\omega_y\tau).
\end{aligned} \tag{5.6}
$$

Relations for the focusing and cooling of an atomic cloud follow, and these are discussed in Refs. [220] and [219]. Reflection and focusing from a temporal atom-optical harmonic mirror have many optical analogues. The trajectories of atoms falling under gravity and reflected from a parabolic potential are shown in Fig. 5.8, demonstrating the effect on the atomic dynamics of the ratio of drop height h to mirror radius of curvature R_y.
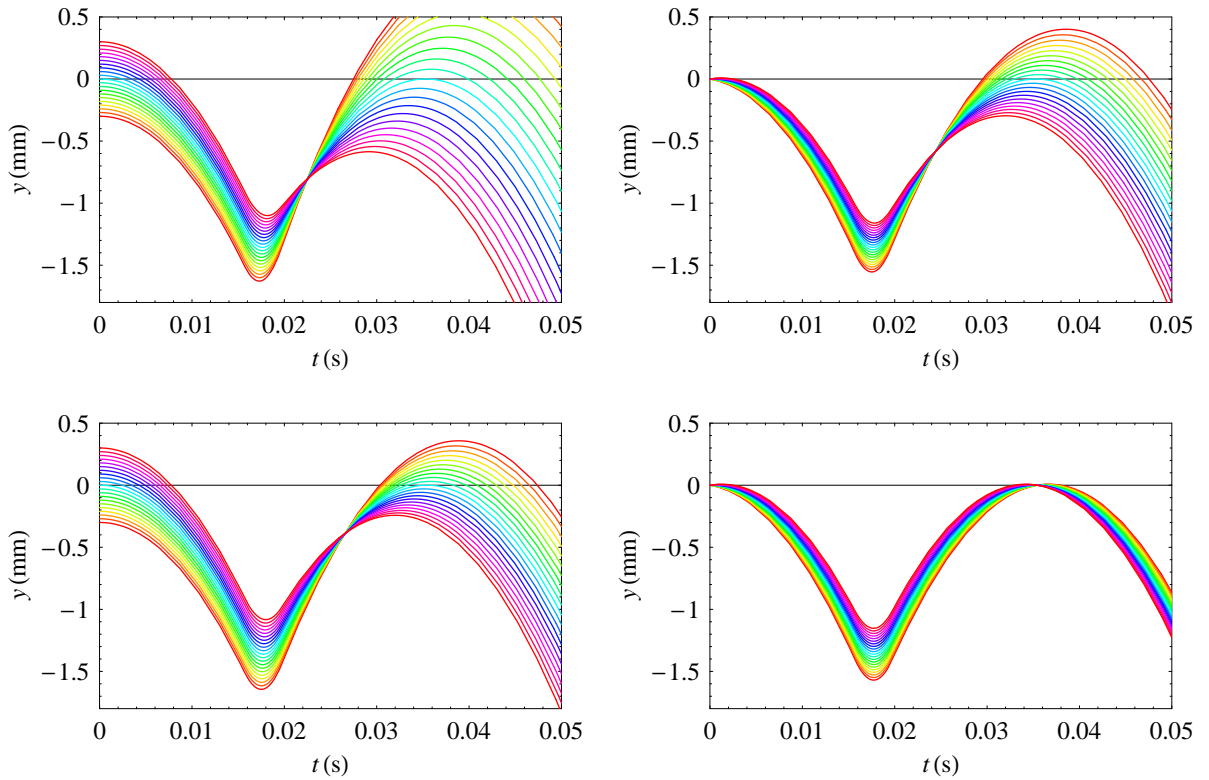

Figure 5.8: One-dimensional bouncing off a pulsed harmonic potential. Atoms with a spread of y positions (left images) and y velocities (right images) fall under gravity g for a time $t_1 = \sqrt{2g/h}$ before being reflected by an upward harmonic force pulsed on for a period τ. The mirror 'hardness' is similar to that of Fig. 5.7. The upper images depict atoms reflected from a potential with a radius of curvature equal to the drop height (i.e. they are released from the centre of the harmonic bouncing potential). The lower images depict atoms reflected from a potential where the drop height is half the mirror radius of curvature.
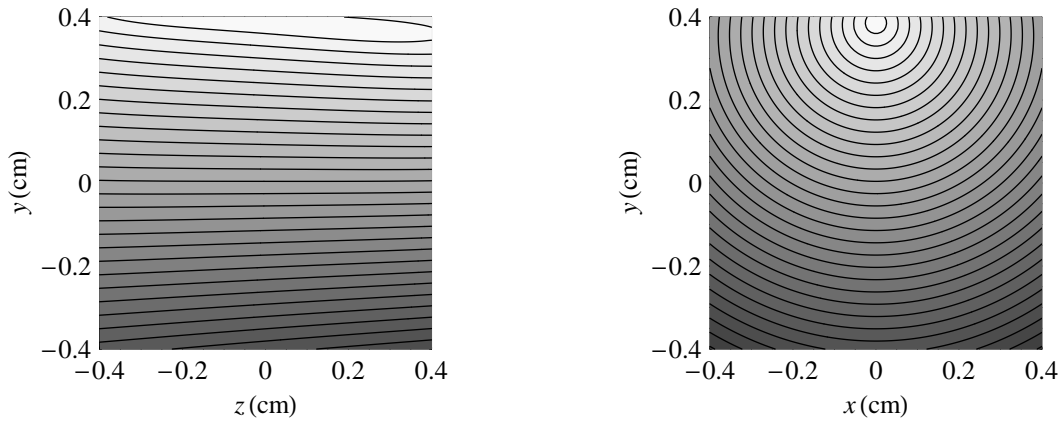
Figure 5.9: Contour plot of the altered magnetic+gravitational 'bouncing' potential when an extra $70\,\mathrm{G}$ vertical (y) constant magnetic field is added (cf. Fig. 5.6). The IP is in the same compressed geometry used for evaporative cooling, however the current is lower by $68\,\%$. The left image depicts the $x = 0$ plane, whereas the right image depicts the $z = 0$ plane.

In the Sussex 'bouncing' experiment the atoms are strongly focused in the x direction, however only weakly in the y and z directions (Fig. 5.6). The full magnetic (Eq. 3.55) and gravitational potential (Fig. 5.6) that the atoms experience when they are bounced is essentially linear in the y direction with a small harmonic contribution. The vertical (y) motion of the atoms is therefore expected to be similar to that of Fig. 5.7. The weak harmonic confinement in the z direction means that the atoms essentially continue to ballistically expand in this dimension. The x direction is interesting however as the harmonic force should provide strong focusing in this direction. By adjusting the centre of the magnetic trap with the Helmholtz 'bounce' coils (Sec. 4.2.6) it is possible to adjust the centre of the 'bouncing' potential, as shown in Fig. 5.9. Alterations can therefore be made to the atomic cloud focusing dynamics in the x direction, with minimal change to the motion in the y and z directions.

5.3.2   Experimental 'bouncing' results

The 'bouncing' potentials of Figs. 5.6 and 5.6 correspond to two regimes of h/R_x – the drop height to potential radius of curvature ratio. When only the IP magnetic field is used for bouncing we have $h/R_x \approx 1$. If a $70\,\mathrm{G}$ constant bias field is added to the IP potential, then we have $h/R_x \approx 1/5.4$. Experimental data from the two bouncing different regimes is presented in Fig. 5.10.

The centre-of-mass motion of the atomic cloud was subtracted in Fig. 5.10, and the complete absorption imaging data sequence in the yz' plane for the situation $h/R_x \approx 1/5.4$ is shown in Fig. 5.11. Two theoretical models (Sec. 2.2.2) were also used to describe the cloud dynamics. The predictions of these models are shown in Fig. 5.12 and show good agreement with the experimental data.

The z' motion of the atomic cloud could be eliminated by removing the tilt in the magnetic coils with
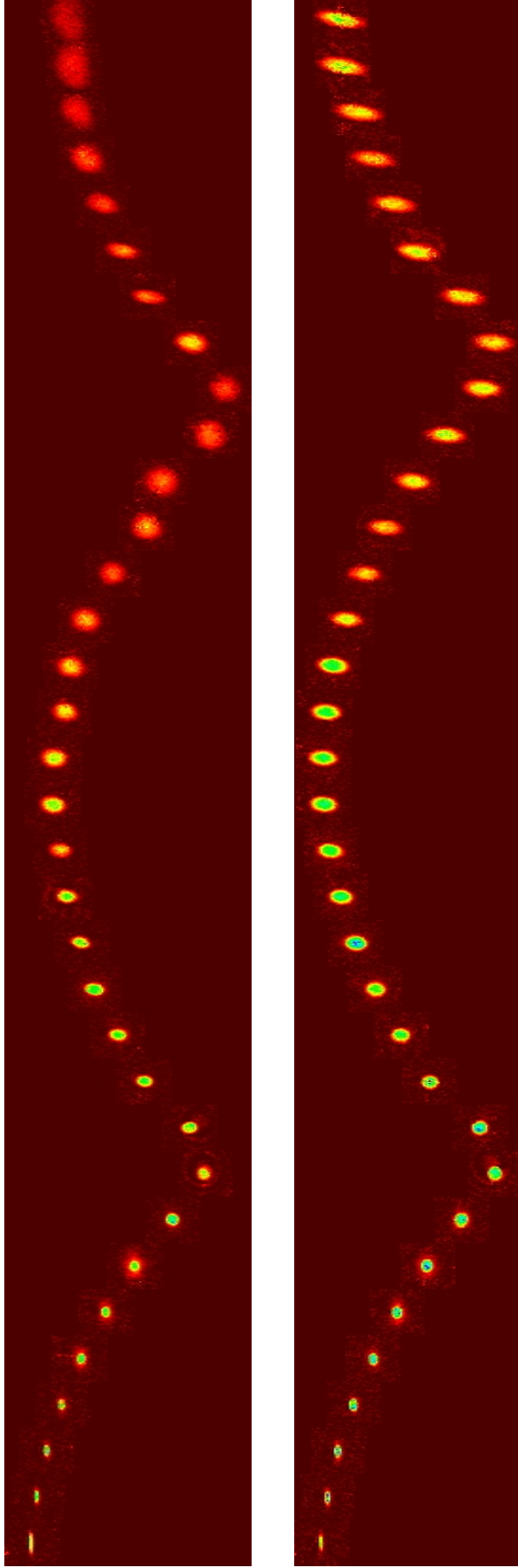
Figure 5.10: Experimental bouncing BEC data for drop height h approximately equal to the mirror's radial radius of curvature R (upper data sequence) and for $h \approx R/5.4$ (lower sequence). Each image is $306\,\mu$m wide, taken at times $t = 2, 4, 6, ..., 68$ ms after the condensate is first released from the IP magnetic trap. Atomic cloud centre-of-mass motion in the z' direction (Fig. 4.16) has been subtracted (cf. Fig. 5.11). In the lower data sequence both the Helmholtz 'bounce' and IP coils are applied, shifting the centre of the potential and changing the radius of curvature of the bouncing 'mirror'.
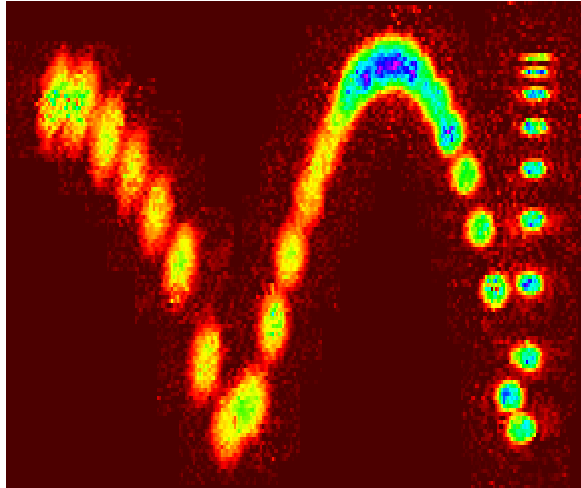
Figure 5.11: Full experimental bouncing BEC data at times $t = 2, 4, 6, ..., 68$ ms for a drop height $h \approx R/5.4$. This is a superposition of the absorption images of Fig. 5.10 showing the complete atomic motion. The image size is $2260 \, \mu$m $\times 1900 \, \mu$m.
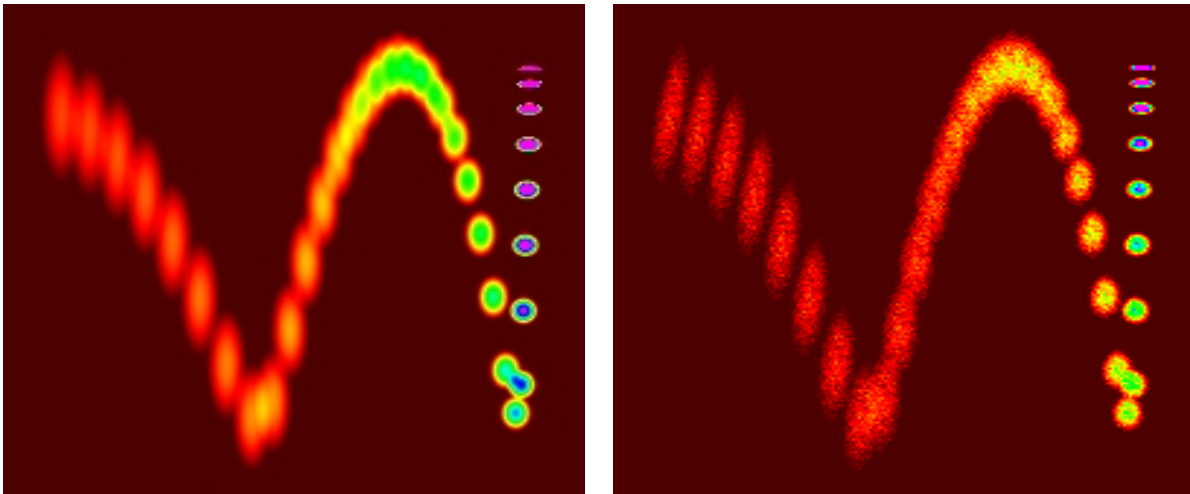

Figure 5.12: Simulation of the bouncing experiment using the theoretical models of section 2.2.2 (left image) and section 2.2.2 (right image). The image dimensions are the same as for Fig. 5.11. Both models assume a BEC population of $N = 1.8 \ 10^5$ atoms initially confined in a magnetic trap with radial and axial frequencies $\nu_r = 223$ Hz and $\nu_z = 11$ Hz. The atomic cloud does not rotate in the left image as the harmonic model does not include the second-order potential term of the form yz. The y axis of the magnetic mirror is assumed to be tilted by an angle of $4°$ with respect to gravity.
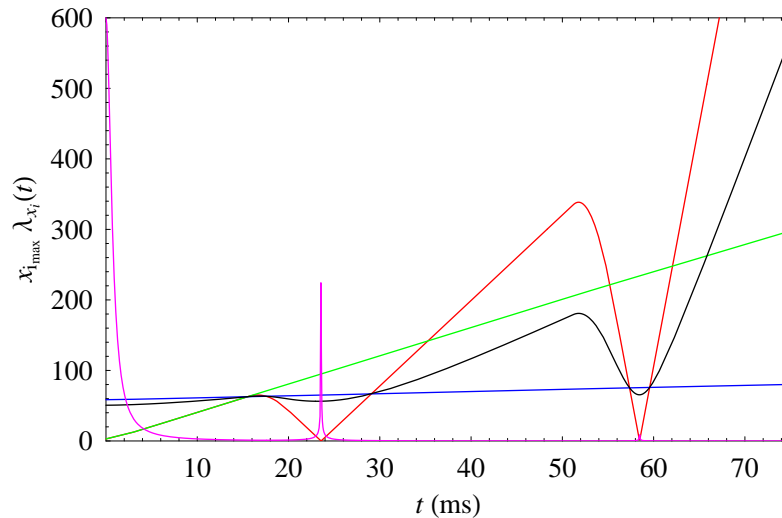
Figure 5.13: Theoretical variation of the width parameters during bouncing from $h \approx R_x$. The different curves describe $x_{max}(0)\lambda_x(t)$ (red), $y_{max}(0)\lambda_y(t)$ (green), $z_{max}(0)\lambda_z(t)$ (blue), $z'_{max}(t)$ (black) and the relative density of the BEC cloud (purple). Due to the absorption imaging viewing angle the extreme focusing in the x direction is not observed. At times $t > 60$ ms the rapid cloud expansion in the x direction is observed experimentally however (Fig. 5.10).

respect to gravity. From Figs. 5.6 and 5.9 it is clear that this will only be effective for one particular drop height however, as the slope of the magnetic contours alters as y varies.

The strengths and weaknesses of the two models illustrated in Fig. 5.12 will now be discussed. The assumption of a locally harmonic potential (Sec. 2.2.2) vastly simplifies calculations, and makes the use of Monte-Carlo methods unnecessary. The model also includes the effect of inter-atomic repulsion. The calculated time-dependent BEC width parameters for bouncing from a height $h \approx R_x$ are shown in Fig. 5.13.

It is interesting to note that the harmonic bouncing model illustrated in Fig. 5.13 predicts the BEC will reach a focus in the x direction with a minimum cloud radius of $x_{max} = 6$ nm at time $t_{focus} \approx 23.6$ ms. For such a tight focus diffraction effects would become important, as the thermal de Broglie wavelength of the BEC atoms is $\Lambda_{dB} = 38$ nm at this stage of the trajectory.

Unfortunately this is where the limitations of the simple harmonic model for describing the Sussex experiment become apparent. Higher order terms in the potential cause aberration in the magnetic mirror, preventing the attainment of such narrow focusing. If a magnetic potential with low high-order Taylor terms were used this may in fact be possible however. In this case it would then be important to be able to view the atoms along the z axis using an imaging system with improved resolution, however experimental imaging resolutions are typically limited to around $1 \, \mu$m.

The monte carlo model of section 2.2.2 has the advantage that higher-order aberrations in the magnetic potential are accounted for by tracing the full classical trajectories of the atoms in the BEC cloud.
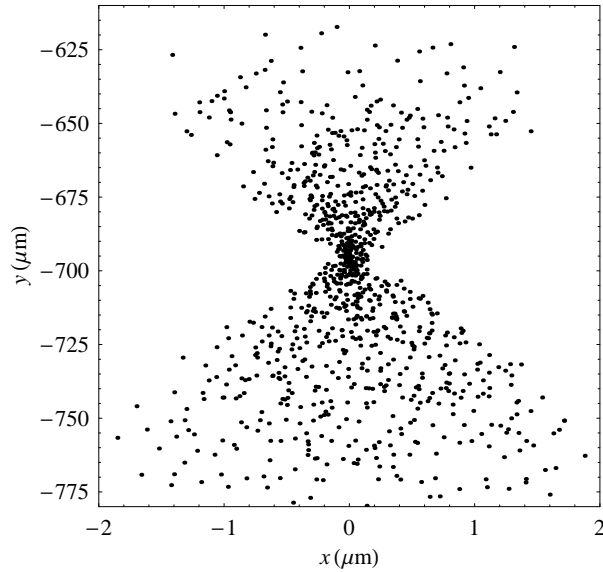
Figure 5.14: The x focus of the BEC modelled by the monte carlo simulation for a drop height $h \approx R_x$, under the same conditions as Fig. 5.13. The xy positions of 1000 atoms (representing an $N = 1.8 \; 10^5$ atom condensate) are plotted at the time $t_{focus} = 23.65 \, \text{ms}$.

The disadvantage of the model is that it cannot be applied in regimes where gradients in the atomic density become high, as interatomic repulsion becomes important. In Fig. 5.14 the calculated atomic column density distribution is displayed for the x focus at time $t_{focus} = 23.65 \, \text{ms}$. The 'bow-tie' shape differs considerably from the parabolic distribution predicted by the harmonic theory, and results from aberrations in the magnetic potential.

As the atomic density in the monte carlo simulation reaches levels $\left(n_{max} = 1.7 \; 10^{13} \, \text{cm}^{-3} \right)$ as high as 10% of the pre-release condensate (Fig. 2.2), and the cloud x dimension during the focus is smaller than the initial condensate dimension by a factor of 10, it is highly likely that interatomic repulsion forces will be important during the focus. For a more quantitative analysis the density of the atomic distribution must be tracked as a function of time, employing a finite sum approximation to Eq. 2.26. This would lead to high levels of computation, and in this case the final word on tight BEC focusing would best be obtained from a three-dimensional solution to the time-dependent Gross-Pitaevskii equation.

In summary, magnetic 'bouncing' of a BEC from a soft temporal mirror has been observed. The magnetic geometry, and in particular the mirror's radius of curvature, can be continuously altered – clear experimental evidence of variation in the BEC's bouncing dynamics was observed. Indirect evidence of focusing is seen, and adjustments to the imaging system should greatly enhance investigations of very tight focusing in the x direction. Good agreement was seen between the experiment and two theoretical models, although both models have some limitations. The magnetic mirror appears to have high atom-optical quality, and could lead to extremely high density, or very cold, atomic sources.

Chapter 6

Conclusions

6.1 Summary

In chapter 1 we began with a brief introduction to the concept of Bose-Einstein condensation (BEC), the mechanisms used to obtain it, and some recent experimental developments in the field.

Finer detail on the theory of BEC followed in chapter 2, with a review of the statistical mechanics of the Bose-Einstein phase transition and the means with which to describe condensate evolution quantum mechanically. The Thomas-Fermi approximation simplified the Gross-Pitaevskii equation considerably, and Castin and Dum's [85] lucid model for the evolution of a condensate in the Thomas-Fermi regime was extended to regimes where the potential is locally harmonic. This enabled the model to be used for analysis of the recent magnetic 'bouncing' BEC experiments at Sussex.

The theory behind the methods used to reach BEC was the topic of chapter 3. In particular laser cooling, trapping and imaging, magnetic trapping and evaporative cooling. Some enhancements of existing models were discussed, namely magneto-optical trap (MOT) atom number calculations and the three-dimensional time-orbiting potential (TOP) trap. Theoretical analysis of heating during all-optical double MOT loading showed that this transfer mechanism can be equally efficient as more complicated transfer schemes. A variety of magnetic trapping fields were reviewed, with particular attention to experimentally relevant parameters. The evaporative cooling analysis demonstrated that the efficiency of this stage of the experiment could be considerably improved in future.

Chapter 4 described the experimental realisation of BEC at Sussex, following the structure of chapter 3. Simplicity and durability are novel aspects of the BEC apparatus design, which incorporates: easy-to-build stable diode lasers, a low power double magneto-optical trap (MOT) employing a loading technique based solely on light-pressure, the omission of dark or compressed MOT stages in the BEC sequence, a stable magnetic trap regulated by straightforward power MOSFET banks and an extra high vacuum essentially maintained by a single low-throughput ion pump. Some mechanisms used for

BEC production do not appear to be necessary, although their use would improve the number of atoms in the BEC. The chapter ends with the first experimental realisation of BEC in the UK.

In chapter 5 experimental manipulation of the BEC were performed. In particular the BEC ground state occupation was determined as a function of temperature, and the ballistic expansion of the BEC was observed. These results were compared with existing theory and experiments. The final, novel, experiment dealt with the realisation of a 'soft' magnetic mirror for manipulating the BEC. 'Bouncing' from the surface of a curved magnetic mirror was observed, and by simply adding a constant vertical magnetic field the radii of the magnetic mirror were altered. This enabled access to the stability region (where the drop height h is less than the mirror radius of curvature R), allowing adjustable control over BEC focusing and storage.

Finally in this chapter possible enhancements of the existing Sussex BEC apparatus are reviewed, and possible directions for future research are discussed.

6.2   Improvements to the BEC size and detection

The double MOT

The laser system works well at present, however the stability of the locking system during the short frequency alterations necessary for optical molasses, optical pumping and probing could be improved using the methods discussed in Sec. 4.1.5.

More precise, stable control of the Rb pressure in the HP MOT would enhance LP MOT loading efficiency and reproducibility. This could be achieved by substituting alkali metal dispensers ('getters') for the rubidium sidearm. Placing a constriction in the HP-LP MOT transfer tube would lead to a higher lifetime ratio between the two MOTs, and hence higher number in the LP MOT, without loss of transfer efficiency. The oversight with the non-evaporable getter pump housing could be rectified, possibly creating a large drop in LP MOT pressure (and thereby enhancing evaporative cooling efficiency).

Although the use of two trap lasers, one for each MOT of the double MOT, would complicate the existing simple design, it should lead to lower LP MOT atom losses during atom transfer and thus higher LP MOT atom number. Problems with the laser beam profile appear to be affecting transfer efficiency and could be investigated. Similarly it might be worth spatially filtering the push laser beam.

Again, although stressing the simplicity of our present design, the implementation of a dark or compressed MOT stage could enhance the density of the atoms prior to magnetic trapping leading to a higher phase space density and more efficient evaporative cooling. A dark MOT also enables the use of a dark molasses, leading to a cooler *and* denser pre-magnetic trap atomic cloud.

Imaging

In future the adoption of non-destructive far-off resonance imaging systems, like those described in Sec. 4.1.4, may be of benefit. A interchangeable lens system with the option of higher magnification yet low distortion would also be advantageous. The optical quality of the vacuum chamber is somewhat dubious, and may need investigation.

The present low-cost video camera used for imaging performs adequately, however a cooled low-noise camera would considerably enhance the signal to noise ratio, enabling clearer interpretation of experimental results, and a tighter check on theory.

Imaging along the MOT beam axes using polarising beamsplitters would allow the BEC to be studied along the magnetic trap axes, and hence in the focal plane of the magnetic focusing effects. The vertical (y) windows of the quartz LP MOT cell also have considerably better optical quality than the other windows. Views of bouncing in the z direction may be of greater interest however, as the strong x focusing can be observed better in this direction. Ideally one could image in both directions.

Magnetic trapping

The optical pumping system could be improved in the manner discussed in Sec. 4.2.2 – retro-reflected optical pumping separate from the probe light could be used to prevent unnecessary atomic heating. This effect would be enhanced if the trap repump light was turned off during optical pumping, with repump light directly overlayed with the pump beam.

At present the magnetic compression stage is not very adiabatic. This may be because the atoms in the relatively hot compressed atomic cloud are sampling anharmonic regions of the Ioffe-Pritchard magnetic potential. Data interpretation could be reviewed in light of this.

A tighter magnetic trap would certainly enhance evaporative cooling, and would also be useful for the bouncing experiment.

Evaporative cooling

As shown in the evaporative cooling theory section, it should be possible to enhance the evaporation efficiency. In general, although all aspects of the experiment work well enough, there are many ways in which the number of atoms in the condensate could be increased. Our present evaporation status on the boundary for runaway evaporation leaves a very small margin for error in the many processes that are needed to achieve a Bose Einstein condensate. An all-over optimisation wouldn't go amiss!

6.3 Future prospects

Probably the simplest and most important thing to do in future is to alter the camera angle, enabling the observation of the BEC's evolution perpendicular to its focus in the x direction. The manipulated Thomas-Fermi model shows that with a parabolic trap it should be possible to obtain tight spatial focusing of atoms, reaching very high densities. This could be valuable for atomic lithography. It is equally possible to create extreme cold, low density atomic beams for use in high precision atom clocks.

At present the atomic focusing is mainly one-dimensional, along the x direction, however by adjusting the IP bias field the curvature in the y and z directions may be greatly enhanced. One-dimensional focusing has been observed with cold atoms, and here we report indirect evidence for similar effects in a BEC. Three dimensional focusing or collimation of the coherent atomic beam should be possible. The use of a magnetic trap capable of reaching a spherically symmetric harmonic potential would greatly enhance any effects, however.

Another important future goal is the use of 'hard' spatial mirrors. Serpentine wires grids could be used, and it may well be possible to reach XHV with improvements to the Sussex Centre for Optical and Atomic Physics' video tape mirrors, perhaps with surface coatings or a higher temperature bake-out of the vacuum system.

These days a good BEC is the size of a small MOT, and many experiments that are enhanced by the low temperatures in a MOT could in theory be improved further through the use of a low density BEC. There remains hope that BEC production will be simplified past the multi-stage technical minefield it can sometimes appear to be at present, and the atomic laser could still be as valuable a tool in future as the optical laser is today.

Who knows what the future holds for this new, mysterious state of matter.

Appendix A

External-cavity diode laser

This appendix contains our journal article about a simple extended-cavity diode laser [203]. Information omitted from this paper for brevity and some recent developments are discussed below.

Laser Diodes

Unfortunately, the remarkably well-behaved SDL-5401 780nm 50mW laser diode is no longer on the market. The main viable 780nm alternatives at present are the 50mW Hitachi HL7851G, and the 75mW Sanyo DL7140-201 (which comes in a $5.6\text{mm}\phi$ package, requiring a different collimation tube). Care must be taken with the pin configuration of laser diodes as this varies between manufacturers.

It also appears that the lifetime of diodes driven for long periods at currents near their tested maximum [203] may be decreased. An SDL degraded unexpectedly after 10 months of continuous, single-mode operation at an output power of 100mW - diode lifetimes of several years are normally typical [201]. It is clear though, that this laser design can yield single-mode operation at high powers, often enabling one to do without the added complication of injection locking.

Current Controllers

We used Wavelength MPL-250 current controllers with a mains-powered Lambda LNS-W-15 rectified 15V DC supply for our lasers. Car batteries with series potentiometers have the advantage that they have extremely low current noise, but have the drawback that they continually run down. The MPLs ensure a constant current supply, and also have a maximum current protection feature. The main problem with these devices is their current noise. By measuring the broadband current noise peaked at 350kHz on a radio-frequency spectrum analyser, we observed current noise of $\approx 10\mu\text{A}$ rms, significantly above the specification of $< 2\mu\text{A}$ rms, which explained early observations of a large ($\approx 10\text{MHz}$) laser linewidth. This noise was present even in conjunction with an MPL powered by a car battery, and thus seems to be generated within the MPL itself. It is now clear that the current controllers from Thorlabs present a
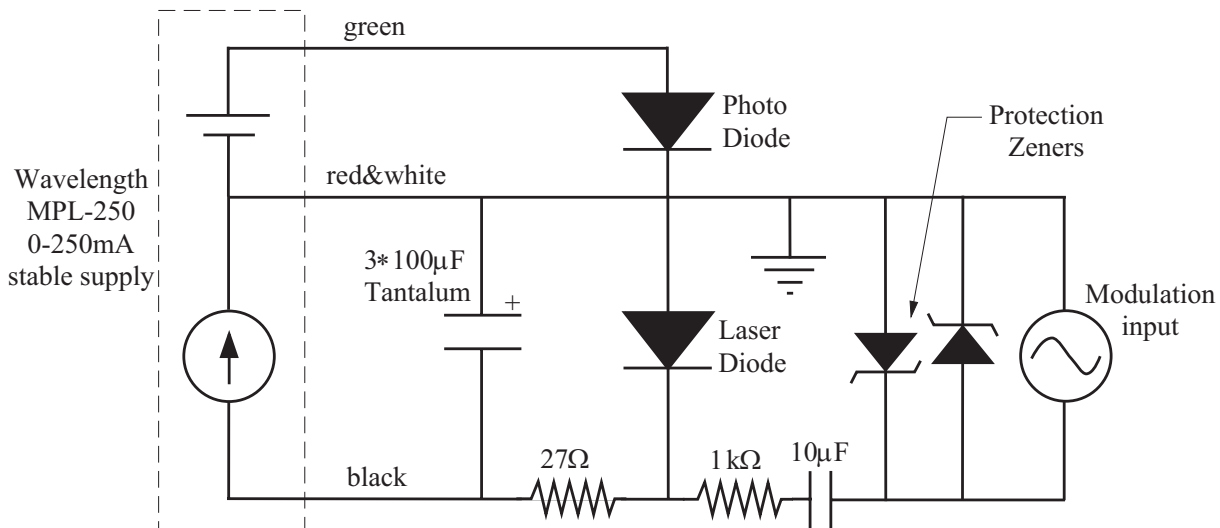
Figure A.1: The laser diode current controller, with low pass filtering and current modulation input. The colours of wires originating from the Wavelength MPL-250 current controller are also indicated.

cheaper and less noisy alternative to the Wavelength controllers.

The circuit in figure A.1 illustrates the low-pass filter necessary to reduce the MPL current noise. Also shown is the modulation input used for the high frequency current feedback output of the integrators used for locking the lasers (see Subsection 4.1.1 and Appendix D).

The positions of the earth in the circuit (corresponding to the laser diode's outer case) and the 27Ω resistor are critically important, as the laser diode is then protected from large voltage spikes which can be generated by fluorescent lights. The Zener diodes and $1\mathrm{k}\Omega$ resistor ensure that current modulations are restricted to an amplitude of $\approx 1\mathrm{mA}$, to prevent laser mode-hops.

The laser diode package's built-in photodiode (PD) can be used as a measure of laser power, however for our lasers stray feedback laser light on the PD tends to make this an unreliable power reading. Any measurement of the laser power quoted in this thesis were taken with a Coherent Labmaster-E power-meter. This powermeter has two separate power-heads: one based on a PD, and a thermal head. The PD head saturates at around $30\,\mathrm{mW}$ and higher powers were measured using the thermal head.

Temperature Controllers

We used Wavelength MPT-5000s, which worked very well in general. The main point to remember with these is to set the internal jumper to 3A maximum current, to prevent overheating of the Peltier thermoelectric cooler. It's also important to set the MPT's gain sufficiently low to prevent oscillation. Quite thin layers of Torr-Seal were used in the construction of the laser diode mount, to ensure good thermal contact.

At High Voltage

The piezoelectric transducers (PZTs) used were PIC-151 disks, from PI. The PZTs receive the low frequency and DC feedback of the integrators used for locking the lasers. The high voltage power supply used was a 1kV Bertran Associates Inc. 603C-15P, as this had lower voltage noise and could source more current than the less robust Start Spellman Ltd. MM1P2.5/12 encapsulated DC to DC converters we had used previously. The high voltage amplifier used to drive the PZT can be found in ref. [221]. The amplifier requires a +/-15V power supply, and draws about 1mA of current. The only problem encountered with this circuit was the occasional death of a BUZ-50 FET.

Boxed In

The laser was placed in an aluminium box (with a hermetic seal) on a layer of heat-conducting grease. An 11-way Fischer plug and socket was used as an airtight electrical feedthrough, with an AR-coated 1" diameter window from CVI for the output laser beam. Once away from air-draughts the laser becomes quite stable: opening and closing doors has only a small effect. The screws on the lid of the box have to be tightened while the feedthrough is loose, otherwise a pressure build-up can change the laser frequency. Once the lid's screws are tightened, the feedthrough can then be made airtight.

Collimating tubes

The Thorlabs LT 110P-B collimating tube was found to give better laser beam quality than the LT 230P-B in the far field.

A simple extended-cavity diode laser

A. S. Arnold, J. S. Wilson,[a] and M. G. Boshier
Sussex Centre for Optical and Atomic Physics, CPES, University of Sussex, Falmer, Brighton BN1 9QH, United Kingdom

Operating a laser diode in an extended cavity which provides frequency-selective feedback is a very effective method of reducing the laser's linewidth and improving its tunability. We have developed an extremely simple laser of this type, built from inexpensive commercial components with only a few minor modifications. A 780 nm laser built to this design has an output power of 80 mW, a linewidth of 350 kHz, and it has been continuously locked to a Doppler-free rubidium transition for several days. © *1998 American Institute of Physics.* [S0034-6748(98)01303-3]

I. INTRODUCTION

Diode lasers are now widely used in many experiments in optical and atomic physics. Although these devices are compact, simple, and relatively inexpensive, unmodified laser diodes do have some undesirable properties, mostly as a result of their short semiconductor cavity. In particular, their frequency is very sensitive to changes in temperature and injection current, and they have large linewidths ($\sim$100 MHz) and poor tunability. It is well known that these shortcomings can be rectified by operating the laser in a longer external cavity which provides frequency-selective optical feedback.[1,2] A particularly simple implementation of this idea uses feedback from a diffraction grating mounted in the Littrow configuration.[3,4] In this case the output facet of the diode must be antireflection coated to ensure stable operation in the presence of the strong feedback from the grating, but most laser diodes with output powers of more than 20 mW now have suitable coatings and a simple single-layer coating is easily applied to lasers with uncoated facets.[5]

In this article we describe a method for constructing an extended-cavity diode laser of this type. Its performance is similar to that of other designs,[5–7] but it is particularly inexpensive and easy to build because it is based on simple modifications of a few commercial optical components.

II. CONSTRUCTION

The essential requirements for the extended cavity are that the laser diode, the diffraction grating, and a collimating lens all be located rigidly with respect to each other, and that the angle of the grating and the position of the lens be precisely adjustable. Our design (Fig. 1) takes advantage of the fact that these requirements can now be satisfied with convenient low-cost commercial components.[8] A collimation tube (ThorLabs LT110P-B) holds the laser diode and the collimating lens (an aspheric optic with $f = 6.2$ mm and NA $= 0.4$). The threaded tube also provides precisely adjustable focusing of the collimating lens, and it accurately locates the

collimating lens axis along the laser diode axis. The cavity itself is constructed on a mirror mount, eliminating the need for the milled baseplate with separate diode, collimating lens, and grating assemblies of other designs. The diffraction grating is mounted on the front plate of the mirror mount, and the collimation tube assembly on the back plate. The beam is coupled out of the cavity in the zeroth-order reflection from the grating. We have used the Newport Ultima U100-P mirror mount because of its good mechanical stability and because its thick plates are convenient for mounting the grating and collimation tube. The minor modifications made to the mirror mount are shown in Fig. 2. Two holes are tapped in the front plate of the mount and a square section of the plate is cut away. In addition, a clearance hole and clamping screw are added to the Ultima UPA-PA1 post adapter to mount the collimation tube. The total length of the extended cavity is about 20 mm, which is long enough to reduce the linewidth below 1 MHz, while at the same time the corresponding mode spacing of $\sim$8 GHz is large enough to give a useful continuous scan range and robust single-frequency operation.

The design shown in Figs. 1 and 2 has a third component, a grating mount (Fig. 3) which is screwed to the front plate of the mirror mount. It is possible to dispense with this extra component and simply mill the plate of the mirror mount directly to the Littrow angle. This further simplifies the design, although the focusing adjustment can become awkward for such a short cavity.

Our standard diffraction grating for near-infrared operation is a gold-coated 1800 lines/mm holographic grating on a $15 \times 15 \times 3$ mm^3 substrate (Richardson Grating Laboratory 35-83-X-330). With the light polarized parallel to the lines of the grating it provides 20% feedback, sufficient for good tunability and stability with many laser diodes, while the 80% output coupling gives high output power. The grating is mounted on a 16 mm diameter$\times$2 mm thick disk piezoelectric transducer (PZT) to provide fine adjustment of the cavity length for scanning the laser frequency.

An advantage of the compact cavity design is that it is easy to control the temperature of the complete laser using a Peltier thermoelectric cooler (TEC). To this end, a small hole

[a] Present address: Christ's College, Cambridge University, Cambridge CB2 3BU, United Kingdom.
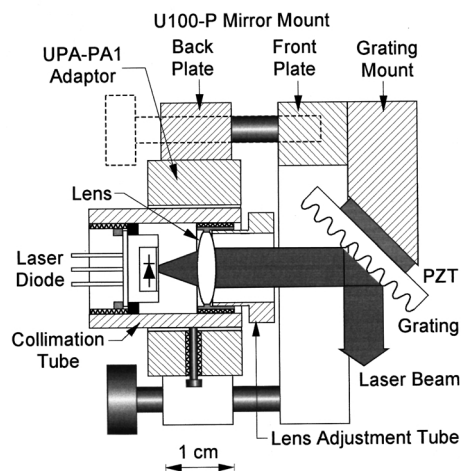
FIG. 1. Schematic diagram of the extended-cavity laser, viewed from above. The Peltier thermoelectric cooler and mounting base are not shown.

is drilled in the mirror mount near the diode, and a thermistor or other temperature sensor glued inside it. A thin metal plate is glued between the base of the mirror mount and the TEC to provide a good thermal connection between the laser and the TEC. We use a 30×30 mm^2 TEC with 33 W of cooling power, in which case the dimensions of the plate are $3 \times 30 \times 40$ mm^3 (a clearance hole must also be drilled in the plate to accommodate a raised bolt head on the mirror mount). The other side of the TEC must be attached to a suitable heatsink. If the laser is to be mounted on an optical table, a standard slotted base (e.g., ThorLabs BA2) works well. All glued joints should be made with a low vapor pressure epoxy such as Torr-Seal to avoid outgassing contamination if the laser is to be operated in a sealed enclosure.

Alignment of the completed laser proceeds as follows. The laser diode is mounted in the collimation tube, and the lens is adjusted to collimate the beam over a distance of several meters. The collimation tube is then clamped in the
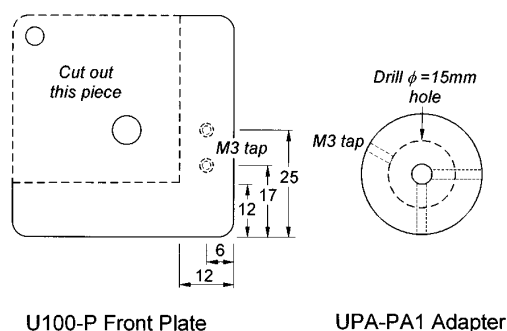

FIG. 2. The modifications made to the u100-P mirror mount. On the front plate of the mirror mount (left), the section bordered with dashed lines is cut out and two tapped holes are added to attach the grating mount. The center hole of the PA1 adapter (right) is drilled out to 15 mm and a tapped hole is added to take the screw which clamps the collimation tube. All dimensions are in mm.
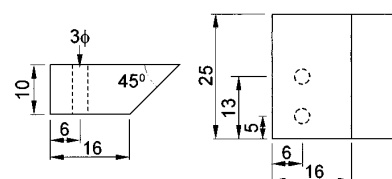

FIG. 3. The aluminium grating mount used with an 1800 lines/mm grating at a wavelength of 780 nm. Top view (left) and front view (right). All dimensions are in mm.

mirror mount as shown in Fig. 1, rotated so that the long axis of the elliptical laser beam is perpendicular to the lines on the grating. Next, the laser current is reduced just below threshold for the solitary laser diode, where the diode is most sensitive to feedback as it cannot lase by itself. Adjusting the mirror mount to direct the Littrow reflection from the grating back into the center of the collimating lens should cause a second beam to become visible near the main zeroth-order output beam. This beam is much weaker than the main one because it has made a complete round trip inside the cavity. Collapsing it into the main output beam by further grating adjustments should then produce a large increase in output power as the feedback from the grating takes the laser above threshold. The output power can be optimized by adjusting the grating angle and the focusing of the collimation lens. The lens adjustment is very critical, corresponding to only a few degrees of rotation of the threaded lens mount. While it can be accomplished by rotating the lens carefully with a small screwdriver, we have found it more convenient to glue to the lens mount a short adjustment tube, extending beyond the end of the collimation tube (Fig. 1). Once the system is lasing, the laser current can be increased to give the desired output power, and the horizontal grating adjustment is used to tune the laser to the required wavelength.

III. PERFORMANCE

We have constructed several systems using Spectra Diode Labs SDL-5401 780 nm 50 mW laser diodes. These devices perform well in the cavity described here and were used to obtain most of the performance data presented in this section.

The short-term linewidth of the free-running laser was measured by two methods. First, two similar lasers were heterodyned, with the width of the beatnote yielding a combined linewidth of less than 1 MHz for a 200 ms averaging time. Second, the linewidth was measured by monitoring the fluctuations in the light transmitted by a Fabry–Perot etalon with the laser tuned approximately half way up a transmission peak. This gave a linewidth of 350 kHz for a 200 ms averaging time. The associated power spectral density is shown in Fig. 4. This performance is typical of short extended-cavity diode lasers and demonstrates the excellent mechanical stability of the mirror mount used in our design as a cavity. Linewidths below a few MHz are only obtained when the laser is driven by a current supply having very low
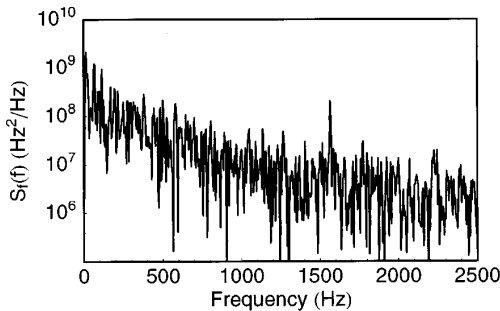
FIG. 4. The power spectral density $S_f(f)$ of the free-running laser's frequency fluctuations. The corresponding laser linewidth is 350 kHz.

noise, typically less than a few μA. This figure may not be met by many low-cost commercial diode laser power supplies without substantial additional low-pass filtering. As an alternative, a simple power supply comprising a 12 V lead-acid car battery, a series potentiometer to control the current, and a few protection components provides excellent performance. If line-powered power supplies are used, care must also be taken to avoid laser damage from transients caused by switching fluorescent lights. In particular, the lowest-impedance path between any grounded points in the circuit and the power supply should not pass through the laser diode.

The laser also has good long-term stability when it is temperature stabilized (to 10 mK) and placed in a box which excludes draughts. A laser stabilized passively in this way and then locked to the peak of a rubidium saturated-absorption line with a simple servo loop remained locked continuously for several days. The lock was eventually lost through laser frequency shifts associated with atmospheric pressure changes. Enclosing the locked laser in a hermetically sealed box reduced the drifts which must be taken out by the servo loop to less than 500 MHz over a few weeks, further improving the long-term reliability of the lock.

Continuous scans of 8 GHz (the cavity mode spacing) can be achieved using the PZT alone, with even larger continuous scans expected with appropriate synchronous translation and rotation of the grating.[9] The laser can also be tuned discontinuously over a range of about 20 nm around the free-running wavelength of the solitary laser diode by rotating the grating. This usually causes the laser to mode hop a few times in steps of 5–8 GHz (roughly equal to the extended-cavity mode spacing), before making a much larger mode hop corresponding to the 50 GHz free spectral range of the solitary laser diode cavity. The resulting ''holes'' in the tuning curve can be shifted away from a region of interest by adjusting the laser temperature. The frequency of the solitary SDL-5401 laser diode tunes with temperature at about 35 GHz/K.

Much smoother tuning is expected from a laser which has a lower reflectivity output facet. In the case of laser diodes supplied with uncoated facets, a very low reflectivity can be obtained from a single-layer coating applied using a

simple technique.[5] We have coated several Hitachi HL7806G 780 nm 5 mW diodes using this method, and found that these diodes do indeed have very much smaller holes in their tuning curves. As a demonstration of this improved tuning we have assembled several laser systems with these lasers, and tuned all of them to the rubidium D2 line within a few minutes by looking for fluorescence from a vapour cell without any specific adjustment of the laser current or temperature. These systems do have lower output power than those using the SDL-5401 lasers, but their smooth tunability can be readily transferred to much higher power devices by injection locking.

Finally, we discuss output power. It is well known that laser diodes fail suddenly and irreversibly as their output power is increased. Until recently the true maximum safe output power was usually quite close to the limit given by the manufacturer. However, this situation has changed, and it now appears that many commercial laser diodes can be run at output powers which considerably exceed the manufacturer's specifications. This true maximum power can be found by imposing a large amplitude 10 kHz ac current modulation on the drive to the laser, and then watching for the appearance of a roll-off in the light versus current characteristic of the solitary laser diode as the maximum current is slowly increased above the manufacturer's specified maximum.[10] The fast modulation and large amplitude of the ac current ensures that the time spent at destructive powers is short enough to avoid permanent damage. The onset of the roll-off indicates the maximum current at which the diode can be operated without damage. We use a modulation amplitude of at least 30 mA for testing devices with a threshold of 30 mA and nominal maximum current of 70 mA. Several of the nominally 50 mW SDL-5401 laser diodes have been tested in this way, and found to exhibit a wide range of true maximum powers, from 55 mW up to 200 mW. One of these laser diodes has been operated in the extended-cavity configuration described here, delivering an output power of 80 mW off the grating. We have also found that most of the nominally 5 mW Hitachi HL7806G lasers can be operated at 15 mW, giving an output power of over 10 mW from the extended cavity. This is sufficient for many experiments in laser cooling and trapping.

ACKNOWLEDGMENTS

[1] C. E. Wieman and L. Hollberg, Rev. Sci. Instrum. **62**, 1 (1991).
[2] P. Zoorabedian, in *Tunable Lasers Handbook*, edited by F. J. Duarte (Academic, London, 1995).
[3] M. W. Flemming and A. Mooradian, IEEE J. Quantum Electron. **17**, 44 (1981).
[4] R. Wyatt and W. J. Devlin, Electron. Lett. **19**, 110 (1983).
[5] M. G. Boshier, D. Berkeland, E. A. Hinds, and V. Sandoghdar, Opt. Commun. **85**, 355 (1991).

[6] K. B. MacAdam, A. Steinbach, and C. Wieman, Am. J. Phys. **60**, 1098 (1992).

[7] L. Ricci, M. Weidemüller, T. Esslinger, A. Hemmerich, C. Zimmermann, V. Vuletic, W. König, and T. W. Hänsch, Opt. Commun. **117**, 541 (1995).

[8] Throughout this article we provide details of the commercial components which we have used, in order to assist the reader who wishes to duplicate our system. Components from other manufacturers may of course deliver similar or better performance.

[9] P. McNicholl and H. J. Metcalf, Appl. Opt. **24**, 2757 (1985).

[10] K. Gibble, Proceedings of the 1997 NASA/JPL Fundamental Physics in Microgravity Workshop, Santa Barbara, 7–9 May 1997.

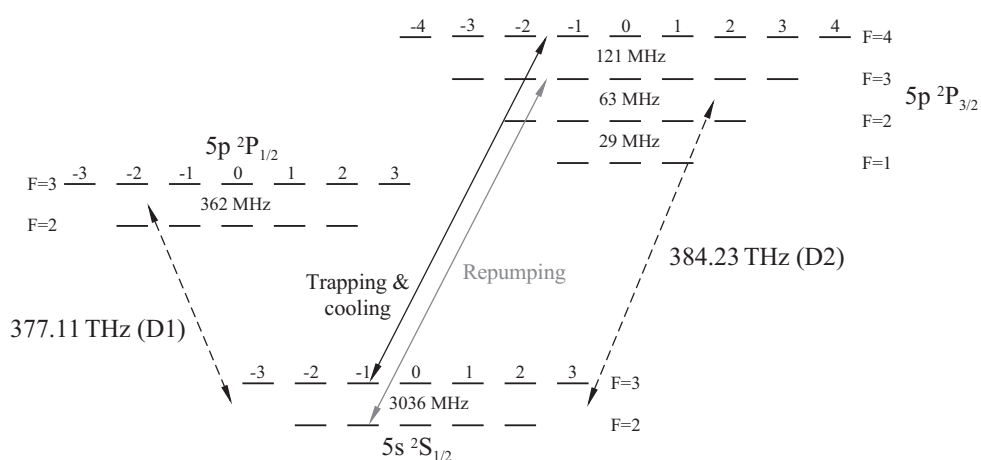# Appendix B

Rubidium energy levels

Figure B.1: The hyperfine splitting of low-lying ^{85}Rb energy levels (not to scale). Integers denote m_F levels, frequencies in MHz indicate the splitting between adjacent F levels. The intervals shown here (and other useful atomic information) can be found in chapter 5 of Ref. [1]
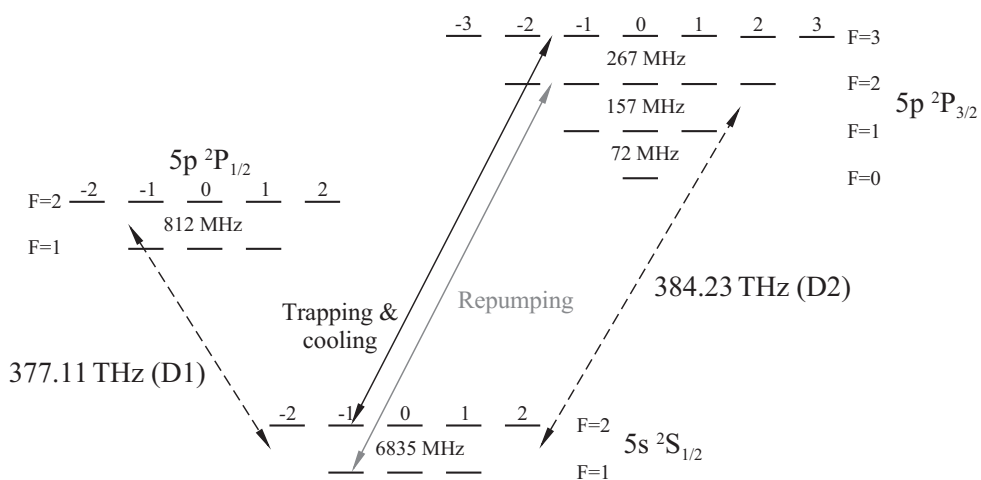

Figure B.2: The hyperfine splitting of low-lying ^{87}Rb energy levels. The vacuum wavelengths of the D1 and D2 lines are 795.0 nm and 780.2 nm respectively.

Appendix C

Rubidium relative oscillator strengths

Throughout this thesis the saturation intensity I_S for a two-level atomic transition is defined: $I/I_S = 2\Omega^2/\Gamma^2$, where I is the light intensity and Γ, Ω are the respective natural linewidth and Rabi frequency for the transition. The relative oscillator strength of a transition from a ground state $|L_g, S, J_g, I, F_g, m_{F_g}\rangle$ to an excited state $|L_e, S, J_e, I, F_e, m_{F_e}\rangle$ is given by:

$$\Omega^2 \quad \propto \quad (2J_g + 1)(2J_e + 1)(2F_g + 1)(2F_e + 1) \times$$
$$\begin{pmatrix} F_g & F_e & 1 \\ m_{F_g} & -m_{F_e} & m_{F_e} - m_{F_g} \end{pmatrix}^2 \begin{Bmatrix} J_g & F_g & I \\ F_e & J_e & 1 \end{Bmatrix}^2 \begin{Bmatrix} L_g & J_g & S \\ J_e & L_e & 1 \end{Bmatrix}^2, \qquad \text{(C.1)}$$

where () and {} are used for 3-J and 6-J symbols respectively. For the ground state of the D1 and D2 alkali metal transitions $J_g = S_g = 1/2$, $L_g = 0$ and the excited state quantum numbers for the D1 and D2 transitions are $J_e = 1/2, S_e = 1/2, L_e = 1$ and $J_e = 3/2, S_e = 1/2, L_e = 1$ respectively.

In absolute terms the saturation intensity for a given ground to excited transition is

$$\frac{1}{I_S} \quad = \quad \frac{36\pi c^2}{\hbar\Gamma\omega^3}(2J_g + 1)(2J_e + 1)(2F_g + 1)(2F_e + 1) \times$$
$$\begin{pmatrix} F_g & F_e & 1 \\ m_{F_g} & -m_{F_e} & m_{F_e} - m_{F_g} \end{pmatrix}^2 \begin{Bmatrix} J_g & F_g & I \\ F_e & J_e & 1 \end{Bmatrix}^2 \begin{Bmatrix} L_g & J_g & S \\ J_e & L_e & 1 \end{Bmatrix}^2 \qquad \text{(C.2)}$$

and the saturation intensity of the 'stretched state' transition

$$|F_g, m_{F_g}\rangle = |\pm(I + 1/2, I + 1/2)\rangle \rightarrow |F_e, m_{F_e}\rangle = |\pm(I + 3/2, I + 3/2)\rangle$$

is $I_S = \frac{\hbar\omega^3\Gamma}{12\pi c^2}$. This is the saturation intensity used throughout this thesis, and for rubidium $I_S = 1.67\,\mathrm{mW/cm}^2$.

	$g_{|1,-1\rangle}$	$g_{|1,0\rangle}$	$g_{|1,1\rangle}$	$g_{|2,-2\rangle}$	$g_{|2,-1\rangle}$	$g_{|2,0\rangle}$	$g_{|2,1\rangle}$	$g_{|2,2\rangle}$
$e_{|0,0\rangle}$	$\frac{1}{3}$	$\frac{1}{3}$	$\frac{1}{3}$	0	0	0	0	0
$e_{|1,-1\rangle}$	$\frac{5}{12}$	$\frac{5}{12}$	0	$\frac{1}{10}$	$\frac{1}{20}$	$\frac{1}{60}$	0	0
$e_{|1,0\rangle}$	$\frac{5}{12}$	0	$\frac{5}{12}$	0	$\frac{1}{20}$	$\frac{1}{15}$	$\frac{1}{20}$	0
$e_{|1,1\rangle}$	0	$\frac{5}{12}$	$\frac{5}{12}$	0	0	$\frac{1}{60}$	$\frac{1}{20}$	$\frac{1}{10}$
$e_{|2,-2\rangle}$	$\frac{1}{2}$	0	0	$\frac{1}{3}$	$\frac{1}{6}$	0	0	0
$e_{|2,-1\rangle}$	$\frac{1}{4}$	$\frac{1}{4}$	0	$\frac{1}{6}$	$\frac{1}{12}$	$\frac{1}{4}$	0	0
$e_{|2,0\rangle}$	$\frac{1}{12}$	$\frac{1}{3}$	$\frac{1}{12}$	0	$\frac{1}{4}$	0	$\frac{1}{4}$	0
$e_{|2,1\rangle}$	0	$\frac{1}{4}$	$\frac{1}{4}$	0	0	$\frac{1}{4}$	$\frac{1}{12}$	$\frac{1}{6}$
$e_{|2,2\rangle}$	0	0	$\frac{1}{2}$	0	0	0	$\frac{1}{6}$	$\frac{1}{3}$
$e_{|3,-3\rangle}$	0	0	0	1	0	0	0	0
$e_{|3,-2\rangle}$	0	0	0	$\frac{1}{3}$	$\frac{2}{3}$	0	0	0
$e_{|3,-1\rangle}$	0	0	0	$\frac{1}{15}$	$\frac{8}{15}$	$\frac{2}{5}$	0	0
$e_{|3,0\rangle}$	0	0	0	0	$\frac{1}{5}$	$\frac{3}{5}$	$\frac{1}{5}$	0
$e_{|3,1\rangle}$	0	0	0	0	0	$\frac{2}{5}$	$\frac{8}{15}$	$\frac{1}{15}$
$e_{|3,2\rangle}$	0	0	0	0	0	0	$\frac{2}{3}$	$\frac{1}{3}$
$e_{|3,3\rangle}$	0	0	0	0	0	0	0	1

Table C.1: Relative oscillator strengths for transitions from the ground state $|F_g, m_{F_g}\rangle = g_{|F_g,m_{F_g}\rangle}$ to the excited state $|F_e, m_{F_e}\rangle = e_{|F_e,m_{F_e}\rangle}$ in ^{87}Rb.

	$g_{|2,-2\rangle}$	$g_{|2,-1\rangle}$	$g_{|2,0\rangle}$	$g_{|2,1\rangle}$	$g_{|2,2\rangle}$	$g_{|3,-3\rangle}$	$g_{|3,-2\rangle}$	$g_{|3,-1\rangle}$	$g_{|3,0\rangle}$	$g_{|3,1\rangle}$	$g_{|3,2\rangle}$	$g_{|3,3\rangle}$
$e_{|1,-1\rangle}$	$\frac{3}{5}$	$\frac{3}{10}$	$\frac{1}{10}$	0	0	0	0	0	0	0	0	0
$e_{|1,0\rangle}$	0	$\frac{3}{10}$	$\frac{2}{5}$	$\frac{3}{10}$	0	0	0	0	0	0	0	0
$e_{|1,1\rangle}$	0	0	$\frac{1}{10}$	$\frac{3}{10}$	$\frac{3}{5}$	0	0	0	0	0	0	0
$e_{|2,-2\rangle}$	$\frac{14}{27}$	$\frac{7}{27}$	0	0	0	$\frac{10}{63}$	$\frac{10}{189}$	$\frac{2}{189}$	0	0	0	0
$e_{|2,-1\rangle}$	$\frac{7}{27}$	$\frac{7}{54}$	$\frac{7}{18}$	0	0	0	$\frac{20}{189}$	$\frac{16}{189}$	$\frac{2}{63}$	0	0	0
$e_{|2,0\rangle}$	0	$\frac{7}{18}$	0	$\frac{7}{18}$	0	0	0	$\frac{4}{63}$	$\frac{2}{21}$	$\frac{4}{63}$	0	0
$e_{|2,1\rangle}$	0	0	$\frac{7}{18}$	$\frac{7}{54}$	$\frac{7}{27}$	0	0	0	$\frac{2}{63}$	$\frac{16}{189}$	$\frac{20}{189}$	0
$e_{|2,2\rangle}$	0	0	0	$\frac{7}{27}$	$\frac{14}{27}$	0	0	0	0	$\frac{2}{189}$	$\frac{10}{189}$	$\frac{10}{63}$
$e_{|3,-3\rangle}$	$\frac{4}{9}$	0	0	0	0	$\frac{5}{12}$	$\frac{5}{36}$	0	0	0	0	0
$e_{|3,-2\rangle}$	$\frac{4}{27}$	$\frac{8}{27}$	0	0	0	$\frac{5}{36}$	$\frac{5}{27}$	$\frac{25}{108}$	0	0	0	0
$e_{|3,-1\rangle}$	$\frac{4}{135}$	$\frac{32}{135}$	$\frac{8}{45}$	0	0	0	$\frac{25}{108}$	$\frac{5}{108}$	$\frac{5}{18}$	0	0	0
$e_{|3,0\rangle}$	0	$\frac{4}{45}$	$\frac{4}{15}$	$\frac{4}{45}$	0	0	0	$\frac{5}{18}$	0	$\frac{5}{18}$	0	0
$e_{|3,1\rangle}$	0	0	$\frac{8}{45}$	$\frac{32}{135}$	$\frac{4}{135}$	0	0	0	$\frac{5}{18}$	$\frac{5}{108}$	$\frac{25}{108}$	0
$e_{|3,2\rangle}$	0	0	0	$\frac{8}{27}$	$\frac{4}{27}$	0	0	0	0	$\frac{25}{108}$	$\frac{5}{27}$	$\frac{5}{36}$
$e_{|3,3\rangle}$	0	0	0	0	$\frac{4}{9}$	0	0	0	0	0	$\frac{5}{36}$	$\frac{5}{12}$
$e_{|4,-4\rangle}$	0	0	0	0	0	1	0	0	0	0	0	0
$e_{|4,-3\rangle}$	0	0	0	0	0	$\frac{1}{4}$	$\frac{3}{4}$	0	0	0	0	0
$e_{|4,-2\rangle}$	0	0	0	0	0	$\frac{1}{28}$	$\frac{3}{7}$	$\frac{15}{28}$	0	0	0	0
$e_{|4,-1\rangle}$	0	0	0	0	0	0	$\frac{3}{28}$	$\frac{15}{28}$	$\frac{5}{14}$	0	0	0
$e_{|4,0\rangle}$	0	0	0	0	0	0	0	$\frac{3}{14}$	$\frac{4}{7}$	$\frac{3}{14}$	0	0
$e_{|4,1\rangle}$	0	0	0	0	0	0	0	0	$\frac{5}{14}$	$\frac{15}{28}$	$\frac{3}{28}$	0
$e_{|4,2\rangle}$	0	0	0	0	0	0	0	0	0	$\frac{15}{28}$	$\frac{3}{7}$	$\frac{1}{28}$
$e_{|4,3\rangle}$	0	0	0	0	0	0	0	0	0	0	$\frac{3}{4}$	$\frac{1}{4}$
$e_{|4,4\rangle}$	0	0	0	0	0	0	0	0	0	0	0	1

Table C.2: Relative oscillator strengths for transitions from ground to excited states in ^{85}Rb.

Appendix D

Electronic circuits

It is important, when operating the various electronic circuits described here, to use several floating power supplies. Earthing problems are often relatively easy to spot, but this is not always the case. In practice the minimal number of earths were used throughout the experimental set-up.
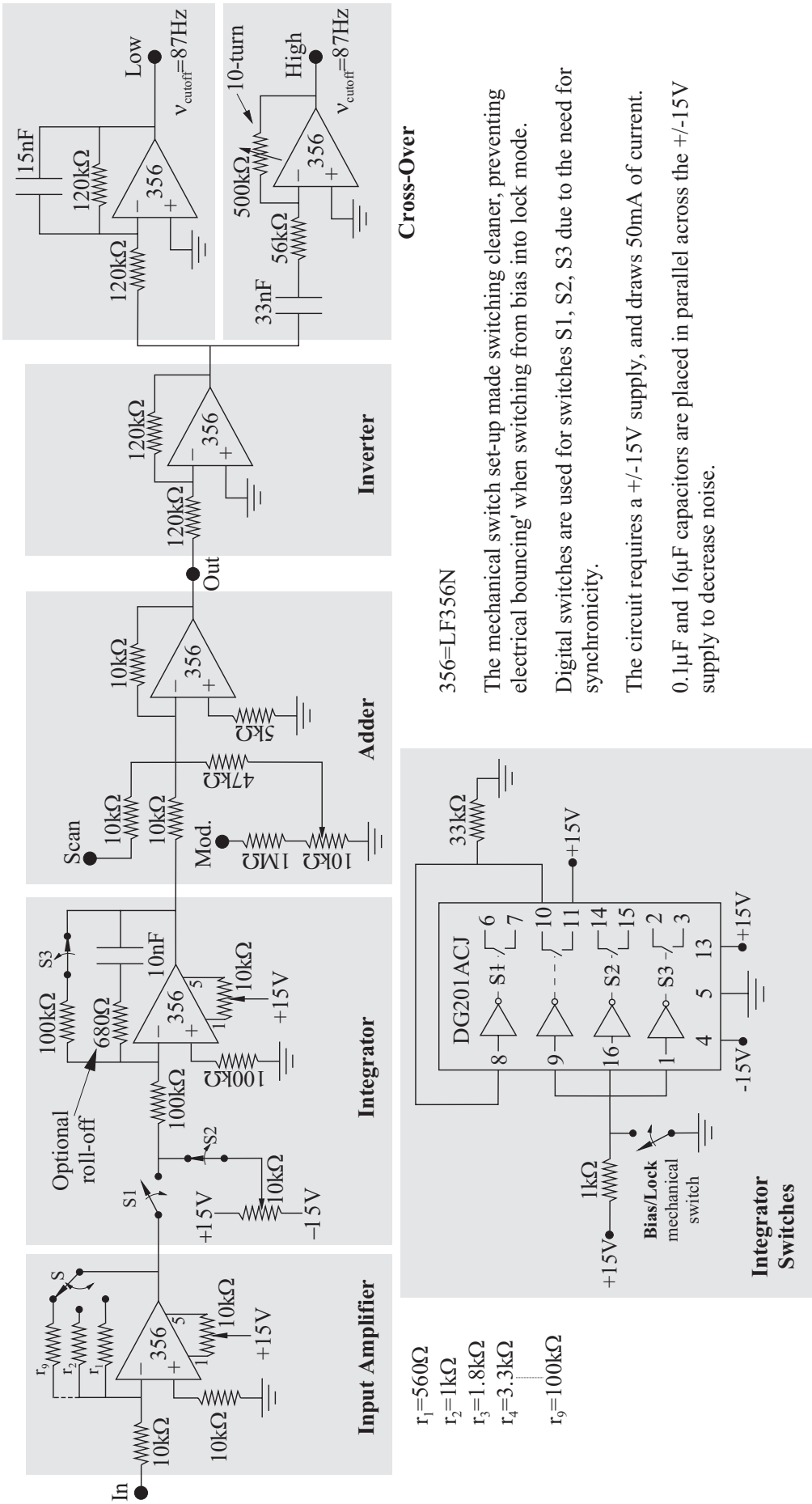
Figure D.1: The integrator circuit diagram. It is important to zero the offsets on the op-amps used in the input amplifier and integration stages. The input amplifier 'in' is grounded, and the pin 1-5 offset trimpot can be adjusted to give 0.0mV op-amp output for all gain stages. The integrator is then switched into 'lock' mode using the mechanical switch, and its pin 1-5 offset trimpot can be adjusted to give an approximately DC signal.

Figure D.2: The lock-in circuit. It is difficult to have low noise levels in the circuit's input amplifier, however this problem was solved on the PCB by physically separating the relatively noisy signal generator and phase shifter components from the more delicate input amplifier and demodulator. Thicker wires on the diagram indicate connections where shielded cable must be used.
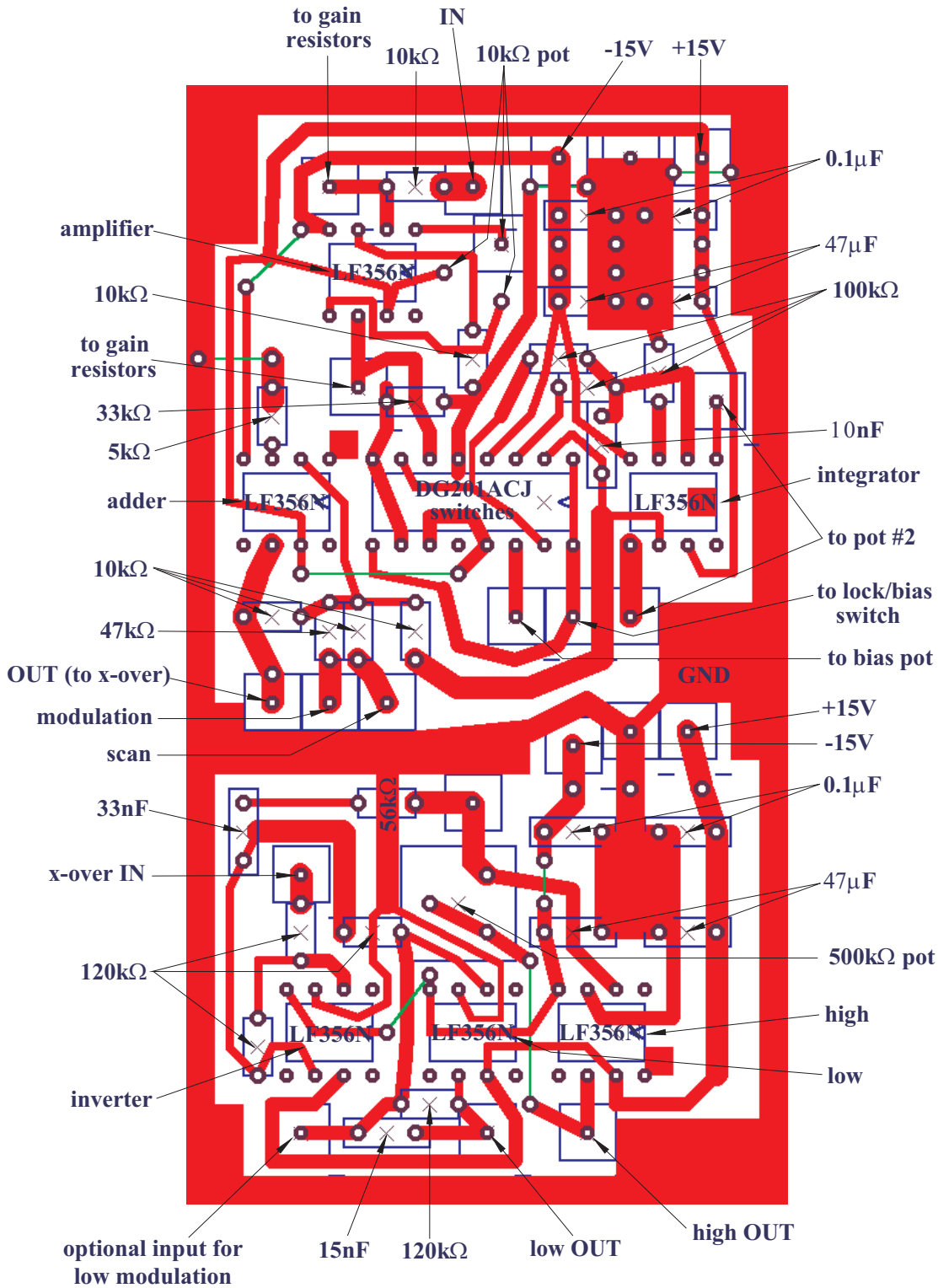
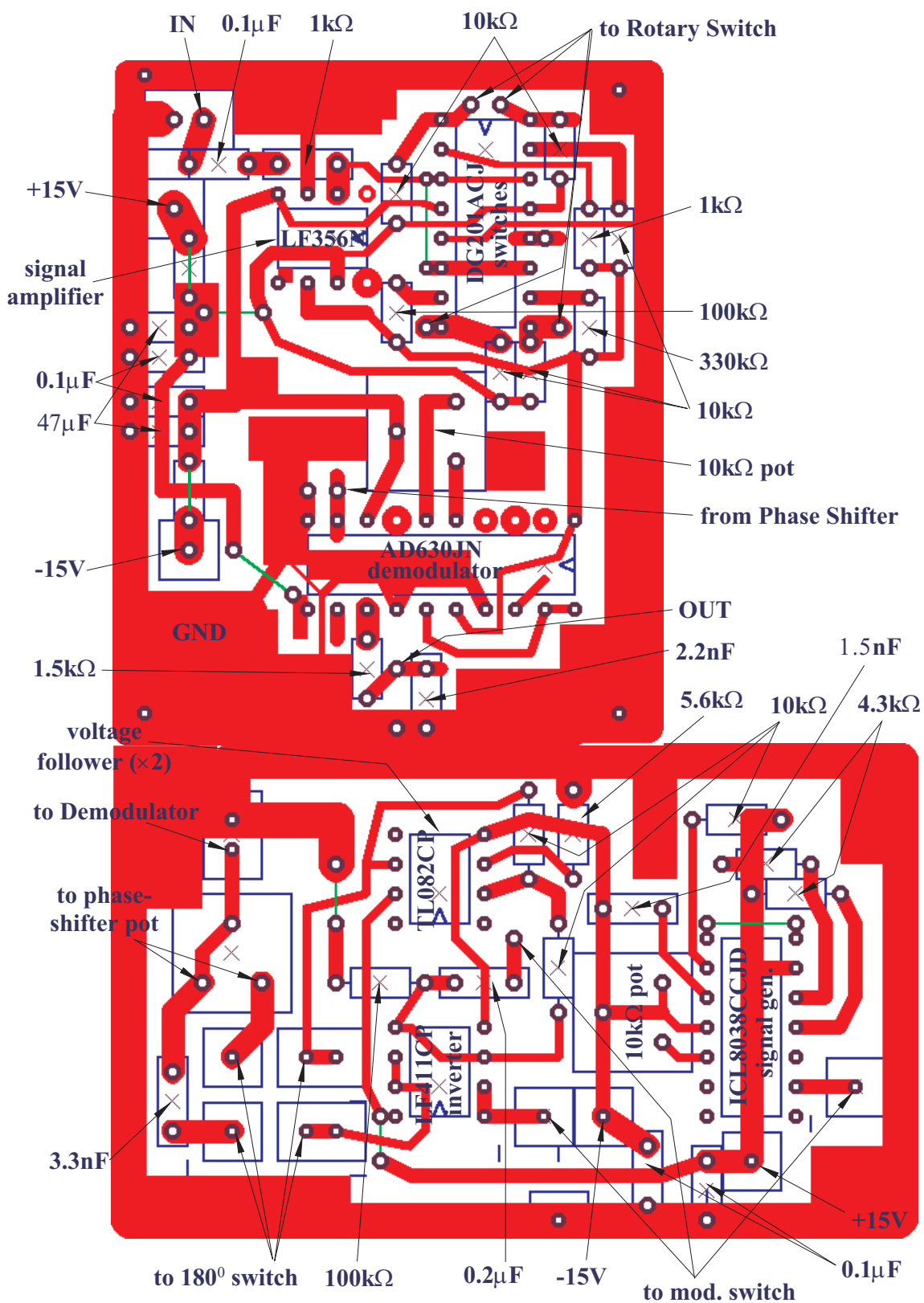Figure D.3: The integrator printed circuit board (PCB).

Figure D.4: The lock-in PCB. The frequency of the lock-in can be changed by altering the capacitive elements.
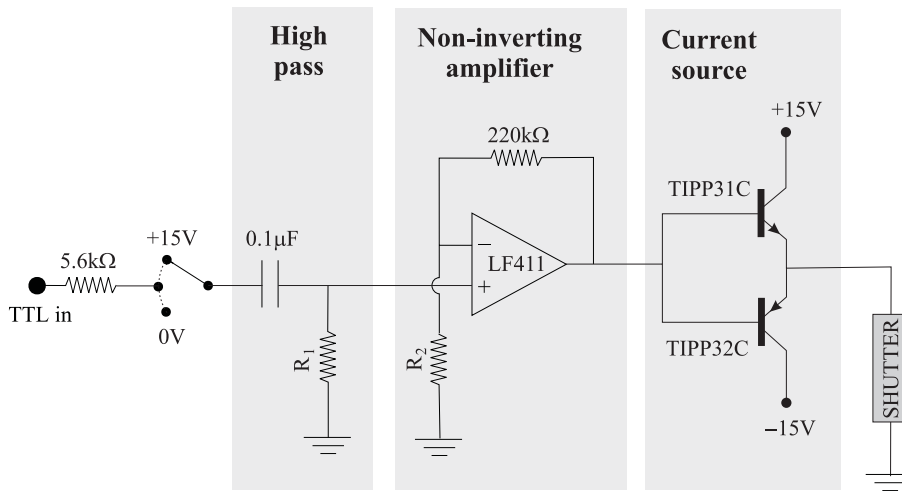
Figure D.5: The shutter-driver circuit. The high pass filter turns positive (negative) going TTL edges into short positive (negative) pulses, which are then amplified by the non-inverting amplifier. A transistor is then turned on to supply (extract) current to (from) the shutter relay. The mechanical switch allows the freedom of manual or computer-controlled operation. Different resistances were used in the circuits for the Newport ($R_1 = 100\,\mathrm{k\Omega}$, $R_2 = 120\,\mathrm{k\Omega}$) and home-made ($R_1 = 56\,\mathrm{k\Omega}$, $R_2 = 22\,\mathrm{k\Omega}$) shutters, due to the differing pulse durations needed to open their respective magnetic relays.
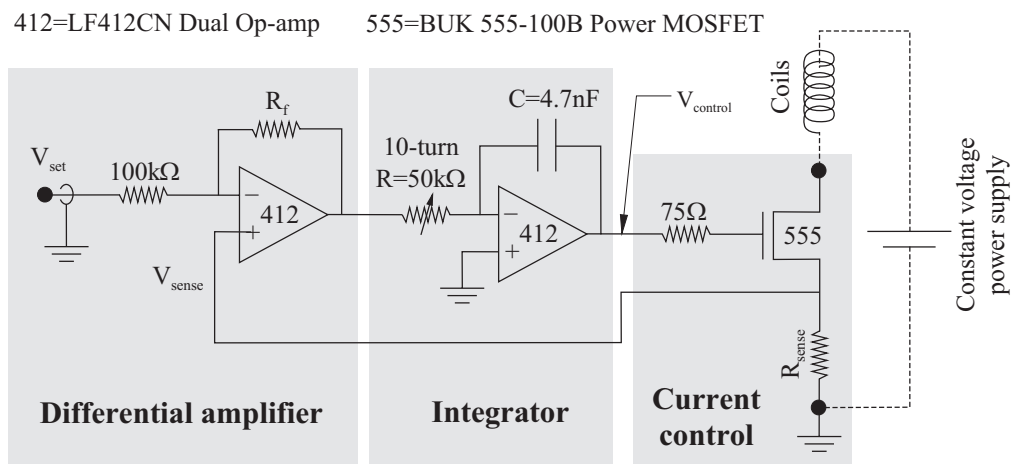

Figure D.6: The coil-driver circuit diagram. $V_{control} = \frac{1}{RC} \int \left(\frac{R_f}{100\,\mathrm{k\Omega}} V_{set} - (1 + \frac{R_f}{100\,\mathrm{k\Omega}}) V_{sense} \right) dt$. The circuits were built on heatsinks, to dissipate the energy generated by the MOSFET. Four identical circuits were made with $R_{sense} = 0.5\,\Omega$, $R_f = 100\,\mathrm{k\Omega}$: the three coil-drivers for the x, y, z bias coils, and also the LP MOT coil driver. Their response is $I_{coils} = 1\,\mathrm{A} \leftrightarrow V_{set} = 1\,\mathrm{V}$. A fifth driver was used to control the Ioffe-Pritchard 'extra' bias (IPEB) coils. As larger currents were used in this situation $R_{sense} = 0.1\,\Omega$, $R_f = 12\,\mathrm{k\Omega}$, and four BUK 456-60H MOSFETs were used in parallel (on a separate heatsink) to control the current flow. The response of this circuit is $I_{coils} = 1\,\mathrm{A} \leftrightarrow V_{set} = 0.93\,\mathrm{V}$. The five coil-drivers share the same $\pm15\,\mathrm{V}$, $200\,\mathrm{mA}$ power supply. Separate DC coil supplies were used, although a single 15 V supply was used in parallel for the x, y, z bias coils.
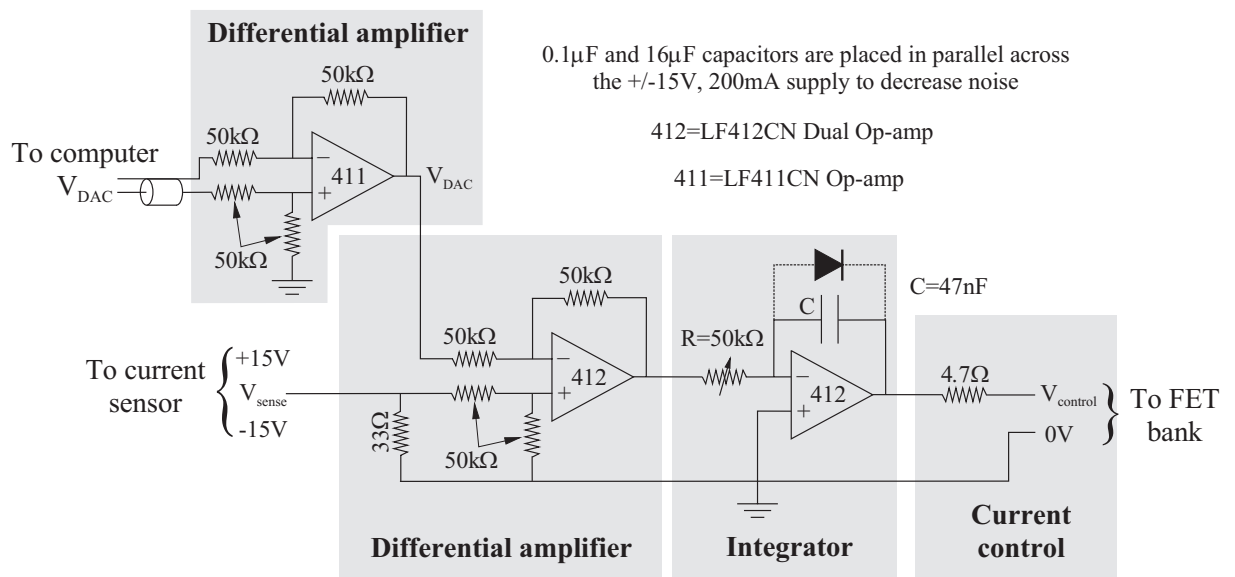
Figure D.7: The Ioffe-Pritchard (IP) coil-driver circuit diagram used for controlling the IP baseball and bias coils: $V_{control} = \frac{1}{RC} \int \left(V_{DAC} - V_{sense} \right) dt$. A similar circuit is used for the Helmholtz 'bounce' coils (Sec. 4.2.6). The optional diode can be used to prevent the control voltage becoming more than $0.7\,\text{V}$ negative. This increases the speed with which the coils can be switched on.
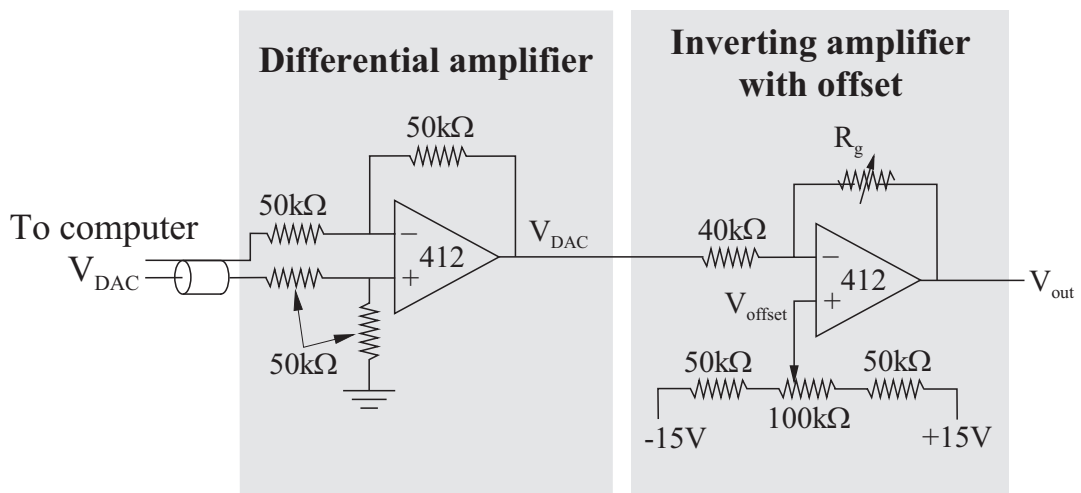
Figure D.8: Inverting amplifier with offset (IAO) circuit diagram. The IPB coils' DAC voltage is first passed through a differential amplifier to prevent noise on the DAC, and then passed through an inverting amplifier with offset. Ten-turn $100\,\text{k}\Omega$ lockable trimpots were used. The output voltage, $V_{out} = (1 + \frac{R_g}{40\,\text{k}\Omega})V_{offset} - V_{DAC}\frac{R_g}{40\,\text{k}\Omega}$, is then used to drive the IPEB coil driver (Fig. D.6).

Bibliography

[1] A. A. Radzig and B. M. Smirnov, *Reference Data on Atoms, Molecules, and Ions* (Springer-Verlag, Berlin, 1985).

[2] G. P. Barwood, P. Gill, and W. R. C. Rowley, "Frequency measurements on optically narrowed Rb-stabilised laser diodes at 780nm and 795nm," Appl. Phys. B **53,** 142–147 (1991).

[3] NIST physical reference data: http://physlab.nist.gov/cuu/Constants/index.html .

[4] U. Volz and H. Schmoranzer, "Precision lifetime measurements on alkali atoms and on helium by beam-gas-laser spectroscopy," Physica Scripta **T65,** 48–56 (1996).

[5] S. N. Bose, Z. Phys. **26,** 178 (1924).

[6] A. Einstein, Sitzber. Kgl. Preuss. Akad. Wiss. p. 261 (1924).

[7] A. Einstein, Sitzber. Kgl. Preuss. Akad. Wiss. p. 3 (1925).

[8] *Bose-Einstein Condensation*, A. Griffin, D. W. Snoke, and S. Stringari, eds., (Cambridge Uni. Press, Cambridge, 1996).

[9] F. Dalfovo, S. Giorgini, and L. P. Pitaevskii, "Theory of Bose-Einstein condensation in trapped gases," Rev. Mod. Phys. **71,** 463–512 (1999).

[10] E. A. Cornell, J. R. Ensher, and C. E. Wieman, "Experiments in dilute atomic Bose-Einstein condensation," preprint: 1998 Enrico Fermi summer school on BEC .

[11] S. Chu, L. Hollberg, J. E. Bjorkholm, A. Cable, and A. Ashkin, "Three-dimensional viscous confinement and cooling of atoms by resonance radiation pressure," Phys. Rev. Lett. **55,** 48–51 (1985).

[12] E. L. Raab, M. Prentiss, A. Cable, S. Chu, and D. E. Pritchard, "Trapping of neutral sodium atoms with radiation pressure," Phys. Rev. Lett. **59,** 2631–2634 (1987).

[13] P. D. Lett, R. N. Watts, C. I. Westbrook, W. D. Phillips, P. L. Gould, and H. J. Metcalf, "Observation of atoms laser cooled below the Doppler limit," Phys. Rev. Lett. **61,** 169–172 (1988).

[14] Special Issue, J. Opt. Soc. Am. B **6,** 2020–2278 (1989).

[15] D. W. Sesko, T. G. Walker, and C. E. Wieman, "Behavior of neutral atoms in a spontaneous force trap," J. Opt. Soc. Am. B **8,** 946–958 (1991).

[16] W. Ketterle, K. B. Davis, M. A. Joffe, A. Martin, and D. E. Pritchard, "High densities of cold atoms in a *dark* spontaneous-force optical trap ," Phys. Rev. Lett. **70,** 2253–2256 (1993).

[17] M. H. Anderson, W. Petrich, J. R. Ensher, and E. A. Cornell, "Reduction of light-assisted collisional loss rate from a low-pressure vapor-cell trap," Phys. Rev. A **50,** R3597–R3600 (1994).

[18] C. G. Townsend, N. H. Edwards, K. P. Zetie, C. J. Cooper, J. Rink, and C. J. Foot, "High-density trapping of cesium atoms in a dark magneto-optical trap," Phys. Rev. A **53,** 1702–1714 (1996).

[19] W. Petrich, M. H. Anderson, J. R. Ensher, and E. A. Cornell, "Behaviour of atoms in a compressed magneto-optical trap," J. Opt. Soc. Am. B **11,** 1332–1335 (1994).

[20] W. Petrich, M. H. Anderson, J. R. Ensher, and E. A. Cornell, "Stable, tightly confining magnetic trap for evaporative cooling of neutral atoms," Phys. Rev. Lett. **74,** 3352–3355 (1995).

[21] Y. V. Gott, M. S. Ioffe, and V. G. Telkovsky, in *Nuclear Fusion, 1962 Suppl., Pt. 3* (International Atomic Energy Agency, Vienna, 1962), pp. 1045–1049,1284.

[22] D. E. Pritchard, "Cooling neutral atoms in a magnetic trap for precision spectroscopy," Phys. Rev. Lett. **51,** 1336–1339 (1983).

[23] C. J. Myatt, N. R. Newbury, R. W. Ghrist, S. Loutzenhiser, and C. E. Wieman, "Multiply loaded magneto-optical trap," Opt. Lett. **21,** 290–292 (1996).

[24] W. D. Phillips and H. Metcalf, "Laser deceleration of an atomic beam," Phys. Rev. Lett. **48,** 596–599 (1982).

[25] T. E. Barrett, S. W. Dapore-Schwartz, M. D. Ray, and G. P. Lafyatis, "Slowing atoms with σ^- polarised light," Phys. Rev. Lett. **67,** 3483–3486 (1991).

[26] V. I. Balykin, V. S. Letokhov, and V. I. Mushin, JETP Lett. **29,** 560 (1979).

[27] W. Ertmer, R. Blatt, J. L. Hall, and M. Zhu, "Laser manipulation of atomic-beam velocities - demonstration of stopped atoms and velocity reversal," Phys. Rev. Lett. **54,** 996–999 (1985).

[28] R. Blatt, W. Ertmer, P. Zoller, and J. L. Hall, "Atomic-beam cooling - a simulation approach," Phys. Rev. A **34,** 3022–3033 (1986).

[29] M. H. Anderson, J. R. Ensher, M. R. Matthews, C. E. Wieman, and E. A. Cornell, "Observation of Bose-Einstein condensation in a dilute atomic vapor," Science **269,** 198–201 (1995).

[30] D. S. Jin, J. R. Ensher, M. R. Matthews, C. E. Wieman, and E. A. Cornell, "Collective excitations of a Bose-Einstein condensate in a dilute gas," Phys. Rev. Lett. **77,** 420–423 (1996).

[31] J. R. Ensher, D. S. Jin, M. R. Matthews, C. E. Wieman, and E. A. Cornell, "Bose-Einstein condensation in a dilute gas: Measurement of energy and ground-state occupation," Phys. Rev. Lett. **77,** 4984–4987 (1996).

[32] D. S. Jin, M. R. Matthews, J. R. Ensher, C. E. Wieman, and E. A. Cornell, "Temperature-dependent damping and frequency shifts in collective excitations of a dilute Bose-Einstein condensate," Phys. Rev. Lett. **78,** 764–767 (1997).

[33] C. J. Myatt, E. A. Burt, R. W. Ghrist, E. A. Cornell, and C. E. Wieman, "Production of two overlapping Bose-Einstein condensates by sympathetic cooling," Phys. Rev. Lett. **78,** 586–589 (1997).

[34] E. A. Burt, R. W. Ghrist, C. J. Myatt, M. J. Holland, E. A. Cornell, and C. E. Wieman, "Coherence, correlations, and collisions: what one learns about Bose-Einstein condensates from their decay," Phys. Rev. Lett. **79,** 337–340 (1997).

[35] M. R. Matthews, D. S. Hall, D. S. Jin, J. R. Ensher, C. E. Wieman, E. A. Cornell, F. Dalfovo, C. Minniti, and S. Stringari, "Dynamical response of a Bose-Einstein condensate to a discontinuous change in internal state," Phys. Rev. Lett. **81,** 243–247 (1998).

[36] D. S. Hall, M. R. Matthews, J. R. Ensher, C. E. Wieman, and E. A. Cornell, "Dynamics of component separation in a binary mixture of Bose-Einstein condensates," Phys. Rev. Lett. **81,** 1539–1542 (1998).

[37] D. S. Hall, M. R. Matthews, C. E. Wieman, and E. A. Cornell, "Measurements of relative phase in two-component Bose-Einstein condensates," Phys. Rev. Lett. **81,** 1543–1546 (1998).

[38] E. A. Cornell, D. S. Hall, M. R. Matthews, and C. E. Wieman, "Having it both ways: Distinguishable yet phase-coherent mixtures of Bose-Einstein condensates," J. Low Temp. Phys. **113,** 151–165 (1998).

[39] K. B. Davis, M. O. Mewes, M. R. Andrews, N. J. van Druten, D. S. Durfee, D. M. Kurn, and W. Ketterle, "Bose-Einstein condensation in a gas of sodium atoms," Phys. Rev. Lett. **75,** 3969–3973 (1995).

[40] M. O. Mewes, M. R. Andrews, N. J. van Druten, D. M. Kurn, D. S. Durfee, and W. Ketterle, "Bose-Einstein condensation in a tightly confining dc magnetic trap," Phys. Rev. Lett. **77,** 416–419 (1996).

[41] M. R. Andrews, M. O. Mewes, N. J. van Druten, D. S. Durfee, D. M. Kurn, and W. Ketterle, "Direct, non-destructive observation of a Bose condensate," Science **273,** 84–87 (1996).

[42] M. O. Mewes, M. R. Andrews, N. J. van Druten, D. M. Kurn, D. S. Durfee, C. G. Townsend, and W. Ketterle, "Collective excitations of a Bose-Einstein condensate in a magnetic trap," Phys. Rev. Lett. **77,** 988–991 (1996).

[43] M. O. Mewes, M. R. Andrews, D. M. Kurn, D. S. Durfee, C. G. Townsend, and W. Ketterle, "Output coupler for Bose-Einstein condensed atoms," Phys. Rev. Lett. **78,** 582–585 (1997).

[44] M. R. Andrews, C. G. Townsend, H. J. Miesner, D. S. Durfee, D. M. Kurn, and W. Ketterle, "Observation of interference between two Bose condensates," Science **275,** 637–641 (1997).

[45] M. R. Andrews, D. M. Kurn, H. J. Miesner, D. S. Durfee, C. G. Townsend, S. Inouye, and W. Ketterle, "Propagation of sound in a Bose-Einstein condensate," Phys. Rev. Lett. **79,** 553–556 (1997).

[46] M. R. Andrews, D. M. Stamper-Kurn, H. J. Miesner, D. S. Durfee, C. G. Townsend, S. Inouye, and W. Ketterle, "Propagation of sound in a Bose-Einstein condensate (vol. 79, p. 553, 1997)," Phys. Rev. Lett. **80,** 2967 (1998).

[47] D. M. Stamper-Kurn, M. R. Andrews, A. P. Chikkatur, S. Inouye, H. J. Miesner, J. Stenger, and W. Ketterle, "Optical confinement of a Bose-Einstein condensate," Phys. Rev. Lett. **80,** 2027–2030 (1998).

[48] S. Inouye, M. R. Andrews, J. Stenger, H. J. Miesner, D. M. Stamper-Kurn, and W. Ketterle, "Observation of Feshbach resonances in a Bose-Einstein condensate," Nature **392,** 151–154 (1998).

[49] H. J. Miesner, D. M. Stamper-Kurn, M. R. Andrews, D. S. Durfee, S. Inouye, and W. Ketterle, "Bosonic stimulation in the formation of a Bose-Einstein condensate," Science **279,** 1005–1007 (1998).

[50] D. M. Stamper-Kurn, H. J. Miesner, S. Inouye, M. R. Andrews, and W. Ketterle, "Collisionless and hydrodynamic excitations of a Bose-Einstein condensate," Phys. Rev. Lett. **81,** 500–503 (1998).

[51] D. M. Stamper-Kurn, H. J. Miesner, A. P. Chikkatur, S. Inouye, J. Stenger, and W. Ketterle, "Reversible formation of a Bose-Einstein condensate," Phys. Rev. Lett. **81,** 2194–2197 (1998).

[52] J. Stenger, S. Inouye, D. M. Stamper-Kurn, H. J. Miesner, A. P. Chikkatur, and W. Ketterle, "Spin domains in ground-state Bose-Einstein condensates," Nature **396,** 345–348 (1998).

[53] H. J. Miesner, D. M. Stamper-Kurn, J. Stenger, S. Inouye, A. P. Chikkatur, and W. Ketterle, "Observation of metastable states in spinor Bose-Einstein condensates," Phys. Rev. Lett. **82,** 2228–2231 (1999).

[54] J. Stenger, S. Inouye, M. R. Andrews, H. J. Miesner, D. M. Stamper-Kurn, and W. Ketterle, "Strongly enhanced inelastic collisions in a Bose-Einstein condensate near Feshbach resonances," Phys. Rev. Lett. **82,** 2422–2425 (1999).

[55] J. Stenger, S. Inouye, A. P. Chikkatur, D. M. Stamper-Kurn, D. E. Pritchard, and W. Ketterle, "Bragg spectroscopy of a Bose-Einstein condensate," Phys. Rev. Lett. **82,** 4569–4573 (1999).

[56] D. M. Stamper-Kurn, H.-J. Miesner, A. P. Chikkatur, S. Inouye, J. Stenger, and W. Ketterle, "Quantum tunneling across spin domains in a Bose-Einstein condensate," Phys. Rev. Lett. **83,** 661–664 (1999).

[57] C. C. Bradley, C. A. Sackett, J. J. Tollett, and R. G. Hulet, "Evidence of Bose-Einstein condensation in an atomic gas with attractive interactions," Phys. Rev. Lett. **75,** 1687–1690 (1995).

[58] C. C. Bradley, C. A. Sackett, J. J. Tollett, and R. G. Hulet, "Evidence of Bose-Einstein condensation in an atomic gas with attractive interactions (vol. 75, p.1687, 1995)," Phys. Rev. Lett. **79,** 1170 (1997).

[59] C. C. Bradley, C. A. Sackett, and R. G. Hulet, "Bose-Einstein condensation of lithium: Observation of limited condensate number," Phys. Rev. Lett. **78,** 985–989 (1997).

[60] C. C. Bradley, C. A. Sackett, and R. G. Hulet, "Analysis of in situ images of Bose-Einstein condensates of lithium," Phys. Rev. A **55,** 3951–3953 (1997).

[61] C. A. Sackett, C. C. Bradley, M. Welling, and R. G. Hulet, "Bose-Einstein condensation of lithium," Appl. Phys. B **65,** 433–440 (1997).

[62] C. A. Sackett, H. T. C. Stoof, and R. G. Hulet, "Growth and collapse of a Bose-Einstein condensate with attractive interactions," Phys. Rev. Lett. **80,** 2031–2034 (1998).

[63] C. A. Sackett, J. M. Gerton, M. Welling, and R. G. Hulet, "Measurements of collective collapse in a Bose-Einstein condensate with attractive interactions," Phys. Rev. Lett. **82,** 876–879 (1999).

[64] D. J. Han, R. H. Wynar, P. Courteille, and D. J. Heinzen, "Bose-Einstein condensation of large numbers of atoms in a magnetic time-averaged orbiting potential trap," Phys. Rev. A **57,** R4114–R4117 (1998).

[65] L. V. Hau, B. D. Busch, C. Liu, Z. Dutton, M. M. Burns, and J. A. Golovchenko, "Near-resonant spatial images of confined Bose-Einstein condensates in a 4-Dee magnetic bottle," Phys. Rev. A **58,** R54–R57 (1998).

[66] L. V. Hau, S. E. Harris, Z. Dutton, and C. H. Behroozi, "Light speed reduction to 17 metres per second in an ultracold atomic gas," Nature **397,** 594–598 (1999).

[67] B. P. Anderson and M. A. Kasevich, "Spatial observation of Bose-Einstein condensation of ^{87}Rb in a confining potential," Phys. Rev. A **59,** R938–R941 (1999).

[68] B. P. Anderson and M. A. Kasevich, "Macroscopic quantum interference from atomic tunnel arrays," Science **282,** 1686–1689 (1998).

[69] U. Ernst, A. Marte, F. Schreck, J. Schuster, and G. Rempe, "Bose-Einstein condensation in a pure Ioffe-Pritchard field configuration," Europhys. Lett. **41,** 1–6 (1998).

[70] U. Ernst, J. Schuster, F. Schreck, A. Marte, A. Kuhn, and G. Rempe, "Free expansion of a Bose-Einstein condensate from an Ioffe-Pritchard magnetic trap," Appl. Phys. B **67,** 719–722 (1998).

[71] T. Esslinger, I. Bloch, and T. W. Hansch, "Bose-Einstein condensation in a quadrupole-Ioffe-configuration trap," Phys. Rev. A **58,** R2664–R2667 (1998).

[72] I. Bloch, T. W. Hansch, and T. Esslinger, "Atom laser with a cw output coupler," Phys. Rev. Lett. **82,** 3008–3011 (1999).

[73] M. Kozuma, L. Deng, E. W. Hagley, J. Wen, R. Lutwak, K. Helmerson, S. L. Rolston, and W. D. Phillips, "Coherent splitting of Bose-Einstein condensed atoms with optically induced Bragg diffraction," Phys. Rev. Lett. **82,** 871–875 (1999).

[74] E. W. Hagley, L. Deng, M. Kozuma, J. Wen, K. Helmerson, S. L. Rolston, and W. D. Phillips, "A well-collimated quasi-continuous atom laser," Science **283,** 1706–1709 (1999).

[75] L. Deng, E. W. Hagley, J. Wen, M. Trippenbach, Y. Band, P. S. Julienne, J. E. Simsarian, K. Helmerson, S. L. Rolston, and W. D. Phillips, "Four-wave mixing with matter waves," Nature **398,** 218–220 (1999).

[76] Y. B. Ovchinnikov, J. H. Müller, M. R. Doery, E. J. D. Vredenbregt, K. Helmerson, S. L. Rolston, and W. D. Phillips, "Diffraction of a released Bose-Einstein condensate by a pulsed standing light wave," Phys. Rev. Lett. **83,** 284–287 (1999).

[77] J. Söding, D. Guéry-Odelin, P. Desbiolles, F. Chevy, H. Inamori, and J. Dalibard, "Three-body decay of a rubidium Bose-Einstein condensate," preprint .

[78] T. C. Killian, D. G. Fried, L. Willmann, D. Landhuis, S. C. Moss, T. J. Greytak, and D. Kleppner, "Cold collision frequency shift of the 1S-2S transition in hydrogen," Phys. Rev. Lett. **81,** 3807–3810 (1998).

[79] D. G. Fried, T. C. Killian, L. Willmann, D. Landhuis, S. C. Moss, D. Kleppner, and T. J. Greytak, "Bose-Einstein condensation of atomic hydrogen," Phys. Rev. Lett. **81,** 3811–3814 (1998).

[80] V. Boyer, B. Desruelle, P. Bouyer, C. Westbrook, and A. Aspect, "Electromagnet for Bose-Einstein condensation," Annales de Physique **23,** 197–198 (1998).

[81] B. Desruelle, V. Boyer, S. G. Murdoch, G. Delannoy, P. Bouyer, and A. Aspect, "Interrupted evaporative cooling of ^{87}Rb atoms trapped in a high magnetic field," Phys. Rev. A **60,** R1759–R1762 (1998).

[82] J. L. Martin, C. R. McKenzie, N. R. Thomas, J. C. Sharpe, D. M. Warrington, P. J. Manson, W. J. Sandle, and A. C. Wilson, "Output coupling of a Bose-Einstein condensate formed in a TOP trap," J. Phys. B **32,** 3065–3075 (1999).

[83] Y. Torii, Y. Suzuki, M. Kozuma, and T. Kuga, "Realization of Bose-Einstein condensation in a rubidium vapor using a simple double magneto-optical trap," http://phys3.c.u-tokyo.ac.jp/torii/bec/proceeding.html .

[84] A. Ashkin, "Trapping of atoms by resonance radiation pressure," Phys. Rev. Lett. **40,** 729–732 (1978).

[85] Y. Castin and R. Dum, "Bose-Einstein condensates in time dependent traps," Phys. Rev. Lett. **77,** 5315–5319 (1996).

[86] M. R. Matthews, B. P. Anderson, P. C. Haljan, D. S. Hall, C. E. Wieman, and E. A. Cornell, "Vortices in a Bose-Einstein condensate," Phys. Rev. Lett. pp. 2498–2501 (1999).

[87] S. Inouye, A. P. Chikkatur, D. M. Stamper-Kurn, J. Stenger, D. E. Pritchard, and W. Ketterle, "Superradiant Rayleigh scattering from a Bose-Einstein condensate," preprint .

[88] B. de Marco and D. S. Jin, "Onset of Fermi degeneracy in a trapped atomic gas," Science **285,** 1703–1706 (1999).

[89] K. Burnett, "Bose-Einstein condensation with evaporatively cooled atoms," Contemp. Phys. **37,** 1–14 (1996).

[90] W. Ketterle, M. R. Andrews, K. B. Davis, D. S. Durfee, D. M. Kurn, M. O. Mewes, and N. J. vanDruten, "Bose-Einstein condensation of ultracold atomic gases," Physica Scripta **T66,** 31–37 (1996).

[91] C. E. Wieman, "The creation and study of Bose-Einstein condensation in a dilute atomic vapour," Phil. Trans. Royal Soc. London A **355,** 2247–2257 (1997).

[92] D. S. Durfee and W. Ketterle, "Experimental studies of Bose-Einstein condensation," Optics Express **2,** 299–313 (1998).

[93] M. R. Andrews, D. S. Durfee, S. Inouye, D. M. Stamper-Kurn, H. J. Miesner, and W. Ketterle, "Studies of Bose-Einstein condensates," J. Low Temp. Phys. **110,** 153–166 (1998).

[94] H. J. Miesner and W. Ketterle, "Bose-Einstein condensation in dilute atomic gases," Solid State Comm. **107,** 629–637 (1998).

[95] A. S. Parkins and D. F. Walls, "The physics of trapped dilute-gas Bose-Einstein condensates," Phys. Rep. **303,** 2–80 (1998).

[96] W. Ketterle, D. S. Durfee, and D. M. Stamper-Kurn, "Making, probing and understanding Bose-Einstein condensates," preprint: 1998 Enrico Fermi summer school on BEC .

[97] GSU BEC web site: http://amo.phy.gasou.edu:80/bec.html .

[98] LANL preprint archive: http://xxx.lanl.gov/, under 'physics' or 'cond-mat' .

[99] M. Morinaga, M. Yasuda, T. Kishimoto, and F. Shimizu, "Holographic manipulation of a cold atomic beam," Phys. Rev. Lett. **77,** 802–805 (1996).

[100] J. J. Berkhout, O. J. Luiten, I. D. Setija, T. W. Hijmans, T. Mizusaki, and J. T. M. Walraven, "Quantum reflection - focusing of hydrogen atoms with a concave mirror," Phys. Rev. Lett. **63,** 1689–1692 (1989).

[101] B. Holst and W. Allison, "An atom-focusing mirror," Nature **390,** 244 (1997).

[102] E. A. Hinds and I. G. Hughes, "Magnetic atom optics: mirrors, guides, traps, and chips for atoms," J. Phys. D **32,** R119–R146 (1999).

[103] K. Sengstock and W. Ertmer, "Laser manipulation of atoms," Adv. Atom. Mol. Opt. Phys. **35,** 1–44 (1995).

[104] S. Chu, J. E. Bjorkholm, A. Cable, and A. Ashkin, "Experimental observation of optically trapped atoms," Phys. Rev. Lett. **57,** 314–317 (1986).

[105] C. S. Adams, H. J. Lee, N. Davidson, M. Kasevich, and S. Chu, "Evaporative cooling in a crossed dipole trap," Phys. Rev. Lett. **74,** 3577–3580 (1995).

[106] N. Davidson, H. J. Lee, C. S. Adams, M. Kasevich, and S. Chu, "Long atomic coherence times in an optical dipole trap," Phys. Rev. Lett. **74,** 1311–1314 (1995).

[107] H. J. Lee, C. S. Adams, M. Kasevich, and S. Chu, "Raman cooling of atoms in an optical dipole trap," Phys. Rev. Lett. **76,** 2658–2661 (1996).

[108] V. Vuletic, C. Chin, A. J. Kerman, and S. Chu, "Degenerate Raman sideband cooling of trapped cesium atoms at very high atomic densities," Phys. Rev. Lett. **81,** 5768–5771 (1998).

[109] V. I. Balykin, V. S. Letokhov, Y. B. Ovchinnikov, and A. I. Sidorov, "Reflection of an atomic beam from a gradient of an optical field," JETP Lett. **45,** 353–356 (1987).

[110] M. A. Kasevich, D. S. Weiss, and S. Chu, "Normal-incidence reflection of slow atoms from an optical evanescent wave," Opt. Lett. **15,** 607–609 (1990).

[111] R. J. Cook and R. K. Hill, "An electromagnetic mirror for neutral atoms," Opt. Commun. **43,** 258–260 (1982).

[112] K. Bongs, S. Burger, G. Birkl, K. Sengstock, W. Ertmer, K. Rzazewski, A. Sanpera, and M. Lewenstein, "Coherent evolution of bouncing Bose-Einstein condensates," Phys. Rev. Lett. **83,** 3577–3580 (1999).

[113] T. M. Roach, H. Abele, M. G. Boshier, H. L. Grossman, K. P. Zetie, and E. A. Hinds, "Realization of a magnetic-mirror for cold atoms," Phys. Rev. Lett. **75,** 629–632 (1995).

[114] G. I. Opat, S. J. Wark, and A. Cimmino, "Electric and magnetic mirrors and gratings for slowly moving neutral atoms and molecules," Appl. Phys. B **54,** 396–402 (1992).

[115] C. V. Saba, P. A. Barton, M. G. Boshier, I. G. Hughes, P. Rosenbusch, B. E. Sauer, and E. A. Hinds, "Reconstruction of a cold atom cloud by magnetic focusing," Phys. Rev. Lett. **82,** 468–471 (1999).

[116] A. S. Arnold, C. MacCormick, and M. G. Boshier, "Magnetic 'bouncing' of a BEC," To appear in: proceedings of the 1999 ICOLS .

[117] N. J. van Druten and W. Ketterle, "Two-step condensation of the ideal Bose gas in highly anisotropic traps," Phys. Rev. Lett. **79,** 549–552 (1997).

[118] G. Baym and C. J. Pethick, "Ground-state properties of magnetically trapped Bose-condensed rubidium gas," Phys. Rev. Lett. **76,** 6–9 (1996).

[119] K. Huang, *Statistical Mechanics* (Wiley, New York, 1987).

[120] W. Ketterle and N. J. van Druten, "Bose-Einstein condensation of a finite number of particles trapped in one or three dimensions," Phys. Rev. A **54,** 656–660 (1996).

[121] V. S. Bagnato, D. E. Pritchard, and D. Kleppner, "Bose-Einstein condensation in an external potential," Phys. Rev. A **35,** 4354–4358 (1987).

[122] W. Krauth, "Quantum Monte Carlo calculations for a large number of bosons in a harmonic trap," Phys. Rev. Lett. **77,** 3695–3699 (1996).

[123] L. P. Pitaevskii, "Bose-Einstein condensation in magnetic traps. Introduction to the theory," Physics – Uspekhi **41,** 569–580 (1998).

[124] J. P. Burke, J. L. Bohn, B. D. Esry, and C. H. Greene, "Prospects for mixed-isotope Bose-Einstein condensates in rubidium," Phys. Rev. Lett. **80,** 2097–2100 (1998).

[125] F. Dalfovo and S. Stringari, "Bosons in anisotropic traps: ground states and vortices," Phys. Rev. A **53,** 2477–2485 (1996).

[126] K. B. Davis, M. O. Mewes, and W. Ketterle, "An analytical model for evaporative cooling of atoms," Appl. Phys. B **60,** 155–159 (1995).

[127] C. R. Monroe, "Experiments with optically and magnetically trapped cesium atoms," PhD thesis, University of Colorado (1992).

[128] O. J. Luiten, M. W. Reynolds, and J. T. M. Walraven, "Kinetic theory of the evaporative cooling of a trapped gas," Phys. Rev. A **53,** 381–389 (1996).

[129] J. T. M. Walraven, "Atomic hydrogen in magnetostatic traps," Proc. Scott. Univ. Summer Sch. Phys. **44,** 315–352 (1996).

[130] R. Frisch, Z. Phys. **86,** 42 (1933).

[131] P. W. Milonni and J. H. Eberly, *Lasers* (Wiley, New York, 1988).

[132] A. S. Arnold, "Cool things you can do with lasers," MSc thesis, University of Otago (1996).

[133] C. Cohen-Tannoudji, J. Dupont-Roc, and G. Grynberg, *Atom-Photon Interactions* (Wiley, New York, 1992).

[134] P. D. Lett, W. D. Phillips, S. L. Rolston, C. E. Tanner, R. N. Watts, and C. I. Westbrook, "Optical molasses," J. Opt. Soc. Am. B **6,** 2084 (1989).

[135] T. W. Hänsch and A. L. Schawlow, "Cooling of Gases by Laser Radiation," Opt. Commun. **13,** 68–69 (1975).

[136] M. Gajda and J. Mostowski, "Three-dimensional theory of the magneto-optical trap: Doppler cooling in the low-intensity limit," Phys. Rev. A **49,** 4864–4875 (1994).

[137] S. Chu, "The manipulation of neutral particles," Rev. Mod. Phys. **70,** 685–706 (1998).

[138] C. N. Cohen-Tannoudji, "Manipulating atoms with photons," Rev. Mod. Phys. **70,** 707–719 (1998).

[139] W. D. Phillips, "Laser cooling and trapping of neutral atoms," Rev. Mod. Phys. **70,** 721–741 (1998).

[140] D. J. Wineland and W. M. Itano, "Laser cooling," Physics Today **40,** 34–40 (1987).

[141] C. J. Foot, "Laser cooling and trapping of atoms," Contemp. Phys. **32,** 369–381 (1991).

[142] H. Metcalf and P. van der Straten, "Cooling and trapping of neutral atoms," Phys. Rep. **244,** 204–286 (1994).

[143] C. S. Adams and E. Riis, "Laser cooling and trapping of neutral atoms," Prog. Quant. Electr. **21,** 1–79 (1997).

[144] Heidelberg atom trapping list: http://pluto.mpi-hd.mpg.de/ato/lasercool/atomtraps.html .

[145] C. Monroe, W. Swann, H. Robinson, and C. Wieman, "Very cold trapped atoms in a vapor cell," Phys. Rev. Lett. **65,** 1571–1574 (1990).

[146] C. Wieman, G. Flowers, and S. Gilbert, "Inexpensive laser cooling and trapping experiment for undergraduate laboratories," Am. J. Phys. **63,** 317–330 (1995).

[147] K. Lindquist, M. Stephens, and C. Wieman, "Experimental and theoretical study of the vapor-cell Zeeman optical trap," Phys. Rev. A **46,** 4082–4090 (1992).

[148] S. D. Gensemer, V. Sanchez-Villicana, K. Y. N. Tan, T. T. Grove, and P. L. Gould, "Trap-loss collisions of ^{85}Rb and ^{87}Rb: Dependence on trap parameters," Phys. Rev. A **56,** 4055–4063 (1997).

[149] C. D. Wallace, T. P. Dinneen, K.-Y. N. Tan, T. T. Grove, and P. L. Gould, "Isotopic difference in trap loss collisions of laser cooled rubidium atoms," Phys. Rev. Lett. **69,** 897–900 (1992).

[150] *Foundations of Vacuum Science and Technology*, J. M. Lafferty, ed., (John Wiley & Sons, New York, 1998), pp. 81–90,625.

[151] M. Stephens, K. Lindquist, and C. Wieman, "Optimizing the capture process in optical traps," Hyperfine Interactions **81,** 203–215 (1993).

[152] M. Stephens and C. Wieman, "High collection efficiency in a laser trap," Phys. Rev. Lett. **72,** 3787–3790 (1994).

[153] F. Reif, *Fundamentals of Statistical and Thermal Physics* (McGraw-Hill, New York, 1965), pp. 574–577.

[154] J. Dalibard and C. Cohen-Tannoudji, "Laser cooling below the Doppler limit by polarization gradients: simple theoretical models," J. Opt. Soc. Am. B **6,** 2023–2045 (1989).

[155] P. J. Ungar, D. S. Weiss, E. Riis, and S. Chu, "Optical molasses and multilevel atoms: theory," J. Opt. Soc. Am. B **6,** 2058–2071 (1989).

[156] S. A. Hopkins and A. V. Durrant, "Parameters for polarisation gradients in three-dimensional electromagnetic standing waves," Phys. Rev. A **56,** 4012–4022 (1997).

[157] C. D. Wallace, T. P. Dinneen, K. Y. N. Tan, A. Kumarakrishnan, P. L. Gould, and J. Javaneinen, "Measurements of temperature and spring constant in a magneto-optical trap," J. Opt. Soc. Am. B **11,** 703–711 (1994).

[158] A. M. Steane and C. J. Foot, "Laser cooling below the doppler limit in a magneto-optical trap," Europhys. Lett. **14,** 231–236 (1991).

[159] A. M. Steane, M. Chowdhury, and C. J. Foot, "Radiation force in the magneto-optical trap," J. Opt. Soc. Am. B **9,** 2142–2158 (1992).

[160] J. Lawall, S. Kulin, B. Saubamea, N. Bigelow, M. Leduc, and C. Cohen-Tannoudji, "Three-dimensional laser cooling of helium beyond the single-photon recoil limit," Phys. Rev. Lett. **75,** 4194–4197 (1995).

[161] J. Dalibard, "Laser Cooling of an Optically Thick Gas: The Simplest Radiation Pressure Trap?," Opt. Commun. **68,** 203–208 (1988).

[162] A. S. Arnold and P. J. Manson, "Atomic density and temperature distributions in magneto-optical traps," to appear in J. Opt. Soc. Am. B .

[163] C. G. Townsend, N. H. Edwards, C. J. Cooper, K. P. Zetie, C. J. Foot, A. M. Steane, P. Szriftgiser, H. Perrin, and J. Dalibard, "Phase-space density in the magneto-optical trap," Phys. Rev. A **52,** 1423–1440 (1995).

[164] D. Hoffman, P. Feng, and T. Walker, "Measurement of Rb trap-loss collision spectra," J. Opt. Soc. Am. B **11,** 712–720 (1994).

[165] C. Gabbanini, A. Evangelista, S. Gozzini, A. Lucchesini, A. Fioretti, J. Müller, M. Colla, and E. Arimondo, "Scaling laws in magneto-optical traps," Europhys. Lett. **37,** 251–256 (1997).

[166] S. Grego, M. Colla, A. Fioretti, J. H. Müller, P. Verkerk, and E. Arimondo, "A cesium magneto-optical trap for cold-collision studies," Opt. Commun. **132,** 519–526 (1996).

[167] K. Ellinger, J. Cooper, and P. Zoller, "Light-pressure force in N-atom systems," Phys. Rev. A **49,** 3909–3933 (1994).

[168] C. J. Cooper, G. Hillenbrand, J. Rink, C. G. Townsend, K. Zetie, and C. J. Foot, "The temperature of atoms in a magneto-optical trap," Europhys. Lett. **28,** 397–402 (1994).

[169] M. Drewsen, P. Laurent, A. Nadir, G. Santarelli, A. Clairon, Y. Castin, D. Grison, and C. Salomon, "Investigation of sub-Doppler cooling effects in a cesium magneto-optical trap," Appl. Phys. B **59,** 283–298 (1994).

[170] K. Ellinger and J. Cooper, "Many-particle effects in laser cooling of one-dimensional optical molasses," Phys. Rev. A **55,** 4351–4376 (1997).

[171] G. Hillenbrand, C. J. Foot, and K. Burnett, "Heating due to long-range photon exchange interactions between cold atoms," Phys. Rev. A **50,** 1479–1489 (1994).

[172] G. Hillenbrand, K. Burnett, and C. J. Foot, "Effect of scattered radiation on sub-Doppler cooling," Phys. Rev. A **52,** 4763–4786 (1995).

[173] C. J. Myatt, "Bose-Einstein condensation experiments in a dilute vapor of rubidium," PhD thesis, University of Colorado (1997).

[174] D. S. Weiss, E. Riis, Y. Shevy, P. J. Ungar, and S. Chu, "Optical molasses and multilevel atoms: experiment," J. Opt. Soc. Am. B **6,** 2072–2083 (1989).

[175] M. Arndt, M. B. Dahan, D. Guéry-Odelin, M. W. Reynolds, and J. Dalibard, "Observation of a zero-energy resonance in Cs-Cs collisions," Phys. Rev. Lett. **79,** 625–628 (1997).

[176] O. Stern, Z. Phys. **7,** 249–253 (1921).

[177] O. Stern and W. Gerlach, Z. Phys. **8,** 110–111 (1921).

[178] W. H. Wing, "On neutral particle trapping in quasistatic electromagnetic fields," Prog. In Quantum Electron. **8,** 181–199 (1984).

[179] R. V. E. Lovelace, C. Mehanian, T. J. Tommila, and D. M. Lee, "Magnetic confinement of a neutral gas," Nature **318,** 30–36 (1985).

[180] C. Sackett, E. Cornell, C. Monroe, and C. Wieman, "A magnetic suspension system for atoms and bar magnets," Am. J. Phys. **61,** 304–309 (1993).

[181] E. A. Cornell, C. Monroe, and C. E. Wieman, "Multiply loaded, AC magnetic trap for neutral atoms," Phys. Rev. Lett. **67,** 2439–2442 (1991).

[182] T. Bergeman, G. Erez, and H. J. Metcalf, "Magnetostatic trapping fields for neutral atoms," Phys. Rev. A **35,** 1535–1546 (1987).

[183] E. R. Peck, *Electricity and Magnetism* (McGraw-Hill, New York, 1952), pp. 206,262–263.

[184] I. S. Gradshteyn and I. M. Ryzhik, *Table of integrals, series, and products* (Academic Press, New York, 1980), pp. 904–925.

[185] A. L. Migdall, J. V. Prodan, W. D. Phillips, T. H. Bergeman, and H. J. Metcalf, "First observation of magnetically trapped neutral atoms," Phys. Rev. Lett. **54,** 2596–2599 (1985).

[186] V. E. Shapiro, "Rotating quadrupole field traps for neutral atoms," Phys. Rev. A **54,** R1018–R1021 (1996).

[187] W. Ketterle and D. E. Pritchard, "Atom cooling by time-dependent potentials," Phys. Rev. A **46,** 4051–4054 (1992).

[188] P. W. H. Pinske, A. Mosk, M. Weidermüller, M. W. Reynolds, T. W. Hijmans, and J. T. M. Walraven, "Adiabatically changing the phase-space density of a trapped Bose gas," Phys. Rev. Lett. **78,** 990–993 (1997).

[189] H. Hess, Bull. Am. Phys. Soc. **30,** 854 (1985).

[190] W. Ketterle and N. J. V. Druten, "Evaporative cooling of trapped atoms," Adv. Atom. Mol. Opt. Phys. **37,** 181–236 (1996).

[191] K. B. Davis, M. O. Mewes, M. A. Joffe, M. R. Andrews, and W. Ketterle, "Evaporative cooling of sodium atoms," Phys. Rev. Lett. **74,** 5202–5205 (1995).

[192] N. R. Newbury, C. J. Myatt, and C. E. Wieman, "S-wave elastic collisions between cold ground-state ^{87}Rb atoms," Phys. Rev. A **51,** R2680–R2683 (1995).

[193] C. A. Sackett, C. C. Bradley, and R. G. Hulet, "Optimization of evaporative cooling," Phys. Rev. A **55,** 3797–3801 (1997).

[194] K. Berg-Sørensen, "Kinetics for evaporative cooling of a trapped gas," Phys. Rev. A **55,** 1281–1287 (1997).

[195] H. Wu and C. J. Foot, "Direct simulation of evaporative cooling," J. Phys. B **29,** L321–L328 (1996).

[196] H. Wu, E. Arimondo, and C. J. Foot, "Dynamics of evaporative cooling for Bose-Einstein condensation," Phys. Rev. A **56,** 560–569 (1997).

[197] J. H. Marquardt, F. C. Cruz, M. Stephens, C. W. Oates, L. W. Hollberg, J. C. Bergquist, D. F. Welch, D. Mehuys, and S. Sanders, "Grating-tuned semiconductor MOPA lasers for precision spectroscopy," Proc. SPIE Conf. **2834,** 34–40 (1996).

[198] A. C. Wilson, J. C. Sharpe, C. R. McKenzie, P. J. Manson, and D. M. Warrington, "Narrow-linewidth MOPA based on a semiconductor tapered amplifier," Appl. Opt. **37,** 4871–4875 (1998).

[199] K. E. Gibble, S. Kasapi, and S. Chu, "Improved magneto-optic trapping in a vapor cell," Opt. Lett. **17,** 526–528 (1992).

[200] K. Gibble, S. Chang, and R. Legere, "Direct observation of s-wave atomic collisions," Phys. Rev. Lett. **75,** 2666–2669 (1995).

[201] K. B. MacAdam, A. Steinbach, and C. Wieman, "A narrow-band tunable diode-laser system with grating feedback, and a saturated absorption spectrometer for Cs and Rb," Am. J. Phys. **60,** 1098–1111 (1992).

[202] A. Mooradian, "Laser linewidth," Physics Today **38,** 42–47 (1985).

[203] A. S. Arnold, J. S. Wilson, and M. G. Boshier, "A simple extended-cavity diode laser," Rev. Sci. Instrum. **69,** 1236–1239 (1998).

[204] W. Demtröder, *Laser Spectroscopy*, 2nd ed. (Springer, Berlin, 1998).

[205] A. Yariv, *Optical Electronics in Modern Communications*, 5th ed. (O.U.P., Oxford, 1997).

[206] K. L. Corwin, Z.-T. Lu, C. F. Hand, R. J. Epstein, and C. E. Wieman, "Frequency-stabilized diode laser with the Zeeman shift in an atomic vapor," Appl. Opt. **37,** 3295–3298 (1998).

[207] B. DeMarco, H. Rohner, and D. S. Jin, "An enriched ^{40}K source for fermionic atom studies," Rev. Sci. Instrum. **70,** 1967–1969 (1999).

[208] E. Hecht, *Optics*, 2nd ed. (Addison-Wesley, Reading, 1987), pp. 570–577.

[209] G. Dudle, N. Sagna, P. Berthoud, and P. Thomann, "Anisotropic magneto-optical trapping of atoms: capture efficiency and induced drift velocities," J. Phys. B **29,** 4659–4673 (1996).

[210] C. Salomon, J. Dalibard, W. D. Phillips, A. Clairon, and S. Guellati, "Laser cooling of cesium atoms below $3\,\mu$K," Europhys. Lett. **12,** 683–688 (1990).

[211] E. Hagley, http://www.itp.ucsb.edu/online/bec/hagley1 .

[212] The Rabi frequency Ω for the $|2,2\rangle \rightarrow |2,1\rangle$ transition is $\hbar\Omega = \mu_B B/2$.

[213] M. Naraschewski and D. M. Stamper-Kurn, "Analytical description of a trapped semi-ideal Bose gas at finite temperature," Phys. Rev. A **58,** 2423–2426 (1998).

[214] I. G. Hughes, P. A. Barton, T. M. Roach, M. G. Boshier, and E. A. Hinds, "Atom optics with magnetic surfaces .1. Storage of cold atoms in a curved 'floppy disk'," J. Phys. B **30,** 647–658 (1997).

[215] I. G. Hughes, P. A. Barton, T. M. Roach, and E. A. Hinds, "Atom optics with magnetic surfaces .2. Microscopic analysis of the 'floppy disk' mirror," J. Phys. B **30,** 2119–2132 (1997).

[216] A. I. Sidorov, R. J. McLean, W. J. Rowlands, D. C. Lau, J. E. Murphy, M. Walkiewicz, G. I. Opat, and P. Hannaford, Quantum Semiclass. Opt. **8,** 713 (1996).

[217] A. I. Sidorov, D. C. Lau, G. I. Opat, R. J. McLean, W. J. Rowlands, and P. Hannaford, "Magneto-static optical elements for laser-cooled atoms," Laser Physics **8,** 642–648 (1998).

[218] D. C. Lau, A. I. Sidorov, G. I. Opat, R. J. McLean, W. J. Rowlands, and P. Hannaford, "Reflection of cold atoms from an array of current-carrying wires," Eur. Phys. J. D **5,** 193–199 (1999).

[219] E. Marechal, S. Guibal, J. L. Bossennec, R. Barbe, J. C. Keller, and O. Gorceix, "Longitudinal focusing of an atomic cloud using pulsed magnetic forces," Phys. Rev. A **59,** 4636–4640 (1999).

[220] J. Summhammer, L. Niel, and H. Rauch, "Focusing of pulsed neutrons by traveling magnetic potentials," Z. Phys. B **62,** 269–278 (1986).

[221] P. Horowitz and W. Hill, *The Art of Electronics*, 2nd ed. (Cambridge Uni. Press, Cambridge, 1993), p. 169.